UC Berkeley

Title

Controlling the Nanostructure of Solution-Processed Thin-Film Organic Electronics

Permalink

Author

Yiu, Alan

Publication Date

2013

Peer reviewed|Thesis/dissertation

Controlling the Nanostructure of
Solution-Processed Thin-Film Organic Electronics

by

Alan Tzi-Hong Yiu

A dissertation submitted in partial satisfaction of the

Requirements for the degree of

Doctor of Philosophy

in

Chemical Engineering

in the

Graduate Division

of the

University of California, Berkeley

Committee in charge:

Professor Jean M. J. Fréchet, Chair
Professor Rachel Segalman
Professor Ana Claudia Arias

Fall 2013

Controlling the Nanostructure of
Solution-Processed Thin-Film Organic Electronics

Abstract

Controlling the Nanostructure of
Solution-Processed Thin-Film Organic Electronics

by

Alan Tzi-Hong Yiu

Doctor of Philosophy in Chemical Engineering

University of California, Berkeley

Professor Jean M. J. Fréchet, Chair

Organic semiconductors hold the promise of electronic devices whose manufacturing scalability and form factor versatility could disrupt the existing electronics market. From a commercial feasibility standpoint, however, the technology is still in its relative infancy. To date, significant research effort has been directed toward developing polymers and small molecules for use in solution-processed thin-film bulk heterojunction organic photovoltaics (BHJ OPVs) and field-effect transistors (OFETs). A key goal of this research is to better understand the structure-property relationships that govern material performance. Molecular structure has been shown to influence material properties such as light absorption, intermolecular electronic compatibility, charge transport characteristics, thin-film morphology, and molecular packing. Similarly, processing steps such as the use of certain electronic interlayers or the incorporation of solvent additives can have a dramatic improvement on device performance.

In this work, polymer and small molecule systems are used to investigate such structure-property relationships, particularly ones governing solid-state nanostructure. Seemingly small changes in structure are shown to have a significant and systematic impact on OPV and OFET device performance. We investigate how a solution-processed organic semiconductor's π-conjugated backbone, end-capping groups, and solubilizing aliphatic side-chains can have a profound impact on nanostructure and device performance. In addition, we study how the processing conditions of polymers used in OPV and OFET devices affect solution-phase thermodynamics, as well as the dynamics of spin-coating and film formation. In both polymer and small molecule systems, we have demonstrated forward-looking design and processing principles that can inform the development of the next generation of ever higher-performing OPV and OFET materials.

To Mom and Dad
for your unending love and support

Acknowledgements

"I have no special talent. I am only passionately curious."
– Albert Einstein

Graduate school has been mundane, but exhilarating; exhausting, but carefree; aimless, but purposeful. It has been a period of tremendous personal growth and has rooted in me a belief in the power of imagination, curiosity, patience, and boldness. At the same time, it has been a period of appreciating and cultivating the outward relationships that I have come to cherish. As surely as I consider the following pages a celebration of my work over the past four years, so do I also consider myself small and insignificant. Nothing I have accomplished would have been possible without the mentors, colleagues, friends, and family with which I was blessed during this journey.

First and foremost, to Professor Fréchet: thank you for making this tremendous opportunity a reality. You taught me that finding the answer is easy—the real challenge is finding the right question. I continue to be inspired by your insatiable curiosity and passion for seeking out and attacking new challenges.

To my collaborators at SSRL, Chris Tassone, Kristin Schmidt, and Mike Toney: thank you for always being so generous with your time and your unparalleled expertise.

I've been privileged to work with some amazing people in the past four years. To Claire Woo, incredible mentor, teacher, and role model: thank you for helping me settle into the right track in my graduate school career. You always knew when to hold my hand and when to let me bang my head against the (proverbial) wall. Following in your footsteps wasn't easy, but it certainly gave me the best example to follow. To Jeremy Niskala, the best labmate, partner in science, and friend that I could have hoped for: thank you for bringing your infectious can-do attitude, unmatched raw research horsepower, creative insight, and just a lot of fun to 20 Lewis. I'll miss Friday afternoon "brainstorming", rounding the bases with you on your should-have-been-a-walk-off moonshot, prepping for the NFL Combine together, and eating about 10,000 calories of junk food at the beamline. To Olivia Lee, Jessica Douglas, Mark Chen, and Pierre Beaujuge: thank you for working all those long nights to synthesize all the materials I used. All of you are obviously gifted and really made life easy for me—without you guys behind the helm upstairs, I'd probably be here until 2050. Finally, I would also like to say a big thank you to rest of the PV team, both past and present, with whom I had the privilege of working: Jill Millstone, Tom Holcombe, Dave Unruh, Claudia Piliego, Gianmarco Griffini, and Seita Onishi. To Chona DeMesa and Cezar Ramiro: thank you for always working behind the scenes to make sure everything went smoothly for us.

Thank you to all my friends, new and old, with whom I've shared these past four years. Late nights, adventurous days, pickup ball, and weekend getaways—signs of a life well-lived. To the men of HQ, to the Pentapod, and especially to George: let's continue to live life to the fullest.

Finally, to Mom, Dad, Pannyun, and Leo: thank you for your constant love and support. I can only hope to one day have the grace, wisdom, and love that you have shown me throughout my life.bau

Table of Contents

Chapter 1

Overview of Organic Electronics – Material and Device Design, Processing, and Characterization

1.1. Motivation

Energy is the basis of life. It is the capacity to resist, at least locally, the unwavering march of entropy. Mankind has long distinguished itself from other species on Earth by its innovative ways of collecting and harnessing energy. Hunting and gathering gave way to livestock and agriculture, wood fires to oil and gas. As our civilization has grown and advanced, so too has our thirst for energy. From something as simple as a spoon to something as complex as a microprocessor, everything we know is made possible by a global infrastructure of energy generation and distribution. It should come as no surprise, then, that energy companies account for eight of the top ten highest revenue companies in the world.[1] Oil wells, offshore drilling, refineries, power plants, combustion engines, and power lines—these are the backbone of the modern economy.

Yet even in all his ingenuity, man falls astronomically short of Mother Nature's example. Some 150 million kilometers away, a blazing ball of fusion power 109 times the diameter[2] and 330,000 times the mass[3] of the Earth has been producing 385 yottawatts of power[4] for a thousand times the duration of human history.[5] A tiny, almost negligible fraction of this power—less than one billionth of it—eventually reaches the Earth in the form of solar radiation. Yet, at 174 petawatts, this fraction could provide in just one hour the amount of energy that all of mankind uses in an entire year.[6] The Sun is essentially the Earth's only steady-state energy input and, as it always has, fuels nearly all life as we know it. Harnessing solar energy therefore represents an ideal and likely inevitable future for human energy production. Amidst growing global concerns over global warming, energy security, and the eventual depletion of non-renewable energy sources, solar power has emerged as a clean, efficient, and reliable generation technology.

The Solar Industry. Despite falling into a lull in the past couple of years, the solar photovoltaics (PV) industry is very much alive. Since the turn of the century, it has grown from a far-off notion to a $100 billion dollar global business, with over 65 GW of PV capacity installed worldwide. Despite the end of substantial government subsidies, PV prices are projected to continue to drop in the next several years as manufacturing capacity doubles and underlying costs decrease by as much as 10 percent each year. By 2020, a fully installed residential PV system could reach costs as low as $1 per watt peak. Even with more conservative cost reduction estimates, an additional 400 to 600 GW of PV capacity is expected to be installed between now and the end of the decade.[7] Conventional semiconductor materials such as silicon (Si), cadmium telluride (CdTe), and copper indium gallium selenide (CIGS) are the dominant PV technologies, as they offer relatively high efficiency (per cost), durability, and known manufacturing practices. Although they are just recently being commercialized at large scale, though, these are decades-old technologies. The dramatic industry growth in the past decade has leaned heavily on industrial and academic R&D expenditure in basic PV technology and manufacturing, much of which grew out of expertise in the semiconductor and microprocessor industry.

Organic Photovoltaics. So-called "plastic" solar cells, based on organic polymers and small molecules, offer an intriguing alternative to conventional (inorganic) PV technologies. Organic photovoltaics (OPVs) can be manufactured from abundant precursors and processed from solution at near-ambient conditions. They have the

potential to be printed in large-area formats in continuous, high-throughput processes with low energy input requirements. In comparison, conventional semiconductor materials suffer a number of processing drawbacks: high energy input requirements (Si), complex and sensitive manufacturing techniques (CIGS), and material component toxicity (CdTe). Furthermore, thin-film plastic solar cells can be printed on a variety of different substrates, including flexible ones, opening up a wide range of potential applications. Given these advantages, OPVs could soon be a disruptive new entrant in the PV industry. However, despite substantial research in both academic and industrial institutions in the past 10-20 years, OPVs have yet to see commercial success. Challenges such as relatively low power conversion efficiency (PCE), poor material durability, and manufacturing scalability have, for the most part, kept OPVs from breaking out of research labs and into a growing PV market.

The current state-of-the-art for OPVs is the "bulk heterojunction" device architecture (**Fig. 1-1**), in which a light-absorbing conjugated polymer is intermixed with an electron-accepting fullerene-based small molecule. For such systems, the highest reported PCEs are 9.2% in academic literature[8] and 12% in commercial labs.[9] For the first time in the history of the field, these efficiency numbers are beginning to approach those of lower-cost inorganic material systems, such as amorphous and polycrystalline Si and CIGS. However, only a few select material systems have achieved such high efficiencies. Furthermore, durability and scalability challenges still loom large. Looking ahead in OPV research—and the broader field of organic semiconductor research—it is apparent that far-reaching gains are still to be had from developing better structure-property relationships. In other words, how can the chemical structure of these polymers and small molecules be designed to give the best material scalability, processability, and performance? What are the key factors that govern these properties, and can we formulate a generalized understanding of all the competing factors at play? These are the types of questions that our lab has sought to answer in our investigation of organic semiconductor materials.
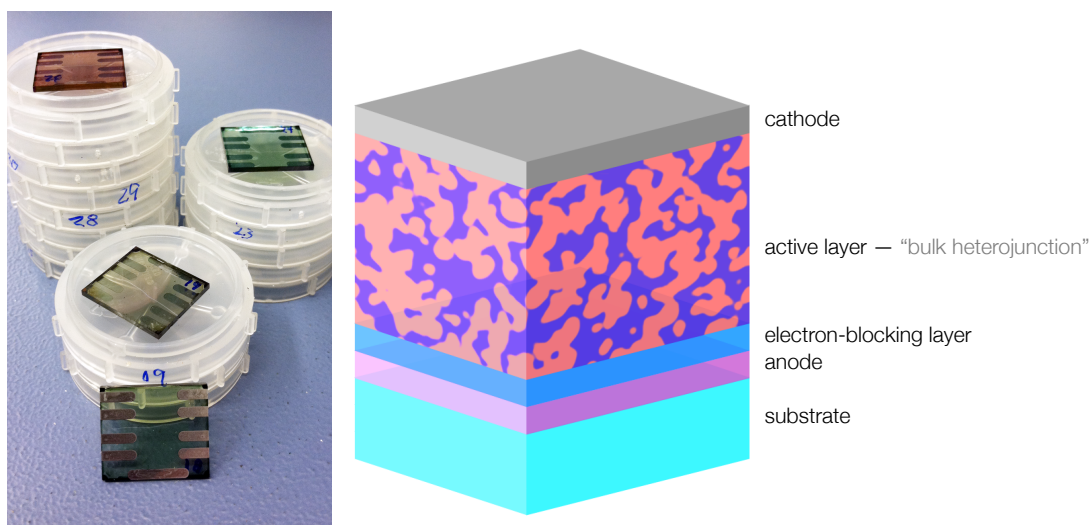
Figure 1-1: Sample organic solar cells manufactured in our lab (left) and a cartoon depicting a cross-section (not to scale) of a bulk heterojunction organic solar cell (right).

1.2. Device Operation

As with any solar cell, the function of an organic solar cell is to convert light energy, in the form of photons, into electric current, in the form of conduction electrons. The first step in this conversion process is photoexcitation of an electron by an incident photon of sufficient energy (**Fig. 1-2a**). Canonically, the "donor" polymer accounts for the majority the light absorption and charge generation, while the "acceptor" molecule is required for the proper flow of charge. In reality, either phase can absorb light and generate charge. In inorganic solar cells, photoexcitation results in the immediate generation of a free electron-hole pair, after which the built in electric field of the p-n junction drives these free charges to their respective electrodes.
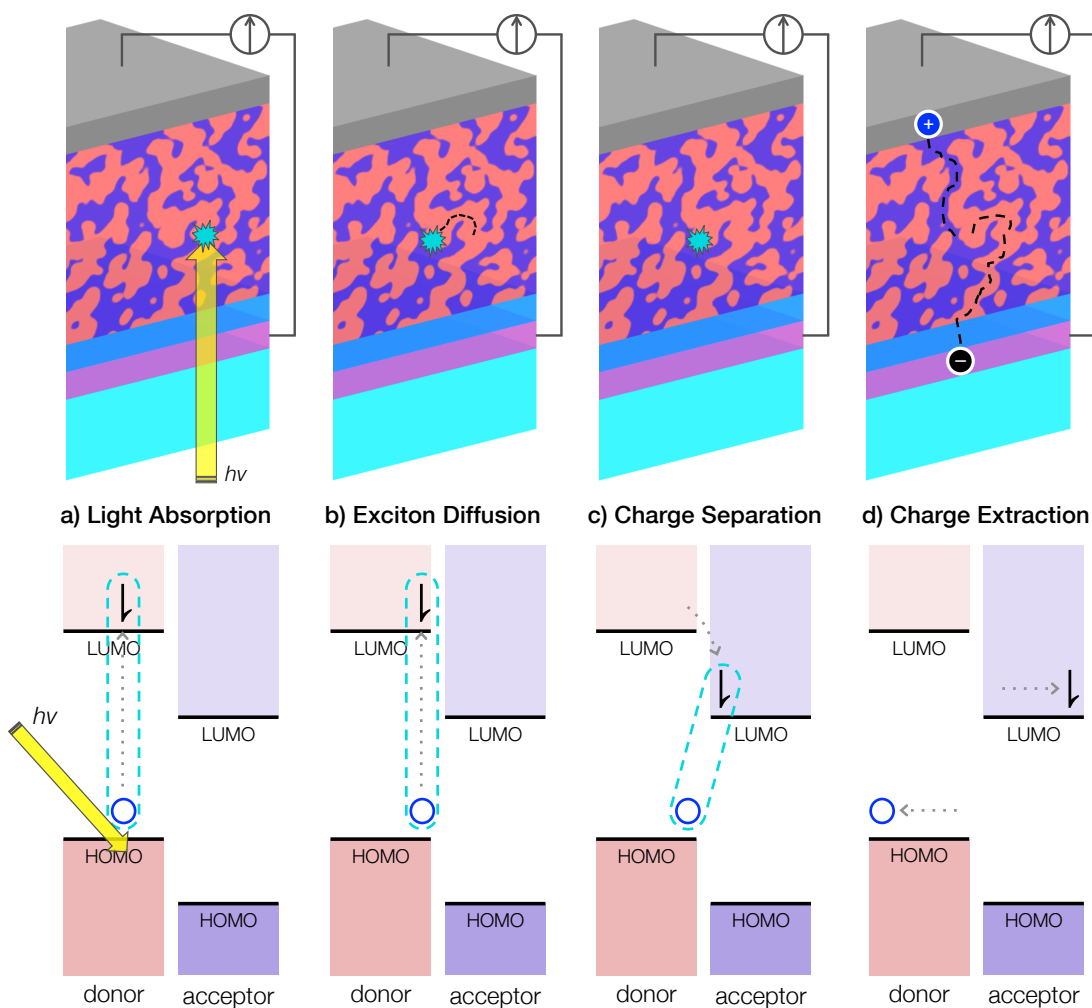
Figure 1-2: Representative device cartoon (top, not to scale) and energy levels (bottom) of the steps in the operation of a BHJ organic solar cell. a) Light absorption in the donor material causes photoexcitation of an electron, which stays adjacent to its conjugate hole in a Coulombically- bound state called an exciton. b) The exciton, which is a neutral mobile species, must diffuse to an interface between the donor and acceptor phases. c) The LUMO-LUMO offset between the donor and acceptor materials provides a driving force for excited electron transfer to the acceptor material. The electron and hole may remain Coulombically bound in the charge transfer state, but can now split into free charges in their respective phases. d) The free electron and hole must now migrate through their respective phases to reach their respective electrodes.

In inorganic solar cells, however, the relatively low dielectric constant and spatial restriction of electronic wavefunctions causes the photoexcited electron to be Coulombically bound to its conjugate hole. This tightly-bound electron-hole pair, called an exciton, is a mobile, electrically-neutral species that can diffuse about within the donor material (**Fig. 1-2b**).[10] Due to its short lifetime before recombination (on the order of nanoseconds), it can typically only diffuse a short distance of ~5–10 nm. In order for the exciton to split into a free hole and electron, it must first diffuse to an interface between the donor and acceptor materials. There, the energetic offset between the two materials' lowest unoccupied molecular orbitals (LUMOs) can provide a driving force for the excited electron to be transferred to the acceptor material. Although the electron and hole are now localized on different materials, they can still be Coulombically bound across the material interface in a "charge transfer (CT) state" (**Fig. 1-2c**).[11-13] Once the CT state has successfully separated into a free hole and electron, each must migrate through its respective material phase to its respective electrode, where it can be collected and flow through the external circuit (**Fig. 1-2d**). The energy level offset between material phases and the chemical potential gradient resulting from the high concentration of holes and electrons at the donor-acceptor interface act as driving forces for charge migration to the electrodes. Charge transport through bulk organic materials proceeds through a combination of band-like conduction through a conjugated regions and charge hopping between regions or molecules.[14-16]

Loss Mechanisms. At every step of device operation, loss mechanisms can limit the overall device efficiency. The overall power conversion efficiency, which is the ratio of the device's output power to the incident solar power, is a product of the efficiency of each step of operation: light absorption, exciton diffusion, charge separation, and charge transport (**Eq. 1-1**). A solar cell that is too thin or has poor light attenuation will not absorb all of the incident light, letting light energy pass through the device unharnessed. A bulk heterojunction film whose phase domains are too large will suffer from excessive exciton recombination, as excitons will not be able to diffuse far enough to reach a donor-acceptor interface. Insufficient donor-acceptor interfacial contact, poor energy level alignment, and interfacial trap sites can inhibit charge separation and lead to recombination in the CT state. Finally, discontinuous phase domains, poor structural order, and low intrinsic charge carrier mobility can lead to uncollected charges or recombination of free charges.

$$\text{PCE} = \eta = \eta_{\text{absorption}} \cdot \eta_{\text{diffusion}} \cdot \eta_{\text{separation}} \cdot \eta_{\text{transport}} \qquad (1\text{-}1)$$

1.3. Device Fabrication and Testing

For conventional lab-scale experimental OPV devices (e.g., **Fig. 1-1**), we begin with glass substrates coated on one surface with indium tin oxide (ITO). ITO is a nearly transparent conductor that serves as the device anode. The ITO-on-glass substrates are cleaned by sonication in a series of solvents, followed by UV-ozone treatment. Next, a ~30-nm thick layer of the ionomer mixture poly(3,4-ethylenedioxythiophene) poly(styrenesulfonate) (PEDOT:PSS) is spin-coated onto the ITO substrates from

aqueous suspension. The PEDOT:PSS films are dried at 140 °C in air to drive off residual water before being transferred to a N_2-filled glovebox. Under inert atmosphere, the active layers are spin-coated from blend solutions of the donor and acceptor molecules in organic solvents such as chlorobenzene, chloroform, dichlorobenzene, THF, etc. Samples are then transferred to a vacuum thermal evaporator, in which the cathode—typically aluminum, often preceded by a thin layer of calcium or lithium fluoride—is deposited on top of the organic active layer.

Devices are tested using a solar simulator that outputs Air Mass 1.5 global (AM 1.5G) illumination (**Fig. 1-3**). The AM 1.5G spectrum corresponds to a solar azimuthal angle of 48.2°, at which the optical path length of solar radiation through the Earth's atmosphere is 1.5 times that of sunlight coming from directly overhead. AM 1.5G is the standard spectrum used for testing solar cells[17] because it reasonably approximates the overall yearly average irradiance for the mid-latitudes, where many of the world's population centers are located (e.g., the United States, China, Europe, Japan).
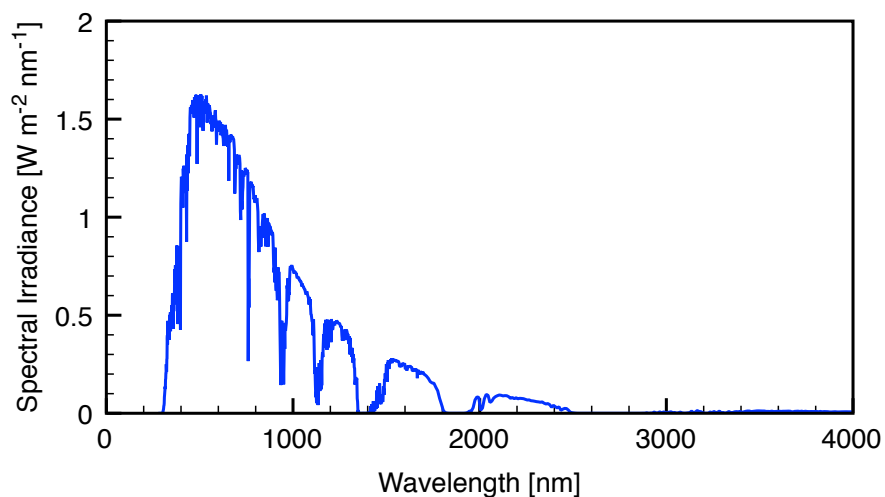
Figure 1-3: The AM 1.5G solar spectrum used for standardized solar cell testing.

Solar cell performance is evaluated by measuring the output current density (J) as a function of applied bias (V) under illumination of a known power density (P_{in}). A typical J-V output curve is shown in **Fig. 1-4**. At each point along the curve, the power density (P) of the device can be calculated according to **Eq. 1-2**, and the point with the highest power density is called the maximum power point (MPP), with output power density P_{MPP} (**Eq. 1-3**). The x-intercept of the curve is the open-circuit voltage (V_{OC}), which is the maximum voltage that the cell can provide to the external circuit. Although it is can be influenced by a variety of factors, the V_{OC} is derived from the difference between electron and hole quasi-Fermi levels—the difference between the HOMO of the donor material and the LUMO of the acceptor material.[18,19] It is also dependent on charge transfer complex formation at the donor-acceptor interface and subsequent charge recombination at this interface.[19-22] The y-intercept of the J-V curve is the short-circuit current density (J_{SC}), which is the current density output by the cell at zero bias. The J_{SC} is derived from the generation and collection of light-generated carriers, and depends on a

number of factors including the quantity and spectrum of light absorbed and the charge collection probability of each photoexcited electron-hole pair. The (x, y) point (V_{OC}, J_{SC}) is called the ideal power point (IPP) and represents the power density (P_{IPP}, **Eq. 1-4**) that could be output by the cell in an ideal scenario. In reality, however, non-idealities cause P_{MPP} to be of a smaller magnitude than P_{IPP}, and the ratio of the two is called the fill factor (*FF*, **Eq. 1-5**). In describing solar cell performance, the metrics typically presented are V_{OC}, J_{SC}, and *FF*, which together can be used to calculate the overall power conversion efficiency (PCE, **Eq. 1-6**).
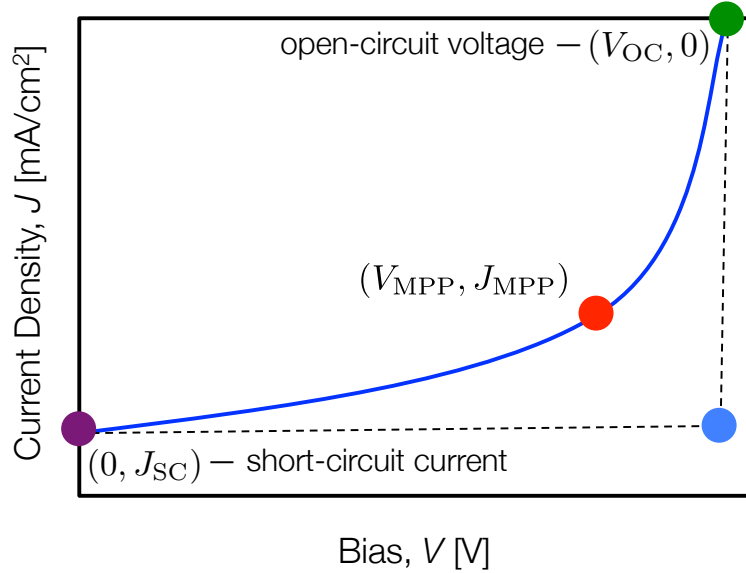
Figure 1-4: Example current density vs. bias (*J-V*) output curve for a solar cell.

$$P = J \cdot V \tag{1-2}$$

$$P_{MPP} = J_{MPP} \cdot V_{MPP} \tag{1-3}$$

$$P_{IPP} = J_{SC} \cdot V_{OC} \tag{1-4}$$

$$FF = \frac{P_{MPP}}{P_{IPP}} = \frac{J_{MPP} \cdot V_{MPP}}{J_{SC} \cdot V_{OC}} \tag{1-5}$$

$$PCE = \frac{P_{MPP}}{P_{in}} = \frac{J_{SC} \cdot V_{OC} \cdot FF}{P_{in}} \tag{1-6}$$

1.4. Material Characterization

In our work, we primarily utilize two techniques for characterizing our materials in neat and blend thin-films. For surface topography and blend morphology, we use atomic force microscopy (AFM). For crystal packing data, we use grazing-incidence wide-angle X-ray scattering (GIWAXS). These two powerful techniques are briefly introduced here.

Atomic Force Microscopy. AFM is a high-resolution form of scanning probe microscopy that allows for mechanical imaging of surface features down to nanometer resolution. At its core, the AFM consists of a miniature Si (or SiN) cantilever with a sharp tip (a few nanometers in tip radius) attached to the underside (see **Fig. 1-5**). As this tip interacts with the surface, the cantilever is deflected from its neutral position, and these deflections are measured via a laser beam reflecting off the top surface into an array of photodetectors. As is common with polymer samples, we operate our AFM in tapping mode. In tapping mode, a small piezoelectric driver oscillates the cantilever up and down at close to its resonant frequency. This mode if preferred for polymer samples because it reduces the chance of the tip "sticking" to the surface and also prevents damage to the sample and the tip. Height (topography) and phase AFM imagery provide valuable insight into the nature of the nano- and micro-scale phase separation and blend morphology of our thin-film samples.
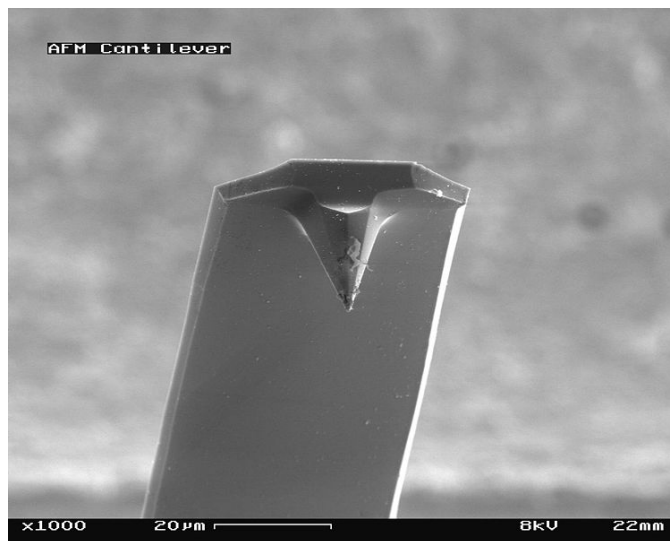

Figure 1-5: Example of an AFM cantilever with the tip clearly visible at the end (image credit: http://en.wikipedia.org/wiki/File:AFM_(used)_cantilever_in_Scanning_Electron_Microscope,_magnificati on_1000x.JPG).

Grazing-Incidence X-ray Scattering. To investigate the crystalline structure of our materials in thin-film, we use GIWAXS. Since organic materials are relatively amorphous and sensitive to X-ray damage compared to inorganic materials, the grazing-incidence geometry (see **Fig. 1-6**) is advantageous for our thin-film samples for a number of reasons. First, the very shallow angle of incidence (around 0.1° for most of our work) results in an extended path length through the film, providing ample material to interact with the incident X-ray beam and good signal-to-noise ratio. Second, the beam footprint is spread out across a relatively large area of the sample rather than being focused on one small target region, reducing the rate of sample degradation. Finally, the two-dimensional diffraction image obtained from grazing-incidence scans allows for rapid screening of a large set of reciprocal space. Wide-angle X-ray scattering is used to probe lattice spacings on the order of angstroms, which allows us to determine important lattice parameters such as π-π stacking distance (3–4 Å) and lamellar spacing (10–30 Å). In addition to

lattice structure, GIWAXS can be used to determine the mosaicity (preferred orientation) of crystallites on the substrate and parameters such as crystallite correlation length. All of these parameters can have important implications in charge transport and, as a result, in overall device performance.
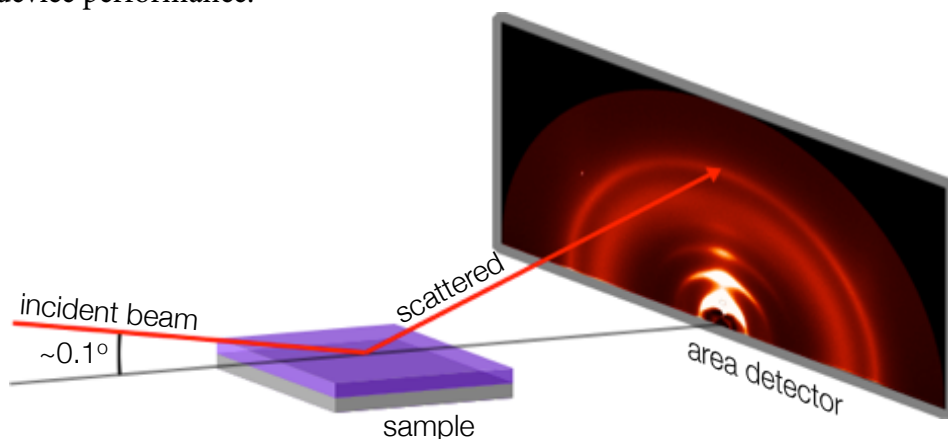
Figure 1-6: Diagram of a grazing-incidence X-ray scattering setup (not to scale). The incident beam encounters the thin-film sample at a very shallow angle (~0.1º) and the scattered beams are collected by an area detector.

1.5. Material Design and Processing Considerations

To push the boundaries of OPV performance, a significant portion of the research in the field has been directed toward developing polymer[8,23-32] and, to a lesser extent, small molecule[33-35] donors for use in BHJ devices with fullerene-based electron acceptors. Unlike with inorganic semiconductors, the synthetic possibilities for organic semiconducting molecules are endless. Every change to chemical structure can induce a cascade of effects on the resulting material and device properties. Thus, a holy grail of OPV material design is to develop an overarching understanding of the structure-property relationships that govern material performance. In the past, chemical structure of the donor material has been shown to influence light absorption,[36-38] molecular energetics,[39-43] charge transport characteristics,[14,44-47] blend film morphology,[48-50] and solid-state molecular packing,[47,51-54] among other properties. Similarly, device processing considerations such as the use of various electronic interlayers[8,55-58] and solvent additives[33,49,54] can have a dramatic effect on device performance. Understanding these relationships in isolation is relatively simple, but understanding them in concert is a tremendous ongoing challenge for the field. In practice, designing a molecule with the aim of improving one given material property will often worsen other properties. In the Chapters that follow, we present several material design and processing studies in which we establish novel material design platforms and processing principles, with the hope of advancing the realm of understanding and possibility in OPV research. Here, we provide a brief introduction to the principles described in these studies.

Side-Chain Tunability with Furan-Containing Backbones. The bulky, branched alkyl side-chains typically found on semiconducting polymers provide critical solution-processability, but they may also worsen electronic performance. As presented in **Chapter 2**, we hypothesized that reducing side-chain bulkiness could improve molecular

packing and promote self-assembly into extended crystalline domains, thereby improving device performance. As a model system, we used the *p*-type polymer backbone P(DPP-FTF), which consists of diketopyrrolopyrrole (DPP) copolymerized with alternating furan (F) and thiophene (T) units. Owing to the uniquely high solubility imparted by furan, P(DPP-FTF) is soluble with just linear alkyl side-chains (*n*-C_{12}, -C_{14}, or -C_{16}). Analysis by GIWAXS confirms our hypothesis, showing that, compared to branched side-chains, linear side-chains improve nanostructural order by reducing π-π stacking distances and increasing the correlation lengths of π-π and lamellar stacking and. Solar cells fabricated from P(DPP-FTF)-C_{14} exhibit power conversion efficiencies (PCEs) as high as 6.5%, which is substantially higher than the PCEs of *ca*. 5% achieved with the branched-alkyl–substituted variants. Thus, by leveraging the enhanced solubility imparted by furan, we show that side-chain design can be used to control nanostructural order and device performance.

Solution-Phase Aggregation Controls Solid-State Orientation. Building on these design principles, we fabricated OFETs from P(DPP-FTF) and P(DPP-3F) with linear (*n*-C_{16}) and branched (2-butyloctyl, 2BO) side-chains. As described in **Chapter 3**, these devices exhibit high average hole mobilities, from 0.19 to 1.82 cm^2/V·s, with P(DPP-3F)-C_{16} performing the best (maximum hole mobility of 2.25 cm^2/V·s). Atomic force microscopy and GIWAXS indicate that, as before, linear side-chains lead to larger crystalline domains, tighter π-π stacking, and longer-range crystalline order than do branched side-chains. In addition, the P(DPP-3F)-C_{16} polymer prefers a crystalline orientation where its π-π stacking direction is in-plane with the substrate, while the 2BO-substituted polymers pack with their π-π stacking primarily out-of-plane—this has a significant impact on charge transport anisotropy. Analysis of the polymer solution prior to film deposition shows a clear correlation between polymer aggregation in solution and π-π packing direction in the polymer film. We propose that early onset crystallite formation in solution leads to preferential deposition on the substrate in the in-plane orientation. This improved packing in the film leads to considerably higher device performance for the variants with linear side-chains, particularly P(DPP-3F)-C_{16}.

Small Molecules that Simulate Polymers. In parallel to this work on polymers, we also investigated small molecule systems. Like polymers, small molecules can be synthesized and solution-processed into devices on a large scale, but their monodispersity eliminates any variation in molecular weight distribution. As a result, they offer relatively straightforward synthesis, purification, and characterization. However, small molecules currently exhibit lower device PCEs than the highest-performing polymers. This relatively low performance may be attributed to limited molecular interconnectivity through the active layer, resulting in low device fill factors (FFs). In work presented in **Chapter 4**, we postulated that the introduction of strongly π-stacking end-groups in small molecules would facilitate end-to-end intermolecular interaction. A series of DPP-based *p*-type small molecules was synthesized with electron-rich end-groups of varying degrees of planarity and symmetry. As we predicted, the use of strongly π-stacking end-groups—in particular, symmetrically (C2) substituted pyrene—results in tight, aligned crystal packing and favorable film morphology dictated by π-π interactions, as supported by single crystal X-ray analysis and GIWAXS. In OPV devices, DPP-C2-pyrene achieves a

maximum PCE above 4% with a FF approaching 0.6, which is one of the highest FFs reported to date in high-performing small molecule BHJ OPVs.

Charge-Generating Non-Fullerene Small Molecule Acceptors. Given the high interconnectivity and charge mobility of DPP-C2-pyrene, we chose it as a model system for testing our novel series of *n*-type small molecules, as shown in **Chapter 5**. These molecules were designed with low electron affinities relative to the canonical fullerene-based *n*-type molecules, resulting in high device open-circuit voltages (V_{OC}) above 0.85 V. With a V_{OC} greater than 1 V and a fill factor of 0.60, our best device reached a PCE of 2.4%[10], which represents the highest-performing non-fullerene, all-small-molecule device in the literature. Interestingly, we show that, unlike in most BHJ OPV devices, charges are mainly generated upon excitation of our new *n*-type material rather than excitation of the *p*-type material. This record-performance for non-fullerene devices shows that light-absorbing fullerene substitutes are viable components for OPVs, which is a significant result in a field heavily dominated by fullerene-based *n*-type molecules.

Substrate Interlayers Modulate Solvent Additive Behavior. High-boiling solvent additives, such as 1,8-diiodooctane, are often used in organic photovoltaic device processing to improve device performance. Such additives are typically thought to modify solution-phase thermodynamics and also slow the rate of drying during spin-coating. However, little work had been done to consider the effects of the substrate in studying the effects of additives. In **Chapter 6**, we show that the extent to which solvent additives affect the nanostructure of thin-film BHJ OPV devices depends on the underlying substrate interlayer. We demonstrate that, in OPV devices, the same additive can produce a modest or dramatic improvement in performance depending on the underlying substrate interlayer. These results confirm our hypothesis that solution-substrate interactions play an important role in the evolution of nanostructure during the film formation process and underscore the need for more comprehensive study of the effect of solvent additives. To explore the different effects of the interlayer, we examine top and bottom surfaces of blend films using atomic force microscopy (AFM) and GIWAXS. GIWAXS data shows a clear correlation between π-π stacking correlation length and device PCE across all additives and interlayers. In addition, we show that additives modulate the π-π stacking correlation length over a much broader range on certain interlayer materials than they do on others.

1.6. References

(1)   In *Fortune* 2012; Vol. 166.
(2)   Brown, T. M.; Christensen-Dalsgaard, J. *The Astrophysical Journal Letters* **1998**, *500*, L195.
(3)   Woolfson, M. *Astronomy & Geophysics* **2000**, *41*, 1.12.
(4)   Williams, D. R. *Sun Fact Sheet*, NASA, 2012.
(5)   Bonanno, A.; Schlattl, H.; Paternò, L. *A&A* **2002**, *390*, 1115.
(6)   Morton, O. *Nature* **2006**, *443*, 19.
(7)   Aanesen, K.; Heck, S.; Pinner, D. *Solar power: Darkest before dawn*, McKinsey & Company, 2012.
(8)   He, Z.; Zhong, C.; Su, S.; Xu, M.; Wu, H.; Cao, Y. *Nat Photon* **2012**, *6*, 591.

(9)   Rohr, S. *Heliatek consolidates its technology leadership by establishing a new world record for organic solar technology with a cell efficiency of 12%*, Heliatek, 2013.

(10)   Gregg, B. A.; Hanna, M. C. *Journal of Applied Physics* **2003**, *93*, 3605.

(11)   Zhu, X. Y.; Yang, Q.; Muntwiler, M. *Accounts of Chemical Research* **2009**, *42*, 1779.

(12)   Loi, M. A.; Toffanin, S.; Muccini, M.; Forster, M.; Scherf, U.; Scharber, M. *Advanced Functional Materials* **2007**, *17*, 2111.

(13)   Muntwiler, M.; Yang, Q.; Tisdale, W. A.; Zhu, X. Y. *Physical Review Letters* **2008**, *101*, 196403.

(14)   Coropceanu, V.; Cornil, J.; da Silva Filho, D. A.; Olivier, Y.; Silbey, R.; Brédas, J.-L. *Chem. Rev.* **2007**, *107*, 926.

(15)   Kim, Y.; Cook, S.; Tuladhar, S. M.; Choulis, S. A.; Nelson, J.; Durrant, J. R.; Bradley, D. D. C.; Giles, M.; McCulloch, I.; Ha, C.-S.; Ree, M. *Nat Mater* **2006**, *5*, 197.

(16)   Street, R. A.; Northrup, J. E.; Salleo, A. *Phys. Rev. B* **2005**, *71*, 165202.

(17)   *Reference Solar Spectral Irradiance: Air Mass 1.5*, NREL.

(18)   Brabec, C. J.; Cravino, A.; Meissner, D.; Sariciftci, N. S.; Fromherz, T.; Rispens, M. T.; Sanchez, L.; Hummelen, J. C. *Advanced Functional Materials* **2001**, *11*, 374.

(19)   Vandewal, K.; Tvingstedt, K.; Gadisa, A.; Inganas, O.; Manca, J. V. *Nat Mater* **2009**, *8*, 904.

(20)   Kirchartz, T.; Mattheis, J.; Rau, U. *Physical Review B* **2008**, *78*, 235320.

(21)   Benson-Smith, J. J.; Goris, L.; Vandewal, K.; Haenen, K.; Manca, J. V.; Vanderzande, D.; Bradley, D. D. C.; Nelson, J. *Advanced Functional Materials* **2007**, *17*, 451.

(22)   Vandewal, K.; Gadisa, A.; Oosterbaan, W. D.; Bertho, S.; Banishoeib, F.; Van Severen, I.; Lutsen, L.; Cleij, T. J.; Vanderzande, D.; Manca, J. V. *Advanced Functional Materials* **2008**, *18*, 2064.

(23)   Thompson, B. C.; Fréchet, J. M. J. *Angew. Chem. Int. Ed.* **2008**, *47*, 58.

(24)   Boudreault, P.-L. T.; Najari, A.; Leclerc, M. *Chem. Mater.* **2011**, *23*, 456.

(25)   Bundgaard, E.; Krebs, F. C. *Sol. Energ. Mat. Sol. Cells* **2007**, *91*, 954.

(26)   Chen, L.-M.; Hong, Z.; Li, G.; Yang, Y. *Advanced Materials* **2009**, *21*, 1434.

(27)   Dennler, G.; Scharber, M. C.; Brabec, C. J. *Adv. Mater.* **2009**, *21*, 1323.

(28)   Gunes, S.; Neugebauer, H.; Sariciftci, N. S. *Chem. Rev.* **2007**, *107*, 1324.

(29)   He, Z.; Zhong, C.; Huang, X.; Wong, W.-Y.; Wu, H.; Chen, L.; Su, S.; Cao, Y. *Advanced Materials* **2011**, *23*, 4636.

(30)   Li, C.; Liu, M.; Pschirer, N. G.; Baumgarten, M.; Müllen, K. *Chem. Rev.* **2010**, *ASAP*.

(31)   Li, Y.; Sonar, P.; Singh, S. P.; Soh, M. S.; van Meurs, M.; Tan, J. *J. Am. Chem. Soc.* **2011**, *133*, 2198.

(32)   Scharber, M. C.; Mühlbacher, D.; Koppe, M.; Denk, P.; Waldauf, C.; Heeger, A. J.; Brabec, C. J. *Adv. Mater.* **2006**, *18*, 789.

(33)   Sun, Y.; Welch, G. C.; Leong, W. L.; Takacs, C. J.; Bazan, G. C.; Heeger, A. J. *Nat Mater* **2012**, *11*, 44.

(34)   Walker, B.; Tamayo, A. B.; Dang, X.-D.; Zalar, P.; Seo, J. H.; Garcia, A.; Tantiwiwat, M.; Nguyen, T.-Q. *Advanced Functional Materials* **2009**, *19*, 3063.

(35)   Lee, O. P.; Yiu, A. T.; Beaujuge, P. M.; Woo, C. H.; Holcombe, T. W.; Millstone, J. E.; Douglas, J. D.; Chen, M. S.; Fréchet, J. M. J. *Advanced Materials* **2011**, *23*, 5359.

(36)   Hou, J.; Tan, Z. a.; Yan, Y.; He, Y.; Yang, C.; Li, Y. *J. Am. Chem. Soc.* **2006**, *128*, 4911.

(37)   Li, Y.; Zou, Y. *Adv. Mater.* **2008**, *20*, 2952.

(38)   Roncali, J. *Macomol. Rapid Comm.* **2007**, *28*, 1761.

(39)   Chen, H.-Y.; Hou, J.; Zhang, S.; Liang, Y.; Yang, G.; Yang, Y.; Yu, L.; Wu, Y.; Li, G. *Nat. Photon.* **2009**, *3*, 649.

(40)   Varotto, A.; Treat, N. D.; Jo, J.; Shuttle, C. G.; Batara, N. A.; Brunetti, F. G.; Seo, J. H.; Chabinyc, M. L.; Hawker, C. J.; Heeger, A. J.; Wudl, F. *Angew. Chem. Int. Ed.* **2011**, *50*, 5166.

(41)   Veldman, D.; Meskers, S. C. J.; Janssen, R. A. J. *Adv. Funct. Mater.* **2009**, *19*, 1939.

(42)   Wienk, M. M.; Turbiez, M.; Gilot, J.; Janssen, R. A. J. *Adv. Mater.* **2008**, *20*, 2556.

(43)   Zhou, H.; Yang, L.; Price, S. C.; Knight, K. J.; You, W. *Angew. Chem. Int. Ed.* **2010**, *49*, 7992.

(44)   Blom, P. W. M.; Mihailetchi, V. D.; Koster, L. J. A.; Markov, D. E. *Adv. Mater.* **2007**, *19*, 1551.

(45)   Johns, J. E.; Muller, E. A.; Frechet, J. M. J.; Harris, C. B. *J. Am. Chem. Soc.* **2010**, *132*, 15720.

(46)   Parmer, J. E.; Mayer, A. C.; Hardin, B. E.; Scully, S. R.; McGehee, M. D.; Heeney, M.; McCulloch, I. *Appl. Phys. Lett.* **2008**, *92*, 113309.

(47)   Salleo, A.; Kline, R. J.; DeLongchamp, D. M.; Chabinyc, M. L. *Adv. Mater.* **2010**, *22*, 3812.

(48)   Di Nuzzo, D.; Aguirre, A.; Shahid, M.; Gevaerts, V. S.; Meskers, S. C. J.; Janssen, R. A. J. *Adv. Mater.* **2010**, *22*, 4321.

(49)   Peet, J.; Senatore, M. L.; Heeger, A. J.; Bazan, G. C. *Advanced Materials* **2009**, *21*, 1521.

(50)   Perez, M. D.; Borek, C.; Forrest, S. R.; Thompson, M. E. *J. Am. Chem. Soc.* **2009**, *131*, 9281.

(51)   Beaujuge, P. M.; Pisula, W.; Tsao, H. N.; Ellinger, S.; Müllen, K.; Reynolds, J. R. *J. Am. Chem. Soc.* **2009**, *131*, 7514.

(52)   Piliego, C.; Holcombe, T. W.; Douglas, J. D.; Woo, C. H.; Beaujuge, P. M.; Fréchet, J. M. J. *J. Am. Chem. Soc.* **2010**, *132*, 7595.

(53)   Rogers, J. T.; Schmidt, K.; Toney, M. F.; Kramer, E. J.; Bazan, G. C. *Adv. Mater.* **2011**, *23*, 2284.

(54)   Woo, C. H.; Beaujuge, P. M.; Holcombe, T. W.; Lee, O. P.; Fréchet, J. M. J. *Journal of the American Chemical Society* **2010**, *132*, 15547.

(55)   Hau, S. K.; Yip, H.-L.; Ma, H.; Jen, A. K. Y. *Applied Physics Letters* **2008**, *93*, 233304.

(56)   Hung, L. S.; Tang, C. W.; Mason, M. G. *Applied Physics Letters* **1997**, *70*, 152.

(57)   Peumans, P.; Forrest, S. R. *Applied Physics Letters* **2001**, *79*, 126.

(58)   White, M. S.; Olson, D. C.; Shaheen, S. E.; Kopidakis, N.; Ginley, D. S. *Applied Physics Letters* **2006**, *89*, 143517.

Chapter 2

Side-Chain Tunability of Furan-Containing Low Band-Gap Polymers Provides Control of Structural Order in Efficient Solar Cells[1]

Abstract

The solution-processability of conjugated polymers in organic solvents has classically been achieved by modulating the size and branching of alkyl substituents appended to the backbone. However, these substituents impact structural order and charge transport properties in thin-film devices. As a result, a tradeoff must be found between material solubility and insulating alkyl content. It was recently shown that the substitution of furan for thiophene in the backbone of the polymer PDPP2FT significantly improves polymer solubility, allowing for the use of shorter branched side-chains while maintaining high device efficiency. In this report, we use PDPP2FT to demonstrate that linear alkyl side-chains can be used to promote thin-film nanostructural order. In particular, linear side-chains are shown to shorten π-π stacking distances between backbones and increase the correlation lengths of both π-π stacking and lamellar spacing, leading to a substantial increase in the efficiency of bulk heterojunction solar cells.


2.1. Introduction

Organic photovoltaic (OPV) technology has the potential for low-cost, high-throughput energy generation, but significant progress must be made before this potential can be realized. To date, much research has been directed toward developing low band-gap polymer donors for use in bulk-heterojunction (BHJ) devices with fullerene-based electron acceptors.[1-9] A key goal in OPV research is to acquire a better understanding of the structure-property relationships that govern material performance. The chemical structure of a polymer donor has been shown to influence properties such as light absorption,[10-12] electronic compatibility with the fullerene acceptor,[13-17] charge transport characteristics,[18-21] thin-film morphology,[22-24] and molecular packing.[25-29] However, structural changes often have competing effects on these properties and, in turn, on device performance. In particular, while using a longer or larger solubilizing alkyl side-chain generally improves solution-processability, it is also expected to increase insulating content and decrease crystallinity. Overcoming performance limitations imposed by these competing effects requires a means of optimizing one property with minimal adverse effect on other properties.

Recently, we demonstrated that furan (F) is a viable alternative to thiophene (T) in conjugated polymers for OPV applications.[29] This concept was shown using model low band-gap polymers based on diketopyrrolopyrrole (DPP), an electron-deficient unit that has raised considerable interest for applications in transistors and solar cells.[15,30-38] From a materials design standpoint, DPP-based building blocks are particularly attractive for their scalable 3–4 step synthesis.[15,29,33] With these model polymers, we showed that incorporation of the furan co-monomer into the polymer backbone imparted markedly improved solubility. As a result, the furan-containing polymer (PDPP2FT, **Fig. 2-1**) with short 2-ethylhexyl (2EH) side-chains is processable in common organic solvents, such as tetrahydrofuran, chloroform, and chlorobenzene. In comparison, the analogous thiophene-based polymer (PDPP3T, **Fig. 2-1**) requires much longer 2-hexyldecyl (2HD) side-chains, as previously reported by Janssen *et al.*[34] In BHJ devices with PC$_{71}$BM, both PDPP2FT-2EH and PDPP3T-2HD achieved comparable power conversion efficiencies (PCEs) of *ca.* 5%, indicating that polymer solubility could be improved while maintaining the same OPV device performance.
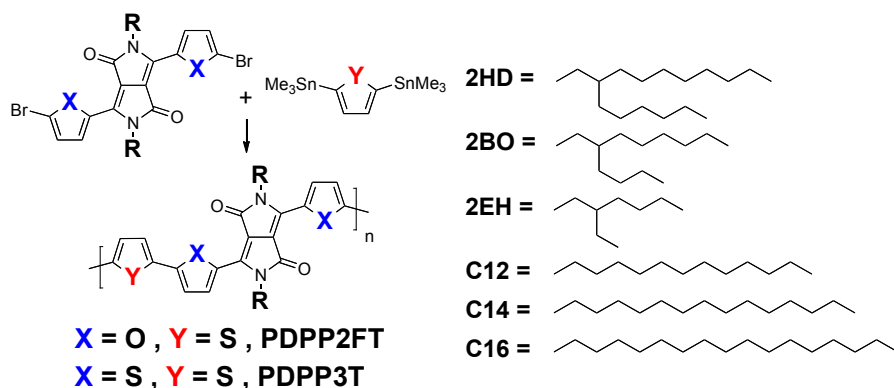
Figure 2-1. Synthesis of PDPP2FT derivatives with alkyl side-chains of varying size and bulk.

In parallel, it is worth noting that, as is the case with PDPP3T, the vast majority of polymer donors exhibiting high PCEs in BHJ devices have branched solubilizing side-chains of various size and sterics.[16,27,39-42] While such branching centers and substituents greatly improve polymer solution-processability in organic solvents, they may not be co-planar with the backbone. We hypothesized that increasing overall polymer planarity may ultimately promote self-assembly into extended crystalline domains with longer-range backbone alignment. Increased molecular ordering in the active layer has often been shown to improve OPV performance, as a result of improved continuity of charge transport pathways.[43,44] The choice of alkyl side-chain structure has been shown to have a pronounced effect on molecular packing and, therefore, on overall device performance.[27]

In this contribution, we demonstrate that linear alkyl side-chains can be used as alternatives to branched side-chains in order to promote nanostructural order. The effects of side-chain structure are studied using a set of PDPP2FT derivatives, each with linear side-chains of a different length. Because of the enhanced solubility of the PDPP2FT backbone, these n-alkyl–substituted derivatives can be solution-processed despite the absence of conventional side-chain branching. In contrast, PDPP3T derivatives with the same n-alkyl side-chains are not soluble enough to be processed into functional devices. In agreement with our initial hypothesis, linear side-chains are shown to improve structural order by reducing the π-π stacking distances between backbones and increasing the correlation lengths of both π-π stacking and lamellar spacing. BHJ solar cells fabricated from n-alkyl–substituted PDPP2FT donors exhibit PCEs reaching 6.5% (PDPP2FT-C_{14}), which is a substantial improvement over the PCEs of $ca.$ 5% achieved with both the branched-alkyl–substituted derivative PDPP2FT-2EH and the original thiophene-based analog PDPP3T-2HD. Thus, by leveraging the enhanced solubility imparted by the furan moiety, we show that side-chain structural design can be used to control thin-film nanostructural order and device performance. This combination of design principles paves a path to reaching PCE values exceeding those presently obtained using other thiophene-based polymer donors with branched side-chains.[15,34]

2.2. Results and Discussion

Synthesis and Optoelectronic Properties. To demonstrate the influence of side-chain design on structural order, PDPP2FT derivatives were synthesized with n-C_{12}, n-C_{14}, or n-C_{16} side-chains (**Fig. 2-1**). This progression of side-chains was chosen in order to determine the optimal side-chain length. Synthetic details and molecular characterizations, including UV-Vis absorption spectra, can be found in the Supporting Information (SI). Thin-film absorption coefficients, optical band gaps, and photoelectron spectroscopy in air (PESA)-estimated highest occupied molecular orbital (HOMO) energy levels are summarized in **Table 2-1**. The optical and electronic properties of all three derivatives are nearly identical and closely match those of the branched-alkyl–substituted analogs PDPP2FT-2EH[29] and PDDP3T-2HD[34]. The branched-alkyl–substituted derivative PDPP2FT-2BO (**Fig. 2-1**) was also prepared in order to further correlate the size of the branched substituents with structural order and solar cell device performance (see SI). Further shortening the side-chain to n-C_{10} resulted in greatly reduced solubility, and the polymerization product could not be solution-processed.

Table 2-1. Optical and electrochemical properties of PDPP2FT polymers.

Derivative	Extinction coefficient[a] [cm^{-1}]	Optical band gap[b] [eV]	HOMO (PESA[c]) [eV]
C$_{12}$	1.1×10^5	1.4	-5.2
C$_{14}$	7.7×10^4	1.4	-5.2
C$_{16}$	6.5×10^4	1.4	-5.3

[a] Measured at λ_{max}. [b] Based on absorption onsets. [c] Photoelectron spectroscopy in air (PESA) measurements.

As control experiments, PDPP3T-C$_{14}$ and -C$_{16}$ were synthesized, but these analogs also showed limited solubility and could not be solution-processed. These findings demonstrate that the incorporation of furan in the polymer backbone allows access to polymer structures that are not otherwise soluble or processable. Previous studies comparing oligofurans to oligothiophenes have similarly reported that oligofurans and alternating furan-thiophene oligomers are more soluble than the analogous oligothiophenes[45-47]. The mechanism behind the improved solubility imparted by the furan co-monomer is not well established, but it is possible that differences in atomic radius and electronegativity between oxygen and sulfur atoms may impact solvent interactions, intermolecular interactions, and intramolecular steric interactions. It is worth noting, however, that no alkyl side-chains were present in these previously reported systems.
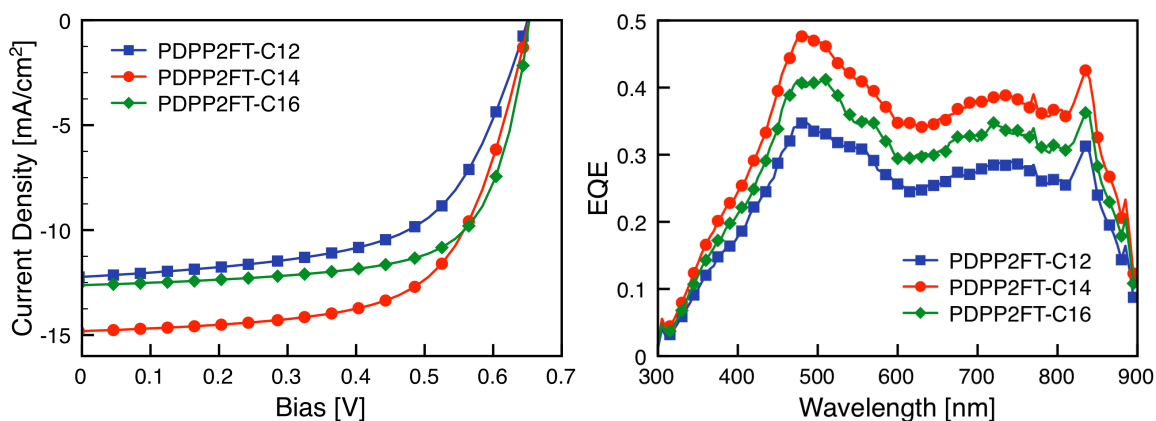
Figure 1-2. Average *J-V* curves (top) and characteristic external quantum efficiency (EQE) spectra (bottom) of solar cells fabricated from PDPP2FT-C$_{12}$, -C$_{14}$, and -C$_{16}$.

**Table 2-2. PV performance of PDPP2FT derivatives with PC$_{71}$BM.**

Derivative	J$_{SC}$ [mA/cm^2]	V$_{OC}$ [V]	FF	Avg. PCE ± Std. Dev. [%]	Max. PCE [%]
C$_{12}$	-12.2	0.65	0.60	4.8 ± 0.3	5.2
C$_{14}$	-14.8	0.65	0.64	6.2 ± 0.2	6.5
C$_{16}$	-12.3	0.65	0.69	5.7 ± 0.4	6.2

Device Fabrication and Testing. Thin-film BHJ solar cells were fabricated using PDPP2FT-C$_{12}$, -C$_{14}$, and -C$_{16}$ as electron donors and [6,6]-phenyl-C$_{71}$-butyric acid methyl ester (PC$_{71}$BM) as the electron acceptor, with a PDPP2FT:PC$_{71}$BM blend ratio of 1:3 by weight. This blend ratio was determined for each derivative individually as part of an

optimization process encompassing a wide range of device fabrication parameters (e.g., spin-coater speed, solvent, solution concentrations). The optimized device architecture was ITO/PEDOT:PSS/polymer:$PC_{71}BM$/LiF/Al. Active layers were spin-coated from chloroform solutions, with a small amount of the processing additive 1-chloronaphthalene (CN)[48] used to improve device performance.[49-51] Devices fabricated from the PDPP2FT-C_{12}, -C_{14}, and -C_{16} derivatives achieved average PCEs of 4.8%, 6.2%, and 5.7%, respectively, with PDPP2FT-C_{14} based devices reaching as high as 6.5% (**Table 2-2**). The n-C_{12} derivative proved relatively difficult to solution-process due to its lower solubility. The performance of the n-C_{14} and n-C_{16} derivatives, on the other hand, is substantially improved over that of the previously reported branched-alkyl–substituted analogs PDPP2FT-2EH and PDPP3T-HD, both of which achieved a PCE of *ca.* 5%. This PCE improvement is mostly attributed to increases in photocurrent and fill factor (FF). As shown in the device current density–voltage (J–V) curves and external quantum efficiency (EQE) spectra (**Fig. 2-2**), PDPP2FT-C_{14} based devices exhibit particularly high short-circuit current (J_{SC}) approaching 15 mA/cm^2 and a broad EQE spectrum approaching 50% efficiency at 500 nm. As all of the derivatives exhibit similar light absorption and electrical properties, it is likely that these performance improvements are due to changes in properties such as charge carrier mobility, film morphology (donor/acceptor phase separation), and nanostructural order.

To determine the impact of side-chains on charge carrier mobility, hole mobility was measured using the space charge limited current (SCLC) model. In hole-only devices (see SI), neat films of PDPP2FT-C_{12}, -C_{14}, and -C_{16} showed mobilities of 4×10^{-4}, 7×10^{-4}, and 2×10^{-3} cm^2/V-s, respectively. The high carrier mobility of these n-alkyl–substituted PDPP2FT derivatives is expected to contribute in part to the high photocurrents and fill factors observed in optimized BHJ devices (**Fig. 2-2**). For comparison, neat films of PDPP2FT-2EH showed a hole mobility of 2×10^{-3} cm^2/V-s. Since this value is similar to the mobilities observed with PDPP2FT-C_{14} and -C_{16}, it is likely that the performance improvement seen with the n-alkyl–substituted derivatives arises from other thin-film parameters.

Thin-Film Morphology. As a polymer's solubilizing side-chains are expected to impact its solubility and miscibility with $PC_{71}BM$, they could in turn affect the film morphology that forms during the spin-coating process. Atomic force microscopy (AFM) was used to investigate the nanoscale topography of the thin-film devices made from PDPP2FT-C_{12}, -C_{14}, and -C_{16} blended with $PC_{71}BM$ (**Fig. 2-3**). Notably, all films exhibit networks of features on the order of *ca.* 20 nm in size. Excitons generated in donor phases of this size scale can diffuse to a donor/acceptor interface, assuming an exciton diffusion length of *ca.* 10 nm.[52,53] Films of PDPP2FT-C_{12}, -C_{14}, and -C_{16} have root mean square (RMS) roughnesses of 2.2 nm, 1.6 nm, and 3.3 nm, respectively. The relative smoothness of the PDPP2FT-C_{14} active layer may point to finer and more evenly-distributed morphological features, which could reduce charge recombination. These results suggest that, with PDPP2FT, n-C_{14} side-chains may provide the most adequate combination of polymer solubility and miscibility with $PC_{71}BM$ to achieve optimal film morphology. Additional studies are underway to confirm the internal morphology of the thin-film active layers.
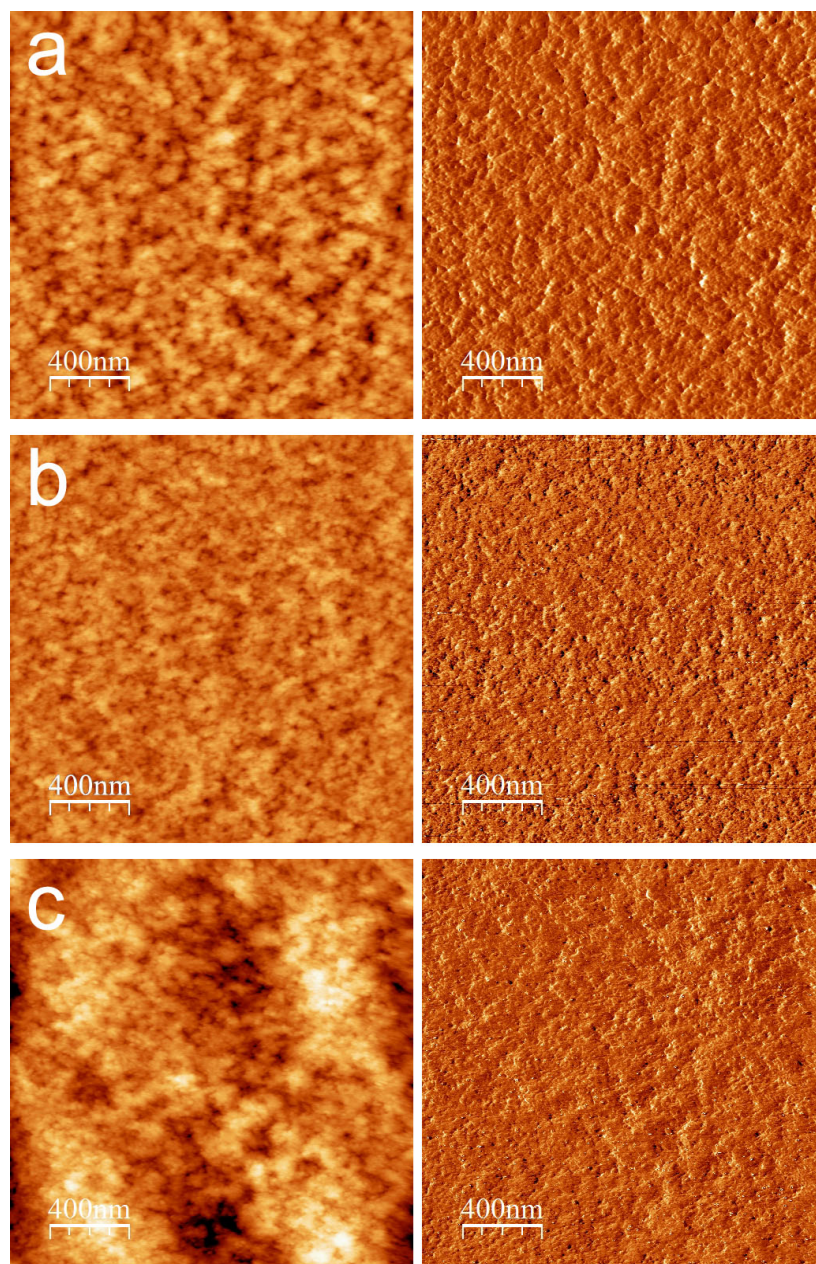
Figure 2-3. AFM height (left) and phase (right) images of the *n*-alkyl–substituted polymers a) PDPP2FT-C_{12}, b) PDPP2FT-C_{14}, and c) PDPP2FT-C_{16}.

Thin-Film Nanostructural Order. To determine the influence of side-chain substitutions on nanostructural order within the active layer, grazing-incidence X-ray scattering (GIXS) was used to examine thin-films of PDPP2FT-C_{12}, -C_{14}, -C_{16}, and -2EH, both in neat polymer films (**Fig. 2-4**) and in optimized BHJ films with $PC_{71}BM$ (see SI). GIXS data can be used to determine the nature and extent of the face-to-face packing of conjugated polymer backbones (π-π stacking). The scattering patterns of neat films of all four derivatives exhibit a π-π stacking peak, visible as a ring or partial arc at $q \sim 1.7$ Å^{-1}. The stronger peak intensity near $q_{xy} \approx 0$ means that the π-π stacking is preferentially oriented out-of-plane, which has been often correlated with high OPV performance.[28,54,55]

19

As shown in **Fig. 2-4**, the extent of out-of-plane orientation of each derivative increases in the order: PDPP2FT-C_{12}, -C_{14}, -C_{16}, and -2EH. This order agrees well with the SCLC hole mobilities presented earlier, as SCLC measures hole mobility in the out-of-plane direction.

In assessing the effect of these π-π interactions on solar cell performance, it is important to consider π-stacking distance. A shorter distance is thought to reduce the energetic barrier for charge hopping between adjacent molecules, promoting charge transport and improving device performance.[20,56,57] Brédas and coworkers have shown in model systems that, for cofacial π-π stacking, electronic couplings decay exponentially with the stacking distance and can vary by as much as a factor of four when the stacking distance increases from 3.4 to 4.0 Å.[20] It is expected that the solubilizing side-chains of a polymer will impact this π-stacking distance. Compared to branched side-chains, which create steric hindrance when polymer chains are packed tightly, linear substituents are expected to be able to organize coplanar with the backbone, allowing for closer π-π stacking distances. In good agreement with this hypothesis, the π-stacking distances of PDPP2FT-C_{12}, -C_{14}, and -C_{16} are all measured to be 3.6 Å. In comparison, the π-stacking distances of PDPP2FT-2EH and -2BO are measured to be 3.7 Å and 3.9 Å, respectively (**Table 2-3**), suggesting that branched side-chains do cause steric hindrance. Empirically, a negative correlation is observed between π-stacking distance and device performance. PDPP2FT-2BO, in particular, exhibits a much larger stacking distance (3.9 Å) and achieves the lowest solar cell performance (avg. PCE of 1.3%, see SI). In parallel, it is important to note that charge transfer between two molecules also depends strongly on their in-plane offset and not just on their cofacial separation distance, as wavefunction overlap plays a critical role in electronic coupling.[20] Nevertheless, as suggested by the empirical correlation drawn above, π-π stacking distance provides a valuable first-order metric for evaluating the charge transport characteristics of complex polymer systems.

In addition to describing the molecular packing distances and orientation of crystallites in thin films, GIXS provides information on the extent of nanostructural order. Specifically, GIXS can be used to determine the correlation length (L_C),[25,58] which is a measure of the length scale over which one can expect a crystal lattice to be preserved. In polymer systems, order is expected to improve with the reduction of (i) the variability in chain position and rotation and (ii) the density of chain ends and lamellar folds.[56] Correlation length can be determined using the Scherrer equation,[31,32] which takes scattering peak breadth as an input. As the order of crystalline domains increases, the corresponding scattering peaks become narrower. To determine the full width at half maximum (FWHM) peak breadths, peaks were fit to GIXS data averaged over quasi-polar angle (χ) for $\chi = 20° \pm 2°$ and $\chi = 60° \pm 2°$. The resulting average correlation lengths are shown for π-π stacking and lamellar spacing peaks in **Table 2-2** and **Fig. 2-5**. For ease of comparison, solar cell efficiencies (PCEs) are also reported in **Fig. 2-5**. Notably, the *n*-alkyl–substituted PDPP2FT derivatives pack with significantly longer π-π stacking correlation lengths (> 3 nm) than does PDPP2FT-2EH (*ca.* 1 nm). Furthermore, device performance is substantially improved in BHJs made with PDPP2FT-C_{14}, which also shows the largest π-π stacking correlation length at 3.6 nm. Recall that PDPP2FT-C_{12} had the lowest solubility of all the derivatives, which may have affected device PCE. A similar trend is observed for lamellar spacing correlation lengths, which are greater for the *n*-

alkyl–substituted derivatives (*ca.* 3–4 nm) than for the branched-alkyl–substituted derivatives (< 3 nm). Although additional studies will be required to determine the interdigitation and packing structure of the side-chains, it is important to note the likely contribution of the linear chains to overall solid-state order and device performance. Increased order, particularly of π-π stacking, likely minimizes the number of defects that can trap charge carriers and hinder their percolation across the active layer.[44,59] As discussed earlier, the π-π stacking in these systems is preferentially oriented out-of-plane, which is also the desired direction for hole transport. As a result, the effect of π-π stacking correlation length on solar cell device performance is expected to be particularly significant among factors contributing to improved performance.
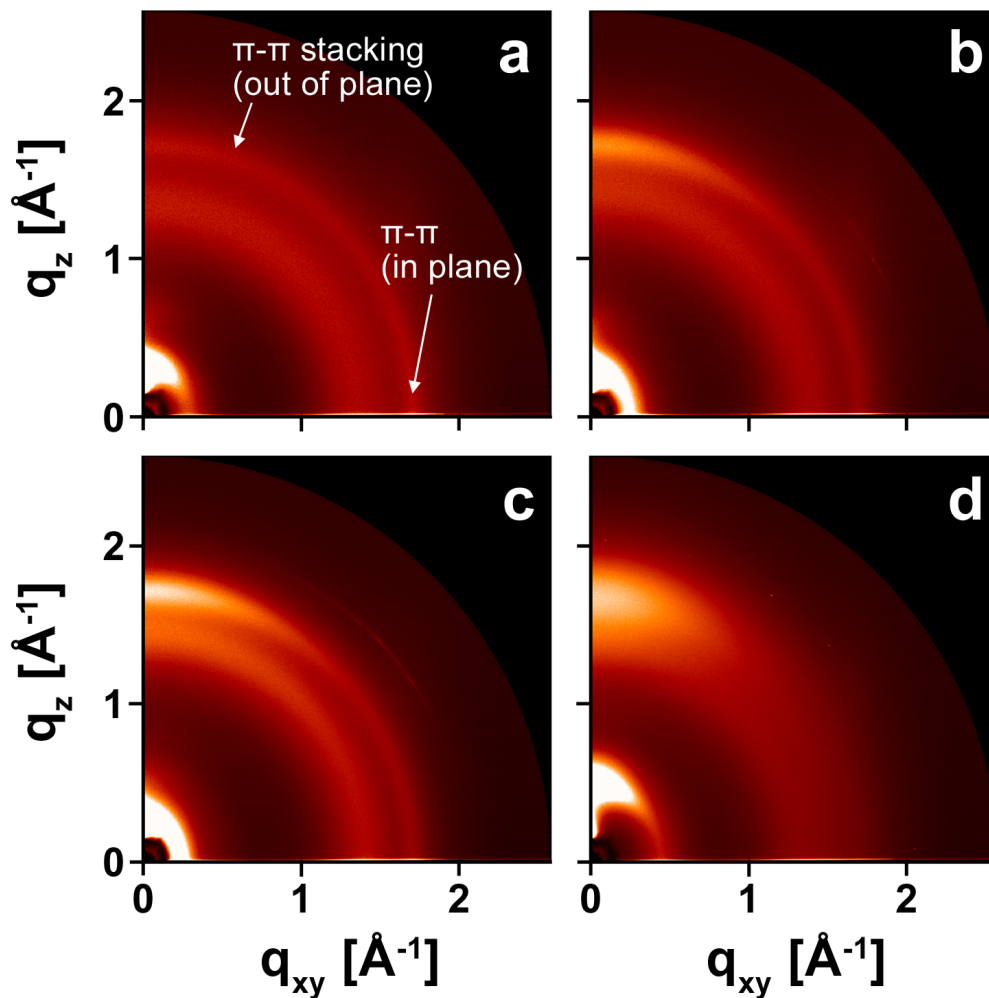
Figure 2-4. 2-D grazing incidence x-ray scattering (GIXS) patterns of thin films of a) PDPP2FT-C$_{12}$, b) PDPP2FT-C$_{14}$, c) PDPP2FT-C$_{16}$, and d) PDPP2FT-2EH.

21

Table 2-3. GIXS peak parameters for PDPP2FT derivatives

Derivative	π-π stacking peak		Lamellar spacing peak	
	d [Å]	L_C [nm]	d [Å]	L_C [nm]
C_{12}	3.6	3.3	21	3.4
C_{14}	3.6	3.6	23	3.6
C_{16}	3.6	3.0	25	4.1
2EH	3.7	1.1	13	2.7
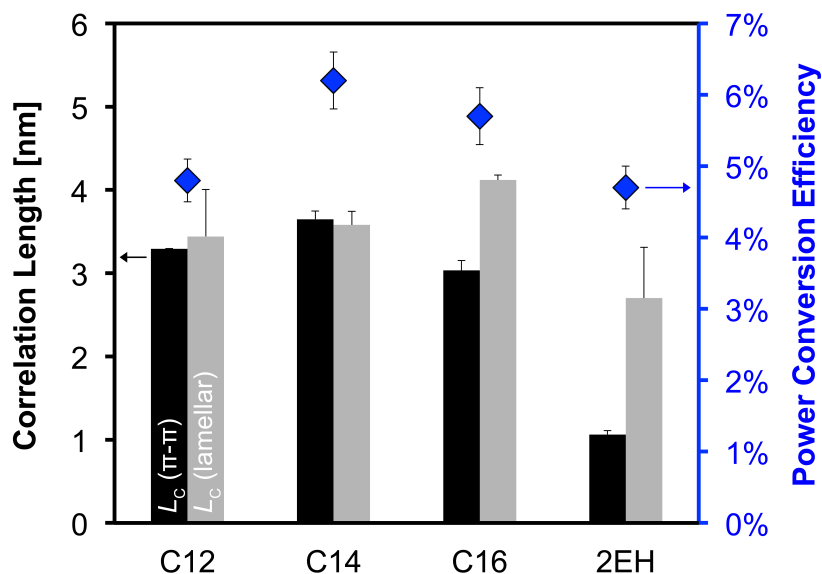
Figure 2-5. π-π stacking (black) and lamellar spacing (gray) correlation lengths for PDPP2FT derivatives in thin-film. Power conversion efficiency in devices is shown (blue diamond) to demonstrate the relationship between π-π stacking correlation length and device performance.

2.3. Conclusions

In this report, we have demonstrated that long linear alkyl side-chains can be used as alternatives to branched side-chains on polymers to promote nanostructural order in thin-film solar cells. The alternating furan-thiophene PDPP2FT polymer backbone was chosen as a model system because of the significant contribution of the furan moiety to overall polymer solubility. Despite the absence of side-chain branching, solution-processability is retained in the *n*-alkyl–substituted derivatives. GIXS shows that linear side-chains in these systems (i) reduce the π-stacking distances between backbones and (ii) increase π-π stacking and lamellar spacing correlation lengths within polymer crystallites. Building from these design principles, we show that BHJ solar cells fabricated from *n*-alkyl–substituted substituted PDPP2FT polymer donors and the electron-acceptor $PC_{71}BM$ exhibit PCEs reaching 6.5% (PDPP2FT-C_{14}). This high performance represents a substantial improvement over the PCE of *ca.* 5% achieved with the branched-alkyl–substituted derivative PDPP2FT-2EH and the original thiophene-based analog PDPP3T-2HD.

This work demonstrates the potential of furan moieties in the design of polymer donors for efficient OPV applications. With their expanded structural design flexibility, alternating furan-thiophene low band-gap polymers pave a path toward achieving PCE values exceeding those presently obtained with branched-alkyl–substituted thiophene-based polymer donors.

2.4. Experimental Details

2.4.1. Synthetic Details

Methods and Materials. All reagents from commercial sources were used without further purification, unless otherwise noted. Flash chromatography was performed using Silicycle SiliaFlash ® P60 (particle size 40-63 μm, 230 – 400 mesh) silica gel. All compounds were characterized by ^{1}H NMR (400 MHz) and ^{13}C NMR (100 MHz) on a Bruker AVQ-400 instrument or ^{13}C NMR (150 MHz) on a Bruker AV-600 instrument. Notations for proton splitting patterns: s = singlet, d = doublet, t = triplet, q = quartet, dd = doublet of doublet, m = multiplet, and a = apparent. Matrix assisted laser desorption/ionization mass spectrometry (MALDI-TOF MS) was performed on a PerSeptive Biosystems Voyager-DE using 2,2':5',2"-terthiophene as the matrix. Samples were prepared by diluting the monomers in chloroform with the matrix. For the molecular weight determination of polymers, samples were dissolved in HPLC grade chloroform at a concentration of 1 mg/ml. The resulting solution was briefly heated and then allowed to return to room temperature prior to filtering through a 0.2 μm polyvinylidene fluoride (PVDF) filter. Size exclusion chromatography (SEC) was performed with HPLC grade chloroform at an elution rate of at 1.0 mL/min through three PLgel Mixed-C columns at room temperature. The particle size in the columns was 5 μm and the columns were maintained at room temperature. The SEC system consisted of a Waters 2695 Separation Module and a Waters 486 Tunable Absorption Detector. The apparent molecular weights and polydispersities (*Mw/Mn*) were determined with a calibration based on linear polystyrene standards using Millennium software from Waters.

The synthetic methods are adapted from those described in our early work on mixed furan-thiophene low band-gap conjugated polymers for solar cell applications: *J. Am. Chem. Soc.*, **2010**, *132* (44), pp 15547–15549.
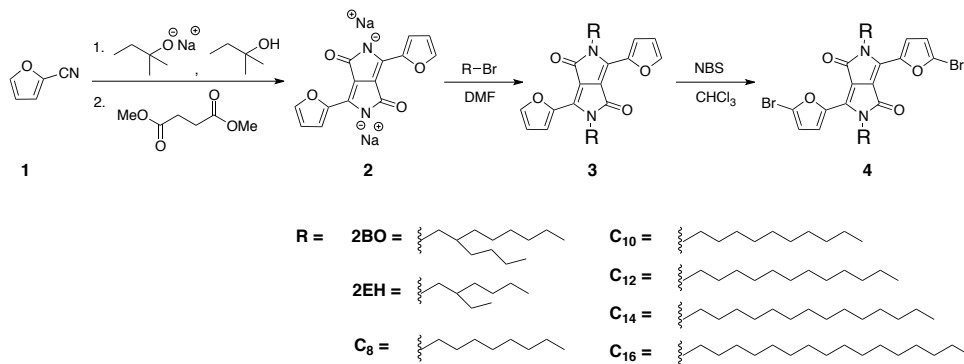
3,6-di(furan-2-yl)pyrrolo[3,4-c]pyrrole-1,4(2H,5H)-dione (2). A 500 mL three-neck round-bottom flask connected to a condenser was charged with a stir bar and *tert*-amyl alcohol (250 mL) under nitrogen atmosphere. Sodium metal pieces (2.47 g, 107 mmol) were added to the warmed solution of *tert*-amyl alcohol (60-70 °C) in small portions. After complete addition of the sodium, the temperature was progressively raised to 120 °C. The mixture was stirred overnight at 120 °C. Furan-2-carbonitrile (**1**) (10.0 g, 107 mmol) was subsequently added to the hot solution of sodium alkoxide. Dimethyl succinate (5.23 g, 35.8 mmol) was then added dropwise over a period of 20 min (the reaction mixture turned dark orange-red), and the resulting mixture was stirred for 1.5 h. The reaction mixture was then cooled to room temperature, and the precipitated sodium salt **2** was filtered over a Buchner funnel for collection and dried under vacuum (14.7 g, 87% yield). Compound **2** was used without further purification.

2,5-didodecyl-3,6-di(furan-2-yl)pyrrolo[3,4-c]pyrrole-1,4(2H,5H)-dione (3-C₁₂). Compound **2** (3.45 g, 11.05 mmol) and 50 mL of dry DMF were added to a 100 mL two-neck round–bottom flask, equipped with a condenser and stir-bar and placed under N_2 atmosphere. The mixture was heated to 120 °C, stirred for 30 min, and 1-bromododecane (6.89 g, 27.63 mmol) was then added quickly (while at 120 °C). The reaction mixture was subsequently stirred at 140 °C for *ca.* 2 h, and cooled to room temperature. The organic phase was precipitated in water, the precipitate was filtered off, and dissolved in chloroform ($CHCl_3$). $CHCl_3$ was evaporated, and the resulting tacky solid (dark red) was purified by column chromatography using $CHCl_3$ as eluent. 1.9 g of **3-C₁₂** were isolated (28% yield). ¹H NMR (400 MHz, CDCl₃): δ (ppm) = 8.30 (d, *J* = 3.6 Hz, 2 H), 7.63 (d, *J* = 0.8 Hz, 2 H), 6.69 (dd, *J* = 1.6 Hz, 3.6 Hz, 2 H), 4.10 (t, *J* = 7.6 Hz, 4 H), 1.72 – 1.65 (m, 4 H), 1.40 – 1.24 (m, 36 H), 0.87 (t, *J* = 6.8 Hz, 6 H). ¹³C NMR (100 MHz, CDCl₃): δ (ppm) = 161.0, 145.3, 144.8, 133.8, 120.3, 113.6, 106.6, 42.6, 32.1, 30.4, 29.8, 29.7, 29.5, 29.4, 17.0, 22.8, 14.3. MALDI-TOF MS (*m/z*): calc'd for $C_{38}H_{56}N_2O_4$ [M⁺] = 492.30; found 492.84.

Other alkyl-substituted derivatives (**3**) were obtained in comparable yields; their corresponding NMR and MALDI data are reported below:

2,5-di-(2-ethylhexyl)-3,6-di(furan-2-yl)pyrrolo[3,4-c]pyrrole-1,4(2H,5H)-dione (3-2EH). ¹H NMR (400 MHz, CDCl₃): δ (ppm) = 8.33 (d, *J* = 3.6 Hz, 2 H), 7.61 (d, *J* = 1.3 Hz, 2 H), 6.69 (dd, *J* = 1.7 Hz, 3.6 Hz, 2 H), 4.04 (d, *J* = 7.8 Hz, 4 H), 1.80 – 1.68 (m, 2 H), 1.39 – 1.26 (m, 16 H), 0.95 – 0.85 (m, 12 H). ¹³C NMR(100 MHz, CDCl₃): δ (ppm) = 161.4, 145.0, 144.8, 134.1, 120.4, 113.6, 106.6, 46.3, 40.1, 30.7, 28.8, 24.0, 23.2, 14.2, 10.9. MALDI-TOF MS (*m/z*): calc'd for $C_{30}H_{40}N_2O_4$ [M⁺] = 492.3; found 492.9.

2,5-di-(2-butyloctyl)-3,6-di(furan-2-yl)pyrrolo[3,4-c]pyrrole-1,4(2H,5H)-dione (3-2BO). ¹H NMR (400 MHz, CDCl₃): δ (ppm) = 8.37 (d, *J* = 3.6 Hz, 2 H), 7.65 (d, *J* = 1.5 Hz, 2 H), 6.73 (dd, *J* = 1.7 Hz, 3.7 Hz, 2 H), 4.08 (d, *J* = 7.5 Hz, 4 H), 1.91–1.76 (m, 2 H), 1.48–1.18 (m, 32 H), 1.00 – 0.82 (m, 12 H). ¹³C NMR (100 MHz, CDCl₃): δ (ppm) = 161.3, 144.8, 144.7, 133.9, 120.2, 113.5, 106.5, 46.5, 38.5, 31.8, 31.5, 29.7, 26.5, 23.1, 22,7, 14.1. MALDI-TOF MS (*m/z*): calc'd for $C_{38}H_{56}N_2O_4$ [M⁺] = 604.42; found 604.65.

2,5-dioctyl-3,6-di(furan-2-yl)pyrrolo[3,4-c]pyrrole-1,4(2H,5H)-dione (3-C8). ¹H NMR (400 MHz, CDCl₃): δ (ppm) = 8.30 (d, *J* = 3.6 Hz, 2 H), 7.63 (as, 2 H), 6.69 (dd, *J* = 1.2 Hz, 3.6 Hz, 2 H), 4.04 (t, *J* = 7.6 Hz, 4 H), 1.75–1.67 (m, 4 H), 1.20–1.45 (m, 20 H),

24

0.86 (t, J = 7.2 Hz, 6 H). ^{13}C NMR(100 MHz, CDCl$_3$): δ (ppm) = 161.0, 145.3, 144.8, 133.8, 120.2, 113.6, 106.5, 42.5, 31.9, 30.4, 29.4, 29.3, 27.0, 22.8, 14.2. MALDI-TOF MS (*m/z*): calc'd for C$_{30}$H$_{40}$N$_2$O$_4$ [M$^+$] = 492.30; found 492.84.

2,5-didecyl-3,6-di(furan-2-yl)pyrrolo[3,4-c]pyrrole-1,4(2H,5H)-dione (3-C10).
^{1}H NMR (400 MHz, CDCl$_3$): δ (ppm) = 8.30 (d, J = 3.6 Hz, 2 H), 7.63 (d, J = 0.8 Hz, 2 H), 6.69 (dd, J = 1.2 Hz, 3.8 Hz, 2 H), 4.11 (t, J = 7.2 Hz, 4 H), 1.75 – 1.65 (m, 4 H), 1.38 – 1.24 (m, 28 H), 0.87 (t, J = 6.8 Hz, 6 H). ^{13}C NMR (100 MHz, CDCl$_3$): δ (ppm) = 161.0, 145.3, 144.8, 133.8, 120.3, 113.6, 106.6, 42.6, 32.0, 30.4, 29.7, 29.4, 27.0, 22.8, 14.3. MALDI-TOF MS (*m/z*): calc'd for C$_{34}$H$_{48}$N$_2$O$_4$ [M$^+$] = 548.36; found 548.77.

2,5-ditetradecyl-3,6-di(furan-2-yl)pyrrolo[3,4-c]pyrrole-1,4(2H,5H)-dione (3-C14). ^{1}H NMR (400 MHz, CDCl$_3$): δ (ppm) = 8.35 (d, J = 3.2 Hz, 2 H), 7.67 (d, J = 1.3 Hz, 2 H), 6.74 (dd, J = 1.7 Hz, 3.6 Hz, 2 H), 4.20-4.09 (m, 4 H), 1.83 – 1.64 (m, 4 H), 1.53 – 1.17 (m, 44 H), 0.93 (t, J = 6.7 Hz, 6 H). ^{13}C NMR (100 MHz, CDCl$_3$): δ (ppm) = 160.9, 145.1, 144.7, 133.6, 120.1, 113.5, 106.4, 42.4, 29.7, 29.6, 29.4, 26.9, 22.7, 14.1. MALDI-TOF MS (*m/z*): calc'd for C$_{42}$H$_{64}$N$_2$O$_4$ [M$^+$] = 660.49; found 660.96.

2,5-dihexadecyl-3,6-di(furan-2-yl)pyrrolo[3,4-c]pyrrole-1,4(2H,5H)-dione (3-C16). ^{1}H NMR (400 MHz, CDCl$_3$): δ (ppm) = 8.35 (d, J = 3.4 Hz, 2 H), 7.67 (d, J = 1.2 Hz, 2 H), 6.74 (dd, J = 1.7 Hz, 3.7 Hz, 2 H), 4.20-4.09 (m, 4 H), 1.83 – 1.65 (m, 4 H), 1.50 – 1.22 (m, 52 H), 0.94 (t, J = 6.7 Hz, 6 H). ^{13}C NMR (100 MHz, CDCl$_3$): δ (ppm) = 160.9, 145.1, 144.7, 133.7, 120.1, 113.5, 106.5, 42.4, 29.7, 29.6, 29.4, 26.9, 22.7, 14.1. MALDI-TOF MS (*m/z*): calc'd for C$_{46}$H$_{72}$N$_2$O$_4$ [M$^+$] = 716.55; found 717.43.

3,6-bis(5-bromofuran-2-yl)-2,5-didodecylpyrrolo[3,4-c]pyrrole-1,4(2H,5H)-dione (4-C12). A 250 mL single-neck round–bottom flask charged with **3-C$_{12}$** (1.56 g, 2.58 mmol) and 100 mL of CHCl$_3$. The mixture was cooled to 0 °C and stirred while *N*-bromosuccinimide (NBS, 0.92 g, 5.16 mmol) was added in small portions. The mixture was maintained at 0 °C and stirred for 1 h following complete addition of NBS. Crushed ice was charged into the organic phase, the whole was transferred into a separatory funnel, and the organic phase was extracted with CHCl$_3$ and washed with water. The CHCl$_3$ was evaporated, and the resulting tacky solid (dark purple-red) was purified by column chromatography using CHCl$_3$ as eluent. 0.63 g of **4-C$_{12}$** were isolated (32% yield). ^{1}H NMR (400 MHz, CDCl$_3$): δ (ppm) = 8.30 (d, J = 3.7 Hz, 2 H), 6.67 (d, J = 3.7 Hz, 2 H), 4.13-4.05 (m, 4 H), 1.80–1.66 (m, 4 H), 1.50–1.21 (m, 36 H), 0.93 (t, J = 6.7 Hz, 6 H). ^{13}C NMR (100 MHz, CDCl$_3$): δ (ppm) = 160.5, 146.2, 132.5, 126.4, 122.1, 115.5, 106.3, 42.5, 30.2, 29.6, 29.4, 26.9, 22.7, 14.1. MALDI-TOF MS (*m/z*): calc'd for C$_{38}$H$_{54}$Br$_2$N$_2$O$_4$ [M$^+$] = 762.25; found 762.33.

Other alkyl-substituted derivatives (**4**) were obtained in comparable yields; their corresponding NMR and MALDI data are reported below:

3,6-bis(5-bromofuran-2-yl)-2,5-di-(2-ethylhexyl)-pyrrolo[3,4-c]pyrrole-1,4(2H,5H)-dione (4-2EH). ^{1}H NMR (400 MHz, CDCl$_3$): δ (ppm) = 8.33 (d, J = 3.6 Hz, 2 H), 7.61 (d, J = 1.3 Hz, 2 H), 6.69 (dd, J = 1.7 Hz, 3.6 Hz, 2 H), 4.04 (d, J = 7.8 Hz, 4 H), 1.80–1.68 (m, 2 H), 1.39–1.26 (m, 16 H), 0.95 – 0.85 (m, 12 H). ^{13}C NMR (100 MHz, CDCl$_3$): δ (ppm) = 161.4, 145.0, 144.8, 134.1, 120.4, 113.6, 106.6, 46.3, 40.1, 30.7, 28.8, 24.0, 23.2, 14.2, 10.9. MALDI-TOF MS (*m/z*): calc'd for C$_{30}$H$_{40}$N$_2$O$_4$ [M$^+$] = 492.3; found 492.9.

3,6-bis(5-bromofuran-2-yl)-2,5-di-(2-butyloctyl)-pyrrolo[3,4-c]pyrrole-1,4(2H,5H)-dione (4-2BO). ^{1}H NMR (400 MHz, CDCl$_3$): δ (ppm) = 8.34 (d, J = 3.7 Hz, 2 H), 6.67 (d, J = 3.7 Hz, 2 H), 4.04 (d, J = 7.4 Hz, 4 H), 1.89 – 1.75 (m, 2 H), 1.50 – 1.18 (m, 32 H), 0.93 (m, 12 H). ^{13}C NMR (100 MHz, CDCl$_3$): δ (ppm) = 160.9, 146.2, 145.5, 132.8, 126.3, 120.2, 115.6, 106.3, 46.6, 38.8, 31.4, 29.8, 26.5, 23.2, 22.7, 14.1. MALDI-TOF MS (m/z): calc'd for C$_{38}$H$_{54}$Br$_2$N$_2$O$_4$ [M$^+$] = 762.25; found 762.89.

3,6-bis(5-bromofuran-2-yl)-2,5-dioctyl-pyrrolo[3,4-c]pyrrole-1,4(2H,5H)-dione (4-C8). ^{1}H NMR (400 MHz, CDCl$_3$): δ (ppm) = 8.25 (d, J = 3.6 Hz, 2 H), 6.63 (d, J = 3.6 Hz, 2 H), 4.05 (t, J = 7.6 Hz, 4 H), 1.69 (m, 4 H), 1.40 – 1.27 (m, 20 H), 0.87 (t, J = 6.0 Hz, 6 H). ^{13}C NMR (100 MHz, CDCl$_3$): δ (ppm) = 160.7, 146.3, 132.6, 126.6, 122.3, 115.7, 106.4, 42.6, 31.9, 30.3, 29.4, 27.0, 22.8, 14.3. MALDI-TOF MS (m/z): calc'd for C$_{30}$H$_{38}$Br$_2$N$_2$O$_4$ [M$^+$] = 650.12; found 650.87.

3,6-bis(5-bromofuran-2-yl)-2,5-didecyl-pyrrolo[3,4-c]pyrrole-1,4(2H,5H)-dione (4-C10). ^{1}H NMR (400 MHz, CDCl$_3$): δ (ppm) = 8.25 (d, J = 3.6 Hz, 2 H), 6.63 (d, J = 3.6 Hz, 2 H), 4.05 (t, J = 7.6 Hz, 4 H), 1.69 (m, 4 H), 1.40 – 1.26 (m, 28 H), 0.87 (t, J = 6.4 Hz, 6 H). ^{13}C NMR (100 MHz, CDCl$_3$): δ (ppm) = 160.5, 126.1, 132.5, 126.4, 122.1, 115.5, 106.2, 42.5, 31.9, 30.2, 29.6, 29.5, 29.3, 29.2, 26.8, 22.7, 14.1. MALDI-TOF MS (m/z): calc'd for C$_{34}$H$_{46}$Br$_2$N$_2$O$_4$ [M$^+$] = 706.18; found 706.37.

3,6-bis(5-bromofuran-2-yl)-2,5-ditetradecyl-pyrrolo[3,4-c]pyrrole-1,4(2H,5H)-dione (4-C14). ^{1}H NMR (400 MHz, CDCl$_3$): δ (ppm) = 8.30 (d, J = 3.7 Hz, 2 H), 6.68 (d, J = 3.7 Hz, 2 H), 4.20-4.00 (m, 4 H), 1.80 – 1.67 (m, 4 H), 1.51 – 1.20 (m, 44 H), 0.94 (t, J = 6.6 Hz, 6 H). ^{13}C NMR (100 MHz, CDCl$_3$): δ (ppm) = 160.5, 146.2, 132.5, 126.4, 122.1, 115.5, 106.3, 42.5, 29.7, 29.6, 29.4, 26.9, 22.7, 14.1, 7.5. MALDI-TOF MS (m/z): calc'd for C$_{42}$H$_{62}$Br$_2$N$_2$O$_4$ [M$^+$] = 818.31; found 818.24.

3,6-bis(5-bromofuran-2-yl)-2,5-dihexadecyl-pyrrolo[3,4-c]pyrrole-1,4(2H,5H)-dione (4-C16). ^{1}H NMR (400 MHz, CDCl$_3$): δ (ppm) = 8.30 (d, J = 3.7 Hz, 2 H), 6.67 (d, J = 3.7 Hz, 2 H), 4.13-4.05 (m, 4 H), 1.78 – 1.68 (m, 4 H), 1.52 – 1.19 (m, 52 H), 0.92 (t, J = 6.6 Hz, 6 H). ^{13}C (150 MHz, CDCl$_3$, 50 °C): δ (ppm) = 160.8, 146.5, 132.8, 126.5, 122.2, 115.7, 106.7, 42.7, 32.1, 30.4, 29.9, 29.8, 29.7, 29.5, 29.4, 27.1, 22.8, 14.2. MALDI-TOF MS (m/z): calc'd for C$_{46}$H$_{70}$Br$_2$N$_2$O$_4$ [M$^+$] = 874.37; found 874.02.

4 **5** **6**
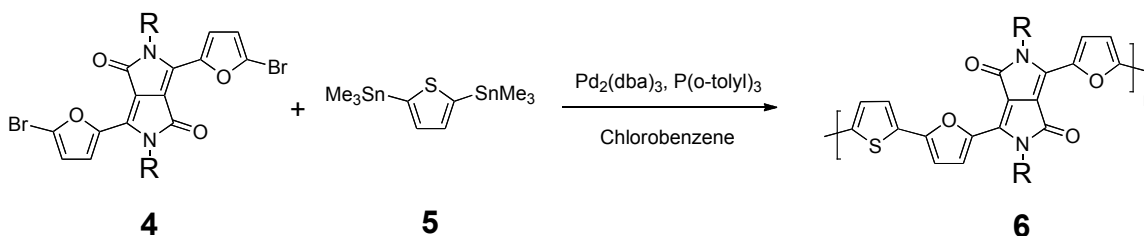
PDPP2FT-C$_{12}$ (6-C$_{12}$). **4** (160 mg, 0.210 mmol), 2,5-bis(trimethylstannyl)-thiophene (**5**) (85.97 mg, 0.210 mmol), Pd$_2$(dba)$_3$ (2 mol %) and P(o-tol)$_3$ (8 mol %) were charged within a 50 mL Schlenk tube, cycled with N$_2$ and subsequently dissolved in 9 mL of degassed chlorobenzene. The mixture was stirred for 24 h at 110 °C. The reaction mixture was allowed to cool to 55 °C, 15 mL of CHCl$_3$ was added, and the strongly complexing ligand *N,N*-diethylphenylazothioformamide (CAS# 39484-81-6) was subsequently added (as a palladium scavenger). The resulting mixture was stirred for 1 h

at 55°C, and precipitated into methanol (200 mL). The precipitate was filtered through a Soxhlet thimble and purified via Soxhlet extraction for 12 h with methanol and 1 h with hexanes, followed by collection in chloroform. The chloroform solution was concentrated by evaporation and precipitated into methanol (200 mL). The polymer **6 (PDPP2FT-C₁₂)** was filtered off as a dark solid (41 mg). SEC analysis: see **Table 2-4**.

The SEC analyses for **PDPP2FT-C₁₄,-C₁₆,-2EH** and **-2BO** are also reported in **Table 2-4**. Polymers **PDPP2FT-C₈** and **-C₁₀** were not sufficiently soluble to be analyzed by SEC, and they were not sufficiently soluble to be tested in solar cell devices.
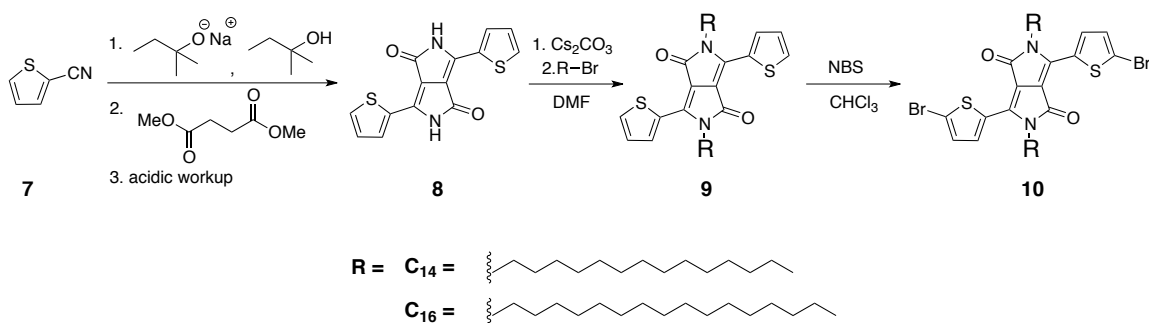
3,6-di(thiophene-2-yl)pyrrolo[3,4-c]pyrrole-1,4(2H,5H)-dione (8). A 500 mL three-neck flask connected to a condenser was charged with a stir bar and tert-amyl alcohol (250 mL). Sodium metal (2.56 g, 108 mmol) immersed in mineral oil was thoroughly washed with hexanes and cut into small pieces. The sodium metal pieces were slowly added to the reaction mixture over a 1.5 h period while the temperature was slowly increased to 120 °C over the same amount of time. After all the sodium metal pieces were dissolved, compound **7** (11.9 g, 108 mmol) was added to the reaction. As dimethyl succinate (5.29 g, 36.2 mmol) was added dropwise to the reaction mixture over 1 h, the solution turned dark red. The reaction contents were stirred at 120 °C for 2 h, and then precipitated into acidic MeOH (400 mL MeOH and 20 mL conc. HCl). Filtration of the suspension through a Buchner funnel yielded **8** as a dark red solid (9.10 g), which was used in subsequent reactions without further purification (83 % yield).

2,5-ditetradecyl-3,6-di(thiophene-2-yl)pyrrolo[3,4-c]pyrrole-1,4(2H,5H)-dione (9-C₁₄). A 250 mL of round bottom flask was charged with **8** (2.00 g, 6.66 $m$mol), Cs₂CO₃ (6.51 g, 19.98 $m$mol) and dry DMF (55 mL). The reaction contents were stirred at 120 °C for 3 h before 1-bromotetradecane (4.62 g, 16.66 $m$mol) was added to the mixture. After the reaction mixture was heated at 130 °C for 20 h, it was precipitated into ice water. The crude materials were subsequently purified by flash chromatography (CHCl₃) to yield 2.07 g of purple solid (43 %). ¹H NMR (400 MHz, CDCl₃): δ (ppm) = 8.93 (d, J = 3.6 Hz, 2 H), 7.63 (d, J = 4.8 Hz, 2 H), 7.28 (dd, J = 4.0 Hz, 4.8 Hz, 2 H), 4.06 (t, J = 8.0 Hz, 4 H), 1.76–1.72 (m, 4 H), 1.45 – 1.24 (m, 44 H), 0.87 (t, J = 6.8 Hz, 6 H). ¹³C NMR (100 MHz, CDCl₃): δ (ppm) = 161.5, 140.2, 135.4, 130.8, 129.9, 128.8, 107.8, 42.4, 32.1, 30.1, 29.8, 29.7, 29.5, 29.4, 27.0, 22.8, 14.3. MALDI-TOF MS (m/z): calc'd for C₄₂H₆₄N₂O₂S₂ [M⁺] = 692.44; found 692.42.

2,5-dihexadecyl-3,6-di(thiophene-2-yl)pyrrolo[3,4-c]pyrrole-1,4(2H,5H)-dione (9-C₁₆). Followed the same synthetic procedure as for **9-C₁₄**. Instead, used **8** (2.00 g, 6.66 $m$mol), Cs₂CO₃ (6.51 g, 19.98 $m$mol), 1-bromohexadecane (5.09 g, 16.66 $m$mol)

and 55 mL of dry DMF. Worked up the reaction mixture by first precipitating it into ice and water, and filtered through a Buchner funnel. Dissolved the crude materials in CHCl$_3$, precipitated the solution into methanol to remove mono-alkylated products, and filtered to 2.99 g of purple solid (60 %). ^{1}H NMR (400 MHz, CDCl$_3$): δ (ppm) = 8.93 (d, J = 3.6 Hz, 2 H), 7.64 (d, J = 5.2 Hz, 2 H), 7.28 (dd, J = 4.4 Hz, 4.8 Hz, 2 H), 4.07 (t, J = 8.0 Hz, 4 H), 1.76–1.72 (m, 4 H), 1.45–1.24 (m, 52 H), 0.87 (t, J = 6.8 Hz, 6 H). ^{13}C NMR (100 MHz, CDCl$_3$): δ (ppm) = 161.5, 140.2, 135.4, 130.8, 129.9, 128.8, 107.8, 42.4, 32.1, 30.1, 29.8, 29.72, 29.68, 29.5, 29.4, 27.0, 22.8, 14.3. MALDI-TOF MS (*m/z*): calc'd for C$_{46}$H$_{72}$N$_2$O$_2$S$_2$ [M$^+$] = 748.50; found 747.92.

3,6-bis(5-bromothiophene-2-yl)-2,5-ditetradecyl-pyrrolo[3,4-c]pyrrole-1,4(2H,5H)-dione (10-C$_{14}$).

A 100 mL single-neck round-bottom flask was charged with a stir bar, **9-C$_{14}$** (1.00g, 1.44 *m*mol) and 20 mL of CHCl$_3$ under N$_2$. After the reaction mixture was stirred in an ice bath at 0 °C for 20 min, NBS (526 *m*g, 2.96 *m*mol) was added in small portions over 30 min. After stirring for another 2 h, the reaction mixture was diluted with 100 mL CHCl$_3$ and washed with water 3 times. The organic layer was dried over MgSO$_4$ and filtered. Since the product was not completely dissolved, hot CHCl$_3$ was used to wash and rinse down the purple solid. The resulting materials were recrystallized twice in CHCl$_3$ to yield the product as a purple solid (308 *m*g, 25 %). Higher yields could have been obtained by further recrystallizing the mother liquor. ^{1}H NMR (400 MHz, CDCl$_3$): δ (ppm) = 8.68 (d, J = 4.0 Hz, 2 H), 7.24 (d, J = 4.0 Hz, 2 H), 3.98 (t, J = 7.6 Hz, 4 H), 1.71–1.69 (m, 4 H), 1.40–1.25 (m, 44 H), 0.87 (t, J = 6.4 Hz, 6 H). ^{13}C NMR (150 MHz, CDCl$_3$, 45°C): δ (ppm) = 161.3, 139.2, 135.4, 131.8, 131.4, 119.2, 108.2, 42.5, 32.1, 30.2, 29.9, 29.83, 29.81, 29.79, 29.72, 29.65, 29.5, 29.4, 27.0, 22.8, 14.2. MALDI-TOF MS (*m/z*): calc'd for C$_{42}$H$_{62}$Br$_2$N$_2$O$_2$S$_2$ [M$^+$] = 850.26; found 849.70.

3,6-bis(5-bromothiophene-2-yl)-2,5-dihexadecyl-pyrrolo[3,4-c]pyrrole-1,4(2H,5H)-dione (10-C16).

Followed the same synthetic procedure as for **10-C$_{14}$**. Instead, used **9-C$_{16}$** (1.50g, 2.00 *m*mol), NBS (730 *m*g, 4.10 *m*mol) and 80 mL of CHCl$_3$ in a 250-mL RBF. The reaction mixture appeared as a purple suspension. After stirring at room temperature after 2 d under N$_2$, the suspension was precipitated into 50 mL of MeOH and filtered. The resulting materials were recrystallized five times in CHCl$_3$ to yield the product as a purple solid (534 *m*g, 30 %). Higher yields could have been obtained by further recrystallizing the mother liquor. ^{1}H NMR (400 MHz, CDCl$_3$): δ (ppm) = 8.68 (d, J = 4.0 Hz, 2 H), 7.23 (d, J = 4.0 Hz, 2 H), 3.98 (t, J = 7.6 Hz, 4 H), 1.73–1.69 (m, 4 H), 1.40–1.25 (m, 52 H), 0.88 (t, J = 6.4 Hz, 6 H). ^{13}C NMR (150 MHz, CDCl$_3$, 45°C): δ (ppm) = 161.3, 139.2, 135.4, 131.8, 131.4, 119.2, 108.2, 42.5, 32.1, 30.2, 29.86, 29.83, 29.82, 29.80, 29.72, 29.65, 29.5, 29.4, 27.0, 22.8, 14.2. MALDI-TOF MS (*m/z*): calc'd for C$_{46}$H$_{70}$Br$_2$N$_2$O$_2$S$_2$ [M$^+$] = 904.32; found 904.81.

10   **5**   **11**
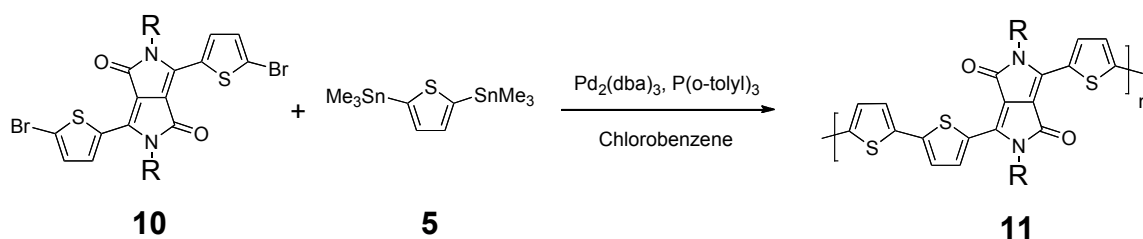
PDPP3T-C$_{14}$ (11-C$_{14}$). The same polymerization protocol as that described for **PDPP2FT-C$_{12}$ (6-C$_{12}$)** was followed. Instead, used **10-C$_{14}$** (150 mg, 176 μmol), **5** (72.2 mg, 176 μmol), Pd$_2$(dba)$_3$ (3.23 mg, 3.53 μmol) and P(o-tol)$_3$ (4.29 mg, 14.1 μmol) in 5.3 mL of degassed chlorobenzene. After 24 h, the reaction was cooled to room temperature and aliquots were taken for SEC analysis (~1 mL was extracted from the reaction mixture and precipitated into ~3 mL of methanol). Results of SEC analysis are shown in **Table 2-4.**

PDPP3T-C$_{16}$ (11-C$_{16}$). The same polymerization protocol as that described for **PDPP2FT-C12 (6-C12)** was followed. Instead, used **10-C$_{16}$** (160 mg, 176 μmol), **5** (72.2 mg, 176 μmol), Pd$_2$(dba)$_3$ (3.23 mg, 3.53 μmol) and P(o-tol)$_3$ (4.29 mg, 14.1 μmol) in 5.5 mL of degassed chlorobenzene. The reaction mixture formed a gel-like materials after 15 min of heating at 110 °C, and it was continued to be heated at 110 °C for 24 h. The reaction was then cooled to room temperature and aliquots were taken for SEC analysis (~1 mL was extracted from the reaction mixture and precipitated into ~3 mL of methanol). Results of SEC analysis is shown in **Table 2-4**.

Table 2-4. SEC analysis of PDPP2FT and PDPP3T derivatives.

Polymers	M_n (kDa)	M_w (kDa)	PDI
PDPP2FT-2EH	56	88	1.57
PDPP2FT-2BO	54	85	1.56
PDPP2FT-C$_{12}$	46	78	1.70
PDPP2FT-C$_{14}$	58	92	1.59
PDPP2FT-C$_{16}$	55	87	1.60
PDPP3T-C$_{14}$	<1	<1	---
PDPP3T-C$_{16}$	0.95	1.9	1.98

Thermal Characterization by Differential Scanning Calorimetry (DSC). PDPP2FT polymers were analyzed by (DSC TA Instruments DSC Q200), but no notable peaks were observed. Representative DSC traces are shown in **Fig. 2-6**.
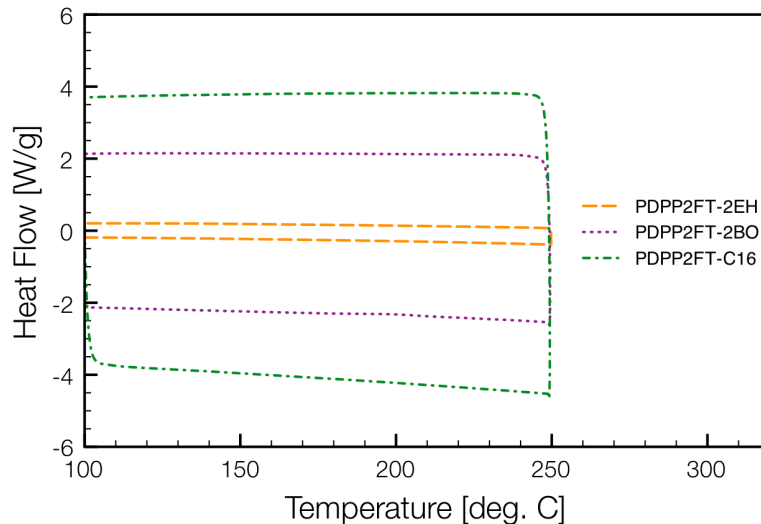
Figure 2-6. Representative DSC traces of PDPP2FT derivatives.

2.4.2. Device Fabrication and Testing

Substrate Preparation. All devices were fabricated on indium tin oxide (ITO)-coated glass substrates (pre-patterned, $R = 20\ \Omega^{-1}$, Thin Film Devices, Inc.). To clean and prepare these substrates for device fabrication, the following procedure was followed:

- Sonicate for 20 minutes in 2% Helmanex soap water, then rinse thoroughly with deionized (DI) water
- Sonicate for 20 minutes in DI water
- Sonicate for 20 minutes in acetone
- Sonicate for 20 minutes in isopropyl alcohol, then dry under a stream of air
- UV-ozone clean for 5 minutes
- Spin-coat a thin layer (30-40 nm) of PEDOT:PSS (Clevios PVP) at 4000 RPM for 40 s, then dry in air for 10 minutes at 140 °C
- Transfer to glovebox under N_2

Solar Cell Device Preparation. Using substrates prepared as described above, the following procedure was followed to prepare solar cell devices:

- Prepare blend solution in $CHCl_3$ with a polymer:$PC_{71}BM$ ratio of 1:3 by mass and a total solids concentration of 10.67 mg/mL for PDPP2FT-C_{12} and -C_{14} and 16 mg/mL for PDPP2FT-C_{16} and -2BO
- Add 5% by volume of high-boiling additive 1-chloronapthalene (CN)
- Spin-coat onto substrate at 2000 RPM for 40 s, followed by 4000 RPM for 5 s
- Dry under low vacuum for 20 minutes
- Thermally evaporate cathodes (1 nm LiF, 100 nm Al) under vacuum (~10^{-7} torr) through a shadow mask defining an active area of 0.03 cm^2

SCLC Device Preparation. Using substrates prepared as described above, the following procedure was followed to prepare SCLC devices:

- Prepare polymer solution in $CHCl_3$ at a concengration of 8 mg/mL for PDPP2FT-C_{12} and -C_{14} and 10 mg/mL for PDPP2FT-C_{16} and -2BO

- Add 5% by volume of high-boiling additive CN
- Spin-coat onto substrate at either 1000 or 2000 RPM for 40 s (to vary thickness), followed by 4000 RPM for 5 s
- Dry under low vacuum for 20 minutes
- Thermally evaporate cathodes (50 nm Au) under vacuum (~10^{-7} torr) through a shadow mask defining an active area of 0.03 cm^2

2.4.3. Material Characterization and Device Testing

UV-Vis Absorption. Thin-film UV-Vis absorption spectra (**Fig. 2-7**) were measured with an Varian Cary 5000 spectrophotometer. Thin-films were spin-coated from CHCl$_3$ onto untreated quartz slides.
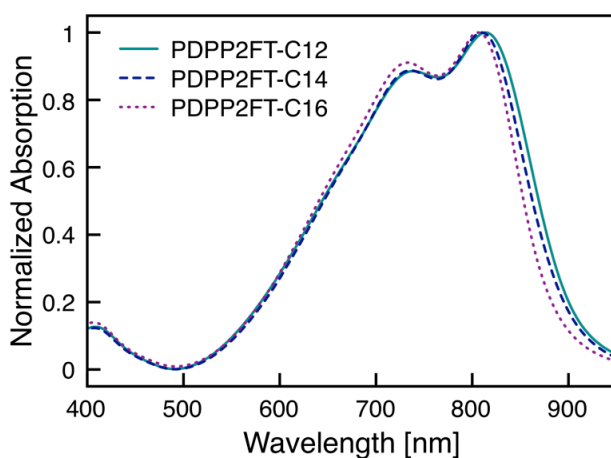

Figure 2-7. UV-Vis absorption spectra of PDPP2FT derivatives.

Device Testing. Current-voltage (*J-V*) curves were measured using a Keithley 2400 source-measure unit. Solar cell devices (*n* = 8 for each derivative) were tested under AM 1.5 G solar illumination at 100 mW cm^{-2} using a Thermal-Oriel 150 @ solar simulator. For SCLC devices of each material, mobility values for two different film thicknesses were averaged to give the values provided.

Devices fabricated from PDPP2FT-2BO had a relatively low average PCE of 1.3%, with a V_{OC} of 0.61 V, a J_{SC} of -3.8 mA/cm^2, and a FF of 0.55 (**Fig. 2-8**).
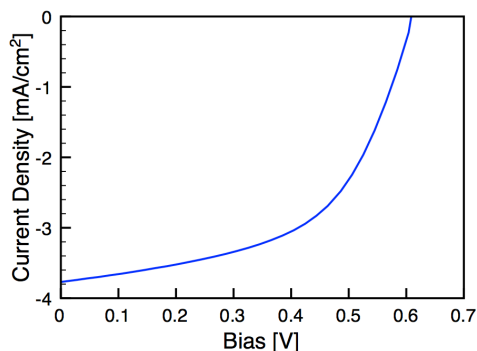

Figure 2-8. Average *J-V* curve for solar cells fabricated from PDPP2FT-2BO.

Surface Topography. Height profiles of the active layers of devices were imaged using a Veeco Multimode V Atomic Force Microscope (AFM) operated in tapping mode.

X-ray Scattering. Grazing-incidence x-ray scattering (GIXS) experiments were conducted at the Stanford Synchotron Radiation Lightsource on beamline 11-3. Substituting Si for ITO on glass, samples were prepared following the aforementioned procedure for SCLC devices (for neat polymer films) or for solar cell devices (for blend films). Samples were irradiated at a fixed incident angle of approximately 0.1° and their GIXS patterns were recorded with a 2-D image detector (MAR345 image plate detector). GIXS patterns were recorded with an X-ray energy of 12.71 keV (λ = 0.975 Å). To maximize the intensity from the sample, the incident angle (~0.08° – 0.12°) was carefully chosen such that the X-ray beam penetrated the sample completely but did not interact significantly with the silicon substrate. Typical exposure times were 30-600 s.

Analysis of GIXS scattering profiles of PDPP2FT-2BO (**Fig. 2-9**) indicate a π-π stacking distance of 3.9 Å, a π-π stacking correlation length of 1.2 nm, a lamellar spacing distance of 14 Å, and a lamellar spacing correlation length of 2.5 nm. The large π-π stacking distance and short correlation lengths agree with the poor performance of devices fabricated from PDPP2FT-2BO. GIXS scattering profiles of blend (BHJ) films (**Fig. 2-10**) exhibit peaks similar peaks to those of the neat films, but the intensity of the $PC_{71}BM$ ring adds difficulty to a correlation length analysis.
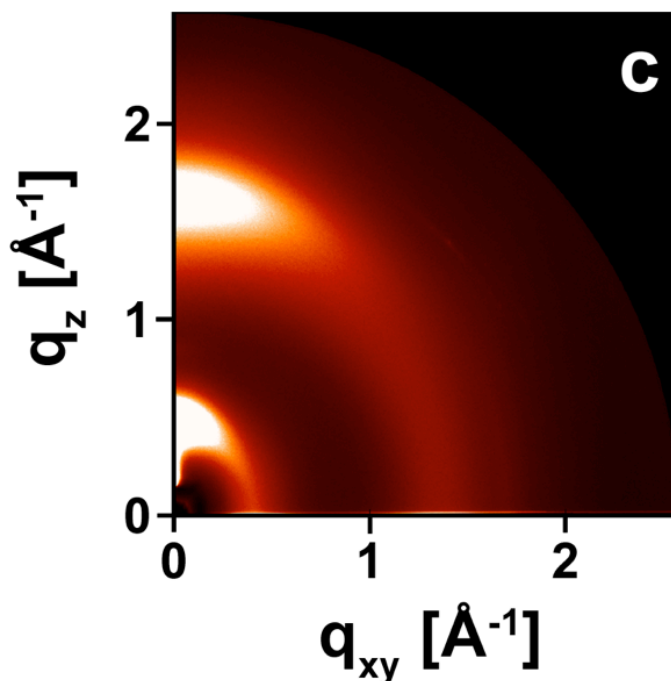
Figure 2-9. GIXS scattering profile of a neat film of PDPP2FT-2BO.
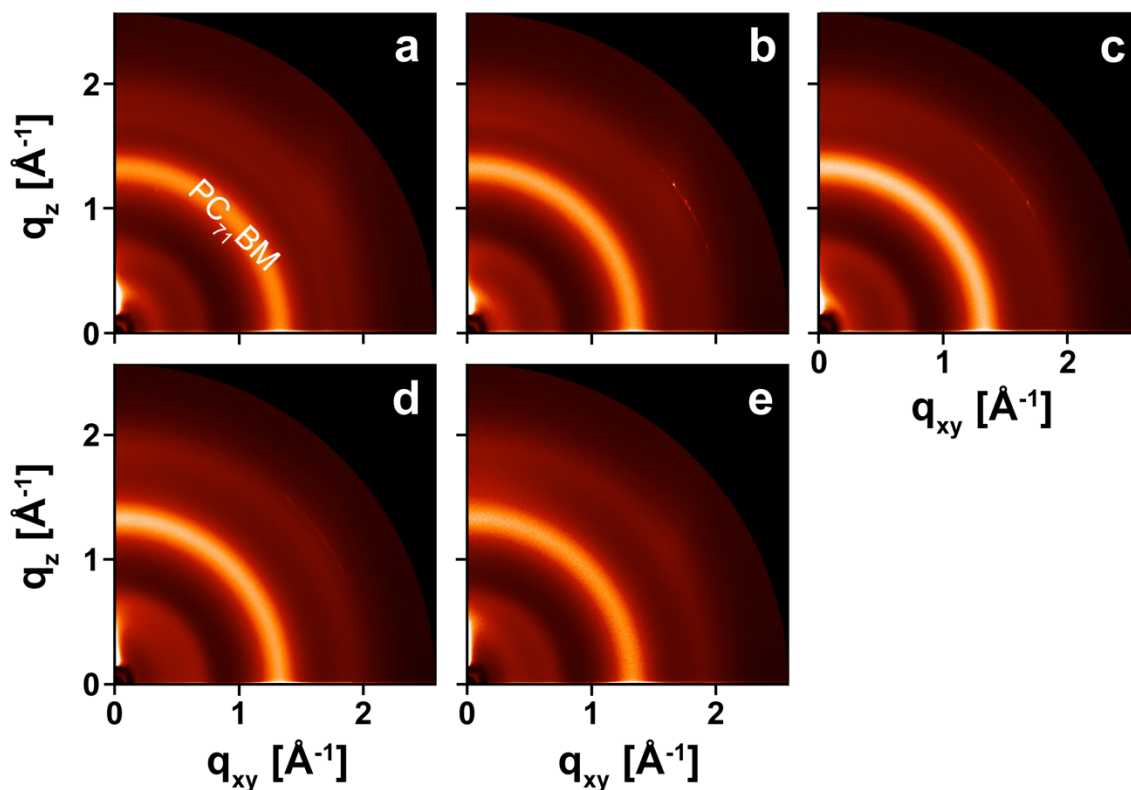
Figure 2-10. GIXS scattering profiles of blend (BHJ) films of a) PDPP2FT-C_{12}, b) PDPP2FT-C_{14}, c) PDPP2FT-C_{16}, d) PDPP2FT-2EH, and e) PDPP2FT-2BO.

2.5. References

(1)   Thompson, B. C.; Fréchet, J. M. J. *Angew. Chem. Int. Ed.* **2008**, *47*, 58.

(2)   Dennler, G.; Scharber, M. C.; Brabec, C. J. *Adv. Mater.* **2009**, *21*, 1323.

(3)   Scharber, M. C.; Mühlbacher, D.; Koppe, M.; Denk, P.; Waldauf, C.; Heeger, A. J.; Brabec, C. J. *Adv. Mater.* **2006**, *18*, 789.

(4)   Chen, J.; Cao, Y. *Acc. Chem. Res.* **2009**, *42*, 1709.

(5)   Gunes, S.; Neugebauer, H.; Sariciftci, N. S. *Chem. Rev.* **2007**, *107*, 1324.

(6)   Li, C.; Liu, M.; Pschirer, N. G.; Baumgarten, M.; Müllen, K. *Chem. Rev.* **2010**, *ASAP*.

(7)   Bundgaard, E.; Krebs, F. C. *Sol. Energ. Mat. Sol. Cells* **2007**, *91*, 954.

(8)   Boudreault, P.-L. T.; Najari, A.; Leclerc, M. *Chem. Mater.* **2011**, *23*, 456.

(9)   Li, Y.; Sonar, P.; Singh, S. P.; Soh, M. S.; van Meurs, M.; Tan, J. *J. Am. Chem. Soc.* **2011**, *133*, 2198.

(10)   Li, Y.; Zou, Y. *Adv. Mater.* **2008**, *20*, 2952.

(11)   Hou, J.; Tan, Z. a.; Yan, Y.; He, Y.; Yang, C.; Li, Y. *J. Am. Chem. Soc.* **2006**, *128*, 4911.

(12)   Roncali, J. *Macomol. Rapid Comm.* **2007**, *28*, 1761.

(13)   Varotto, A.; Treat, N. D.; Jo, J.; Shuttle, C. G.; Batara, N. A.; Brunetti, F. G.; Seo, J. H.; Chabinyc, M. L.; Hawker, C. J.; Heeger, A. J.; Wudl, F. *Angew. Chem. Int. Ed.* **2011**, *50*, 5166.

(14) Veldman, D.; Meskers, S. C. J.; Janssen, R. A. J. *Adv. Funct. Mater.* **2009**, *19*, 1939.

(15) Wienk, M. M.; Turbiez, M.; Gilot, J.; Janssen, R. A. J. *Adv. Mater.* **2008**, *20*, 2556.

(16) Chen, H.-Y.; Hou, J.; Zhang, S.; Liang, Y.; Yang, G.; Yang, Y.; Yu, L.; Wu, Y.; Li, G. *Nat. Photon.* **2009**, *3*, 649.

(17) Zhou, H.; Yang, L.; Price, S. C.; Knight, K. J.; You, W. *Angew. Chem. Int. Ed.* **2010**, *49*, 7992.

(18) Blom, P. W. M.; Mihailetchi, V. D.; Koster, L. J. A.; Markov, D. E. *Adv. Mater.* **2007**, *19*, 1551.

(19) Parmer, J. E.; Mayer, A. C.; Hardin, B. E.; Scully, S. R.; McGehee, M. D.; Heeney, M.; McCulloch, I. *Appl. Phys. Lett.* **2008**, *92*, 113309.

(20) Coropceanu, V.; Cornil, J.; da Silva Filho, D. A.; Olivier, Y.; Silbey, R.; Brédas, J.-L. *Chem. Rev.* **2007**, *107*, 926.

(21) Johns, J. E.; Muller, E. A.; Frechet, J. M. J.; Harris, C. B. *J. Am. Chem. Soc.* **2010**, *132*, 15720.

(22) Peet, J.; Heeger, A. J.; Bazan, G. C. *Acc. Chem. Res.* **2009**, *42*, 1700.

(23) Di Nuzzo, D.; Aguirre, A.; Shahid, M.; Gevaerts, V. S.; Meskers, S. C. J.; Janssen, R. A. J. *Adv. Mater.* **2010**, *22*, 4321.

(24) Perez, M. D.; Borek, C.; Forrest, S. R.; Thompson, M. E. *J. Am. Chem. Soc.* **2009**, *131*, 9281.

(25) Rogers, J. T.; Schmidt, K.; Toney, M. F.; Kramer, E. J.; Bazan, G. C. *Adv. Mater.* **2011**, *23*, 2284.

(26) Salleo, A.; Kline, R. J.; DeLongchamp, D. M.; Chabinyc, M. L. *Adv. Mater.* **2010**, *22*, 3812.

(27) Piliego, C.; Holcombe, T. W.; Douglas, J. D.; Woo, C. H.; Beaujuge, P. M.; Fréchet, J. M. J. *J. Am. Chem. Soc.* **2010**, *132*, 7595.

(28) Beaujuge, P. M.; Pisula, W.; Tsao, H. N.; Ellinger, S.; Müllen, K.; Reynolds, J. R. *J. Am. Chem. Soc.* **2009**, *131*, 7514.

(29) Woo, C. H.; Beaujuge, P. M.; Holcombe, T. W.; Lee, O. P.; Fréchet, J. M. J. *J. Am. Chem. Soc.* **2010**, *132*, 15547.

(30) Khlyabich, P. P.; Burkhart, B.; Ng, C. F.; Thompson, B. C. *Macromolecules* **2011**, *44*, 5079.

(31) Mei, J.; Graham, K. R.; Stalder, R.; Tiwari, S. P.; Cheun, H.; Shim, J.; Yoshio, M.; Nuckolls, C.; Kippelen, B.; Castellano, R. K.; Reynolds, J. R. *Chem. Mater.* **2011**, *23*, 2285.

(32) Bronstein, H.; Chen, Z.; Ashraf, R. S.; Zhang, W.; Du, J.; Durrant, J. R.; Shakya Tuladhar, P.; Song, K.; Watkins, S. E.; Geerts, Y.; Wienk, M. M.; Janssen, R. A. J.; Anthopoulos, T.; Sirringhaus, H.; Heeney, M.; McCulloch, I. *J. Am. Chem. Soc.* **2011**, *133*, 3272.

(33) Walker, B.; Tamayo, A., B.; Dang, X.-D.; Zalar, P.; Seo, J. H.; Garcia, A.; Tantiwiwat, M.; Nguyen, T.-Q. *Adv. Funct. Mater.* **2009**, *19*, 3063.

(34) Bijleveld, J. C.; Zoombelt, A. P.; Mathijssen, S. G. J.; Wienk, M. M.; Turbiez, M.; de Leeuw, D. M.; Janssen, R. A. J. *J. Am. Chem. Soc.* **2009**, *131*, 16616.

(35) Loser, S.; Bruns, C. J.; Miyauchi, H.; Ortiz, R. P.; Facchetti, A.; Stupp, S. I.; Marks, T. J. *J. Am. Chem. Soc.* **2011**, *133*, 8142.

(36)   Sonar, P.; Singh, S. P.; Li, Y.; Soh, M. S.; Dodabalapur, A. *Adv. Mater.* **2010**, *22*, 5409.

(37)   Tamayo, A. B.; Dang, X.-D.; Walker, B.; Seo, J.; Kent, T.; Nguyen, T.-Q. *Appl. Phys. Lett.* **2009**, *94*, 103301.

(38)   Bijleveld, J. C.; Karsten, B. P.; Mathijssen, S. G. J.; Wienk, M. M.; de Leeuw, D. M.; Janssen, R. A. J. *J. Mater. Chem.* **2011**, *21*, 1600.

(39)   Hou, J.; Chen, H.-Y.; Zhang, S.; Li, G.; Yang, Y. *J. Am. Chem. Soc.* **2008**, *130*, 16144.

(40)   Park, S. H.; Roy, A.; Beaupre, S.; Cho, S.; Coates, N.; Moon, J. S.; Moses, D.; Leclerc, M.; Lee, K.; Heeger, A. J. *Nat. Photon.* **2009**, *3*, 297.

(41)   Scharber, M. C.; Koppe, M.; Gao, J.; Cordella, F.; Loi, M. A.; Denk, P.; Morana, M.; Egelhaaf, H.-J.; Forberich, K.; Dennler, G.; Gaudiana, R.; Waller, D.; Zhu, Z.; Shi, X.; Brabec, C. J. *Adv. Mater.* **2010**, *22*, 367.

(42)   Hsiang-Yu, C.; Jianhui, H.; Amy, E. H.; Hoichang, Y.; Houk, K. N.; Yang, Y. *Adv. Mater.* **2010**, *22*, 371.

(43)   McCulloch, I.; Heeney, M.; Bailey, C.; Genevicius, K.; MacDonald, I.; Shkunov, M.; Sparrowe, D.; Tierney, S.; Wagner, R.; Zhang, W.; Chabinyc, M. L.; Kline, R. J.; McGehee, M. D.; Toney, M. F. *Nat. Mater.* **2006**, *5*, 328.

(44)   Wang, C.; Jimison, L. H.; Goris, L.; McCulloch, I.; Heeney, M.; Ziegler, A.; Salleo, A. *Adv. Mater.* **2010**, *22*, 697.

(45)   Hucke, A.; Cava, M. P. *The Journal of Organic Chemistry* **1998**, *63*, 7413.

(46)   Gidron, O.; Diskin-Posner, Y.; Bendikov, M. *Journal of the American Chemical Society* **2010**, *132*, 2148.

(47)   Miyata, Y.; Nishinaga, T.; Komatsu, K. *The Journal of Organic Chemistry* **2005**, *70*, 1147.

(48)   Hoven, C. V.; Dang, X.-D.; Coffin, R. C.; Peet, J.; Nguyen, T.-Q.; Bazan, G. C. *Adv. Mater.* **2010**, *22*, E63.

(49)   Peet, J.; Kim, J. Y.; Coates, N. E.; Ma, W. L.; Moses, D.; Heeger, A. J.; Bazan, G. C. *Nat. Mater.* **2007**, *6*, 497.

(50)   Lee, J. K.; Ma, W. L.; Brabec, C. J.; Yuen, J.; Moon, J. S.; Kim, J. Y.; Lee, K.; Bazan, G. C.; Heeger, A. J. *J. Am. Chem. Soc.* **2008**, *130*, 3619.

(51)   Peet, J.; Heeger, A. J.; Bazan, G. C. *Acc. Chem. Res.* **2009**, *42*, 1700.

(52)   Yu, G.; Heeger, A. J. *J. Appl. Phys.* **1995**, *78*, 4510.

(53)   Halls, J. J. M.; Walsh, C. A.; Greenham, N. C.; Marseglia, E. A.; Friend, R. H.; Moratti, S. C.; Holmes, A. B. *Nature* **1995**, *376*, 498.

(54)   Guo, J.; Liang, Y.; Szarko, J.; Lee, B.; Son, H. J.; Rolczynski, B. S.; Yu, L.; Chen, L. X. *J. Phys. Chem. B* **2009**, *114*, 742.

(55)   Beiley, Z. M.; Hoke, E. T.; Noriega, R.; Dacuña, J.; Burkhard, G. F.; Bartelt, J. A.; Salleo, A.; Toney, M. F.; McGehee, M. D. *Adv. Energ. Mater.* **2011**, n/a.

(56)   Street, R. A.; Northrup, J. E.; Salleo, A. *Phys. Rev. B* **2005**, *71*, 165202.

(57)   Kim, Y.; Cook, S.; Tuladhar, S. M.; Choulis, S. A.; Nelson, J.; Durrant, J. R.; Bradley, D. D. C.; Giles, M.; McCulloch, I.; Ha, C.-S.; Ree, M. *Nat Mater* **2006**, *5*, 197.

(58)   Warren, B. E. *X-Ray Diffraction*; Addison-Wesley: Reading, MA, 1969.

(59)   Rivnay, J.; Noriega, R.; Northrup, J. E.; Kline, R. J.; Toney, M. F.; Salleo, A. *Phys. Rev. B* **2011**, *83*, 121306

Chapter 3

Enhanced Solid-State Order and Field-Effect Hole Mobility through Control of Nanoscale Polymer Aggregation

Abstract

Efficient charge carrier transport in organic field-effect transistors (OFETs) requires thin films that demonstrate solid-state order and proper polymer alignment. Polymers that provide high field-effect mobilities are known, but currently there are few general strategies for ensuring that π-π packing within films is oriented in-plane with the substrate. In order to study solid-state packing, furan-containing diketopyrrolopyrrole (DPP) polymers were synthesized with either linear hexadecyl or branched 2-butyloctyl side chains with similar optoelectronic properties as determined by UV-vis-NIR spectroscopy and cyclic voltammetry. Observed differences in polymer solubility are attributed to variation in side chain shape and polymer backbone curvature. Average field-effect hole mobilities of the polymers range from 0.19 to 1.82 cm2/V·s, where PDPP3F-C16 is the least soluble polymer and provides the highest maximum mobility of 2.25 cm2/V·s. Analysis of the films by AFM and GIXD reveal that less soluble polymers, often with linear side chains, have larger crystalline domains, pack considerably tighter, and align with a greater preference for in-plane π-π packing. Characterization of the polymer solutions prior to spin-coating reveals a correlation between early onset nanoscale aggregation and the formation of films that favor in-plane π-stacking. Further support for this effect is observed when non-solvent is added to PDPP3F-BO solutions to induce aggregation, which results in films that show increased nanostructural order, in-plane π-π orientation, and field-effect mobilities. Since nearly all π-conjugated materials may be coaxed to aggregate, this strategy for enhancing solid-state properties and OFET performance has applicability to a wide variety of organic electronic materials.

3.1 Introduction

Solution-processed organic field-effect transistors (OFETs) attract considerable research attention for their potential applications as low-cost components in large-area flexible displays,[1-3] radio frequency identification (RFID) tags,[4,5] sensors,[6] and logic circuits.[7] Through advancements in material design,[8-13] processing conditions,[14,15] and understanding of device physics,[16-19] significant progress has been achieved in OFET development, where polymer-based devices display charge mobilities well beyond 1 cm^2/V·s.[10,11,13,20-22] In spite of these high-performing OFET polymers, it remains a challenge to correlate macromolecular structure with device performance. Specifically, since organic thin films are integral components of OFETs, it is essential to understand how polymer structural properties affect solid-state order.[23,24]

Semiconducting films that demonstrate high field-effect mobility often consist of planar, π-conjugated polymers in order to enhance effective conjugation length and charge delocalization. In the solid-state, highly coplanar polymer backbones promote packing with short cofacial distances[17,28] and highly crystalline order,[19] thereby reducing the energy barrier for charge hopping between adjacent molecules.[29-31] Since these polymers tend to self-assemble and aggregate, solubility is achieved by appending alkyl side-chains to the backbones. Variation of these side chains has been shown to greatly influence many solid-state properties, including film morphology, crystallinity, and packing order.[25-27]

Although these design principles promote tight π-π packing in films, control of the orientation of this packing orientation is still not well understood. Optimal OFET performance is often achieved when the majority of π-π packing aligns parallel to the substrate (in-plane), between the source and drain electrodes. Conversely, charge mobility is usually diminished when cofacial packing aligns perpendicular to the substrate and π-stacking is oriented out-of-plane. Most strategies for aligning conjugated polymers focus on film formation techniques (i.e. surface modification), but do not address the effects of macromolecular structure. The few synthetic strategies for varying π-stacking orientations involve manipulation of polymer regioregularity and molecular weight. By doing so, films of poly(3-hexylthiophene) have demonstrated improvements in field-effect mobility by as much as two orders of magnitude when films favored in-plane π-stacking.[57] While effective, these strategies are not necessarily applicable to new classes of donor-acceptor polymers that often contain complex heterocyclic structures.
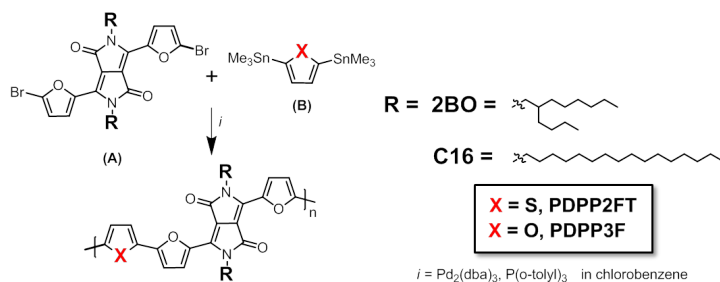

Figure 3-1. Synthesis of PDPP2FT and PDPP3F with linear or branched alkyl side chains *via* Stille cross-coupling polycondensation.

Diketopyrrolopyrrole (DPP) polymers are one such class of donor-acceptor polymers that provide good electronic performance, including some of the highest polymer-based field-effect mobilities to date (co-monomer **A, Fig. 3-1**).[12,23,32,42,43] The DPP subunit is a planar, electron-deficient chromophore that is relatively simple to synthesize and can be flanked with various moieties that include: phenyls,[33-35] thiophenes,[12,20,35-39] thienylthiophenes,[40] selenophenes,[38,41] and most recently furans.[44-46] Incorporation of furan subunits is a nascent strategy for new conjugated materials, despite the similarities between furan and its common sulfur analog, thiophene. Oligofurans offer the potential for renewable molecular sourcing along with properties that should benefit solid-state order, like short inter-ring bond lengths and high backbone coplanarity.[47,48] Additionally furan versus thiophene substitution has shown to improve the solubility of DPP-polymers, which enables the use of smaller side chains for solution processability.[25,43] Smaller side chains promote tighter solid-state packing and substantially improved power conversion efficiency in organic photovoltaics. Although not noted previously, the orientation of π-π packing was observed to vary with the size of side chain substitution, suggesting that solubility affects polymer-packing alignment.

Herein, we thoroughly examine the relationships between side-chain structure, aggregation behavior, solid-state order and OFET performance. Significantly, we discovered that the highest performing OFET polymer (hole mobility up to 2.25 cm^2/V·s) is also the least soluble and therefore has the greatest preference for aggregation in solution. It is inferred that these nanoscale solution phase aggregates facilitate the formation of films that are optimal for OFET operation (i.e. crystallinity, tight packing, in-plane π-stacking). Correlation between aggregation is further supported by the enhancement of solid-state packing and field-effect mobility upon addition of non-solvent to polymer solutions prior to film deposition.

3.2 Results and Discussion

Polymer Synthesis and Characterization. Diketopyrrolopyrrole polymers were prepared by Stille cross-coupling polycondensation between a dibrominated DPP2F monomer (monomer **A, Fig. 3-1**) and 2,5-bis(trimethylstannyl)thiophene (**T**) or 2,5-bis(trimethylstannyl)-furan (**F**) to furnish PDPP2FT and PDPP3F. Each polymer backbone was substituted with either linear hexadecyl (C16) or branched 2-butyloctyl (BO) side chains. SEC analysis of the polymers reveal that they have similar number average molecular weights (M_n) between 46–59 kDa and relatively narrow polydispersities. Both polymer backbones display considerable solubility in chloroform (> 10 mg/mL), even when appended with linear hexadecyl groups. This solubility highlights the profound effect of a simple atomic substitution, since analogous thiophene-containing DPP-polymers require branched side chains for equivalent levels of solution processability.
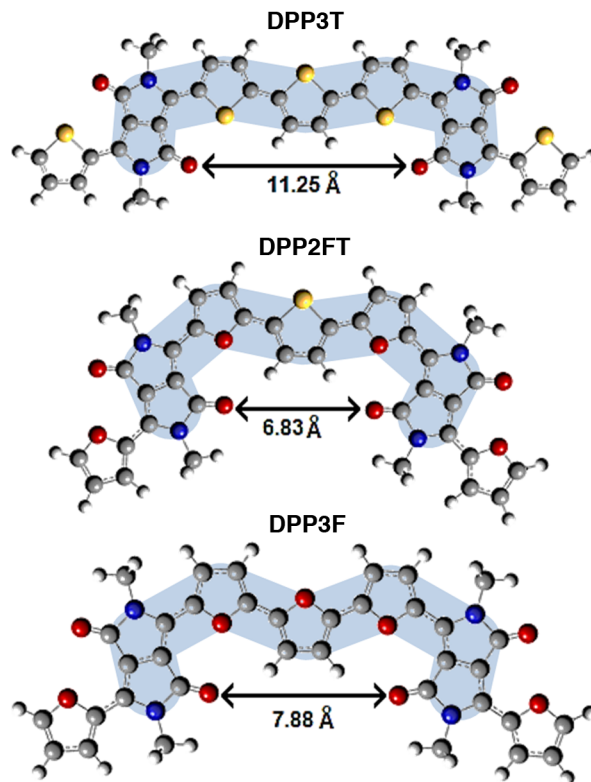
Figure 3-2. Geometry optimized structures of DPP3T, DPP2FT, and DPP3F trimers obtained by DFT calculations. The extent of backbone curvature is depicted for each structure (blue highlight), along with the inter-ketone distance between DPP subunits.

In order to investigate the effects of furan substitution on polymer structure, density functional theory (DFT) calculations were carried out on methyl-substituted trimers of DPP3T, DPP2FT, and DPP3F using Gaussian 09 with a hybrid B3LYP correlation functional and 6-31G(d) basis set. Geometry optimized structures reveal that each trimer approaches complete planarity with very small inter-ring torsion angles (< 4°, **Figs. 3-10** and **3-11**). What varies the most between trimers is molecular curvature, based on the through-space distance between DPP carbonyls (**Fig. 3-2**). DPP2FT shows the shortest inter-carbonyl distance of 6.83 Å due to the largest bend in the conjugated backbone; DPP3F has the next shortest distance of 7.88 Å, and DPP3T exhibits the longest distance (11.25 Å). By this analysis, DPP3T is considerably more linear than the conjugated backbones of DPP2FT and DPP3F trimers. Interestingly, the backbone that displays the greatest amount of curvature among the trimers (DPP2FT) also provides the most qualitatively soluble polymers (PDPP2FT). These data support prior studies that correlate conjugated polymers with greater backbone curvature exhibit greater solubility.[49] Compared to linear polymers, polymers with curved backbones exhibit weaker interchain interactions, thereby diminishing aggregation and increasing solubility. Additionally, polymers with curved geometries may form coils in solution that are entropically favored. Therefore, the greater solubility of furan versus thiophene-containing DPP-polymers is likely the result of greater backbone curvature.
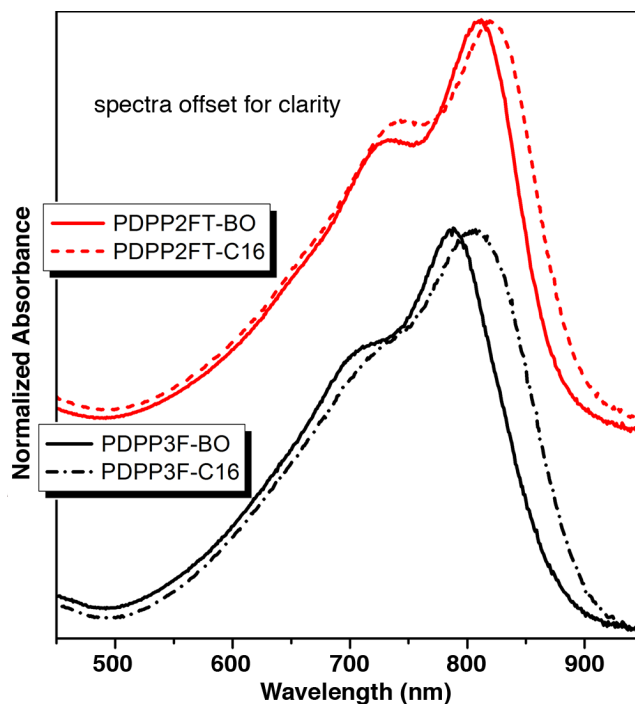
Figure 3-3. UV-vis-NIR absorption spectra of PDPP2FT or PDPP3F films spun from chloroform. A redshift in λ_{max} is observed for polymers substituted with linear versus branched side chains.

Characterization of the polymers by cyclic voltammetry and UV-vis-NIR spectroscopy reveal that they all have comparable optoelectronic properties. Similar highest occupied molecular orbital (HOMO) and lowest unoccupied molecular orbital (LUMO) energy levels are measured for each polymer (**Fig. 3-12**). Additionally, the polymers demonstrate near-identical absorption profiles with λ_{max} values and onsets that vary only by a few nanometers (**Fig. 3-3**). Based on these similarities, if the polymers perform differently in OFETs, the variation is likely due to solid-state properties rather than the intrinsic optoelectronics of each material.

OFET Fabrication and Performance. Hole mobility was measured from OFETs with bottom gate/top contact geometry (detailed fabrication methods are supplied in the supporting information). Devices were fabricated by spin-coating polymer solutions from chloroform (1-3 mg/mL) onto OTS-treated SiO_2 (300 nm)/n^{++}-Si substrates, followed by thermal deposition of Au electrodes through a shadow mask with predetermined features. Short channel effects were minimized by choosing channel lengths and widths of 40–100 μm and 400–1600 μm, respectively. Top performing devices were thermally annealed at 140 °C for 30 minutes prior to top contact deposition, followed by 5 days of vacuum annealing at 110 °C (~ 1 mbar). Although differential scanning calorimetry revealed no discernible phase transitions (**Fig. 3-13**), annealed films displayed redshifted absorption spectra that may have arisen from the removal of residual solvent and minor decreases in interpolymer spacing.
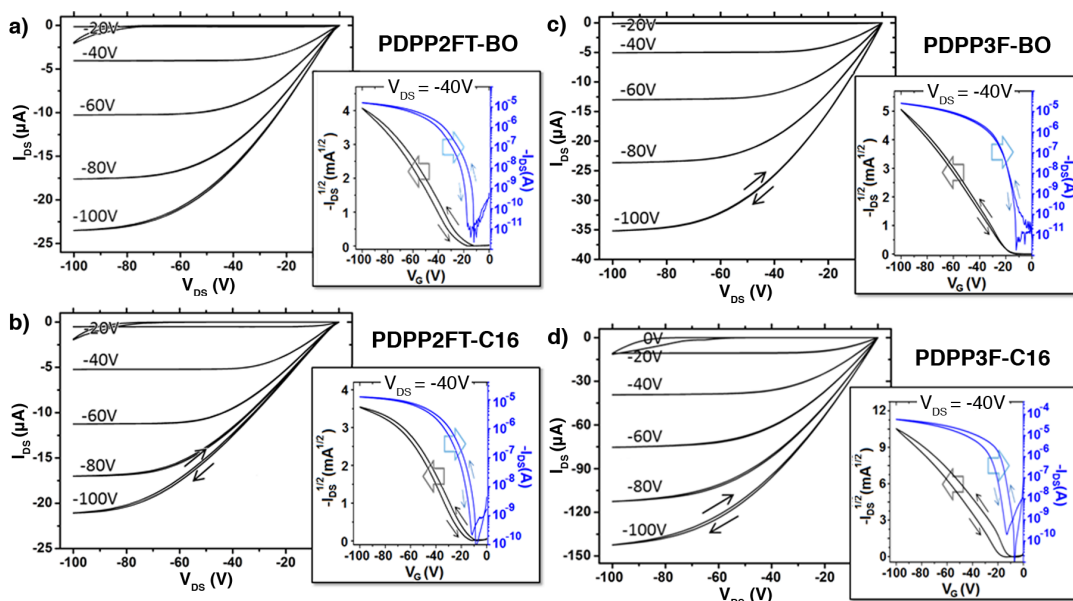
Figure 3-4. Output and transfer curves for OFETs fabricated with PDPP2FT and PDPP3F polymers.

All four polymers display saturation under p-channel operation with minimal hysteresis, similar threshold voltages (V_{th}), and good hole mobility (**Fig. 3-4**), where mobility was calculated from the linear portion of the transfer curve *via* the saturation regime model (**Table 3-2**).[53] PDPP2FT-C16 and PDPP2FT-BO provide hole mobilities of 0.26 cm²/V·s and 0.19 cm²/V·s, respectively. Higher mobility (0.46 cm²/V·s) is obtained with PDPP3F-BO. PDPP3F-C16 is the top-performing polymer in the series, where it demonstrates the largest I_{on}/I_{off} ratio and a maximum mobility of 2.25 cm²/V·s (average μ_h = 1.82 cm²/V·s). Our observation that the least soluble polymer provides the highest field-effect mobilities, suggests that the strong interpolymer interactions present in solutions of PDPP3F-C16 contribute to the formation of well-ordered thin films.

Table 3-2. Organic field effect transistor (OFET) characteristics.

Polymer	I_{on}/I_{off}	V_{th} [V]	$\mu_h{}^a$ [cm²/V·s]
PDPP2FT-BO	10^5	-21	0.19 (0.31)
PDPP2FT-C16	10^5	-12	0.26 (0.35)
PDPP3F-BO	10^5	-18	0.48 (0.56)
PDPP3F-C16	10^6	-11	1.82 (2.25)

^{a} Reported values are an average of at least 10 devices. Data in parentheses are maximum values.

Thin-Film Morphology. Atomic force microscopy (AFM) was employed to analyze the morphology and nanotopography of each polymer film. Films of PDPP2FT-BO and PDPP2FT-C16 show relatively small features (< 50 nm) and root-mean-square roughness (R_{RMS}) values of 0.542 nm and 0.761 nm, respectively (**Fig. 3-5**). Since PDPP2FT films do not from large crystalline domains, it explains why they also show lower hole mobilities. In contrast, the morphology of PDPP3F films (BO and C16) show large features (≥ 50 nm) and grain patterns that suggest the presence of long-range order.

42

Films of PDPP3F-BO show a R_{RMS} of 0.819 nm, while those composed of PDPP3F-C16 are the roughest (R_{RMS} = 1.233 nm). PDPP3F-C16 films even show several long, ribbon-like features that are 50 nm or more in length. These large features and increased R_{RMS} are likely the result of enhanced polymer crystallization and ordering during the film forming process. While film crystallinity is beneficial for high OFET performance, it only partially explains how a polymer like PDPP3F-C16 achieves hole mobilities that exceed 2 cm^2/V·s.
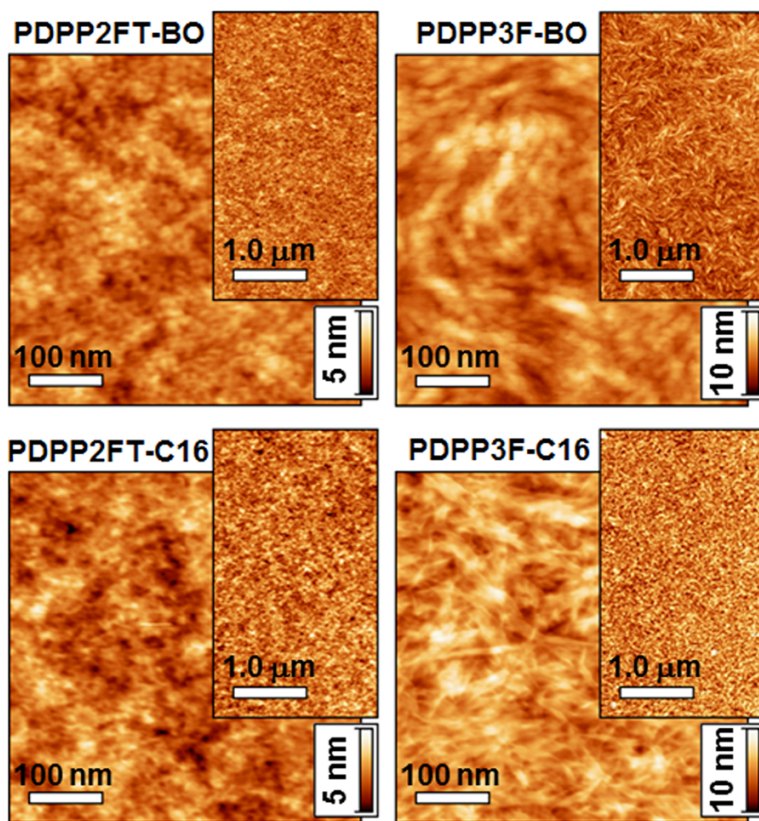
Figure 3-5. Atomic force microscopy images of films composed of PDPP2FT and PDPP3F with BO or C16 side chains. Note the long, ribbon-like domains observable in PDPP3F-C16 films (lower right).

Thin-Film Nanostructural Order. Grazing incidence X-ray diffraction (GIXD) was used to determine the nanostructural order of the polymer thin films. Specifically, diffraction data enabled the measurement of cofacial polymer packing (π-π spacing), overall crystallinity, and π-stacking orientation relative to the substrate. Small π-π spacing is preferable since it reduces the energetic barrier for interchain charge hopping, which is the predominant charge transport mechanism in polymer OFETs.[54] The π-π spacing peak is visible as a ring or partial arc at $q \sim 1.7$ Å^{-1} that corresponds to π-stacking distances of 3.82 and 3.85 Å for PDPP2FT-BO and PDPP3F-BO films, respectively (**Fig. 3-6**). Films of PDPP2FT-C16 and PDPP3F-C16 display reduced π-π spacings of 3.68 Å and 3.52 Å, respectively (**Table 3-3**). This side-chain effect is similar to what we observed in a previous study, where less sterically-bulky linear versus branched side chains promoted tighter π-π packing.[25] The tight cofacial packing of C16-polymers likely contributes greatly to the high hole mobilities observed in OFETs.

43

In addition to packing distances, GIXD data also provide correlation length (L_C), a measurement of the distance over which a crystalline structure is preserved. In polymer films, a reduction in the variability of chain position and rotation corresponds to narrow peak breadth and a longer L_C.[55] Using the full width at half maximum (FWHM) of scattering peaks, we can determine the L_C of various packing parameters via the Scherrer equation.[55,56] Films of PDPP2FT-BO display a π-π L_C of 1.14 nm while those of PDPP2FT-C16 show a L_C of 2.15 nm. PDPP3F-C16 films exhibit the longest L_C for π-π spacing in the series (3.85 nm) and more than doubles L_C values obtained for PDPP3F-BO films (1.35 nm). It is evident from these data, that linear versus branched side chains allow polymer backbones to form crystalline structures with greater long-range order. This enhanced crystallinity of C16-polymer films is yet another property, alongside tight π-π spacing, that enables PDPP3F-C16 films to achieve such high field-effect mobilities.
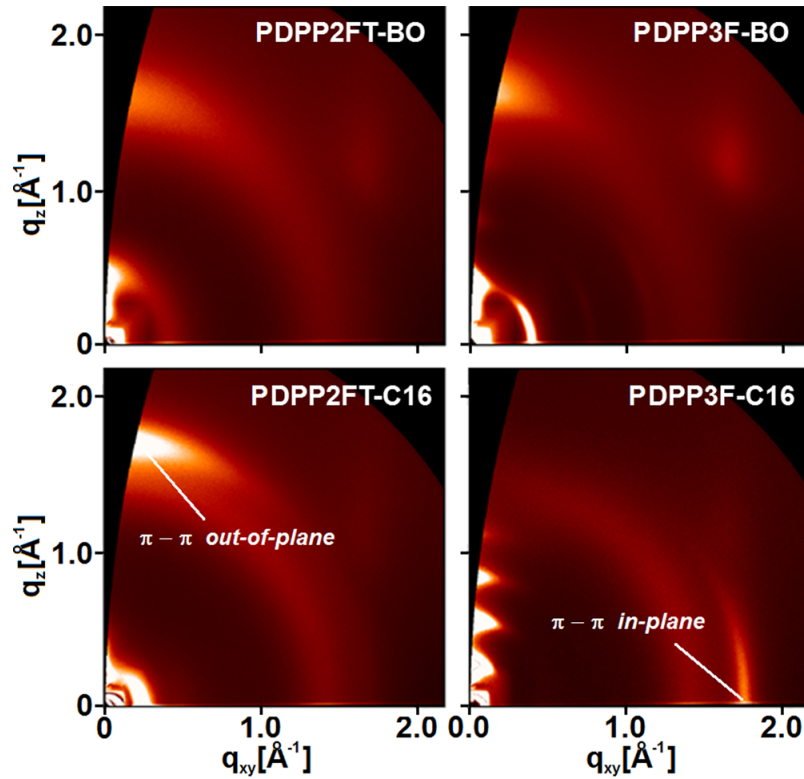
Figure 3-6. Grazing incidence X-ray diffraction data from PDPP2FT and PDPP3F films. PDPP3F-C16 exhibits in-plane π-π spacing while the other three polymers pack with out-of-plane π-π spacing.

Another important factor in OFET performance is the orientation of π-stacking with respect to the substrate. If π-π packing has an isotropic distribution in films, diffraction patterns will display an arc of scattering intensity across all polar angles (χ). However, films with preferential orientation display anisotropic scattering intensities: where in-plane π-π packing leads to greater scattering intensity at low χ, along the q_{xy} axis ($q_z \sim 0$), while out-of plane packing leads to more scattering intensity along the q_z axis ($q_{xy} \sim 0$). Ratios of in-plane to out-of-plane π-π scattering intensity ($R_{in/out}$) for PDPP2FT-BO and PDPP2FT-C16 films are 1.49 and 1.43, respectively, which correspond to roughly even distributions of oriented packing (see SI). Films of PDPP3F-BO show a slight

preference for in-plane orientation ($R_{in/out}$ of 1.77), while PDPP3F-C16 films show that nearly all π-π-packing occurs in-plane to the substrate ($R_{in/out}$ = 13.04). We postulate that this dramatic enhancement in π-stacking orientation is one of the major reasons why PDPP3F-C16 performs so well in OFETs.

**Table 3-3. Thin film polymer packing parameters determined by GIXD.**

Polymer	π-π spacing			lamellar spacing	
	d [Å]	L_C [nm]	$R_{in/out}$	d [Å]	L_C [nm]
PDPP2FT-BO	3.82	1.14	1.49	14.68	3.05
PDPP2FT-C16	3.68	2.15	1.43	28.88	3.94
PDPP3F-BO	3.85	1.35	1.77	15.88	11.04
PDPP3F-C16	3.52	3.85	13.04	30.41	9.71

Factors that Control Orientation of Polymer π-Stacking. We initially hypothesized that the variation in π-stacking orientation between polymers derived from polymer-substrate interactions. Previous studies have shown that these forces can mediate molecular organization at the organic-substrate interface.[58,59] Nevertheless, when we alter the surface energy of the silicon substrates *via* functionalization with various self-assembled monolayers (i.e. ODTS, HMDS, TS, PFOTS), π-stacking orientation remains unaffected (**Fig. 3-15** and **3-16**). All PDPP3F-C16 films maintain a high degree of in-plane packing with $R_{in/out}$ between 11.94 and 15.87, while the films of BO-polymers still show mixed orientations of packing with $R_{in/out}$ ranging from 1.51 to 2.31. Therefore, it is unlikely that polymer-substrate interactions significantly influence how these polymers orient in thin films.

If nanostructural order is relatively independent of substrate interactions, then π-stacking orientation in these films is likely governed by interpolymer interactions that can induce nanoscale polymer aggregation. Solution phase polymer aggregates have been employed previously in methods to control film morphology in OFETs and organic photovoltaics (OPVs).[60-62,63] Non-solvents have been added to polymer solutions in order to pre-determine film morphologies for OPVs and OFETs by inducing crystallite formation.[64,65] Recently, n-type polymer-based OFETs achieved high electron mobility through improved film morphology, which was attributed to solution phase aggregation.[66]

In order to investigate polymer aggregation behavior, solutions in chloroform-d were examined by nuclear magnetic resonance (NMR) spectroscopy. ^{1}H NMR spectra of PDPP2FT-BO show well-defined peaks for the protons at 8.54 and 6.67 ppm, which correspond to protons on the C3 and C4 positions of furan (**Fig. 3-7**). Comparatively, PDPP2FT-C16 shows significant broadening of the aromatic peaks, alongside a minor shift upfield to 8.43 and 6.66 ppm. ^{1}H NMR spectra of PDPP3F-BO display well-defined aromatic peaks at 8.47 and 6.64 ppm, while PDPP3F-C16 spectra show dramatic upfield peak shifts (~ 8.10 and ~ 6.36 ppm) along with signals that are nearly indistinguishable from the baseline due to extreme line broadening. Both side-chain dependent changes in ^{1}H NMR are strongly suggestive of aggregation in solution. Peak broadening may arise

from confinement effects and loss of motion averaging as a result of polymer aggregation.[67,68] Upfield shifts may arise from increased electronic shielding of protons, which likely occurs in aggregates due to greater degrees of π-orbital overlap.
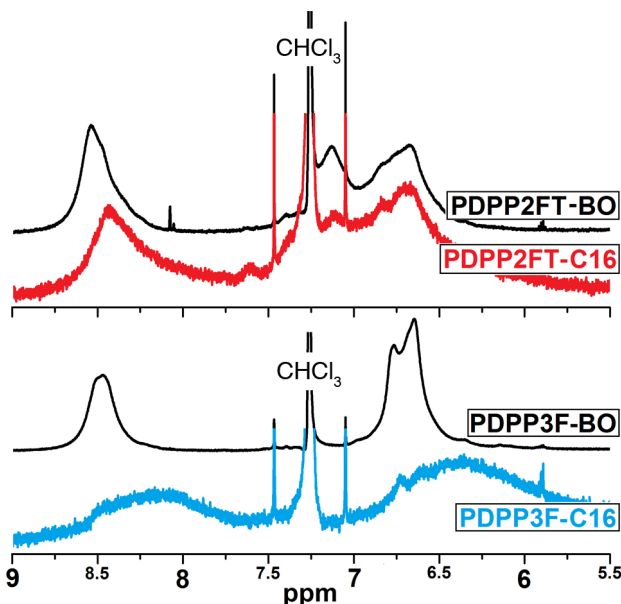

Figure 3-7. ^{1}H NMR spectra of DPP2FT (top) and DPP3F (bottom) solutions in CDCl$_3$ at 40°C.

Solution phase polymer aggregation can also be monitored by variable temperature UV-vis-NIR absorption spectroscopy. At room temperature, n-alkyl-substituted polymers display redshifted absorption profiles compared to BO-substituted polymers in both film and solution. This side-chain effect is especially pronounced for PDPP3F polymers, where C16- versus BO-substitution causes the λ_{max} to redshift by 44 nm. In polymer systems, this redshift is generally attributed to interpolymer cofacial aggregation.[50-52] When solutions are heated to 60°C, a blueshift in absorption is observed that corresponds with the high temperature dissolution of polymer aggregates (**Table 3-1**, **Fig. 3-17**). Spectral blueshifts are larger for C16-substituted polymers and is the greatest for DPP3F-C16 (λ_{max} blueshift = 21 nm). Overall, these data confirm that PDPP3F-C16 is the least soluble polymer in the series, and support the presence of polymer aggregates in solution.

Dynamic light scattering (DLS) analysis was employed to determine the relative size of polymer aggregates (**Fig. 3-18**). DLS spectra reveal that DPP2FT-C16 particles have an average diameter of 69 ± 9 nm while the average size of DPP2FT-BO particles is 41 ± 6 nm. Similarly, the solution aggregates of DPP3F-C16 and DPP3F-BO are measured to be 96 ± 21 nm and 24 ± 3 nm, respectively. It is evident from these results that side-chain choice greatly affects aggregation, where C16- versus BO-polymers have a stronger tendency to self-assemble and therefore form larger nanoparticles in solution.

From these studies, we conclude that a polymer's lack of solubility (propensity to aggregate) correlates well with its preference for edge-on polymer packing. Low solubility materials, such as PDPP3F-C16, can form a suspension of nanoscale aggregates that, when deposited, form highly ordered domains that greatly favor in-plane π-stacking.

Conversely, highly soluble polymers (i.e. BO-polymers) do not readily aggregate and may freely interact with the substrate, thereby allowing for kinetically favorable packing with out-of-plane π-stacking.
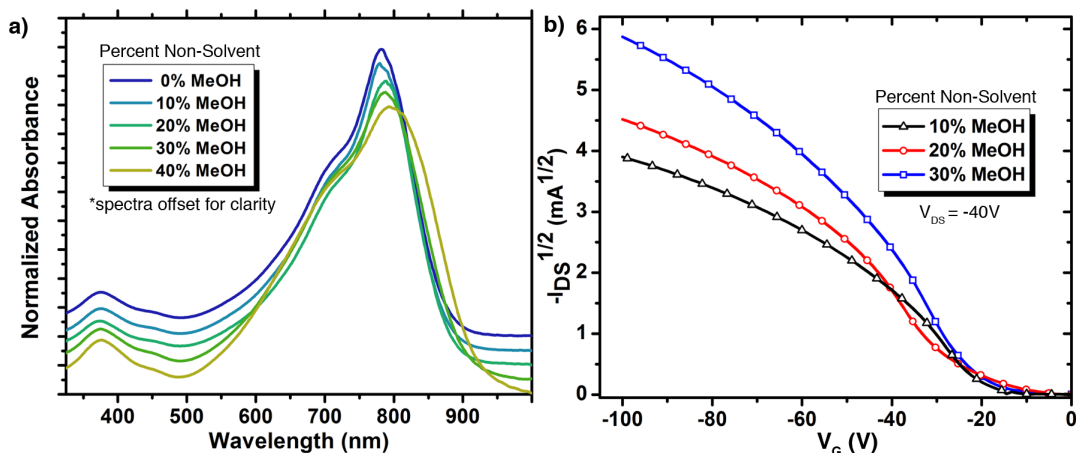
Figure 3-8. Effects of non-solvent additive (MeOH) on (a) solution UV-vis-NIR absorption and (b) OFET transfer curves of PDPP3F-BO.

Effects of non-solvent on morphology and device performance. Based on the previous discussion, if polymer solutions are induced to form more aggregates it is probable that π-stacking orientation, film crystallinity, and OFET performance may show further improvement. Therefore, varying amounts of non-solvent methanol (MeOH) were added to chloroform solutions of PDPP3F in order to promote aggregation. Using UV-vis-NIR spectroscopy, we observe that MeOH added to PDPP3F-C16 solutions ($\leq$ 20%, by volume) lead to a redshift in λ_{max} (~5 nm) compared to polymer solutions in pure chloroform (**Fig. 3-19a**). Films produced from these MeOH-doped solutions show no improvement in crystallinity by GIXD (**Fig. 3-19b**), and actually achieve lower field-effect hole mobility (1.56 cm^2/V·s). Nonetheless, this lack of improvement in film properties is not surprising since solution spectroscopy suggested there was only a minor change in aggregate concentration.

Table 3-4. GIXD and OFET data for PDPP3F-BO films cast from mixed chloroform / methanol solutions.

Solution	GIXD		OFET Performance		
	π-π d [Å]	$R_{in/out}$	I_{on}/I_{off}	V_{th} [V]	μ_h [cm^2/V·s]
10% MeOH	3.81	1.93	10^5	-20	0.40 (0.45)
20% MeOH	3.78	3.38	10^6	-23	0.54 (0.63)
30% MeOH	3.79	4.23	10^6	-21	0.61 (0.77)

Comparatively, MeOH-doped solutions of PDPP3F-BO ($\leq$ 40%, by volume) cause a λ_{max} redshift of 17 nm (**Fig. 8a**). Resultant films exhibit larger visible domains and a steady increase in film roughness (R_{RMS}) as MeOH-doping increases from 0 to 30%, by volume (**Fig. 3-20**). From GIXD data, increasing MeOH concentration promotes tighter

π-π spacing (**Table 3-4**, **Fig. 3-19**) and enhances in-plane π-stacking, where films spun from 10, 20, and 30% MeOH solutions provide $R_{\text{in/out}}$ values of 1.93, 3.38, and 4.23, respectively. Furthermore, PDPP3F-BO films demonstrate a steady rise in field-effect mobility as they are spun from solutions with higher MeOH concentrations, up to a maximum hole mobility of 0.77 cm²/ V·s (**Fig. 8b**). Significantly, these results verify that inducing solution phase aggregation can improve thin film morphology, solid-state order, and importantly OFET performance.

3.3 Conclusion

In this study, we examined the relationship between polymer side-chain structure on solubility, morphology, and field-effect mobility using furan-containing diketopyrrolopyrrole polymers. We synthesized and characterized two polymer backbones, PDDP2FT and PDPP3F, that were substituted with either linear *n*-hexadecyl (C16) or branched 2-butyloctyl (BO) side chains. In OFETs, the C16-polymers out-perform their branched counterparts, where PDPP3F-C16 provides a maximum hole mobility of 2.25 cm²/V·s. AFM and GIXD analysis of PDPP3F-C16 films reveal that they exhibit the greatest degrees of crystallinity, tightest π-π spacing, and greatest preference for in-plane π-stacking alignment. Analyses of PDPP3F-C16 solutions by NMR, variable temperature UV-vis-NIR spectroscopy, and DLS reveal that this polymer also has the strongest propensity for aggregation in solution prior to film deposition.

We propose that solution phase aggregation leads to the formation of films with solid-state properties that are more favorable for OFET operation. In order to substantiate our postulate, a non-solvent additive (MeOH) was added to the PDPP3F solutions to induce polymer aggregation. While little change in nanostructural order or device performance is observed with PDPP3F-C16, PDPP3F-BO demonstrates improved film crystallinity, tighter π-π spacing, greater in-plane π-stacking orientation, and higher field-effect mobility. Overall, this work elucidates fundamental structure-property relationships between polymer solubility, solid-state order, and electronic device performance.

3.4 Experimental Details

3.4.1. General Methods

For the molecular weight determination of polymers, samples were dissolved in HPLC grade chloroform at a concentration of 1 mg/ml. The resulting solution was briefly heated and then allowed to return to room temperature prior to filtering through a 0.2 μm polyvinylidene fluoride (PVDF) filter. Size exclusion chromatography (SEC) was performed with HPLC grade chloroform at an elution rate of at 1.0 mL/min through three PLgel Mixed-C columns at room temperature. The particle size in the columns was 5 μm and the columns were maintained at room temperature. The SEC system consisted of a Waters 2695 Separation Module and a Waters 486 Tunable Absorption Detector. The apparent molecular weights and polydispersities (M_w/M_n) were determined with a

calibration based on linear polystyrene standards using Millennium software from Waters.

UV-vis-NIR spectral data were measured at room temperature with a Varian Cary 50 Conc spectrophotometer. Thin film measurements were collected by spin-coating a chloroform solution of the polymer on to an octyltrichlorosilane (OTS) functionalized quartz substrate. Films were subjected to the same conditions as those outlined for the optimized OFET devices prior to UV-vis analysis.

Cyclic voltammograms were collected using a Solartron 1285 potentiostat under the control of CorrWare II software. A standard three electrode cell based on a Pt wire working electrode, a silver wire pseudo-reference electrode (calibrated vs. Fc/Fc$^+$), and a Pt wire counter electrode was purged with nitrogen and maintained under a nitrogen atmosphere during all measurements. Acetonitrile was purchased anhydrous from Aldrich and tetrabutylammonium hexafluorophosphate (0.1 M) was used as the supporting electrolyte. Polymer films were drop cast onto a Pt wire working electrode from a 1% (w/w) chloroform solution and dried under nitrogen prior to measurement.

Polymer solubility (milligrams per milliliter) in chloroform were determined by making a saturated solution (> 40 mg/mL) of each material and allowing the solutions to stir overnight at 60 °C. The hot solutions were then filtered through a 0.2 μm PTFE syringe filter to remove undissolved polymer. A known volume of the filtered solution was transferred to a tarred glass vial, evaporated to dryness, and the weight was determined.

The topography of the active layers were imaged using a Veeco Multimode V atomic force microscope (AFM) operated in tapping mode under ambient conditions using aluminum coated silicon cantilevers (Veeco; TAP150Al, fo = 122-169 kHz, k = 5N/m). The average root mean square roughness (R_{RMS}) of the films was obtained from a minimum of five distinct AFM images gathered from three independently fabricated devices. R_{RMS} values were gathered over a 1 μm x 1μm image. AFM images were analyzed using the WSxM 5.0 software.[69]

Grazing-incidence x-ray scattering (GIXD) experiments were conducted at the Stanford Synchotron Radiation Lightsource (SSRL) on beamline 11-3. Samples were prepared following the same procedure for fabricating OFET devices using the optimized device conditions and were irradiated at a fixed incident angle of approximately 0.1°. The GIXD patterns were recorded with a 2-D image detector (MAR345 image plate detector) using an x-ray energy of 12.71 keV (λ = 0.975 Å). To maximize the intensity from the sample, the incident angle was carefully chosen such that the x-ray beam penetrated the sample completely but did not interact significantly with the silicon substrate. Typical exposure times were between 30 and 900 s.

Differential scanning calorimetry was performed on each of the polymers using 2-6 mg of material in a TA Instruments DSC Q200. Samples were scanned from 50 to 250°C at a rate of 5°C/min.

^{1}H NMR spectra of the polymer samples in chloroform-d were obtained using a Bruker AV-500 instrument with an inverse probe at 40 °C.

Dynamic light scattering (DLS) was performed using a Zetasizer Nano ZS (Malvern Instruments). Samples were measured from 0.5 mg/mL solutions in chloroform

using a 1-cm-path-length quartz cuvette and averaged over a minimum of five separately prepared samples.

3.4.2. Synthetic Procedures

Monomers were synthesized following previously reported procedures, and the synthetic methods were adapted from those described in our earlier work on furan-containing low band-gap conjugated polymers for solar cell applications.[25,43] All commercially available reagents obtained from suppliers were used without further purification. Unless otherwise noted, all reactions were carried out under nitrogen with standard Schlenk techniques, and glassware used in dry reactions was flame dried under high-vacuum prior to use. Dichloromethane (DCM), tetrahydrofuran (THF), dimethylformamide (DMF) and toluene were purified and dried by passing through two columns of neutral alumina, under nitrogen, prior to use. Flash chromatography was performed using Silicycle SiliaFlash® P60 (particle size 40-63 μm, 230-400 mesh) silica gel.
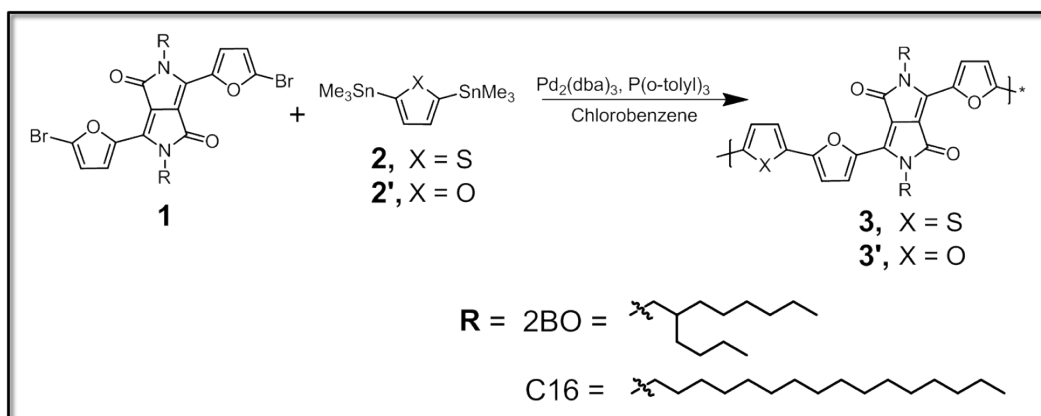
Figure 3-9: Representative procedure for the synthesis of **PDPP2FT-R (3)** and **PDPP3F-R (3')**.

PDPP2FT-R (3), or PDPP3F-R (3'). Monomer **1** (0.210 mmol), 2,5-bis(trimethyl-stannyl)-thiophene (**2**) or 2,5-bis(trimethylstannyl)-furan (**2'**) (0.210 mmol), $Pd_2(dba)_3$ (2 mol %) and P(o-tol)$_3$ (8 mol %) were charged within a 50 mL Schlenk tube, cycled with N_2 and subsequently dissolved in 7-8 mL of degassed chlorobenzene. The mixture was stirred for 24 h at 110 °C. The reaction mixture was allowed to cool to 55 °C, 15 mL of $CHCl_3$ was added, and the strongly complexing ligand *N,N*-diethylphenylazothio-formamide (CAS# 39484-81-6) was subsequently added (as a palladium scavenger). The resulting mixture was stirred for 1 h at 55°C, and precipitated into methanol (200 mL). The precipitate was filtered through a Soxhlet thimble and purified via Soxhlet extraction for 12 h with methanol and 1 h with hexanes, followed by collection in chloroform. The chloroform solution was concentrated by evaporation and precipitated into methanol (200 mL). The precipitated polymer (**3** or **3'**) was filtered off as a dark solid.

3.4.3. DFT Calculated Structures of Oligomers

Optimized molecular geometries of the representative trimer structures were obtained by performing DFT calculations (B3LYP/6-31G(d)) with Gaussian09.
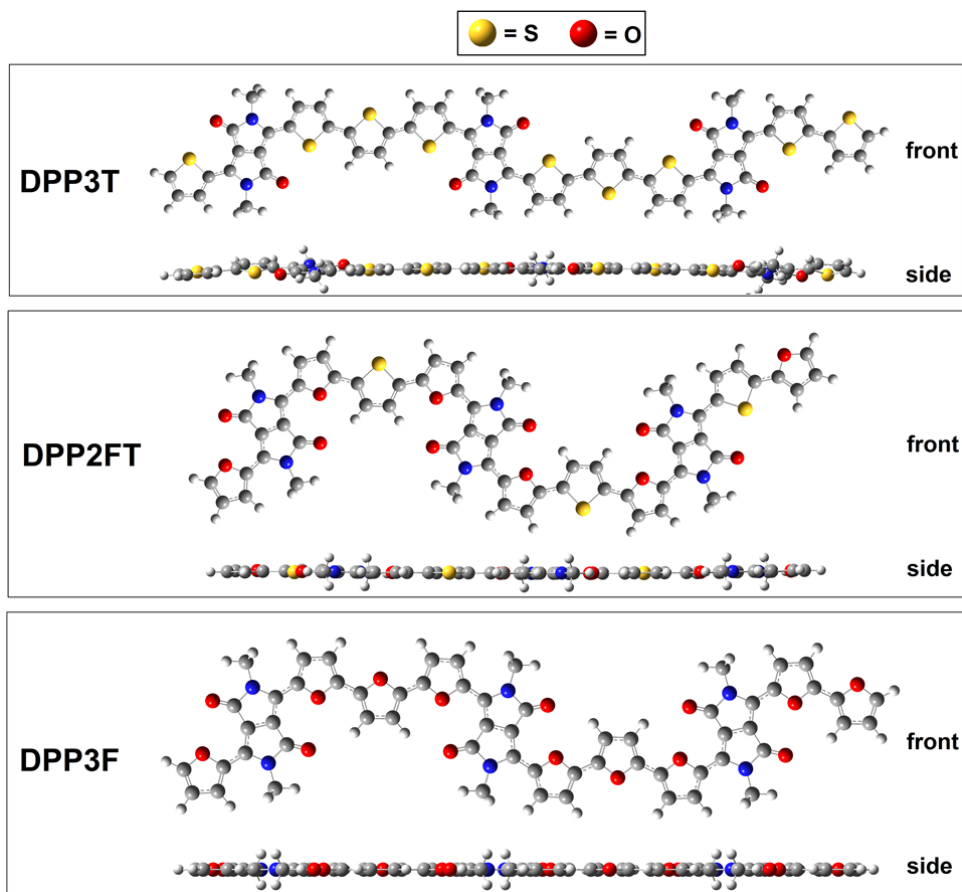
Figure 3-10. Optimized molecular geometries of terthiophene diketopyrrolopyrrole (DPP3T), bifuran-thiophene diketopyrrolopyrrole (DPP2FT), and terfuran diketopyrrolopyrrole (DPP3F).
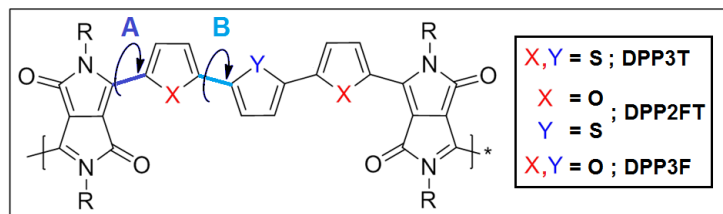
	Torsion A (θ)	Torsion B (θ)	Bond Length A (Å)	Bond Length B (Å)
DPP3T	3.65°	2.11°	1.436	1.440
DPP2FT	0.10°	0.10°	1.426	1.433
DPP3F	0.00°	0.00°	1.426	1.426

Figure 3-11. Inter-ring torsions and bond lengths of optimized polymer structures. Due to the symmetry of the molecule, bond angles and bond lengths were averaged from structurally equivalent bonds and the averages are shown.

3.4.4. Supplement Polymer Properties Data
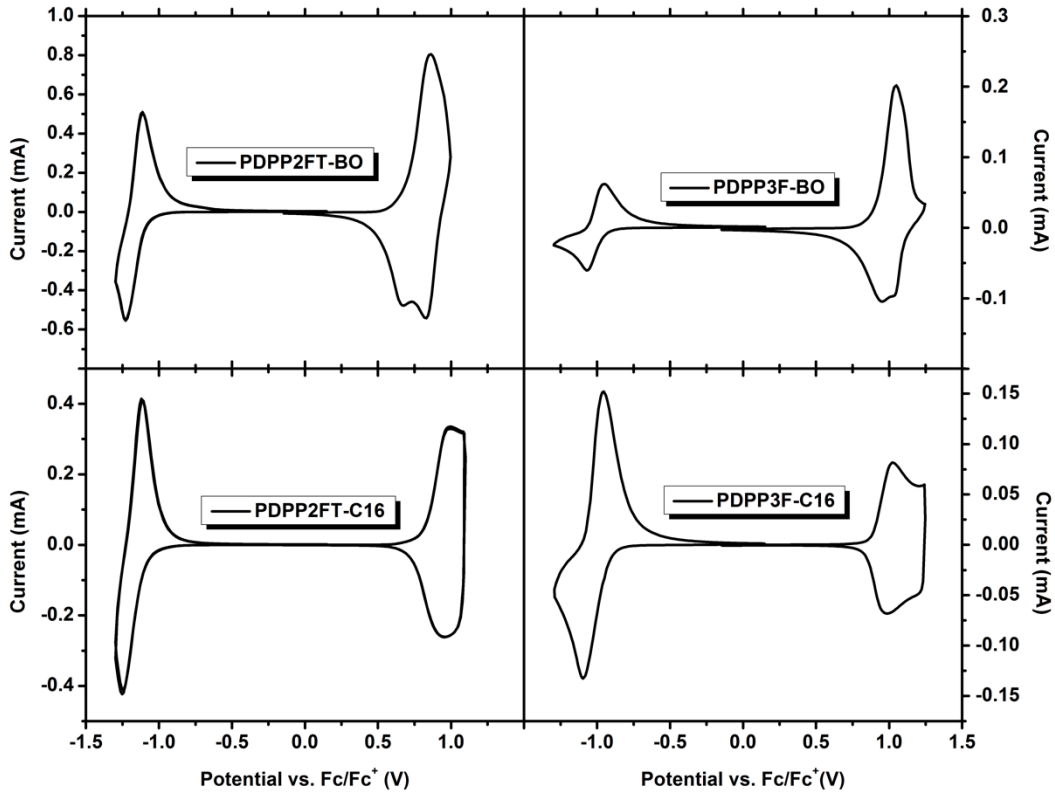
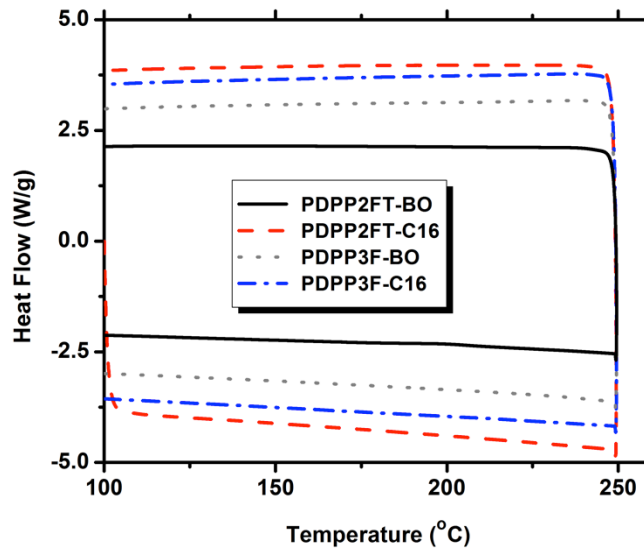**Figure 3-12.** Cyclic voltammograms of PDPP2FT and PDPP3F films.

Figure 3-13. Differential scanning calorimetry of PDPP2FT and PDPP3F.

## 3.4.5. OFET Fabrication and Characterization Procedures

Bottom gate/top contact field effect transistors were fabricated on heavily doped silicon (Addison Engineering) substrates that contained a thermally grown silicon dioxide gate dielectric (300 nm). For optimal performance and reproducibility, it was

imperative that the surface of the substrates was as clean as possible. Consequently, the Si/SiO_x substrates were subjected to several cleaning steps prior to spin-coating the polymer active layer. To remove surface bound particulates, the substrates were sonicated sequentially in detergent (Hellmanex III in distilled water), distilled water, acetone, and isopropyl alcohol (20 min each). The substrates were then submerged in a solution of DI water, ammonium hydroxide (14.8 M), and hydrogen peroxide (30% in water) at a 2:1:1 ratio for 15 min to remove organic impurities from the surface. Afterwards, the wafers were rinsed thoroughly with water and isopropyl alcohol, dried with a stream of nitrogen, and further treated with UV/ozone cleaning for 20 minutes. The surfaces were functionalized with octyltrichlorosilane (OTS) by submerging the substrates in a 40 mM solution in dry hexane for ~24 h, and then soaked in a dilute pyridine solution (0.1 mM) for 1 h. Finally, functionalized substrates were sonicated in toluene for 30 s to remove physisorbed molecules, rinsed with isopropyl alcohol, and dried with a light N_2 stream.

All solution preparation, film formation, and electrical characterization were performed under N_2 inside a glovebox. Polymer solutions were prepared in chloroform and allowed to stir at 60 °C overnight. The hot solutions filtered through a 0.45 μm PTFE filter, then pseudo-spuncoat on to a freshly prepared substrate at 2000 RPM for 1 s. Casting the film by this method mimics drop-casting as the film is allowed to dry slowly over a few seconds after the spin sequence is completed. However, contrary to drop-casting, pseudo-spincoating forms a uniform and comparatively thin (80 - 100 nm) polymer film (determined via profilometry, Veeco Dektat 150). The films were allowed to dry under ambient glovebox conditions for a minimum of 30 min prior to deposition of the top electrodes. Gold electrodes (35 nm at 6 Å/s) were thermally deposited on top the films through a shadowmask with predefined features. Field effect characteristics were obtained using an HP 4155C semiconductor parameter analyzer. This work focuses principally on hole field effect mobility given that bottom gate OFET architectures using SiO_2 are typically better for hole transport given that the exposed hydroxyl groups on the gate dielectric are known to readily trap electrons.[70] Mobility was calculated via the saturation regime model using the fitted slope of the linear portion of the transfer curve and the standard saturation regime equation.[71] Threshold voltage (V_{th}) was obtained from the zero crossing value of the linear fit. The on/off ratio ($I_{on/off}$) was determined from the ratio of the source-drain current (I_{DS}) at maximum source-drain bias (-100 V_{DS}) and while in the off state.

3.4.6. Extraction of GIXD Packing Parameters

To extract crystalline information from x-ray diffraction patterns, the 2D GIXD profiles were averaged over a quasi-polar angle (χ) for $\chi = 15 \pm 2°$ and $\chi = 75 \pm 2°$. Diffraction peaks in the cross-sectional scattering profile were then fitted to Lorenzian functions using peak fitting software (Fityk) and the peak center and full width at half max values were extracted.
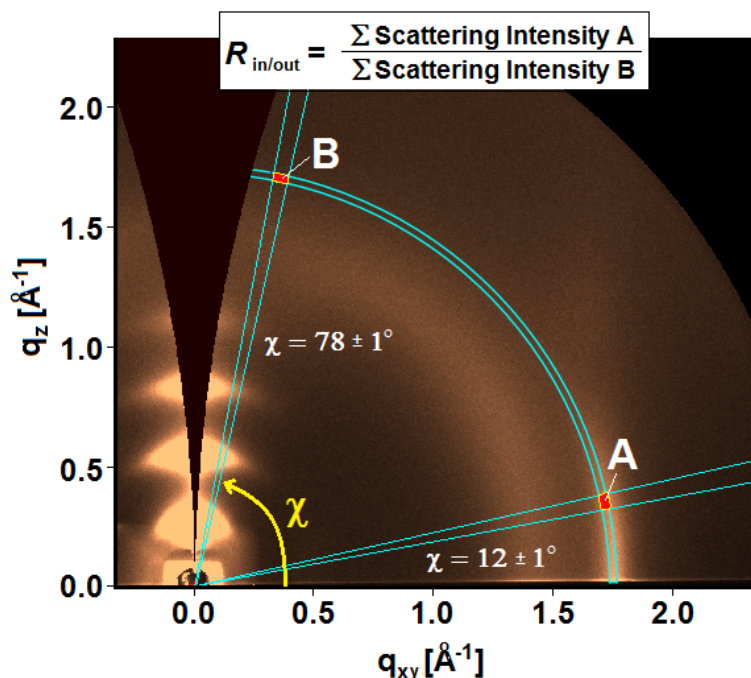
Figure 3-14. Determining the extent of in-plane polymer packing. The relative ratio of in-plane to out-of-plane crystallites ($R_{in/out}$) is determined by integrating the scattering intensity at A (in-plane scattering) and dividing by the integrated out-of-plane scattering intensity (at B). Note that the scattering intensities at each χ is corrected by multiplying by cos(χ).

To determine the degree of in-plane π-stacking for each polymer film, the ratio of in-plane to out-of-plane scattering intensity ($R_{in/out}$) was calculated. To do this, a scattering intensity versus χ plot was attained by integrating the collective intensity of the π-stacking peak (q = peak max ± 0.2 Å^{-1}) over possible χ (χ = 0 to 80°). After the scattering intensities at each χ were multiplied by the geometrical correction factor cos(χ),[71] the intensities were averaged over two quasi-polar angles, one for each polymer packing orientation. For in-plane polymer packing, the scattering intensity was integrated at the intersection of χ = 12 ± 1° and the π-stacking peak (area A, **Fig. 3-14**). The out-of-plane contribution to the scattering profile was integrated at the peak max and χ = 78 ± 1° (area B, **Fig. 3-14**). The ratio of the scattering intensity, $R_{in/out}$ = A/B, defines the degree of in-plane π-stacking for each polymer film with larger ratios for films with more in-plane π-stacking.

3.4.7. OFET Fabrication on Various Self-Assembled Monolayers

To investigate the effect of polymer-substrate interactions on solid-state order and molecular packing, devices were fabricated on substrates functionalized with a variety of self-assembled monolayers as well as on bare, unfunctionalized SiO$_2$. Substrates were cleaned following the same cleaning procedure outlined in the OFET fabrication section. The surfaces were functionalized with either octadecyltrichlorosilane (ODTS), hexa methyldisilazane (HMDS), trichlorosilane (TS), phenyltrichlorosilane (PTS), phenethyl-trichlorosilane (PETS), vinyltrichlorosilane (VTS), trifluoropropyltrichlorosilane (TFPTS), or perfluorooctyltrichlorosilane (PFOTS) by submerging the substrates in a 40

mM solution in hexane for 8 to 24 hours. Functionalized substrates were sonicated in toluene for 30 s to remove physisorbed molecules, rinsed with isopropyl alcohol, and dried with a light N_2 stream. Surfaces were functionalized with hexamethyldisilazane (HMDS) by subjecting freshly cleaned wafers to HMDS vapor at 80°C for 5 hours.
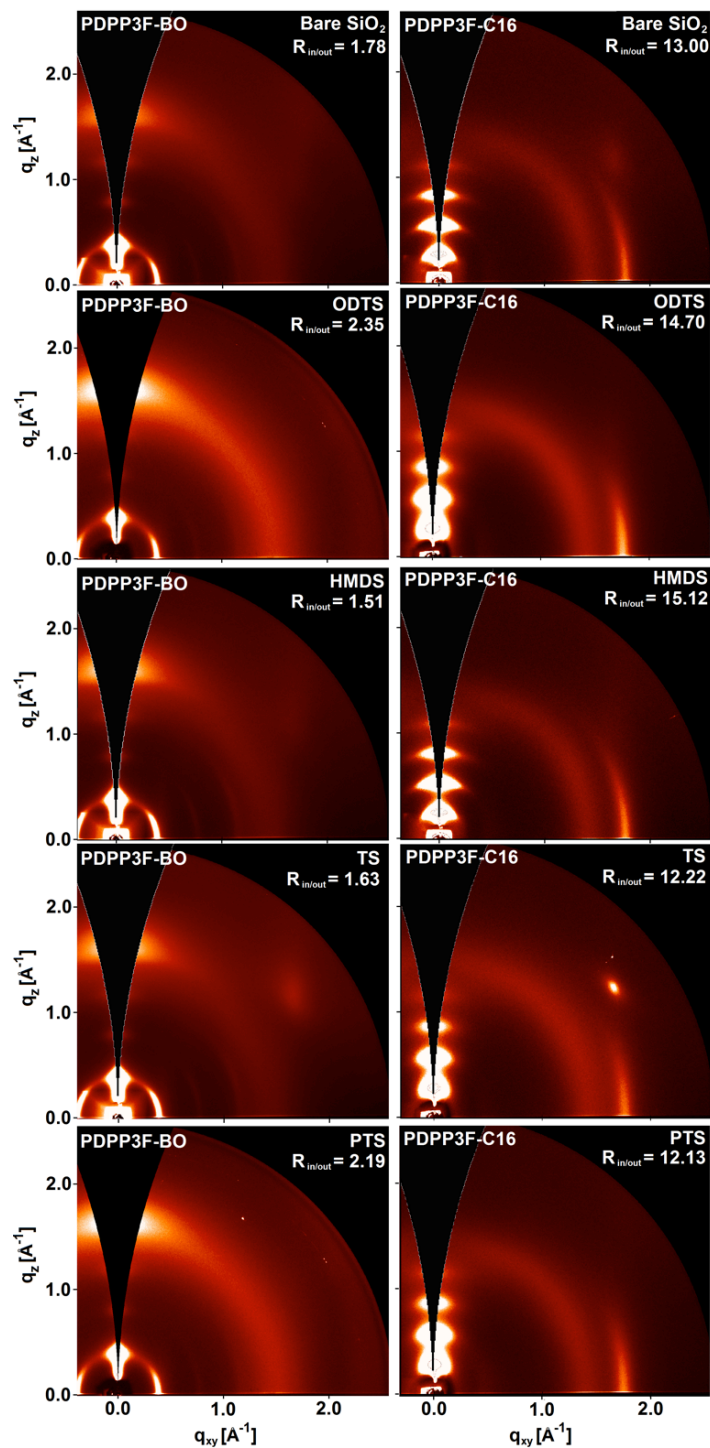
Figure 3-15. GIXD of PDPP3F-BO and PDPP3F-C16 films on bare SiO_2, ODTS, HMDS, TS, and PTS functionalized surfaces.
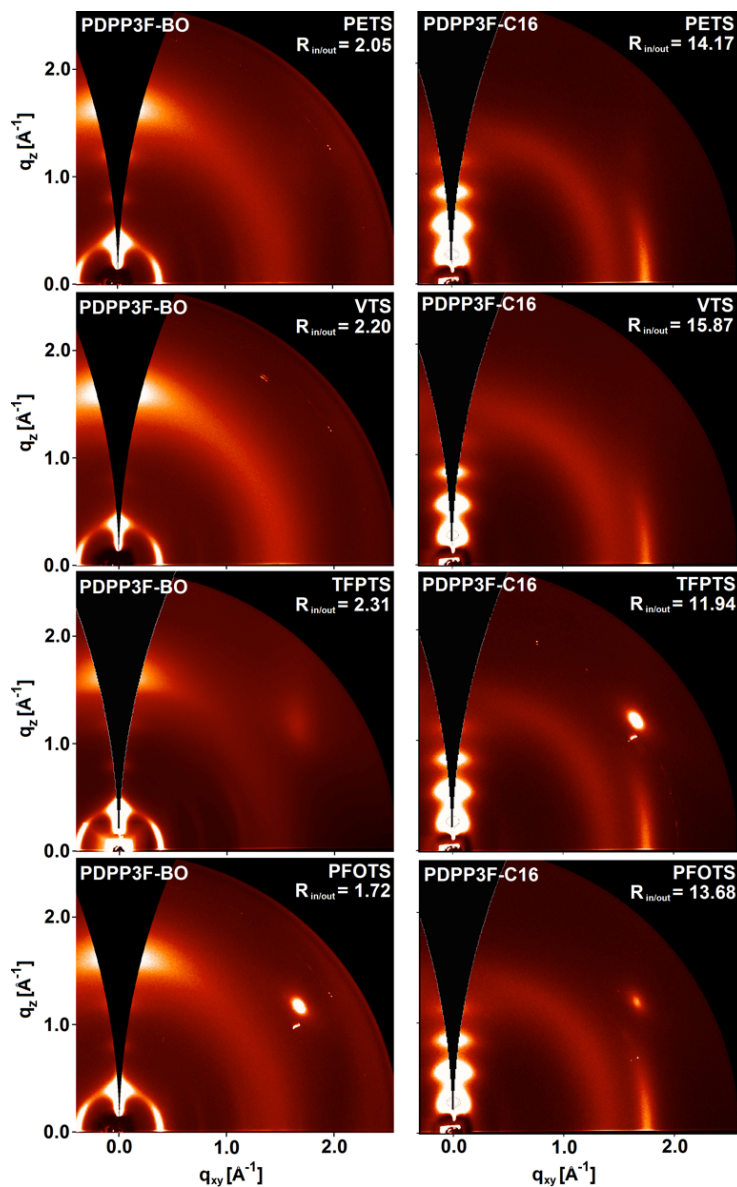
Figure 3-16. GIXD of PDPP3F-BO and PDPP3F-C16 films on PETS, VTS, TFPTS, and PFOTS functionalized substrates.

3.4.8. Variable Temperature UV-vis-NIR Spectra

Variable temperature UV-vis-NIR absorption was performed with dilute polymer solutions (~ 0.02 mg/mL) in 1-cm-path-length quartz cuvettes using a Varian Cary 50 Bio spectrometer equipped with a Unisoku – CoolSpek UV (USP-203-B) temperature controller. The solutions were held at each respective temperature for 5 minutes prior to a spectral scan.
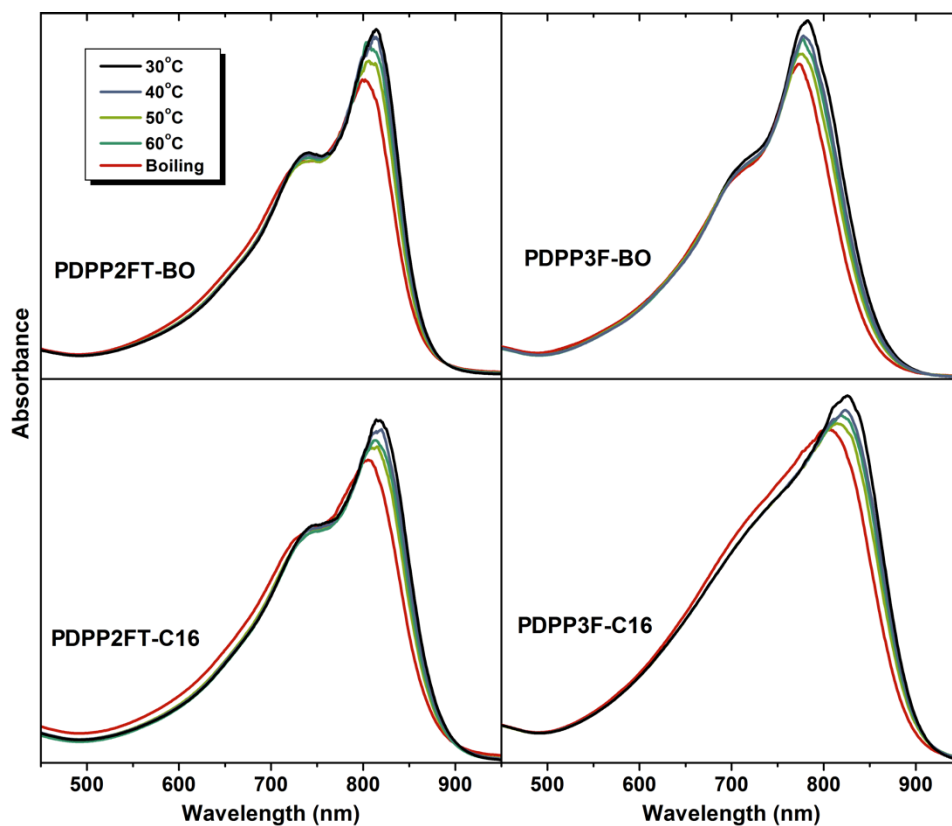
Figure 3-17. Variable temperature UV-vis-NIR spectra of PDPP2FT and PDPP3F in chloroform.

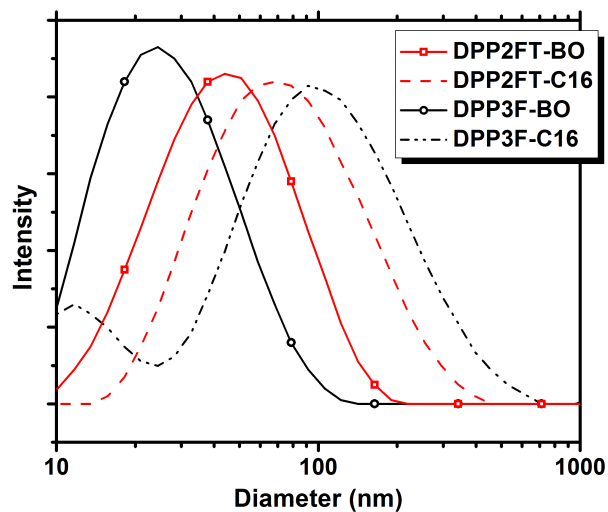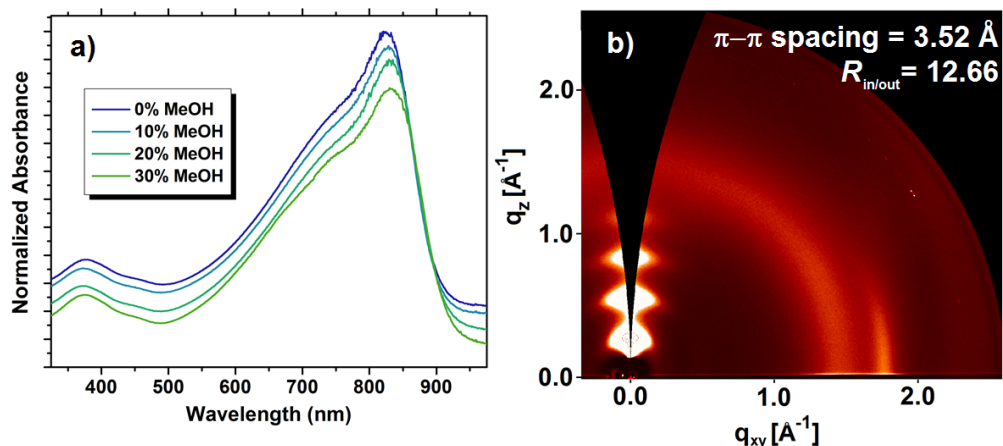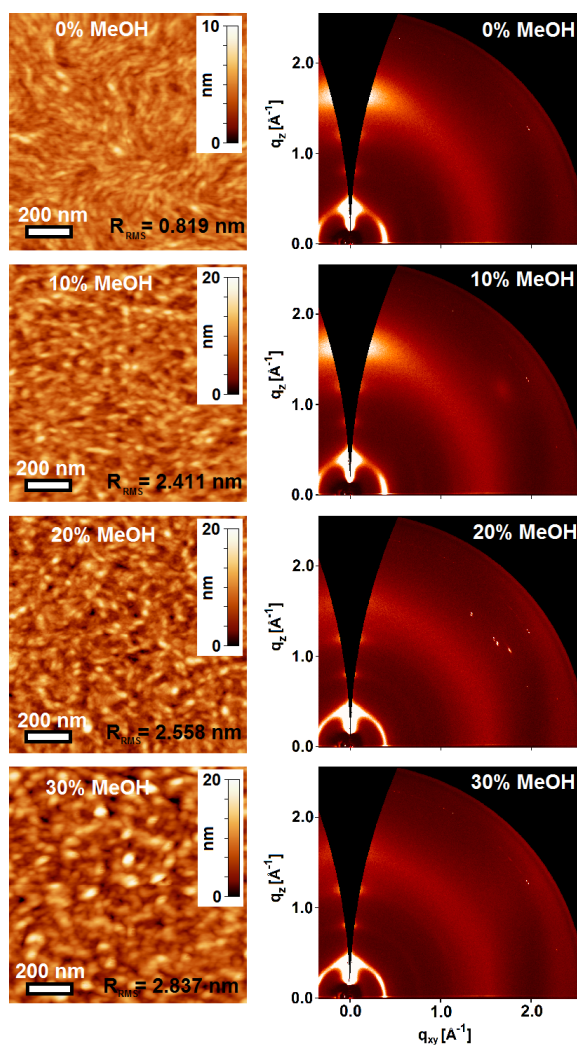## 3.4.9. Dynamic Light Scattering of Aggregates

Figure 3-18. Representative dynamic light scattering data for PDPP2FT and PDPP3F

3.4.10. Effects of Methanol Additive on PDPP3F Films

Figure 3-19. The effect of non-solvent additive (MeOH) on UV-vis-NIR absorption (a) and GIXD (b) of PDPP3F-C$_{16}$.

Figure 3-20. AFM images (left column) and GIXD (right column) of PDPP3F-BO films spun from solutions with 0%, 10%, 20%, and 30% (v/v) MeOH additive.

3.5 References

(1) Hamilton, R.; Heeney, M.; Anthopoulos, T.; McCulloch, I. *Organic Electronics: Materials, Processing, Devices and Applications* **2010**, 393.

(2) Cicoira, F.; Santato, C. *Advanced Functional Materials* **2007**, *17*, 3421-3434.

(3) Gelinck, G. H.; Huitema, H. E. A.; van Veenendaal, E.; Cantatore, E.; Schrijnemakers, L.; van der Putten, J. B. P. H.; Geuns, T. C. T.; Beenhakkers, M.; Giesbers, J. B.; Huisman, B. H. *Nature materials* **2004**, *3*, 106-110.

(4) Berggren, M.; Nilsson, D.; Robinson, N. D. *Nature materials* **2007**, *6*, 3-5.

(5) Subramanian, V.; Chang, P. C.; Lee, J. B.; Molesa, S. E.; Volkman, S. K. *Components and Packaging Technologies, IEEE Transactions on* **2005**, *28*, 742-747.

(6) Crone, B.; Dodabalapur, A.; Gelperin, A.; Torsi, L.; Katz, H. E.; Lovinger, A. J.; Bao, Z. *Applied Physics Letters* **2001**, *78*, 2229-2231.

(7) Drury, C.; Mutsaers, C.; Hart, C.; Matters, M.; De Leeuw, D. *Applied Physics Letters* **1998**, *73*, 108-110.

(8) Boudreault, P. L. T.; Najari, A.; Leclerc, M. *Chemistry of Materials* **2011**, *23*, 456.

(9) Allard, S.; Forster, M.; Souharce, B.; Thiem, H.; Scherf, U. *Angewandte Chemie International Edition* **2008**, *47*, 4070-4098.

(10) Mei, J.; Kim, D. H.; Ayzner, A. L.; Toney, M. F.; Bao, Z. *Journal of the American Chemical Society* **2011**, *133*, 20130-20133.

(11) Tsao, H. N.; Cho, D. M.; Park, I.; Hansen, M. R.; Mavrinskiy, A.; Yoon, D. Y.; Graf, R.; Pisula, W.; Spiess, H. W.; Müllen, K. *Journal of the American Chemical Society* **2011**, *133*, 2605-2612.

(12) Bijleveld, J. C.; Zoombelt, A. P.; Mathijssen, S. G. J.; Wienk, M. M.; Turbiez, M.; de Leeuw, D. M.; Janssen, R. A. J. *Journal of the American Chemical Society* **2009**, *131*, 16616-16617.

(13) Lee, J.; Han, A. R.; Kim, J.; Kim, Y.; Oh, J. H.; Yang, C. *Journal of the American Chemical Society* **2012**.

(14) Chua, L. L.; Zaumseil, J.; Chang, J. F.; Ou, E. C. W.; Ho, P. K. H.; Sirringhaus, H.; Friend, R. H. *Nature* **2005**, *434*, 194-199.

(15) Wang, S.; Kappl, M.; Liebewirth, I.; Müller, M.; Kirchhoff, K.; Pisula, W.; Müllen, K. *Advanced Materials* **2012**.

(16) Kline, R.; McGehee, M. *Journal of Macromolecular Science Part C: Polymer Reviews* **2006**, *46*, 27-45.

(17) Sirringhaus, H.; Bird, M.; Zhao, N. *Advanced Materials* **2010**, *22*, 3893-3898.

(18) Tsao, H. N.; Cho, D.; Andreasen, J. W.; Rouhanipour, A.; Breiby, D. W.; Pisula, W.; Müllen, K. *Advanced Materials* **2008**, *21*, 209-212.

(19) Rivnay, J.; Noriega, R.; Northrup, J. E.; Kline, R. J.; Toney, M. F.; Salleo, A. *Physical Review B* **2011**, *83*, 121306.

(20) Kang, I.; An, T. K.; Hong, J.-a.; Yun, H.-J.; Kim, R.; Chung, D. S.; Park, C. E.; Kim, Y.-H.; Kwon, S.-K. *Advanced Materials* **2012**, n/a-n/a.

(21) Chen, H.; Guo, Y.; Yu, G.; Zhao, Y.; Zhang, J.; Gao, D.; Liu, H.; Liu, Y. *Advanced Materials* **2012**.

(22) Lei, T.; Dou, J. H.; Ma, Z. J.; Yao, C.; Liu, C. J.; Wang, J. Y.; Pei, J. *Journal of the American Chemical Society* **2012**.

(23) Zhang, X.; Richter, L. J.; DeLongchamp, D. M.; Kline, R. J.; Hammond, M. R.; McCulloch, I.; Heeney, M.; Ashraf, R. S.; Smith, J. N.; Anthopoulos, T. D. *Journal of the American Chemical Society* **2011**, *133*, 15073-15084.

(24) Beaujuge, P. M.; Fréchet, J. M. J. *Journal of the American Chemical Society* **2011**, *133*, 20009-20029.

(25) Yiu, A. T.; Beaujuge, P. M.; Lee, O. P.; Woo, C. H.; Toney, M. F.; Fréchet, J. M. J. *Journal of the American Chemical Society* **2011**, *134*, 2180-2185.

(26) Sauvé, G.; Javier, A. E.; Zhang, R.; Liu, J.; Sydlik, S. A.; Kowalewski, T.; McCullough, R. D. *J. Mater. Chem.* **2010**, *20*, 3195-3201.

(27) Cho, S.; Seo, J. H.; Kim, S. H.; Song, S.; Jin, Y.; Lee, K.; Suh, H.; Heeger, A. J. *Applied Physics Letters* **2008**, *93*, 263301.

(28) Osaka, I.; McCullough, R. D. *Accounts of Chemical Research* **2008**, *41*, 1202-1214.

(29) Coropceanu, V.; Cornil, J.; da Silva Filho, D. A.; Olivier, Y.; Silbey, R.; Brédas, J.-L. *Chemical Reviews* **2007**, *107*, 926-952.

(30) Street, R. A.; Northrup, J. E.; Salleo, A. *Physical Review B* **2005**, *71*, 165202.

(31) Salleo, A.; Kline, R. J.; DeLongchamp, D. M.; Chabinyc, M. L. *Advanced Materials* **2010**, *22*, 3812-3838.

(32) Nielsen, C. B.; Turbiez, M.; McCulloch, I. *Advanced Materials* **2012**, n/a-n/a.

(33) Chen, L.; Deng, D.; Nan, Y.; Shi, M.; Chan, P. K. L.; Chen, H. *The Journal of Physical Chemistry C* **2011**, *115*, 11282-11292.

(34) Li, W.; Lee, T.; Oh, S. J.; Kagan, C. R. *ACS Applied Materials & Interfaces* **2011**, *3*, 3874-3883.

(35) Wu, P. T.; Kim, F. S.; Jenekhe, S. A. *Chemistry of Materials* **2011**, *23*, 4618-4624.

(36) Ha, J. S.; Kim, K. H.; Choi, D. H. *Journal of the American Chemical Society* **2011**, *133*, 10364-10367.

(37) Li, Y.; Sonar, P.; Singh, S. P.; Soh, M. S.; van Meurs, M.; Tan, J. *Journal of the American Chemical Society* **2011**, *133*, 2198-2204.

(38) Kronemeijer, A. J.; Gili, E.; Shahid, M.; Rivnay, J.; Salleo, A.; Heeney, M.; Sirringhaus, H. *Advanced Materials* **2012**, *24*, 1558-1565.

(39) Lin, H. W.; Lee, W. Y.; Chen, W. C. *Journal of Materials Chemistry* **2012**, *22*, 2120-2128.

(40) Bronstein, H.; Chen, Z.; Ashraf, R. S.; Zhang, W.; Du, J.; Durrant, J. R.; Shakya Tuladhar, P.; Song, K.; Watkins, S. E.; Geerts, Y. *Journal of the American Chemical Society* **2011**, *133*, 3272.

(41) Shahid, M.; McCarthy-Ward, T.; Labram, J.; Rossbauer, S.; Domingo, E. B.; Watkins, S. E.; Stingelin, N.; Anthopoulos, T. D.; Heeney, M. *Chemical Science* **2012**, *3*, 181-185.

(42) Wienk, M. M.; Turbiez, M.; Gilot, J.; Janssen, R. A. J. *Advanced Materials* **2008**, *20*, 2556-2560.

(43) Woo, C. H.; Beaujuge, P. M.; Holcombe, T. W.; Lee, O. P.; Fréchet, J. M. J. *Journal of the American Chemical Society* **2010**, *132*, 15547-15549.

(44) Li, Y.; Sonar, P.; Singh, S. P.; Zeng, W.; Soh, M. S. *Journal of Materials Chemistry* **2011**, *21*, 10829-10835.

(45) Sonar, P. M. *Chemical Communications* **2012**.

(46)   Sonar, P.; Singh, S. P.; Williams, E. L.; Li, Y.; Soh, M. S.; Dodabalapur, A. *Journal of Materials Chemistry* **2012**, *22*, 4425-4435.

(47)   Gidron, O.; Diskin-Posner, Y.; Bendikov, M. *Journal of the American Chemical Society* **2010**, *132*, 2148-2150.

(48)   Bunz, U. H. F. *Angewandte Chemie International Edition* **2010**, *49*, 5037-5040.

(49)   Rieger, R.; Beckmann, D.; Mavrinskiy, A.; Pisula, W.; Kastler, M.; Müllen, K. 2010.

(50)   Li, Y.; Vamvounis, G.; Holdcroft, S. *Macromolecules* **2002**, *35*, 6900-6906.

(51)   Koeckelberghs, G.; De Cremer, L.; Persoons, A.; Verbiest, T. *Macromolecules* **2007**, *40*, 4173-4181.

(52)   Xu, B.; Holdcroft, S. *Macromolecules* **1993**, *26*, 4457-4460.

(53)   Bao, Z.; Locklin, J. *Organic field-effect transistors*; CRC, 2007; Vol. 128.

(54)   Coropceanu, V.; Cornil, J. r. m.; da Silva Filho, D. A.; Olivier, Y.; Silbey, R.; BrÃ©das, J.-L. *Chemical Reviews* **2007**, *107*, 926-952.

(55)   Rogers, J. T.; Schmidt, K.; Toney, M. F.; Kramer, E. J.; Bazan, G. C. *Advanced Materials* **2011**, *23*, 2284-2288.

(56)   Roe, R. J. *Methods of X-Ray and Neutron Scattering in Polymer Science (Topics in Polymer Science)*; Oxford University Press, New York, Oxford, 2000.

(57)   Sirringhaus, H.; Brown, P.; Friend, R.; Nielsen, M.; Bechgaard, K.; Langeveld-Voss, B.; Spiering, A.; Janssen, R. A. J.; Meijer, E.; Herwig, P. *Nature* **1999**, *401*, 685-688.

(58)   Surin, M.; Leclère, P.; De Feyter, S.; Abdel-Mottaleb, M. M. S.; De Schryver, F. C.; Henze, O.; Feast, W. J.; Lazzaroni, R. *The Journal of Physical Chemistry B* **2006**, *110*, 7898-7908.

(59)   Coffey, D. C.; Ginger, D. S. *Journal of the American Chemical Society* **2005**, *127*, 4564-4565.

(60)   Qian, D.; Ye, L.; Zhang, M.; Liang, Y.; Li, L.; Huang, Y.; Guo, X.; Zhang, S.; Tan, Z. a.; Hou, J. *Macromolecules* **2012**.

(61)   Nguyen, T.-Q.; Doan, V.; Schwartz, B. J. *The Journal of Chemical Physics* **1999**, *110*, 4068-4078.

(62)   Amrutha, S.; Jayakannan, M. *The Journal of Physical Chemistry B* **2008**, *112*, 1119-1129.

(63)   Moule, A. J.; Allard, S.; Kronenberg, N. M.; Tsami, A.; Scherf, U.; Meerholz, K. *The Journal of Physical Chemistry C* **2008**, *112*, 12583-12589.

(64)   Moulé, A. J.; Meerholz, K. *Advanced Materials* **2008**, *20*, 240-245.

(65)   Millstone, J. E.; Kavulak, D. F. J.; Woo, C. H.; Holcombe, T. W.; Westling, E. J.; Briseno, A. L.; Toney, M. F.; Fréchet, J. M. J. *Langmuir* **2010**, *26*, 13056-13061.

(66)   Steyrleuthner, R.; Schubert, M.; Howard, I.; Klaumünzer, B.; Schilling, K.; Chen, Z.; Saalfrank, P.; Laquai, F.; Facchetti, A.; Neher, D. *Journal of the American Chemical Society* **2012**, *134*, 18303-18317.

(67)   Collison, C. J.; Rothberg, L. J.; Treemaneekarn, V.; Li, Y. *Macromolecules* **2001**, *34*, 2346-2352.

(68)   Brown, S. P.; Spiess, H. W. *Chemical Reviews* **2001**, *101*, 4125-4156.

(69)   Horcas, I.; Fernandez, R.; Gomez-Rodriguez, J. M.; Colchero, J.; Gomez-Herrero, J.; Baro, A. M. *Review of Scientific Instruments* **2007**, *78*, 013705-013708.

(70)   Bao, Z.; Locklin, J. *Organic field-effect transistors*; CRC, 2007; Vol. 128.

(71)   Rivnay, J.; Mannsfeld, S. C. B.; Miller, C. E.; Salleo, A.; Toney, M. F. *Chemical Reviews* **2012**, *112*, 5488-5519.

Chapter 4

Efficient Small Molecule Bulk Heterojunction Solar Cells with High Fill Factors via Pyrene-Directed Molecular Self-Assembly[2]

Abstract

In organic photovoltaics, the relatively low performance of small molecules compared to polymers may be attributed to limited molecular interconnectivity through the active layer, resulting in low device fill factors (FFs). We postulated that the introduction of strongly π-stacking end-groups in small molecules would facilitate end-to-end intermolecular interaction. A series of DPP-based *p*-type small molecules was synthesized with electron-rich end-groups of varying degrees of planarity and symmetry. As we predicted, the use of strongly π-stacking end-groups—in particular, symmetrically (C2) substituted pyrene—resulted in tight, aligned crystal packing and favorable film morphology dictated by π-π interactions, as supported by single crystal X-ray analysis and GIXS. In OPV devices, DPP-C2-pyrene achieved a maximum PCE above 4% with a FF approaching 0.6, which is one of the highest FFs reported to date in high-performing small molecule BHJ OPVs.

4.1. Introduction

Organic photovoltaics (OPVs) are a promising technology for cost-effective and scalable production of renewable energy.[1-3] Current research in OPV materials focuses primarily on the design and synthesis of semiconducting polymers capable of both light absorption and charge transport. In OPV cells utilizing a bulk heterojunction (BHJ) architecture, conjugated polymers have demonstrated promising device efficiency; however, they can suffer from drawbacks such as batch-to-batch variation and chain-end contamination, which can reduce overall performance and device consistency.[4,5]

In order to develop OPV materials that exhibit not only favorable electronic properties but also batch-to-batch consistency, electroactive small molecules have recently received attention as alternatives to polymers.[4,6-9] While small molecules can be synthesized and solution-processed into devices just like polymers, they do not suffer from the inherent polydispersity of polymeric materials. They can be synthesized and purified as single molecular entities, thus eliminating the sort of device variability that can arise from material inhomogeneity. Despite these potential advantages, current data shows that the photovoltaic efficiencies of small molecules lag behind those of the highest-performing polymers.[5,10]

The relatively low performance of small molecules may be attributed to their limited interconnectivity through the active layer, resulting in low device fill factors. Earlier studies[11-14] have shown that polymers with higher molecular weight (M_n) perform better in BHJ solar cells than lower M_n polymers. In low M_n polymers, charge transport is limited by the short chain length.[11] By extension, as small molecules represent the lower limit of M_n, their device performance can suffer from inadequate interconnectivity and inefficient charge extraction. Herein, we demonstrate that the interconnectivity of small molecule semiconductors can be greatly improved by directed molecular self-assembly. Small molecules designed with this principle are shown to form highly ordered and interconnected domains and exhibit large fill factors and efficiencies in OPV devices.

We postulated that the introduction of π-stacking moieties onto the ends of small molecules would facilitate favorable end-to-end π-π interactions, leading to enhanced charge transport between adjacent molecules. To investigate this approach, a series of small molecules was synthesized, each with different electron-rich end-groups (**Fig. 4-1**). End-groups were selected for their varying degrees of planarity, which can affect their tendency to π-stack. Triphenylamine (TPA) has a non-planar structure with its phenyl groups twisting into a propeller motif.[15] Benzo[1,2-*b*;4,5-*b'*]dithiophene (BDT) contains a planar fused ring but has non-coplanar alkoxy substituents. Pyrene is a completely planar moiety and has a strong propensity to π-stack. In addition, the regio-connectivity between pyrene and the chromophoric core was varied in order to study the effect of end-group symmetry. As a platform for investigating the effects of these end-groups, diketopyrrolopyrrole (DPP) was chosen to be the electron-deficient core, since this moiety allows for control of small molecule solution-processability and solid-state molecular ordering through modulation of the *N*-alkyl substituents.[16] The DPP core has also demonstrated promising optical properties, charge carrier mobility, and photovoltaic performance in numerous small molecule and polymeric materials;[5,17-28] in particular,

Nguyen *et al.* have reported a DPP-containing small molecule donor that achieved 4.4 % efficiency with phenyl-C_{71}-butyric acid methyl ester ($PC_{71}BM$) in BHJ devices.[5]
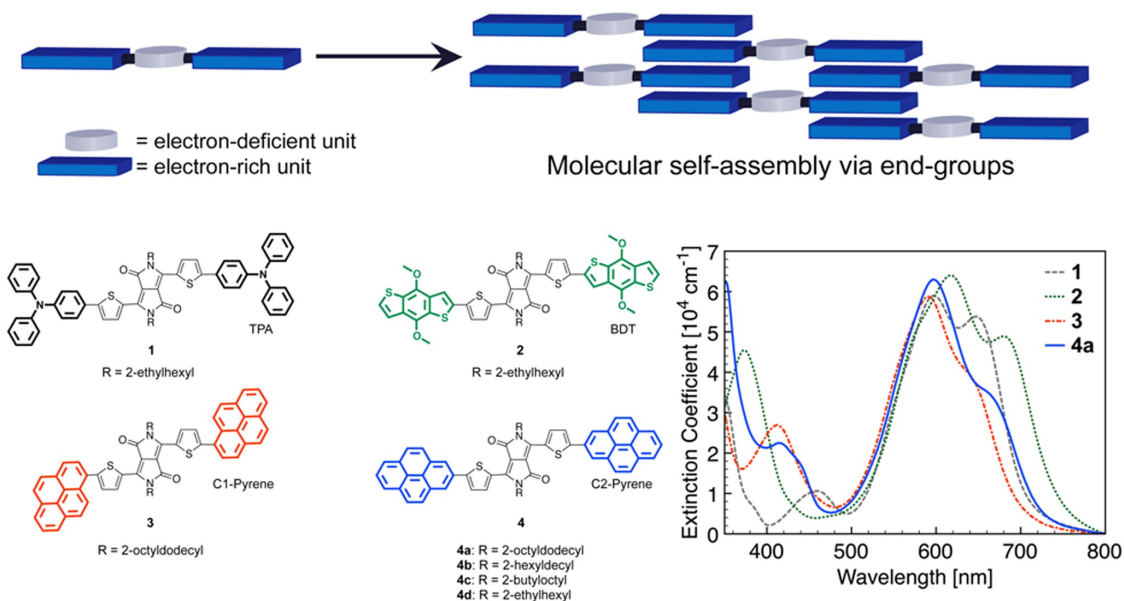
Figure 4-1. Donor-acceptor small molecules are designed to self-assemble through the electron-rich π-stacking units (top). Molecules **1**, **2**, **3**, and **4** are based on a DPP core moiety flanked by electron-rich end-groups (bottom left). The UV-Vis absorption spectra of **1**, **2**, **3**, and **4a** were obtained as thin films (bottom right).

4.2. Results and Discussion

Syntheses of the small molecules were achieved through Suzuki or Stille cross-coupling reactions to append the end-groups to the DPP core (see Supporting Information, SI).[5,29] Notably, the C2-pyrene boronate ester was obtained by Ir(I)-catalyzed C-H functionalization for selective access to the C2 position.[30-31] All four molecules have comparable absorption profiles (**Fig. 4-1**) and HOMO/LUMO energy levels (SI) that are suitable for OPV applications.

To determine the OPV performance of the small molecule materials, thin-film BHJ devices were prepared with the following architecture: ITO/PEDOT:PSS/small molecule:$PC_{71}BM$/Al. Upon extensive device optimization, small molecule **4a** exhibits a notable maximum power conversion efficiency (PCE) of 2.7%, whereas **1**, **2** and **3** exhibit lower device PCEs of 1.3%, 1.7% and 0.7%, respectively (**Table 4-1**, **Fig. 4-2**). While **1**, **2** and **4a** possess similar optoelectronic properties, their varying device performances suggest that PCE is highly dependent on end-group planarity. However, end-group planarity alone does not ensure high device efficiency, as demonstrated by the low PCE of **3**. Changing the site of pyrene substitution from C1 (**3**) to C2 (**4a**) led to an enhancement of device performance, indicating that end-group symmetry can also have a dramatic influence on PCE. Further structural optimization of the C2-pyrene-based molecules was achieved by varying the *N*-alkyl solubilizing side-chains on the core moiety. Previous studies have shown that side-chains can affect crystallinity, intermolecular spacing, and

OPV device performance.[32-33] To determine whether shorter alkyl chains could tighten molecular packing and improve OPV performance, the 2-octyldodecyl groups on **4a** were replaced with 2-hexyldecyl (**4b**), 2-butyloctyl (**4c**), and 2-ethylhexyl (**4d**) groups. Molecule **4b** exhibits the highest PCE (4.1% max.) in this series and has the one of the highest fill factors (0.58) for a solution-processed small molecule OPV system.[34-37] Further decreasing the size of the alkyl groups resulted in limited solubility and processing challenges, giving **4c** a lower device performance than **4b**. Molecule **4d** lacked sufficient solubility to be processed into a functional device.

Table 4-1. Average PV performance of **1-4** blended with PC$_{71}$BM.

|	Blend Ratio[a]	J_{SC} [e] [mA cm^{-2}]	V_{OC} [f] [V]	FF [g]	PCE [%]	Max. PCE [%]
1	1:4[b]	-4.3	0.73	0.31	1.0	1.3
2	1:4[c]	-6.2	0.81	0.30	1.3	1.7
3	1:4[b]	-3.2	0.73	0.29	0.7	0.7
4a	2:1[b]	-5.7	0.77	0.55	2.4	2.7
4b	2:1[b]	-8.3	0.76	0.58	3.7	4.1
4c	2:1[d]	-6.6	0.78	0.48	2.4	3.0

(a) Mass ratio of small molecule donor to PC$_{71}$BM. (b) Devices prepared from solution in chloroform. (c,d) Devices prepared from solution in mixed solvent: chlorobenzene/1,2-dichlorobenzene [(c) 66.7/33.3 v/v; (d) 75/25 v/v]. (e) J_{sc} = short-circuit current density. (f) V_{oc} = open-circuit voltage. (g) FF = fill factor.
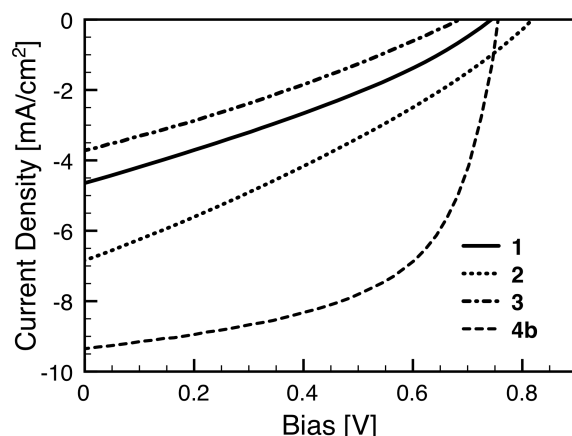
Figure 4-2. Characteristic *J-V* curves of solar cells fabricated from **1**, **2**, **3** and **4b** illuminated under AM 1.5 G, 100 mW cm^{-2}.

As shown in **Table 4-1** and **Fig. 4-2**, the high device PCE of C2-pyrene-based molecules can be mainly attributed to their high fill factors (FFs). FF is known to depend largely on carrier mobility, charge recombination, current leakage, and balanced transport of holes and electrons through the device active layer.[1-3,34,38-40] Molecules **4a** and **4b** exhibit device FFs of 0.55 and 0.58, whereas molecules **1**, **2** and **3** exhibit FFs of 0.29, 0.30 and 0.31, respectively. The high FFs are unique to **4a–4c**, even at different donor:PC$_{71}$BM ratios (**Fig. 4-3b**). Devices fabricated with **1**, **2** and **3** were optimized at a 1:4 donor:PC$_{71}$BM ratio; further increasing the donor content reduced device FF and PCE even though the hole mobility of these devices increased (**Fig. 3**). In contrast, for

molecules containing C2-pyrene end-groups (**4a–4c**), increasing the donor content enhanced both FF and hole mobility, contributing to the high device efficiency at the optimized ratio of 2:1 donor:PC$_{71}$BM ratio. These results suggest that, relative to the other end-groups studied, the C2-pyrene end-group affects intermolecular interactions which may promote molecular packing and active layer morphology favorable for high device PCE.
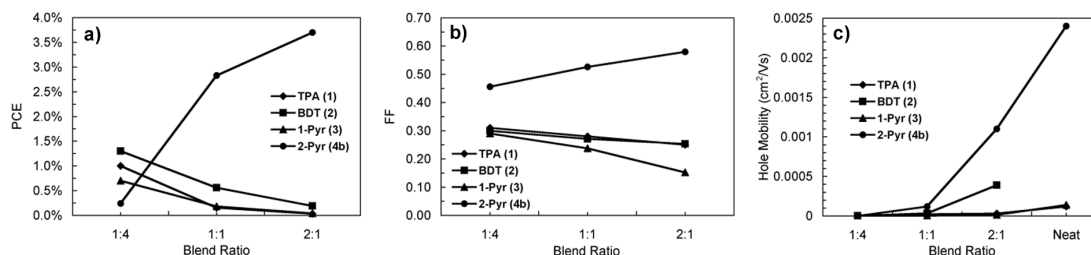

Figure 4-3. Effects of different blend ratios (small molecule:PC$_{71}$BM) on (a) PCE, (b) FF, and (c) space-charge-limited current (SCLC) hole mobility of the devices fabricated from molecules **1**, **2**, **3** and **4b**. As donor content increases, the FF and PCE are enhanced only in molecules with C2-pyrene end-groups.

To understand how the C2-pyrene end-group can promote molecular assembly, the nanoscale film morphology and solid-state packing of DPP-C2-pyrene were investigated by atomic force microscopy (AFM) and X-ray diffraction. By AFM characterization, the active layers of the thin-film devices fabricated from **1** and **3** appear smooth and relatively amorphous, while the device active layer of **2** exhibits domains approaching the 1-μm length scale. In contrast, the device active layers of **4a** and **4b** display a network of highly-crystalline features sized ~10-30 nm (SI). Grazing-incidence X-ray scattering (GIXS) pattern of a thin-film BHJ of **4b** and PC$_{71}$BM shows sharply defined rings and peaks, suggesting that the packing of **4b** is both more crystalline and more aligned than that of **1**, **2**, and **3**, whose scattering patterns indicate relatively amorphous films (**Fig. 4-4**). Single crystal X-ray analysis of **4a** shows a closely-packed, interdigitated crystal structure with extensive overlap of C2-pyrene moieties (**Fig. 4-5**). The interplanar distance between two pyrene units is 3.50 Å, confirming strong face-to-face π-π interaction between molecules. With this packing configuration, charges can move both parallel (*c* direction) and perpendicular (*b* direction) to the long-axis of the molecule, which accounts for the high hole mobilities measured for **4b**.

4.3. Conclusion

In summary, we demonstrate that efficient OPV materials can be constructed by the attachment of completely planar, symmetric end-groups to electroactive small molecules. Appending C2-pyrene as the small molecule end-group results in materials with tight, aligned crystal packing and favorable morphology dictated by π-π interactions. The intermolecular connectivity promoted by C2-pyrene allows devices containing blends of **4b** and PC$_{71}$BM to reach a maximum PCE above 4% with a FF approaching 0.6. This device FF is one of the highest values reported to date in high-performing small molecule BHJ OPVs. The use of end-groups to direct molecular self-assembly represents an effective strategy for designing high-performance small molecule OPV devices.
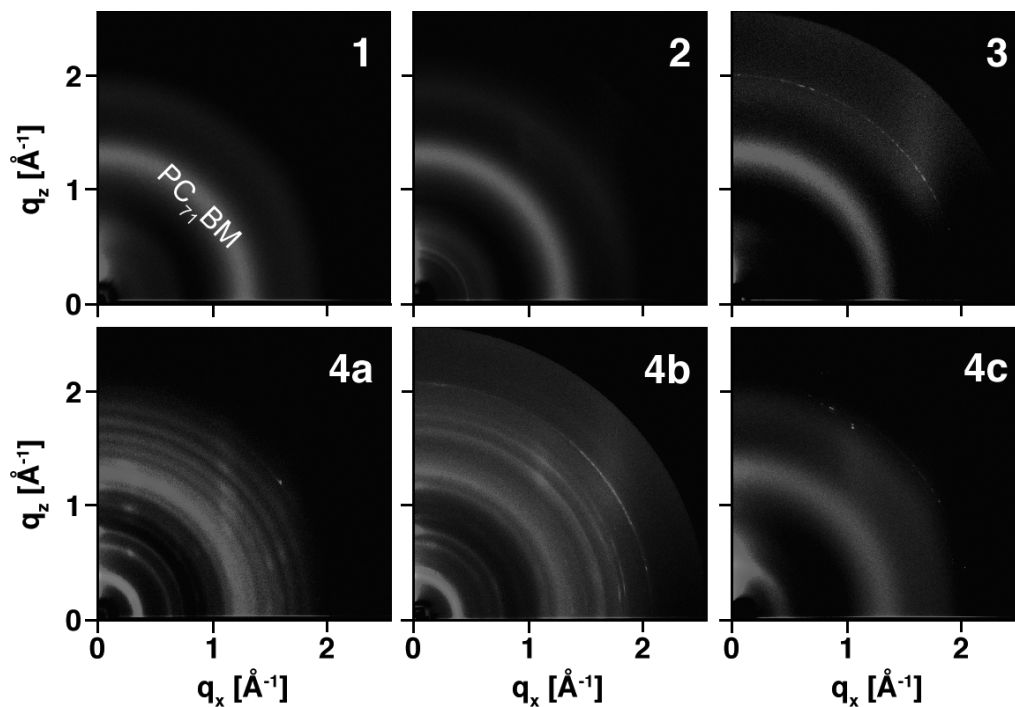
Figure 4-4. 2-D GIXS patterns of thin films of **1**, **2**, **3** and **4b** blended with PC$_{71}$BM, prepared under the same conditions as for optimized device fabrication.
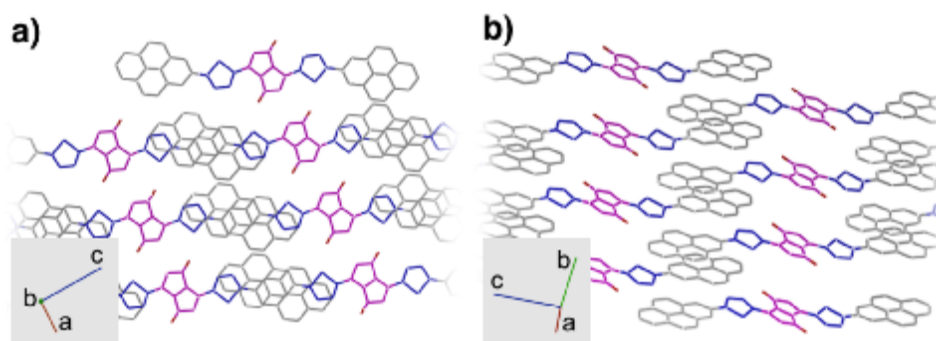
Figure 4-5. (a) View down the *b*-axis and (b) an angle view of the single crystal structure of **4a**, as determined by X-ray crystallography. Alkyl side chains are omitted for clarity. The pyrene-pyrene interplanar distance is ~3.50 Å, confirming close π-π stacking between pyrene moieties.

4.4. Experimental Details

4.4.1. Synthetic Details

Materials and Methods. All commercially available reagents obtained from suppliers were used without further purification. Unless otherwise noted, all reactions were carried out under nitrogen with standard Schlenk techniques, and all glassware used in dry reactions were flame dried under high-vacuum prior to use. All organic extracts were dried over magnesium sulfate (MgSO$_4$) powder, and solvents were removed under reduced pressure with a rotary evaporator. Toluene, tetrahydrofuran (THF) and dimethylformamide (DMF) were purified and dried by passing through two columns of

neutral alumina under nitrogen prior to use. All solvents used in Pd-catalyzed cross-coupling reactions were degassed by freeze-pump-thaw prior to use. Flash chromatography was performed using Silicycle SiliaFlash® P60 (particle size 40-63 μm, 230-400 mesh) silica gel.

All ^{1}H and ^{13}C NMR spectra were obtained in chloroform-d, unless otherwise noted, with a Bruker AVQ-400, AVB-400, DRX-500, AV-500 or AV-600 instrument. ^{13}C spectra were measured with a proton-decoupling pulse program. All chemical shifts (ppm) were calibrated to the residual peak of the deuterated solvent. Matrix-assisted laser desorption/ionization-time of flight mass spectrometry (MALDI-TOF MS) was performed on a PerSeptive Biosystems Voyager-DE using 2,2':5',2"-terthiophene as the matrix. Samples were prepared by diluting the monomers in chloroform with the matrix. Data from high-resolution mass spectrometry (HRMS) using electron impact (EI) were obtained by the UC Berkeley mass spectrometry facility. Elemental analysis (CHN) was performed by the UC Berkeley microanalysis laboratory. Melting points were measured on an Electrothermal Melt-Temp apparatus.
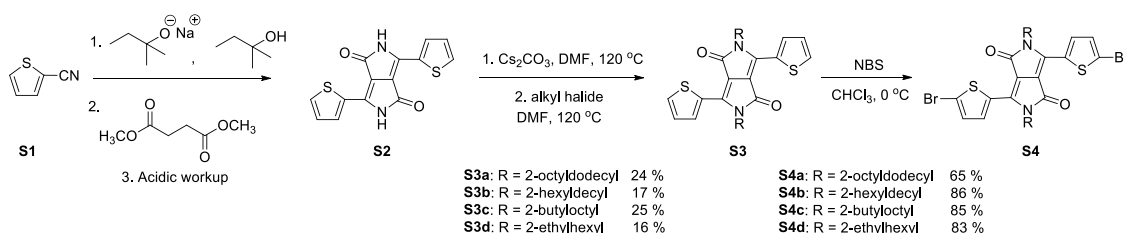
3,6-di(thiophen-2-yl)pyrrolo[3,4-c]pyrrole-1,4(2H,5H)-dione (S2). A 500 mL 3-neck flask connected to a condenser was charged with a stir bar and *tert*-amyl alcohol (250 mL). Sodium metal (2.56 g, 108 mmol) immersed in mineral oil was thoroughly washed with hexanes and cut into small pieces. Sodium metal pieces were slowly added to the reaction mixture over a 1.5 h period while the temperature was slowly increased to 120 °C over the same amount of time. Upon heating, the metal pieces began to bubble, and the reaction mixture turned light yellow. After all sodium metal pieces were dissolved, 2-thiophenecarbonitrile **S1** (11.9 g, 108 mmol) was added to the reaction. As dimethyl succinate (5.29 g, 36.2 mmol) was added dropwise to the reaction mixture over 1 h, the solution turned dark red. The reaction contents were stirred at 120 °C for 2 h, and then precipitated into acidic MeOH (400 mL MeOH and 20 mL conc. HCl). Filtration of the suspension through a Buchner funnel yielded a maroon solid (9.10 g), which was used in subsequent reactions without further purification.

2,5-bis(2-octyldodecyl)-3,6-di(thiophen-2-yl)pyrrolo[3,4-c]pyrrole-1,4(2H,5H)-dione (S3a). *A* 250 mL of round bottom flask was charged with **S2** (3.50 g, 11.7 mmol), Cs$_2$CO$_3$ (11.4 g, 35.0 mmol) and dry DMF (120 mL). The reaction mixture was stirred at 120 °C for 3 h before 2-octyldodecyl iodide [1] (11.9 g, 29.1 mmol) was added to the reaction. The reaction contents were heated at 140 °C for 16 h. The reaction contents were then cooled to 0 °C, filtered through a Büchner funnel and washed with chloroform. Excess DMF and chloroform were removed from the filtrate under reduced pressure with heating to 70 °C to yield a purple solid. The crude material was purified by

69

flash chromatography (loaded crude materials with chloroform and eluted with 40 % hexanes in toluene) to yield 2.41 g of purple tacky solid (24 %). Mp: 76.0 – 77.8 °C. ^{1}H NMR (600 MHz, CDCl$_3$, δ): 8.88 (d, J = 3.9 Hz, 2 H), 7.62 (d, J = 5.0 Hz, 2 H), 7.27 (dd, J = 3.9 Hz, 5.0 Hz, 2 H), 4.02 (d, J = 7.75 Hz, 4 H), 1.91 (m, 2 H), 1.25 (m, 64 H), 0.86 (adt, J = 7.1 Hz, 9.2 Hz, 12 H). ^{13}C (150 MHz, CDCl$_3$, δ): 161.9, 140.6, 135.3, 130.6, 130.0, 128.5, 108.1, 46.2, 37.7, 31.9, 31.8, 31.1, 30.0, 29.6, 29.54, 29.48, 29.34, 29.28, 26.2, 22.67, 22.65, 14.1. MALDI-TOF MS (m/z): [M]$^+$ calcd for C$_{54}$H$_{88}$N$_2$O$_2$S$_2$, 860.6; found, 861.1. Anal. calcd for C$_{54}$H$_{88}$N$_2$O$_2$S$_2$: C, 75.29; H, 10.30; N, 3.25; found: C, 75.41; H, 10.50; N, 3.17.

2,5-bis(2-hexyldecyl)-3,6-di(thiophen-2-yl)pyrrolo[3,4-c]pyrrole-1,4(2H,5H)-dione (S3b). Reaction conditions were the same as for **S3a**, except **S2** (4.50 g, 15.0 mmol), Cs$_2$CO$_3$ (14.60 g, 45.0 mmol), 2-hexyldecyl iodide [1] (7.24 g, 37.5 mmol) were used. Purification of the crude material through flash chromatography (loaded crude materials with chloroform and eluted with 15 % hexanes in toluene) yielded 1.89 g of maroon tacky solid (17 %). ^{1}H NMR (400 MHz, CDCl$_3$, δ): 8.89 (d, J = 3.9 Hz, 2 H), 7.61 (d, J = 5.0 Hz, 2 H), 7.26 (dd, J = 4.0 Hz, 4.9 Hz, 1 H), 4.02 (m, 4 H), 1.91 (m, 2 H), 1.26 (m, 48 H), 0.85 (aq, J = 7.3 Hz, 8.8 Hz, 12 H). ^{13}C (100 MHz, CDCl$_3$, δ): 161.8, 140.5, 135.4, 130.6, 130.0, 129.1, 128.5, 128.3, 108.0, 46.3, 37.8, 32.0, 31.9, 31.3, 30.1, 29.8, 29.6, 29.4, 26.3, 22.80, 22.76, 14.3, 14.2. MALDI-TOF MS (m/z) [M]$^+$ calcd for C$_{46}$H$_{72}$N$_2$O$_2$S$_2$, 748.5; found: 748.7.

2,5-bis(2-butyloctyl)-3,6-di(thiophen-2-yl)pyrrolo[3,4-c]pyrrole-1,4(2H,5H)-dione (S3c). Reaction conditions were the same as for **S3a**, except 2-butyloctyl iodide [1] (8.63 g, 37.5 mmol) and dry DMF (120 mL) were used. Purification of the crude material through flash chromatography (loaded crude materials with chloroform and eluted with increasing gradient from 25 % to 0 % hexanes in toluene) yielded 1.87 g of purple tacky solid (25 %). Mp: 108.8 – 110.7 °C. ^{1}H NMR (400 MHz, CDCl$_3$, δ): 8.86 (d, J = 3.9 Hz, 2 H), 7.62 (d, J = 5.0 Hz, 2 H), 7.25 (dd, J = 4.0 Hz, 4.5 Hz, 1 H), 4.02 (d, J = 7.7 Hz, 4 H), 1.90 (m, 2 H), 1.24 (m, 32 H), 0.84 (adt, J = 2.6 Hz, 6.7 Hz, 12 H). ^{13}C (150 MHz, CDCl$_3$, δ): = 161.7, 140.4, 135.1, 130.4, 129.8, 128.4, 108.0, 46.2, 37.7, 31.7, 31.2, 30.9, 29.7, 28.4, 26.2, 23.0, 22.6, 14.03, 13.97. MALDI-TOF MS (EI, m/z) [M]$^+$ calc'd for C$_{38}$H$_{56}$N$_2$O$_2$S$_2$, 636.4; found, 636.9. Anal. calcd for C$_{38}$H$_{56}$N$_2$O$_2$S$_2$: C, 71.65; H, 8.86; N, 4.40; found: C, 72.02; H, 8.92; N, 4.29.

2,5-bis(2-ethylhexyl)-3,6-di(thiophen-2-yl)pyrrolo[3,4-c]pyrrole-1,4(2H,5H)-dione (S3d). Reaction conditions were the same as for **S3a**, except **S2** (4.50 g, 15.0 mmol), Cs$_2$CO$_3$ (14.60 g, 45.0 mmol), 2-ethylhexyl bromide (7.24 g, 37.5 mmol) and dry DMF (120 mL) were used. Purification of the crude material through flash chromatography (CHCl$_3$) yielded 1.24 g of purple tacky solid (16 %). ^{1}H NMR (400 MHz, CDCl$_3$, δ): 8.89 (d, J = 3.9 Hz, 2 H), 7.61 (d, J = 5.0 Hz, 2 H), 7.25 (at, J = 4.5 Hz, 1 H), 4.01 (m, 4 H), 1.85 (m, 2 H), 1.29 (m, 16 H), 0.85 (adt, J = 7.3 Hz, 8.8 Hz, 12 H). ^{13}C (100 MHz, CDCl$_3$, δ): 161.8, 140.5, 135.4, 130.6, 130.0, 128.5, 108.0, 45.9, 39.2, 30.3, 28.4, 23.6, 23.2, 14.1, 10.6. HRMS (EI, m/z) [M]$^+$ calcd for C$_{30}$H$_{40}$N$_2$O$_2$S$_2$, 524.2531; found, 524.2535. Anal. calcd for C$_{30}$H$_{40}$N$_2$O$_2$S$_2$: C, 68.66; H, 7.68; N, 5.34; found: C, 68.73; H, 7.90; N, 5.34.
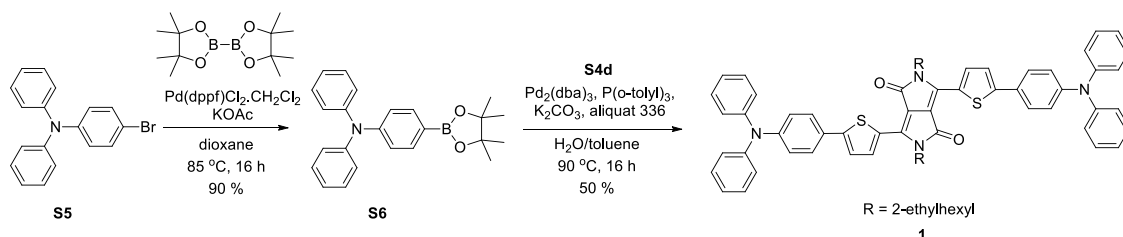
3,6-bis(5-bromothiophen-2-yl)-2,5-bis(2-octyldodecyl)pyrrolo[3,4-c]pyrrole-1,4(2H,5H)-dione (S4a). A 100 mL round bottom flask was charged with a stir bar, **S3a** (1.20 g, 1.39 mmol) and chloroform (0.1 m, 14 mL) under ambient conditions. After the

reaction mixture was stirred in an ice bath at 0 °C for 20 min, *N*-bromosuccinimide (NBS) (508 mg, 2.86 mmol) was added in small portions over 30 min. After stirring for another 20 min, the reaction was washed with distilled water (3 × 50 mL). The organic extract was dried over MgSO$_4$, and solvent was removed under reduced pressure. Purification by flash chromatography (40 % hexanes in toluene) yielded 929 mg of a purple solid (65 %). Mp 95.0 – 96.9 °C. ^{1}H NMR (400 MHz, CDCl$_3$, δ): 8.63 (d, *J* = 4.2 Hz, 2 H), 7.21 (d, *J* = 4.2 Hz, 2 H), 3.91 (d, *J* = 7.7 Hz, 4 H), 1.87 (m, 2 H), 1.25 (m, 64 H), 0.86 (adt, *J* = 5.3 Hz, 6.9 Hz, 12 H). ^{13}C (125 MHz, CDCl$_3$, δ): 161.4, 139.4, 135.3, 131.4, 131.2, 118.9, 108.0, 46.3, 37.7, 31.91, 31.87, 31.20, 30.0, 29.63, 29.55, 29.5, 29.4, 29.3, 26.2, 22.68, 22.66, 14.11. MALDI-TOF MS (*m/z*) [M]$^+$ calcd for C$_{54}$H$_{86}$Br$_2$N$_2$O$_2$S$_2$, 1018.5; found, 1018.3. Anal. calcd for C$_{54}$H$_{86}$Br$_2$N$_2$O$_2$S$_2$: C, 63.64; H, 8.50; N, 2.75; found: C, 63.73; H, 8.71; N, 2.73.
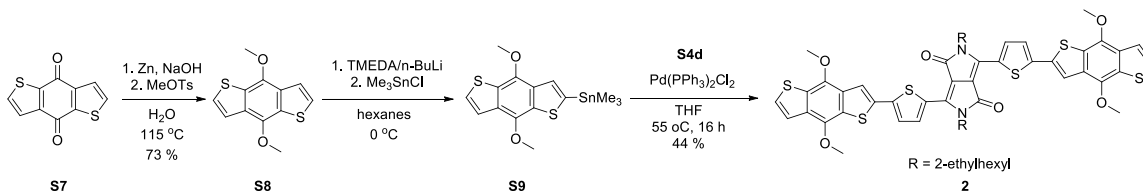
3,6-bis(5-bromothiophen-2-yl)-2,5-bis(2-hexyldecyl)pyrrolo[3,4-c]pyrrole-1,4(2H,5H)-dione (S4b). Reaction conditions and workup were the same as for **S4a**, except **S3b** (1.02 g, 1.36 mmol) and NBS (497 mg, 2.79 mmol) were used. Purification by flash chromatography (25 % hexanes in toluene) yielded 1.06 g of a purple solid (86 %). Mp 114.5 – 116.0 °C. ^{1}H NMR (400 MHz, CDCl$_3$, δ): 8.62 (d, *J* = 4.2 Hz, 2 H), 7.21 (d, *J* = 4.2 Hz, 2 H), 3.92 (d, *J* = 7.8 Hz, 4 H), 1.88 (m, 2 H), 1.26 (m, 48 H), 0.85 (m, 12 H). ^{13}C (100 MHz, CDCl$_3$, δ): 161.1, 139.4, 135.3, 131.4, 131.2, 118.9, 108.1, 46.4, 37.8, 31.9, 31.7, 31.2, 30.0, 29.6, 29.5, 29.3, 26.2, 26.1, 22.7, 22.6, 14.09, 14.06. MALDI-TOF MS (*m/z*) [M]$^+$ calcd for C$_{46}$H$_{70}$Br$_2$N$_2$O$_2$S$_2$, 904.3; found, 904.2. Anal. calcd for C$_{46}$H$_{70}$Br$_2$N$_2$O$_2$S$_2$: C, 60.91; H, 7.78; N, 3.09; found: C, 60.99; H, 7.93; N, 3.10.

3,6-bis(5-bromothiophen-2-yl)-2,5-bis(2-butyloctyl)pyrrolo[3,4-c]pyrrole-1,4(2H,5H)-dione (S4c). Reaction conditions and workup were the same as for **S4a**, except **S3c** (1.00 g, 1.57 mmol) and NBS (573 mg, 3.22 mmol) were used. Purification by flash chromatography (35 % hexanes in CHCl$_3$) yielded 1.07 g of a purple solid (85 %). Mp 151.2 – 153.7 °C. ^{1}H NMR (400 MHz, CDCl$_3$, δ): 8.61 (d, *J* = 4.2 Hz, 2 H), 7.22 (d, *J* = 4.2 Hz, 2 H), 3.92 (m, 4 H), 1.87 (m, 2 H), 1.25 (m, 32 H), 0.85 (adt, *J* = 3.4 Hz, 6.7 Hz, 12 H). ^{13}C (100 MHz, CDCl$_3$, δ): 161.4, 139.4, 135.2, 131.4, 131.2, 118.9, 108.1, 46.3, 37.7, 31.7, 31.1, 30.9, 29.6, 28.4, 26.1, 23.0, 22.6, 14.1, 14.0. MALDI-TOF MS (*m/z*) [M]$^+$ calcd for C$_{38}$H$_{54}$Br$_2$N$_2$O$_2$S$_2$, 792.2; found, 792.2. Anal. calcd for C$_{38}$H$_{54}$Br$_2$N$_2$O$_2$S$_2$: C, 57.43; H, 6.85; N, 3.52; found: C, 57.63; H, 6.96; N, 3.48.

3,6-bis(5-bromothiophen-2-yl)-2,5-bis(2-ethylhexyl)pyrrolo[3,4-c]pyrrole-1,4(2H,5H)-dione (S4d). Reaction conditions and workup were the same as for **S4a**, except **S3d** (1.21 g, 2.31 mmol) and NBS (821 mg, 4.61 mmol) were used. Purification by flash chromatography (20 % hexanes in CHCl$_3$) yielded 1.30 g of a purple solid (83 %). ^{1}H NMR (400 MHz, CDCl$_3$, δ): 8.64 (d, *J* = 4.2 Hz, 2 H), 7.22 (d, *J* = 4.2 Hz, 2 H), 3.92 (m, 4 H), 1.82 (m, 2 H), 1.26 (m, 16 H), 0.87 (aq, *J* = 7.3 Hz, 12 H). ^{13}C (100 MHz, CDCl$_3$, δ): 161.5, 139.5, 135.5, 131.6, 131.3, 119.2, 108.1, 46.1, 39.2, 30.3, 28.4, 23.7, 23.2, 14.2, 10.6. HRMS (EI, *m/z*) [M]$^+$ calcd for C$_{30}$H$_{38}$Br$_2$N$_2$O$_2$S$_2$, 682.0721; found, 682.0733. Anal. calcd for C$_{30}$H$_{38}$Br$_2$N$_2$O$_2$S$_2$: C, 52.79; H, 5.61; N, 4.10; found: C, 52.90; H, 5.52; N, 4.21.

Pd(dppf)Cl₂·CH₂Cl₂ — scheme 1: S5 → (Pd(dppf)Cl₂.CH₂Cl₂, KOAc, dioxane, 85 °C, 16 h, 90 %) → S6 → (S4d, Pd₂(dba)₃, P(o-tolyl)₃, K₂CO₃, aliquat 336, H₂O/toluene, 90 °C, 16 h, 50 %) → 1, R = 2-ethylhexyl

N,N-diphenyl-4-(4,4,5,5-tetramethyl-1,3,2-dioxaborolan-2-yl)aniline (S6). A 3-neck 250 mL round bottom flask was charged with a stir bar, 4-bromotriphenylamine **S5** (4.00 g, 12.4 mmol), *bis*(pinacolato)diboron (B₂pin₂) (3.29 g, 13.0 mmol), anhydrous potassium acetate (KOAc) (3.31 g, 33.6 mmol), dichloro[1,1'-bis(diphenylphosphino)-ferrocene]palladium(II) dichloromethane adduct (Pd(dppf)Cl₂·CH₂Cl₂) (271 mg, 0.332 mmol) and degassed dioxane (120 mL). After the reaction mixture was heated at 85 °C for 16 h, it was extracted with diethyl ether and washed with distilled water. The organic extract was dried over MgSO₄, and solvent was removal under reduced pressure yielded a brown viscous oil. Purification with flash chromatography (25 % hexanes in CH₂Cl₂) yielded 4.30 g of tacky off-white solid (95 %). ^{1}H NMR (600 MHz, CDCl₃, δ): 7.67 (d, J = 8.5 Hz, 2 H), 7.26 (t, J = 7.9 Hz, 4 H), 7.11 (d, J = 7.6 Hz, 4 H), 7.04 (m, 4 H), 1.34 (s, 12 H). ^{13}C (150 MHz, CDCl₃, δ): 150.7, 147.5, 136.0, 129.43, 125.1, 123.5, 121.9, 83.7, 25.0. HRMS (EI, m/z) [M]$^+$ calcd for $C_{24}H_{26}BNO_2$, 371.2057; found, 371.2068. Anal. calcd for $C_{24}H_{26}BNO_2$: C, 77.64; H, 7.06; N, 3.77; found: C, 77.61; H, 7.04; N, 3.93.

3,6-bis(5-(4-(diphenylamino)phenyl)thiophen-2-yl)-2,5-bis(2-ethylhexyl)pyrrolo[3,4-c]pyrrole-1,4(2H,5H)-dione (1). A 50 mL Schlenk tube was charged with the following materials: a stir bar, **S4d** (841 mg, 1.23 mmol), **S6** (1.01 g, 2.71 mmol), bis(dibenzylideneacetone)palladium (0) (Pd₂(dba)₃) (22.6 mg, 24.6 mol), tri-*o*-tolylphosphine (P(*o*-tol)₃) (30.1 mg, 98.6 μmol), anhydrous K₂CO₃ (1.60 g, 11.6 mmol), 2 drops of aliquat 336, freeze-pump-thawed toluene (23.2 mL) and freeze-pump-thawed distilled water (5.8 mL). The reaction mixture was heated at 90 °C for 16 h before being precipitated into 250 mL of MeOH. The precipitates were filtered through a 20 μm nylon membrane. Purification by flash chromatography (10 % hexanes in chloroform) yielded 703 mg of the desired product as a metallic purple solid (56 %). ^{1}H NMR (500 MHz, CDCl₃, δ): 8.53-9.75 (s, 1 H), 7.5-7.8 (s, 2 H), 7.41 (s, 1H), 7.35 (t, J = 7.8 Hz, 4 H), 7.19 (d, J = 7.7 Hz, 4 H), 7.13 (d, J = 8.6 Hz, 4 H), 4.12 (s, 2 H), 2.01 (m, 1 H), 1.43 (m, 5 H), 1.32 (m, 3 H), 0.96 (t, J = 7.4 Hz, 3H), 0.91 (t, J = 7.0 Hz, 3 H). HRMS (FAB, m/z) [M]$^+$ calcd for $C_{66}H_{66}N_4O_2S_2$, 1010.4627; found, 1010.4653. Anal. calcd for $C_{66}H_{66}N_4O_2S_2$: C, 78.38; H, 6.58; N, 5.54; found: C, 78.12; H, 6.20; N, 5.62.

scheme 2: S7 → (1. Zn, NaOH; 2. MeOTs; H₂O, 115 °C, 73 %) → S8 → (1. TMEDA/n-BuLi; 2. Me₃SnCl; hexanes, 0 °C) → S9 → (S4d, Pd(PPh₃)₂Cl₂, THF, 55 °C, 16 h, 44 %) → 2, R = 2-ethylhexyl

Benzo[1,2-b:4,5-b']dithiophene-4,8-dione (S7). Synthesized according to published procedures in literature [2].

4,8-Dimethoxybenzo[1,2-b:4,5-b']dithiophene (S8). Compound **2** (2.00 g, 9.08 mmol), zinc powder (2.08 g, 31.8 mmol) and water (50 mL) were combined in a 100 mL

flask, followed by sodium hydroxide (5.48 g, 137 mmol). The mixture was heated at reflux for 2 h, until the reaction contents turned bright yellow. The reaction mixture was then cooled to room temperature, methyl tosylate (6.76 g, 36.3 mmol) was added to the mixture, and the reaction contents were heated at 50°C for 12 h. The reaction mixture was cooled to room temperature and quenched with water. The mixture was extracted with diethyl ether (3 x 50 mL), dried and volatile solvents were evaporated. The organic extract was purified by column chromatography on silica gel with a mixed mobile phase of chloroform and hexanes (90:10) to yield compound **3** as a colorless solid (1.65 g, 73 %). ^{1}H NMR (400 MHz, CDCl$_3$, δ): 7.51 (d, J = 5.54 Hz, 2H), 7.40 (d, J = 5.53 Hz, 2H), 4.14 (s, 6H). ^{13}C NMR (100 MHz, CDCl$_3$, δ): 145.47, 131.40, 129.92, 126.41, 120.22, 61.14. HRMS (EI, m/z) [M]$^+$ calcd for C$_{12}$H$_{10}$O$_2$S$_2$, 250.0122; found, 250.0128. Anal. calcd for C$_{12}$H$_{10}$O$_2$S$_2$: C, 57.57; H, 4.03; found: C, 57.31; H, 3.90.

2-Trimethyltin-4,8-dimethoxybenzo[1,2-b:4,5-b']dithiophene (S9). Compound 3 (2.02 g, 8.07 mmol), tetramethylethylenediamine (dried over CaH$_2$ and vacuum distilled, 1.80 mL, 12.2 mmol) and dry THF (50 mL) were combined in a dry 100 mL flask. The reaction contents were cooled to 0 °C and n-butyllithium (3.39 mL, 2.50 M, 8.48 mmol) was added to the flask via syringe. After stirring for 2 h at room temperature, the reaction mixture was cooled back to 0 °C and trimethyltin chloride (2.57 g, 12.9 mmol) was added. After stirring for 8 h at room temperature, the reaction contents were quenched with water. The mixture was extracted with diethyl ether (3 x 50 mL), dried and volatile solvents were evaporated. To remove the distanylated byproduct, the organic extract was purified by column chromatography on silica gel with a mixed mobile phase of 75% chloroform in hexanes to yield the mixed mono- and non-stanylated products. The mixture of products was used in the subsequent reaction without further purification.
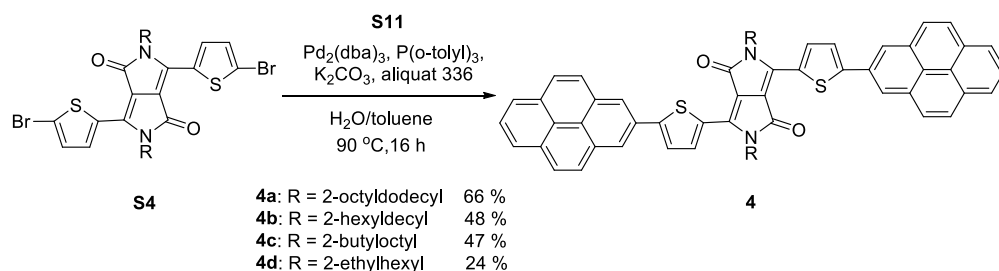
3,6-bis(5-(4,8-dimethoxybenzo[1,2-b:4,5-b']dithiophen-2-yl)thiophen-2-yl)-2,5-bis(2-ethylhexyl)pyrrolo[3,4-c]pyrrole-1,4(2H,5H)-dione (2). A 50 mL Schlenk tube was charged with **S4d** (401 mg, 0.586 mmol), **S9** (731 mg, 1.77 mmol), Pd(PPh$_3$)$_2$Cl$_2$ (20.6 mg, 29.3 μmol) and freeze-pump-thawed THF (24 mL). As mentioned previously, **S9** contained a mixture of non- and mono-stannylated compounds; the calculation was done assuming that the materials contained only the mono-stannylated product, and an excess of **S9** (3 equiv.) was used in this reaction. The reaction mixture was stirred at 55 °C for 3 h and then at 60 °C for 16 h. After cooling the reaction contents to room temperature, the crude mixture was precipitated into 200 mL of MeOH and filtered through a 20 μm nylon membrane. Purification by flash chromatography (CHCl$_3$) yielded 264 mg of a metallic purple solid (44 %). ^{1}H NMR (500 MHz, CDCl$_3$, δ): 8.97 (d, J = 3.10 Hz, 2 H), 7.68 (s, 2 H), 7.48 (d, J = 5.48 Hz, 2 H), 7.44 (d, J = 4.07 Hz, 2 H), 7.41 (d, J = 5.38 Hz, 2 H), 4.18 (s, 6 H), 4.14 (s, 6 H), 4.08 (m, 4 H), 1.96 (m, 2 H), 1.39 (m, 16 H), 0.93 (m, 12 H). HRMS (FAB, m/z) [M]$^+$ calcd for C$_{54}$H$_{56}$N$_2$O$_6$S$_6$, 1020.2463; found, 1020.2477. Anal. calcd for C$_{54}$H$_{56}$N$_2$O$_6$S$_6$: C, 63.50; H, 5.53; N, 2.74; found: C, 63.38; H, 5.26; N, 2.88.
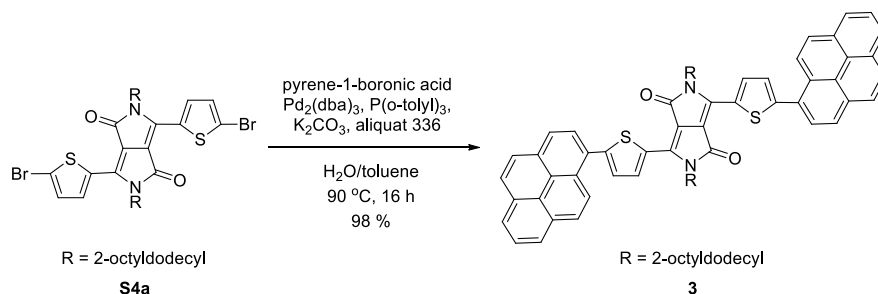
2,5-bis(2-octyldodecyl)-3,6-bis(5-(pyren-1-yl)thiophen-2-yl)pyrrolo[3,4-c]pyrrole-1,4(2H,5H)-dione (3). A 50 mL Schlenk tube was charged with the following materials: a stir bar, **S4a** (292 mg, 0.286 mmol), pyrene-1-boronic acid (256 mg, 0.630 mmol), Pd$_2$(dba)$_3$ (5.24 mg, 5.73 μmol), P(o-tol)$_3$ (6.97 mg, 22.9 μmol), anhydrous K$_2$CO$_3$ (316 mg, 2.29 mmol), 1 drop of aliquat 336, freeze-pump-thawed toluene (5.7 mL) and freeze-pump-thawed distilled water (1.1 mL). The reaction mixture was heated at 90 °C for 16 h before being precipitated into 200 mL of MeOH. The precipitates were filtered through a 20.0 μm nylon membrane. Purification by flash chromatography twice (40 % hexanes in chloroform, and then 100 % chloroform) yielded 353 mg of the desired product as a tacky metallic purple solid (98 %). Mp 127.1 – 129.2 °C. ^{1}H NMR (500 MHz, CDCl$_3$, δ): 9.17 (s, 2 H), 8.57 (d, J = 9.3, 2H), 8.24 (m, 6H), 8.15 (m, 6 H), 8.11 (d, J = 8.9 Hz, 2 H), 8.06 (t, J = 7.6 Hz, 2 H), 7.6 (d, J = 3.9 Hz, 2 H), 4.16 (d, J = 7.7 Hz, 4H), 2.11 (m, 2 H), 1.45 – 1.10 (m, 64 H), 0.81 (aq, J = 7.0 Hz, 12 H). MALDI-TOF MS (m/z) [M]$^+$ calcd for C$_{86}$H$_{104}$N$_2$O$_2$S$_2$, 1260.8; found, 1260.9. Anal. calcd for C$_{86}$H$_{104}$N$_2$O$_2$S$_2$: C, 81.86; H, 8.31; N, 2.22; found: C, 81.47; H, 8.50; N, 2.14.
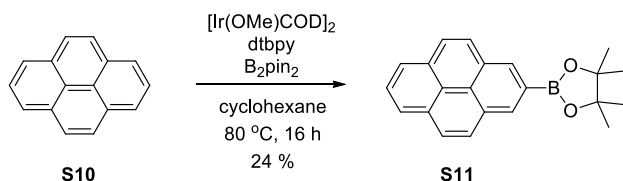
4,4,5,5-tetramethyl-2-(pyren-2-yl)-1,3,2-dioxaborolane (S11). A 50 mL round bottom flask was charged with a stir bar, pyrene (1.0 equiv, 809 mg, 4.00 mmol), di-μ-methoxobis(1,5-cyclooctadiene)diiridium(I) ([Ir(OMe)COD]$_2$) (5 mol%, 132 mg, 0.200 mmol), 4,4'-di-$tert$-butyl-2,2'-bipyridine (dtbpy) (10 mol%, 107 mg, 0.400 mmol), bis(pinacolato)diboron (B$_2$pin$_2$) (1.1 equiv, 1.12 g, 4.40 mmol) and cyclohexane (15 mL). After the reaction mixture was heated at 80 °C for 20 h, solvent was removed with rotary evaporator to yield a brown solid. The crude product was purified by flash chromatography (50 % hexanes in CH$_2$Cl$_2$), and solvent removal from the combined fractions yielded an off-white solid (320 mg, 24 %). ^{1}H NMR (400 MHz, CDCl$_3$, δ): 8.64 (s, 2 H), 8.17 (d, J = 7.6 Hz, 2 H), 8.11 (d, J = 9.0 Hz, 2 H), 8.06 (d, J = 9.0 Hz, 2 H), 8.02 (t, J = 7.6 Hz, 1 H), 1.47 (s, 12 H). ^{13}C (100 MHz, CDCl$_3$, δ): 131.8, 131.5, 130.6, 127.9, 127.4, 126.5, 125.0, 84.3, 25.6. HRMS (EI, m/z) [M]$^+$ calcd for C$_{22}$H$_{21}$BO$_2$, 328.1635; found, 328.1647. Anal. calcd for C$_{22}$H$_{21}$BO$_2$: C, 80.51; H, 6.45; found: C 80.63; H, 6.55.

S11
Pd$_2$(dba)$_3$, P(o-tolyl)$_3$,
K$_2$CO$_3$, aliquat 336

H$_2$O/toluene
90 °C, 16 h

S4

4a: R = 2-octyldodecyl   66 %
4b: R = 2-hexyldecyl   48 %
4c: R = 2-butyloctyl   47 %
4d: R = 2-ethylhexyl   24 %

4

2,5-bis(2-octyldodecyl)-3,6-bis(5-(pyren-2-yl)thiophen-2-yl)pyrrolo[3,4-c]pyrrole-1,4(2H,5H)-dione (4a). A 50 mL Schlenk tube was charged with the following materials: a stir bar, **S4d** (278 mg, 0.272 mmol), **S11** (197 mg, 0.598 mmol), Pd$_2$(dba)$_3$ (4.99 mg, 5.45 μmol), P(o-tol)$_3$ (6.63 mg, 21.8 μmol), anhydrous K$_2$CO$_3$ (354 mg, 2.0 mmol/mL H$_2$O), 1 drop of aliquat 336, freeze-pump-thawed toluene (5.1 mL) and freeze-pump-thawed distilled water (1.3 mL). The reaction mixture was heated at 90 °C for 16 h before being precipitated into 200 mL of MeOH. The precipitates were filtered through a 20.0 μm nylon membrane. Purification by flash chromatography twice (40 % hexanes in chloroform, and then 100 % chloroform) yielded 228 mg of the desired product as a metallic, dark purple solid (66 %). ^{1}H NMR (500 MHz, CDCl$_3$, δ): 9.06 (d, J = 4.1 Hz, 2 H), 8.43 (s, 4H), 8.19 (d, J = 7.6 Hz, 4H), 8.10 (m, 8 H), 8.01 (at, J = 7.6 Hz, 2 H), 7.77 (d, J = 4.1 Hz, 2 H), 4.18 (d, J = 7.7 Hz, 4 H), 2.08 (m, 2 H), 1.27 (m, 64 H), 0.79 (add, J = 6.4 Hz, 7.5 Hz, 12 H). HRMS (FAB, m/z) [M]$^+$ calcd for C$_{86}$H$_{104}$N$_2$O$_2$S$_2$, 1260.7539; found, 1260.7560. Anal. calcd for C$_{86}$H$_{104}$N$_2$O$_2$S$_2$: C, 81.86; H, 8.31; N, 2.22; found: C, 81.56, H, 8.48; N, 2.46.

2,5-bis(2-hexyldecyl)-3,6-bis(5-(pyren-2-yl)thiophen-2-yl)pyrrolo[3,4-c]pyrrole-1,4(2H,5H)-dione (4b). Reaction conditions and workup were the same as for **4a**, except **S4b** (300 mg, 0.331 mmol), **S11** (179 mg, 0.728 mmol), Pd$_2$(dba)$_3$ (6.01 mg, 6.62 μmol), P(o-tol)$_3$ (8.05 mg, 26.4 μmol), anhydrous K$_2$CO$_3$ (366 mg, 2.0 mmol/mL H$_2$O), 1 drop of aliquat 336, freeze-pump-thawed toluene (6.6 mL) and freeze-pump-thawed distilled water (1.3 mL) were used. Purification by flash chromatography (loaded crude materials in CHCl$_3$, and eluted with increasing gradient from 50 % to 80 % CHCl$_3$ in hexanes) yielded 182 mg of a metallic, dark purple solid (48 %). Mp 261.2 – 262.4 °C. ^{1}H NMR (500 MHz, CDCl$_3$, δ): 9.04 (d, J = 4.0 Hz, 2 H), 8.30 (s, 4H), 8.10 (d, J = 7.6 Hz, 4H), 8.00 (q, J = 8.9 Hz, 8 H), 7.92 (t, J = 7.6 Hz, 2 H), 7.68 (d, J = 4.1 Hz, 2 H), 4.13 (d, J = 7.7 Hz, 4 H), 2.05 (m, 2 H), 1.45 – 1.18 (m, 48 H), 0.84 (t, J = 6.8 Hz, 6 H), 0.80 (t, J = 6.7 Hz, 6 H). MALDI-TOF MS (m/z) [M]$^+$ calcd for C$_{78}$H$_{88}$N$_2$O$_2$S$_2$, 1148.6; found, 1146.2. Anal. calcd for C$_{78}$H$_{88}$N$_2$O$_2$S$_2$: C, 81.49; H, 7.72; N, 2.44; found: C, 81.19, H, 7.70; N, 2.41.

2,5-bis(2-butyloctyl)-3,6-bis(5-(pyren-2-yl)thiophen-2-yl)pyrrolo[3,4-c]pyrrole-1,4(2H,5H)-dione (4c). Reaction conditions and workup were the same as for **4a**, except **S4c** (300 mg, 0.338 mmol), **S11** (204 mg, 0.624 mmol), Pd$_2$(dba)$_3$ (6.91 mg, 7.55 μmol), P(o-tol)$_3$ (9.19 mg, 30.2 μmol), anhydrous K$_2$CO$_3$ (417 mg, 2.0 mmol/mL H$_2$O), 1 drop of aliquat 336, freeze-pump-thawed toluene (7.5 mL) and freeze-pump-thawed distilled water (1.5 mL) were used. Purification by flash chromatography (loaded crude materials in CHCl$_3$, and eluted with increasing gradient from 40 % to 85 % CHCl$_3$ in hexanes) yielded 185 mg of a metallic, dark purple solid (47 %). Mp 268.1 – 271.3 °C. ^{1}H NMR (500 MHz, CDCl$_3$, δ): 9.06 (d, J = 4.1 Hz, 2 H), 8.46 (s, 4H), 8.20 (d, J = 7.6 Hz, 4H),

8.12 (m, 8 H), 8.01 (at, J = 7.6 Hz, 2 H), 7.79 (d, J = 4.1 Hz, 2 H), 4.19 (d, J = 7.8 Hz, 4 H), 2.07 (m, 2 H), 1.50 – 1.25 (m, 32 H), 0.91 (t, J = 7.1 Hz, 6 H), 0.83 (t, J = 6.9 Hz, 6 H). MALDI-TOF MS (m/z) [M]$^+$ calcd for $C_{70}H_{72}N_2O_2S_2$, 1036.5; found, 1036.9. Anal. calcd for $C_{70}H_{72}N_2O_2S_2$: C, 81.04; H, 7.00; N, 2.70; found: C, 80.67, H, 6.95; N, 2.65.

2,5-bis(2-ethylhexyl)-3,6-bis(5-(pyren-2-yl)thiophen-2-yl)pyrrolo[3,4-c]pyrrole-1,4(2H,5H)-dione (4d). Reaction conditions and workup were the same as for **4a**, except **S4d** (290 mg, 0.425 mmol), **S11** (307 mg, 0.935 mmol), Pd$_2$(dba)$_3$ (8.52 mg, 9.3 μmol), P(o-tol)$_3$ (11.4 mg, 37.4 μmol), anhydrous K$_2$CO$_3$ (553 mg, 2.0 mmol/mL H$_2$O), 1 drop of aliquat 336, freeze-pump-thawed toluene (8.0 mL) and freeze-pump-thawed distilled water (2.0 mL) were used. Purification by flash chromatography with CHCl$_3$ yielded 95 mg of a metallic, dark purple solid (24 %). ^{1}H NMR (400 MHz, CDCl$_3$): due to the low solubility of **4d**, the sample concentration was below the NMR detection limit. MALDI-TOF MS (m/z) [M]$^+$ calcd for $C_{62}H_{56}N_2O_2S_2$, 924.4; found, 924.6.

4.4.2. Device Fabrication

All devices were fabricated on ITO-coated glass substrates (pre-patterned, R = 20 Ω^{-1}, Thin Film Devices, Inc.). The substrates were sonicated for 20 minutes in 2% Helmanex soap water and rinsed extensively with deionized (DI) water. They were then sonicated for 20 minutes in DI water, 20 minutes in acetone, and 20 minutes in isopropyl alcohol, followed by drying under a stream of air. The substrates were then UV-ozone cleaned for 5 minutes. A thin layer (30-40 nm) of PEDOT:PSS (Clevios PH) was spin-coated onto each substrate at 4000 RPM for 40 s, followed by 10 minutes of drying at 140 ºC in air. The samples were then transferred to a glovebox under N$_2$, where the active layers were spin-coated at 2000 RPM for 40 s. The cathode was thermally evaporated under vacuum (~10^{-7} torr) through a shadow mask that defines an active area of ~0.03 cm^2. Some of the samples were then thermally annealed by placing them substrate-side down (active layer facing up) on a hot plate. Details of the solution concentrations, cathode deposition, and annealing steps for each molecule are shown in **Table 4-2**. Current-voltage (J-V) curves were measured using a Keithley 2400 source-measure unit under AM 1.5 G solar illumination at 100 mW cm^{-2} (1 sun) using a Thermal-Oriel 150 W solar simulator.

Table 4-2. Device Fabrication Parameters

	Solution Conc. [μg/ml]		Solvent	Cathode	Annealing
	Donor	PC$_{71}$BM			
1	5	20	CHCl$_3$	Al (100 nm)	110º C, 10 min.
2	5	20	2:1 CB:DCB	Al (100 nm)	110º C, 10 min.
3	4	16	CB	Al (100 nm)	100 ºC, 10 min.
4a	15	7.5	CHCl$_3$	Al (100 nm)	130 ºC, 25 min.[†], 130 ºC, 10 min.
4b	15	7.5	CHCl$_3$	Al (100 nm)	130 ºC, 25 min.[†], 130 ºC, 10 min.
4c	15	7.5	CB	Al (100 nm)	130 ºC, 1 min.[†], 130 ºC, 1 min.

† = annealed prior to cathode deposition; CB = chlorobenzene; DCB = 1,2-dichlorobenzene

SCLC devices for **1**, **2**, **3**, and **4b** were fabricated following the same substrate preparation, spin-coating parameters, and annealing conditions as for the respective solar cell devices. Neat donor small molecule films were spin-cast from solutions of: 15 mg/mL in $CHCl_3$ for **1**, 15 mg/mL in CB for **2**, 20 mg/mL in CB for **3**, and 20 mg/mL in $CHCl_3$ for **4b**. Blend films were spin-cast from these same solutions mixed with solutions of $PC_{71}BM$: 30 mg/mL in $CHCl_3$ for **1**, 30 mg/mL in CB and DCB (mixed to obtain 2:1 overall CB:DCB) for **2**, 20 mg/mL in CB for **3**, and 30 mg/mL in $CHCl_3$ for **4b**. For each molecule and blend ratio, two different film thicknesses were prepared to provide a more accurate measurement. Gold was used as the cathode material rather than Al in order to promote hole-only transport. Dark current J-V characteristics were measured using the same setup used for testing solar cell devices. Voltage was corrected for the built-in voltage and the voltage drop from series resistance. Hole mobility was obtained by fitting J-V data to the Mott-Gurney Law.

4.4.3. Instrumentation

UV-Vis spectral data were measured with Varian Cary 50 spectrophotometer. Thin film measurements were collected by spin-casting thin-films onto untreated quartz slides. For extinction coefficient measurements, films of varying thicknesses were obtained by spin-casting from a series of increasingly dilute solutions, starting with the same solutions used for SCLC device preparation (see above for details).

Cyclic voltammograms were collected using a Solartron 1285 potentiostat under the control of CorrWare II software. A standard three electrode cell based on a Pt wire working electrode, a silver wire pseudo reference electrode (calibrated vs. Fc/Fc⁺, which is assumed to have an absolute energy level of -4.80 eV to vacuum)[3], and a Pt wire counter electrode was purged with nitrogen and maintained under a nitrogen atmosphere during all measurements. Acetonitrile was purchased anhydrous from Aldrich and tetrabutylammonium hexafluorophosphate (0.1 M) was used as the supporting electrolyte. Small molecule films were drop cast onto a Pt wire working electrode from a 1% (w/w) chloroform solution and dried under nitrogen prior to measurement.

Height profiles of the active layers of devices made using **1-4c** (**Fig. 4-7**) were imaged using a Veeco Multimode V Atomic Force Microscope (AFM) operated in tapping mode.

X-ray crystal packing structure of **4a** was determined by Dr. Antonio DiPasquale at the UC Berkeley College of Chemistry X-Ray Crystallography Facility. Molecule **4a** was recrystallized from toluene (solvent) and isopropanol (precipitant) by vapor diffusion over a two-week period to yield red rods. A red rod 0.10 x 0.10 x 0.04 mm in size was mounted on a Cryoloop with Paratone oil. Data were collected in a nitrogen gas stream at 100(2) K using phi and omega scans. Crystal-to-detector distance was 60 mm and exposure time was 10 seconds per frame using a scan width of 1.0°. Data collection was 96.0% complete to 50.00° in q. A total of 8622 reflections were collected covering the indices, -6<=h<=7, -15<=k<=15, -16<=l<=16. 3547 reflections were found to be symmetry independent, with an R_{int} of 0.0411. Indexing and unit cell refinement indicated a primitive, triclinic lattice. The space group was found to be P-1 (No. 2). The

data were integrated using the Bruker SAINT software program and scaled using the SADABS software program. Solution by direct methods (SIR-2008) produced a complete heavy-atom phasing model consistent with the proposed structure. All non-hydrogen atoms were refined anisotropically by full-matrix least-squares (SHELXL-97). All hydrogen atoms were placed using a riding model. Their positions were constrained relative to their parent atom using the appropriate HFIX command in SHELXL-97.

CCDC 831594 contains the supplementary crystallographic data for this work. These data can be obtained free of charge from The Cambridge Crystallographic Data Centre via www.ccdc.cam.ac.uk/data_request/cif.

Grazing-incidence x-ray scattering (GIXS) experiments were conducted at the Stanford Synchotron Radiation Laboratory on beamline 11-3. Samples were irradiated at a fixed incident angle on the order of 0.1° and their GIXS patterns were recorded with a 2-D image detector (MAR345 image plate detector). GIXS patterns were recorded with an X-ray energy of 12.71 keV (λ = 0.975 Å). To maximize the intensity from the sample, the incident angle (~0.1° – 0.12°) was carefully chosen such that the X-ray beam penetrated the sample completely but did not interact with the silicon substrate. Typical exposure times were 30-600 s. To ensure that surface conditions matched those used for device fabrication, a thin layer (~40 nm) of PEDOT:PSS was spin-coated onto silicon substrates that were pretreated with UV-ozone for 5 min. Then the GIXS samples were prepared by spin-coating the same solutions used for device fabrication at 2000 rpm for 40 s. GIXS patterns for **4a** at various annealing times are shown in **Fig. 4-8**.

Table 4-3. Optical and Electrochemical Properties of 1-4a in Thin-Films.

|	Extinction Coefficient[a] [cm^{-1}]	Optical band gap[b] [eV]	HOMO (PESA[c]) [eV]	HOMO (CV[d]) [eV]	LUMO (CV[d]) [eV]
1	5.9×10^4	1.76	5.2	5.2	3.4
2	6.4×10^4	1.66	5.1	5.2	3.5
3	6.4×10^4	1.81	5.1	5.3	3.2
4a	6.3×10^4	1.70	5.1	5.2	3.2

(a) Measured at λ_{max}. (b) Based on absorption onsets. (c) Photoelectron spectroscopy in air (PESA) measurements. (d) Cyclic voltammetry (CV) measurements, vs. (Fc/Fc$^+$).
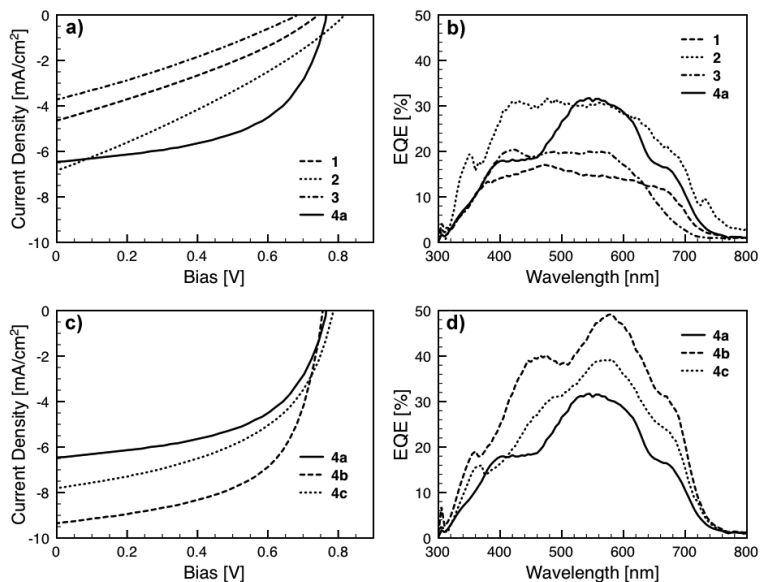
Figure 4-6. Characteristic *J-V* curves of solar cells fabricated from (a) **1**-**4a**, and (c) **4a**-**4c**, illuminated under AM 1.5 G, 100 mW/cm². External quantum efficiency (EQE) spectra of devices based on (b) **1**-**4a** and (d) **4a**-**4c**.
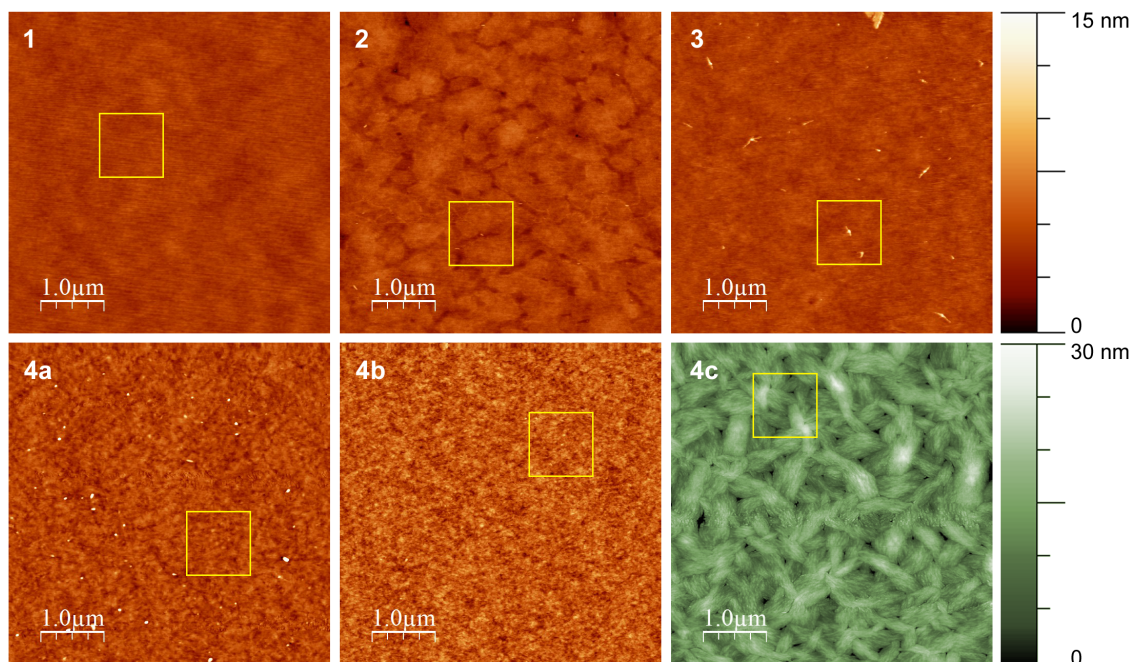
Figure 4-7a. Tapping-mode AFM height images of the active layers of devices made using **1**-**4c**. Yellow boxes indicate the magnified portions shown in **Fig. 4-7b**. Note the unique height scale of **4c**.
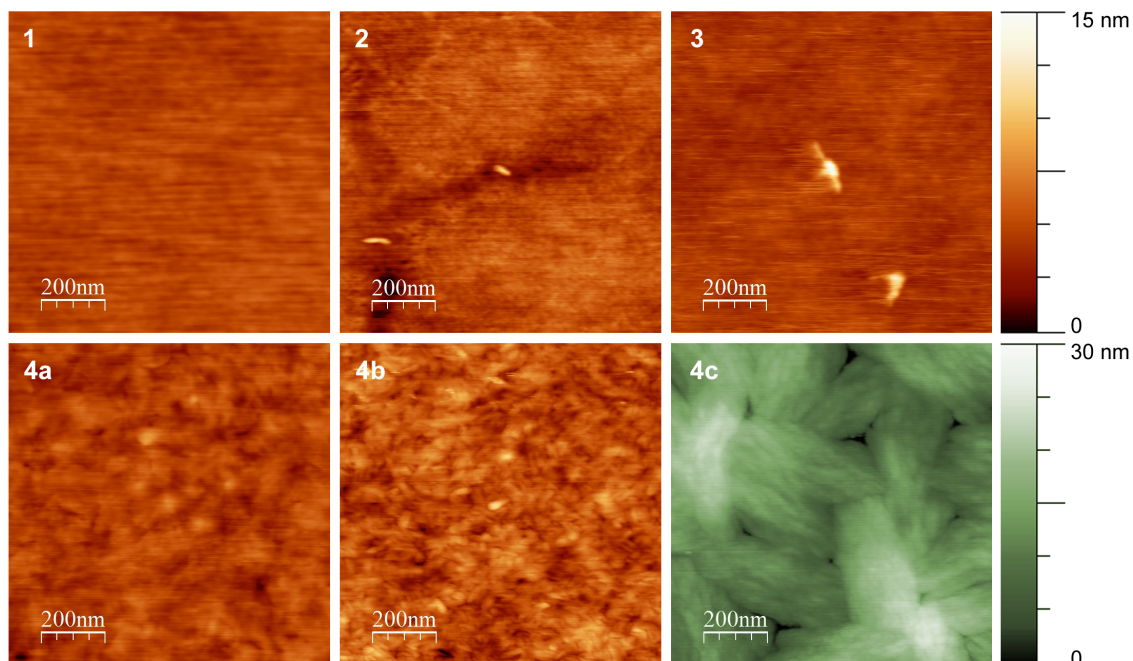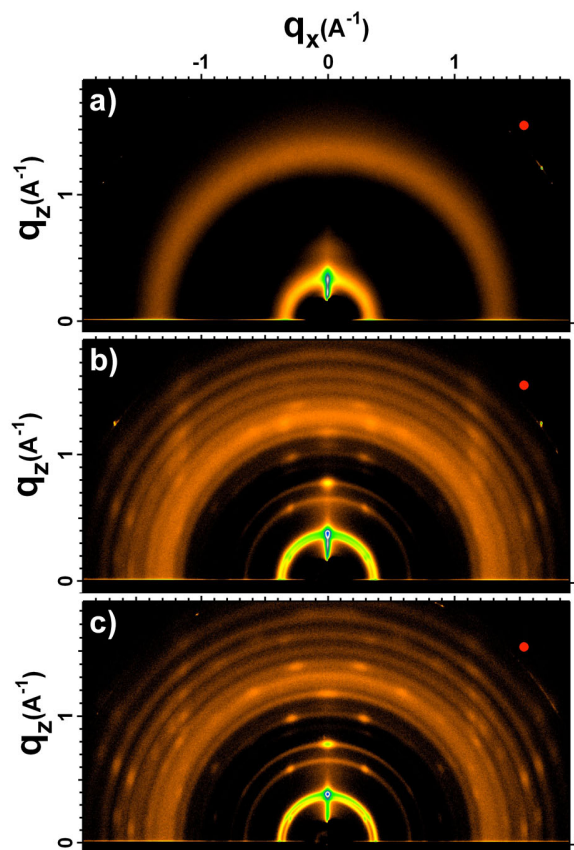
Figure 4-7b Magnified tapping-mode AFM height images, covering the corresponding regions outlined in yellow in **Fig. 4-7a**. Note the unique height scale of **4c**.
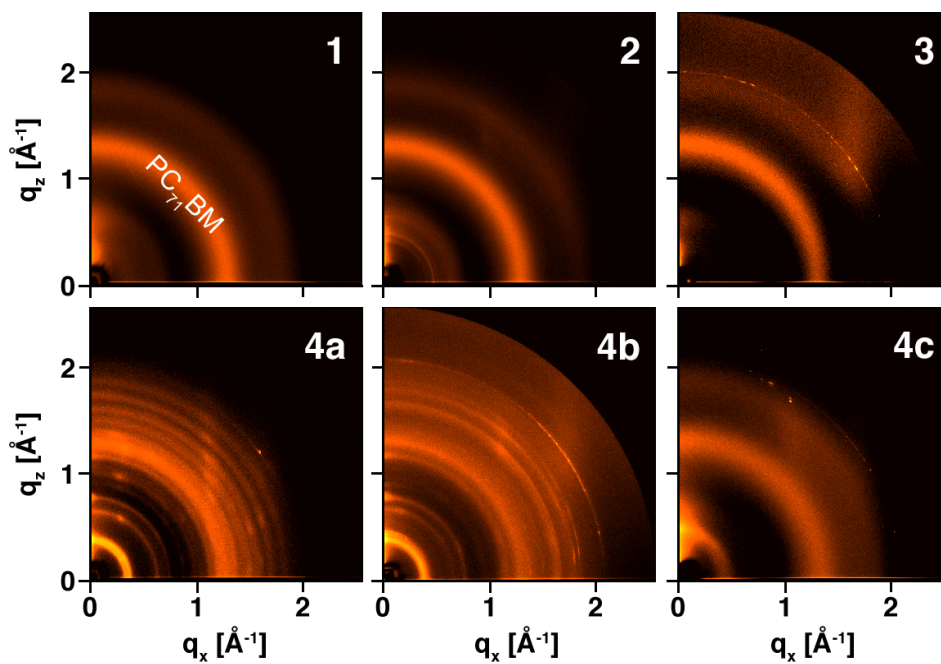
Figure 4-8. 2-D GIXS patterns of thin films of **1-4c** blended with $PC_{71}BM$, prepared under the same conditions as for optimized device fabrication.

Figure 4-9. 2-D GIXS patterns of thin films of **4a** blended with PC$_{71}$BM. Films were prepared under the same conditions as for optimized device fabrication, with the exception of annealing: a) as-cast, b) annealed 15 minutes at 130 ℃, and c) annealed 5 hours at 130 ℃.

4.5. References

(1)   Hains, A. W.; Liang, Z.; Woodhouse, M. A.; Gregg, B. A. *Chem. Rev.* **2010**, *110*, 6689.

(2)   Arias, A. C.; MacKenzie, J. D.; McCulloch, I.; Rivnay, J.; Salleo, A. *Chem. Rev.* **2010**, *110*, 3.

(3)   Thompson, B.C.; Fréchet, J. M. J. *Angew. Chem. Int. Ed.* **2008**, *47*, 58.

(4)   J. Roncali. *Acc. Chem. Res.* **2009**, *42*, 1719.

(5)   B. Walker; A. B. Tamayo; X.-D. Dang; P. Zalar; J. H. Seo; A. Garcia; M. Tantiwiwat.; T.-Q. Nguyen. *Adv. Funct. Mater.* **2009**, *19*, 3063.

(6)   H. Bürckstümmer; N. M. Kronenberg; M. Gsänger; M. Stolte; K. Meerholz. *J. Mater. Chem.* **2010**, *20*, 240.

(7)   B. Walker; C. Kim; T.-Q.Nguyen. *Chem. Mater.* **2011**, *23*, 470.

(8)   R. Y. C. Shin; P. Sonar; P. S. Siew; Z.-K. Chen; A. Sellinger. *J. Org. Chem.* **2009**, *74*, 3293.

(9)   L. C. Palilis; P. A. Lane; G. P. Kushto; B. Purushothaman; J. E. Anthony; Z. H. Kafafi. *Org. Electron.* **2008**, *9*, 747.

(10)   Y. Liang; L. Yu. *Acc. Chem. Res.* **2010**, *43*, 1227; b) Y. Liang; Z. Xu; J. Xia; S. Tsai; Y. Wu; G. Li; C. Ray; L. Yu. *Adv. Mater.* **2010**, *22*, E135.

(11)   R. J. Kline; M. D. McGehee; E. N. Kadnikova; J. Liu; J. M. J. Fréchet; M. F. Toney. *Macromolecules*, **2005**, *38*, 3312.

(12)   A. Zen; J. Pflaum; S. Hirschmann; W. Zhuang; F. Jaiser; U. Asawapirom; J. P. Rabe; U. Scherf; D. Neher. *Adv. Funct. Mater.* **2004**, *14*, 757.

(13)   M. Tong; S. Cho; J. T. Rogers; K. Schmidt; B. B. Y. Hsu; D. Moses; R. C. Coffin; E. J. Kramer; G. C. Bazan; A. J. Heeger. *Adv. Funct. Meter.* **2010**, *20*, 3959.

(14)   C. Müller; E. Wang; L. M. Andersson; K. Tvingstedt; Y. Zhou; M. R. Andersson; O. Inganäs. *Adv. Funt. Mater.* **2010**, *20*, 2124.

(15)   W. Tang; J. Hai; Y. Dai; Z. Huang; B. Lu; F. Yuan; J. Tang; F. Zhang. *Sol. Energ. Mat. Sol. C* **2010**, *94*, 1963.

(16)   A. B. Tamayo; M. Tantiwiwat; B. Walker, T.-Q. Nguyen. *J. Phys. Chem. C* **2008**, *112*, 15543.

(17)   S. Loser; C. J. Bruns; H. Miyauchi; R. P. Ortiz; A. Facchetti; S. I. Stupp; T. J. Marks. *J. Am. Chem. Soc.* **2011**, *133*, 8142.

(18)   J. C. Bijleveld; V. S. Gevaerts; D. D. Nuzzo; M. Turbiez; S. G. J. Mathijssen; D. M. de Leeuw; M. M. Wienk; R. A. J. Janssen. *Adv. Mater.* **2010**, *22*, E242.

(19)   E. Zhou; S. Yamakawa; K. Tajima; C. Yang; K. Hashimoto. *Chem. Mater.* **2009**, *21*, 4055.

(20)   A. B. Tamayo; X.-D. Dang; B. Walker; J. Seo; T. Kent; T.-Q. Nguyen. *Appl. Phys. Lett.* **2009**, *94*, 103301.

(21)   J. C. Bijleveld; A. P. Zoombelt; S. G. J. Mathijssen; M. M. Wienk; M. Turbiez; D. M. de Leeuw; R. A. J. Janssen. *J. Am. Chem. Soc.* **2009**, *131*, 16616.

(22)   M. M. Wink; M. Turbiez; J. Gilot; R. A. J. Janssen. *Adv. Mater.* **2008**, *20*, 2556.

(23)   H. Bronstein; Z. Chen; R. S. Ashraf; W. Zhang; J. Du; J. R. Durrant; P. S. Tuladhar; K. Song; S. E. Watkins; Y. Geerts; M. M. Wienk; R. A. J. Janssen; T. Anthopoulos; H. Sirringhaus; M. Heeney; I. McCulloch. *J. Am. Chem. Soc.* **2011**, *133*, 3272

(24)   Y. Li; P. Sonar; S. P. Singh; M. S. Soh; M. van Meurs; J. Tan. *J. Am. Chem. Soc.* **2011**, *133*, 2198

(25)   P. Sonar; S. Singh; Y. Li; M. Soh; A. Dodabalapur. *Adv. Mater.* **2010**, *22*, 5409

(26)   T. L. Nelson; T. M. Young; J. Liu; S. P. Mishra; J. A. Belot; C. L. Balliet; A. E. Javier; T. Kowalewski; R. D. McCullough. *Adv. Mater.* **2010**, *22*, 4617

(27)   L. Bürgi; M. Turbiez; R. Pfeiffer; F. Bienewald; H. J. Kirner; C. Winnewisser. *Adv. Mater.* **2008**, *20*, 2217

(28)   M. Tantiwiwat; A. B. Tamayo; N. Luu; X.-D. Dung; T.-Q. Nguyen. *J. Phys. Chem. C* **2008**, *112*, 17402.

(29)   C. J. H. Morton; R. L. Riggs; D. M. Smith; N. J. Westwood; P. Lightfoot; A. M. E. Slawin. *Tetrahedron* **2005**, *61*, 727.

(30)   I. Mkhalid; J. Barnard; T. Marder; J. Murphy; J. Hartwig. *Chem. Rev.* **2009**, *110*, 890.

(31)   D. N. Coventry; A. S. Batsanov; A. E. Goeta; J. A. K. Howard; T. B. Marder; R. N. Perutz. *Chem. Commun.* **2005**, 2172.

(32)   C. Piliego; T. W. Holcombe; J. D. Douglas; C. H. Woo; P. M. Beaujuge; J. M. J. Fréchet. *J. Am. Chem. Soc.* **2010**, *132*, 7595.

(33)   J. M. Szarko; J. Guo; Y. Liang; B. Lee; B. S. Rolczynski; J. Strzalka; T. Xu; S. Loser; T. J. Marks; L. Yu; L. X. Chen. *Adv. Mater.* **2010**, *22*, 5468.

(34)   W. W. H. Wong; T. B. Singh; D. Vak; W. Pisula; C. Yan; X. Feng; E. L. Williams; K. L. Chan; Q. Mao; D. J. Jones; C. Ma; K. Müllen; P. Bäuerle; A. B. Holmes. *Adv. Funct. Mater.* **2010**, *20*, 927.

(35)   H. Shang; H. Fan; Y. Liu; W. Hu; Y. Li; X. Zhan. *Adv. Mater.* **2011**, *23*, 1554.

(36)   J. Mei; K. R. Graham; R. Stalder; S. P. Tiwari; H. Cheun; J. Shim; M. Yoshio; C. Nuckolls; B. Kippelen; R. K. Castellano; J. R. Reynolds. *Chem. Mater.* **2011**, *23*, 2285.

(37)   M. Schubert; C. Yin; M. Castellani; S. Bange; T. L. Tam; A. Sellinger; H.-H. Hörhold; T. Kietzke; D. Neher. *J. Chem. Phys.* **2009**, *130*, 094703.

(38)   M. Kim; B. Kim; J. Kim. *ACS Appl. Mater. Interfaces* **2009**, *1*, 1264.

(39)   H. Kagayama; H. Ohishi; M. Tanaka; Y. Ohmori; Y. Shirota. *Adv. Funct. Mater.* **2009**, *19*, 3948.

(40)   J. Wagner; M. Gruber; A. Hinderhofer; A. Wilke; B. Bröker; J. Frisch; P. Amsalem; A. Vollmer; A. Opitz; N. Koch; F. Schreiber; W. Brütting. *Adv. Funct. Mater.* **2010**, *20*, 4295

Chapter 5

Non-Fullerene Materials for Small-Molecule, Solution-Processed Organic Photovoltaics that Generate Charge Carriers through Hole Transfer

Abstract

Solution-processed organic photovoltaic (OPV) devices containing p-type and non-fullerene n-type small molecules obtain power conversion efficiencies (PCEs) as high as 2.4%. This is the highest PCEs report in the literature for a solution-processed all–small-molecule non-fullerene OPV device. Additionally, we report the unique optoelectronic properties of n-type material BT(TTI-n12)$_2$ that allow our devices to display high open-circuit voltages (>0.85 V) and generate charge carriers through hole transfer. By comparison, most fullerene-based devices reported in the literature only generate charge carriers through the electron transfer pathway.

5.1. Introduction

Organic photovoltaics (OPVs) continue to attract considerable attention for their potential to be flexible, lightweight, and inexpensive devices for power generation.[1–3] Recent synthetic work has primarily focused on the development of p-type polymers for bulk heterojunction (BHJ) devices with fullerene-based phenyl-C_{61}-butyric acid methyl ester ($PC_{61}BM$) and $PC_{71}BM$ as n-type materials. Although polymer:PCBM solar cells have achieved power conversion efficiencies (PCEs) beyond 8%,[4–7] the reproducibility of these OPVs is limited by batch-to-batch variations in the device components.[8,9] Semiconducting polymers are polydisperse, and fullerene derivatives are costly to synthesize and difficult to purify.[10,11] An attractive alternative to polymer:PCBM systems is one comprised entirely of small molecules, none of which are fullerene-based.

Despite their high cost of production, fullerene derivatives have become the canonical n-type material in OPVs due to their unmatched chemical properties that promote efficient exciton dissociation[12,13] and electron transport.[14] The high electron affinities of fullerene derivatives, however, are difficult to tune and often lead to devices with low open-circuit voltages (V_{oc}).[11,15] In addition, fullerene derivatives such as $PC_{61}BM$ are plagued with low extinction coefficients in the visible spectrum[10,16] and a tendency to form large crystallites upon annealing in BHJ blends.[17,18] These characteristics suppress charge generation from the fullerene material because poor light absorption limits exciton generation, and large n-type domains restrict exciton diffusion to an interface and subsequent hole transfer.[19] New n-type materials have the potential to enhance device V_{oc} and photocurrent generation because they can be engineered to exhibit higher LUMO energy levels, stronger absorptions in the visible spectrum, and smaller solid-state domains than fullerene derivatives.

Solution-processable, non-fullerene n-type materials have been investigated as both small molecules and polymers.[20–29] The highest-performing fullerene alternative, reported by Blocking *et al.*, is a small molecule which has obtained an average PCE of 2.3% in blends with poly(3-hexylthiophene) (P3HT).[26] This OPV device has a V_{oc} roughly 0.4 V higher than standard P3HT:$PC_{61}BM$ devices because the new n-type material has a lower electron affinity than PCBM. Non-fullerene materials with higher LUMO energies that can maintain efficient electron transfer are advantageous because they provide favorable energy level alignment between the p- and n-type materials, resulting in devices with maximized voltages.

In order to further enhance material purity and the reproducibility of OPV active layers, p-type small molecules have been developed as an alternative to polymers. Small molecules are attractive polymer substitutes because they are intrinsically monodisperse, due to their well-defined chemical structure, and can be definitively purified and characterized.[30–32] Recently, PCEs over 5% have been obtained with solution-processed small molecule:PCBM BHJ devices.[33–39] Much like their polymer counterparts, these high-performing small molecules have been rationally designed to have favorable π-π interactions that enhance molecular interconnectivity. In particular, our group previously developed a diketopyrrolopyrrole-based small molecule (DPP-Py) that self-assembles through planar pyrene end-groups to form highly ordered domains that favor efficient charge transport.[40]

We propose that batch-to-batch variations with polymer synthesis and PCBM purification can be avoided by fabricating small-molecule, non-fullerene devices. By developing both p- and n-type materials with synthetically tunable electronic properties, we can create active layers of monodisperse materials with high purity, complementary absorptions, and optimally aligned energy levels. These features are beneficial for devices since 1) pure materials improve OPV fabrication reproducibility, 2) extended absorption profiles improve exciton generation, and 3) proper energy level alignment enhances device V_{oc} while maintaining efficient exciton dissociation. Active layer materials that have been engineered with the aforementioned properties would provide reproducible solar cells that have two photoactive and charge generating components.

Herein, we demonstrate that solution-processed BHJ solar cells, with efficiencies as high as 2.4%, can be obtained in small-molecule, non-fullerene blends. Compared to PCBM, our n-type materials exhibit improved extinction coefficients and decreased electron affinities, thereby promoting photon absorption and achieving open-circuit voltages above 0.85 V in devices. External quantum efficiency (EQE) analysis shows that photoexcitation of our n-type materials, followed by hole transfer, significantly contributes to charge generation. With an open circuit voltage above 1 V and a fill factor of 0.60, our best DPP-Py:non-fullerene solution-processed OPV represents the highest performing non-fullerene, small-molecule device in the literature.[28]

The n-type small molecules presented in this report contain a symmetric donor (D) - acceptor (A) motif of A-D-A-D-A, with solubilizing chains extending from the terminal acceptors (Scheme 1). To ensure that the new molecules have a high electron affinity, electron-deficient π-conjugated subunits, benzothiadiazole (BT) and isothianaphthene-nitrile (ITNCN), were chosen for the structural cores. BT is a well-known acceptor monomer that has been incorporated into a variety of high performing p- and n-type materials,[26,41–47] and ITNCN is a promising core that we recently used to synthesize a n-type polymer.[48] As a flanking donor unit, thiophene (T) was appended to the core subunits to extend conjugation and increase the absorption breadth of the small molecules. Phthalimide (PI) and thienoimide (TI) were chosen as the terminal acceptor units for their electron-withdrawing imide functionality and solubilizing aliphatic side chains. In particular, TI was an attractive moiety because of its isomeric relationship to the thienopyrroledione (TPD) building block, which is used in several high-performing OPV polymers.[5,49–51] Since the extent of side-chain branching has been shown to affect OPV device performance,[49,52–54] linear *n*-dodecyl (*n*12) and 2-ethylhexyl (EH) alkyl groups were appended to the small molecules to provide a range of material processability.

5.2. Results and Discussion

Small-molecules BT(TPI)$_2$, ITNCN(TPI)$_2$, and BT(TTI)$_2$ were synthesized through a convergent route that culminated in a Suzuki cross-coupling between the core (BT or ITNCN) and the end-group coupling partners (TPI or TTI) (**Scheme 5-1**). Since the PI and TI moieties have side chains that impart solubility to their intermediates, we determined that appending the thiophene linker to the end-group units, rather than the cores, would ease the overall synthesis. The PI-containing coupling partner was synthesized with a bromide (**4**) and a boronate ester (**5**) to allow for cross-coupling with

BT (**6**) and ITNCN (**7**), thereby providing BT(TPI)₂ and ITNCN(TPI)₂, respectively. The TI-based coupling partner was synthesized with a bromide (**14**) and coupled with BT (**6**) to furnish BT(TTI)₂.
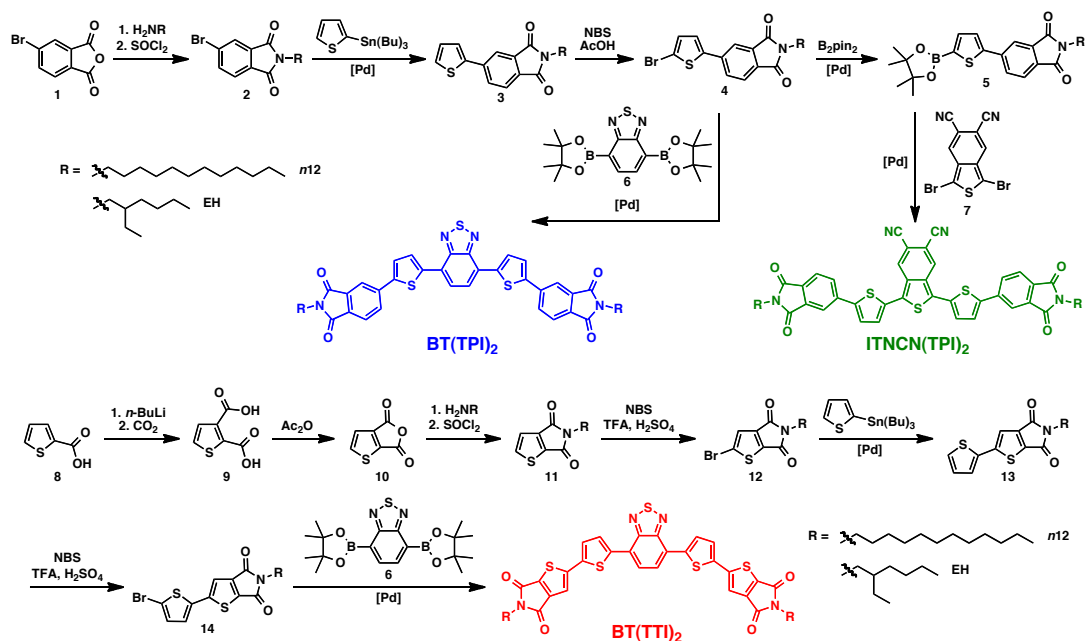

Scheme 5-1. Synthetic routes toward phthalimide-functionalized small-molecules BT(TPI)₂ and ITNCN(TPI)₂ (top), and thienoimide-functionalized small-molecule BT(TTI)₂.

In order to analyze the conformation of our molecules, we performed density functional theory (DFT) calculations with a hybrid B3LYP correlation functional and a 6-31G(d) basis set. Our calculations show that the BT core is nearly coplanar with its flanking thiophene units, while the ITNCN core is twisted 30.3° (**Figs. 5-5 and 5-6**). The six-membered phthalimide ring was also found to lie out of plane with adjacent thiophene linkers, which leads to BT(TPI)₂ and ITNCN(TPI)₂ veering from coplanarity by 22.2° and 24.0°, respectively. Although small-molecule BT(TTI)₂ was postulated to be the most planar molecule in the series, it also experienced a dihedral twist of 12.0° between its thienoimide end group and thiophene linker units.

The thin-film (**Fig. 5-1**) and solution (**Fig. 5-7**) absorption spectra of the six n-type materials show that quinoidal character and backbone coplanarity affect the optical properties of the n-type molecules. With an alternating phenyl-thiophenyl backbone structure, the BT(TPI)₂ molecules have the most blue-shifted onsets of absorption (*n*12 at 615 nm and EH at 620 nm) and the largest band gaps (2.02 eV for *n*12 and 2.00 eV for EH) in the series. Replacement of PI for TI yields BT(TTI)₂ molecules with an increased degree of coplanarity and slightly lower optical band gaps (1.89 eV for *n*12 and 1.92 eV for EH). Since the BT(TPI)₂ and BT(TTI)₂ molecules have the same electronic core, this shift in absorption is likely the result of increased intermolecular interaction between the relatively planar BT(TTI)₂ molecules. The ITNCN(TPI)₂ small molecules have the most red-shifted onsets of absorption (710 nm for *n*12 and EH) in the series because the isothianaphthene portion of the molecules imparts a significant degree of quinoidal character to the compounds, thereby decreasing the band gaps (1.75 eV for *n*12 and

EH).[55] Toward broadening the active layer absorption profile, the BT(TPI)$_2$ and BT(TTI)$_2$ small molecules have complementary absorption spectra with p-type material DPP-Py (onset at 710 nm, 1.75 eV band gap). The narrow band gap of DPP-Py gives our small-molecule devices an increased absorption breadth relative to P3HT:non-fullerene devices. In addition, these non-fullerene devices are anticipated to absorb more light than PCBM-based solar cells because all six of the new small molecules exhibit higher extinction coefficients than PC$_{71}$BM (measured $\alpha = 3.26 \times 10^4$ cm^{-1} at λ_{max}, **Table 5-1**).
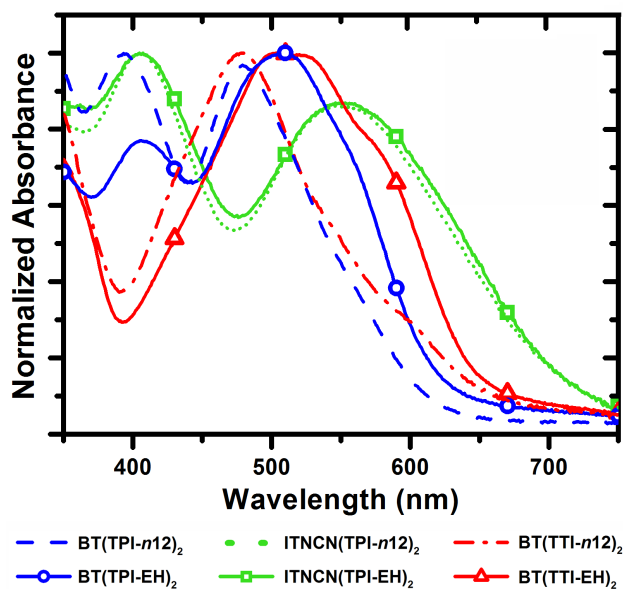
Figure 5-1. Thin-film absorption spectra of the six synthesized n-type molecules.

The electrochemical properties of the six small molecules were measured by cyclic voltammetry (CV). The relative HOMO and LUMO energy levels of the materials were strongly influenced by the central acceptor subunits, where ITNCN-containing materials had narrower band gaps than their BT-based counterparts. The competing aromatic and quinoidal resonance forms of isothianaphthene cause ITN-based materials to have a destabilized HOMO and a stabilized LUMO relative to molecules with less quinoidal character.[56,57] For the same molecular backbone, changing the side-chain branching does not significantly affect the material energy levels. In addition, when comparing BT(TPI)$_2$ and BT(TTI)$_2$, the end-groups have minimal influence on the HOMO and LUMO energy levels (variations within 0.1 eV).

The OPV performance of the non-fullerene materials was evaluated in all-small-molecule BHJ devices with the following architecture: ITO/PEDOT:PSS/DPP-Py:non-fullerene n-type/Ca/Al (**Fig. 5-2**). It was found that annealing at 130 °C improved the performance of all the devices, while solvent additives were not necessary to achieve optimal performance. Under AM 1.5 G illumination at 100 mW cm^{-2}, devices fabricated with BT(TPI-n12)$_2$ and BT(TPI-EH)$_2$ obtained V_{oc} values above 1 V but were plagued with low short-circuit current densities (J_{sc}) and subsequently low PCEs (0.8% and 0.2%, respectively). The relatively low extinction coefficients and narrow absorption ranges of the BT(TPI)$_2$ molecules likely restricted the J_{sc} of these devices. In contrast, the ITNCN(TPI)$_2$ molecules had higher extinction coefficients and broader absorption

profiles, which gave ITNCN(TPI)$_2$ devices greater J_{sc} and PCE values. With the highest extinction coefficients and device currents, BT(TTI-n12)$_2$ and BT(TTI-EH)$_2$-based solar cells obtained average efficiencies of 2.3% and 1.6%, respectively. To the best of our knowledge, with a maximum PCE of 2.4%, the solution-processed OPVs based on BT(TTI-n12)$_2$ are the highest performing small molecule, non-fullerene devices.
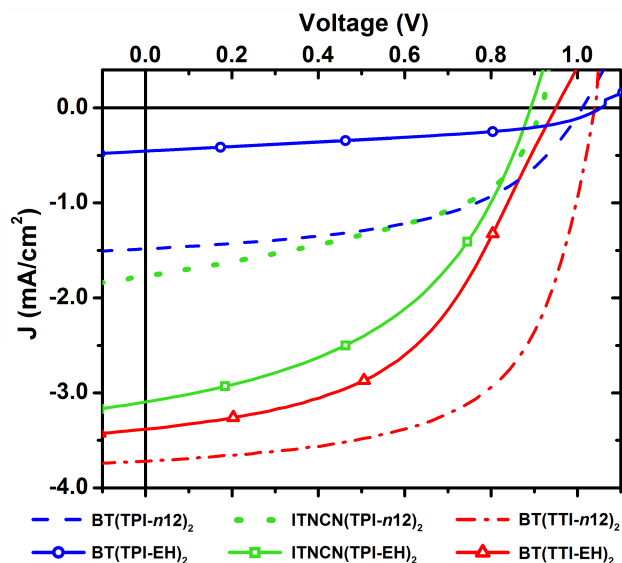

Figure 5-2. Representative *J-V* plots for DPP-Py:acceptor BHJ devices.

Table 5-1. Small molecule optoelectronic and device properties

Non-fullerene Small Molecule	Electronic Properties				Device Properties			
	HOMO[a] [eV]	LUMO[a] [eV]	E_g[b] [eV]	α[c] [x 10^4 cm^{-1}]	V_{oc} [V]	J_{sc} [mA cm^{-2}]	FF	PCE [%]
BT(TPI-n12)$_2$[d]	5.93	3.47	2.02	5.81	1.01	-1.44	0.54	0.78 (0.85)
BT(TPI-EH)$_2$[e]	5.86	3.55	2.00	8.68	1.07	-0.46	0.41	0.20 (0.23)
ITNCN(TPI-n12)$_2$[f]	5.81	3.96	1.75	8.45	0.92	-1.77	0.47	0.77 (0.82)
ITNCN(TPI-EH)$_2$[g]	5.85	3.89	1.75	10.1	0.89	-3.13	0.46	1.29 (1.44)
BT(TTI-n12)$_2$[h]	5.99	3.53	1.89	18.5	1.05	-3.72	0.60	2.34 (2.40)
BT(TTI-EH)$_2$[i]	5.96	3.61	1.92	11.0	0.95	-3.37	0.49	1.57 (1.71)

Average device PCEs are reported with maximum values in parentheses. (a) CV-determined HOMO and LUMO values are reported relative to Fc/Fc$^+$ at -5.13 eV. (b) Optical band gaps in thin films are calculated based on the onset of absorption. (c) Thin-film extinction coefficients were measured at λ_{max}. PC$_{71}$BM was measured to have and extinction coefficient of 3.26 x 10^4 cm^{-1}. (d) DPP-Py:BT(TPI-n12)$_2$ blend ratio of 1:2 in chloroform and annealed at 130 °C for 10 min. (e) DPP-Py:BT(TPI-EH)$_2$ blend ratio of 1:2 in chloroform and annealed at 130 °C for 10 min. (f) DPP-Py:ITNCN(TPI-n12)$_2$ blend ratio of 1:1 in chloroform and annealed at 130 °C for 5 min. (g) DPP-Py:ITNCN(TPI-EH)$_2$ blend ratio of 1:1 in chloroform and annealed at 130 °C for 5 min. (h) DPP-Py:BT(TTI-n12)$_2$ blend ratio of 1:2 in chloroform and annealed at 130 °C for 15 min. (i) DPP-Py:BT(TTI-EH)$_2$ blend ratio of 1:2 in chloroform and annealed at 130 °C for 15 min.

Grazing-incidence X-ray diffraction (GIXD) and atomic force microscopy (AFM) were used to study the device active layer nanostructure and morphology, which could be correlated to overall OPV performance. The nearly planar small molecule BT(TTI-n12)$_2$ is the most crystalline material in neat and blended GIXD films (**Figs. 5-9** and **5-10**),

contributing to the high J_{sc} of DPP-Py:BT(TTI-n12)$_2$ devices (3.72 mA/cm^2). The GIXD data also show that side chains affect intermolecular packing, where EH-substituted materials appear to have less order than their n12-substituted counterparts. AFM height images of the active layer surfaces show that the high-performing BT(TTI)$_2$ molecules have the finest intermixing and the lowest RMS roughness (**Fig. 5-11**). Both BT(TTI-n12)$_2$ and BT(TTI-EH)$_2$ blends display favorable film morphologies that likely contribute to the molecules' demonstration of high fill factors, short-circuit current density and overall performance in OPV devices. While a nanoscale film morphology is critical for harvesting excitons, other parameters such as energy-level alignment between the p- and n-type materials can strongly influence how charge carriers are separated at the interface.

Energy conversion by an OPV device begins with photon absorption by an active layer component, and subsequent exciton formation via excitation of an electron from the material's HOMO to its LUMO. As an exciton diffuses to a p-n interface, charge carriers can be generated through two mechanisms. In most OPV solar cells, the p-type material is the major light absorber, and excitons formed on the p-type material dissociate into free charges via electron transfer from the LUMO$_{p-type}$ to the LUMO$_{n-type}$.[58] In contrast, when a n-type material absorbs light, free charges are formed upon hole transfer from the photogenerated vacancy on the HOMO$_{n-type}$ to the HOMO$_{p-type}$.[59,60]

In a device where p- and n-type materials exhibit complementary absorptions, such as with n-type BT-containing molecules and p-type DPP-Py, external quantum efficiency (EQE) analysis can help identify which active layer component most efficiently generates excitons. In the case of BT(TPI)$_2$ devices, poor device currents correspond with low EQE spectra, which are difficult to analyze because quantum efficiencies below 15% are observed (**5-12**). With higher device J_{sc} values, the BT(TTI)$_2$ blends have EQEs of 15-25% in the 400-600 nm spectral region, which matches the absorption of the BT(TTI)$_2$ acceptors (**Fig. 5-3**). This overlap between EQE and absorption spectra indicates that there is a strong contribution from the n-type materials to the overall device photocurrent in DPP-Py:BT(TTI)$_2$ blends, and that charge generation is more efficient from excitation of the n-type, rather than the p-type material.
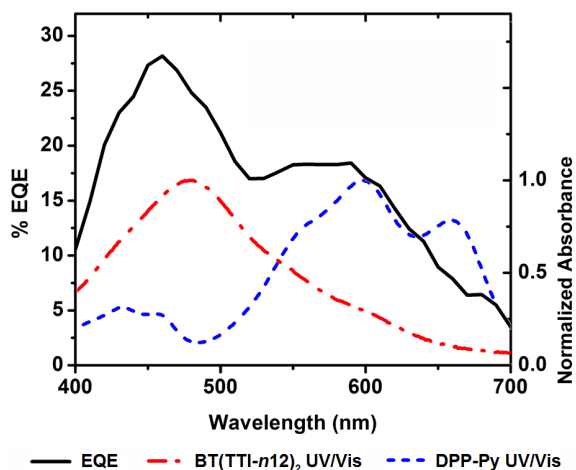
Figure 5-3. The EQE spectrum of DPP-Py:BT(TTI-n12)$_2$ overlaid with the absorption spectra of the individual device components in thin films.

With both charge generation mechanisms, a greater $LUMO_{p-type}$-$LUMO_{n-type}$ or $HOMO_{p-type}$-$HOMO_{n-type}$ energy offset provides a stronger driving force for exciton dissociation.[61] Blends of DPP-Py and BT(TTI-n12)$_2$ have a small LUMO-LUMO offset (singlet excited state of -3.59 eV and LUMO of -3.53 eV, respectively) while the difference in HOMO levels is much larger (-5.34 eV and -5.99 eV, respectively). In this system, there is a lack of energetic driving force for electron transfer upon excitation of the p-type material (**Fig. 5-4a**), while there is sufficient potential for hole transfer after n-type photoexcitation (**Fig. 5-4b**). The process of generating free charges in DPP-Py:BT(TTI)$_2$-based devices appears to rely on the driving force for hole transfer from $HOMO_{n-type}$ to $HOMO_{p-type}$. In addition, the higher extinction coefficient of BT(TTI-n12)$_2$ versus DPP-Py (α =1.9 x 10^5 cm^{-1} vs. 6.3 x 10^4 cm^{-1}) further enhances charge generation via formation of excitons within the n-type material. Lastly, the fine blend morphology in BT(TTI)$_2$ devices facilitates effective exciton diffusion to a p-n interface and subsequent hole transfer. Although photoexcitation of the n-type material is rarely invoked as a mechanism for generating free charges,[62,63] our devices demonstrate that it can be a significant pathway for charge current generation in non-fullerene OPV devices.
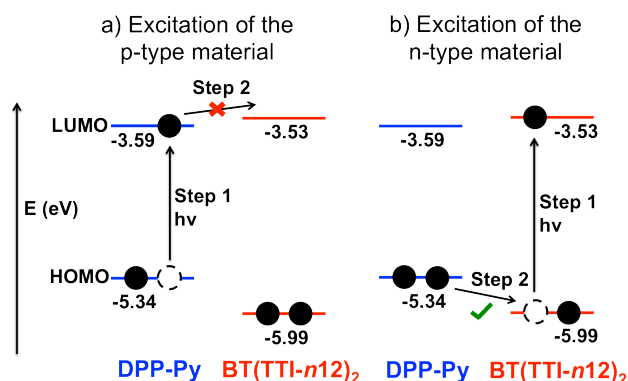
Figure 5-4. Charge generation in DPP-Py:BT(TTI-n12)$_2$ blends a) is not efficient from excitation of p-type DPP-Py, but b) is effective from excitation of n-type BT(TTI-n12)$_2$.

5.3. Conclusion

In conclusion, we report the synthesis and OPV performance of six non-fullerene n-type materials in small-molecule devices. We correlate the molecular planarity and quinoidal character of our molecules with data from DFT calculations, UV-vis spectroscopy, CV, GIXD, AFM and observed OPV device parameters. As the most planar and crystalline n-type molecule in the series, BT(TTI-n12)$_2$ exhibits a V_{oc} above 1 V, a FF of 0.60, and a device efficiency as high as 2.4% in BHJ blends with DPP-Py. We demonstrate that devices fabricated with this molecule generate charge carriers through excitation of the n-type material and subsequent hole transfer to the p-type material. Charge generation upon light absorption by the n-type material is promoted in these OPVs because the active layer components have a large HOMO-HOMO energy level offset and a nanoscale morphology. This record-performance for non-fullerene devices shows that light absorbing fullerene-substitutes are viable components for OPVs.

5.4. Experimental Details

5.4.1. Material Synthesis and Characterization

Materials and Methods. All commercially available reagents obtained from suppliers were used without further purification. P-type material DPP-Py was synthesized according to the procedure reported in *Adv. Mater.* **2011**, *23*, 5359-5363, and building block ITNCN-Br$_2$ was synthesized according to the procedure in *Macromolecules*, **2012**, *45*, 4069-4074. Unless otherwise noted, all reactions were carried out under nitrogen with standard Schlenk techniques, and all glassware used in dry reactions was flame dried under high-vacuum prior to use. Tetrahydrofuran (THF), dimethylformamide (DMF) and toluene were purified and dried by passing through two columns of neutral alumina, under nitrogen, prior to use. Water was degassed by free-pump-thaw, and degassed, dry dioxane was used from a Sure-seal bottle. Flash chromatography was performed using Silicycle SiliaFlash ® P60 (particle size 40-63 μm, 230-400 mesh) silica gel.

All ^{1}H and ^{13}C NMR spectra were obtained with a Bruker AVQ-400, AVB-400, AV-500 or AV-600 instrument, and ^{13}C spectra were collected with a proton-decoupling pulse program. NMR abbreviations: at = apparent triplet, bs = broad singlet, d = doublet, m = multiplet, s = singlet, and t = triplet. Elemental analysis (CHN) was performed by the UC Berkeley microanalysis laboratory. Data from high-resolution mass spectrometry (HRMS) using electron impact (EI) were obtained by the UC Berkeley mass spectrometry facility. Matrix-assisted laser desorption/ionization-time of flight mass spectrometry (MALDI-TOF MS) was performed on a PerSeptive Biosystems Voyager-DE using 2,2':5',2"-terthiophene as the matrix. Samples were prepared by diluting the monomers in chloroform with the matrix.

GC-MS data was collected on an Agilent 7890A GC system fitted with an Agilent HP-5 chromatography column. Helium carrier gas at a flow rate of 2.2 mL/min was used as the mobile phase. The sample inlet was 250 °C and a pressure of 8.8 PSI was used to load the vaporized compounds onto the column at a split ratio of 50:1. The oven temperature was equilibrated at 50 °C for 30 seconds, and then a temperature program was run as follows: 50 °C for 1 minute, ramp to 310 °C at 20 °C/min, hold at 310 °C for 5 minutes. The total run time is 19 minutes. An auxiliary heater is kept at 150 °C between the GC column and the Agilent 5975C VL MSD system (electron impact (EI)) in order to keep the separated compounds from precipitating from the He carrier gas at the MSD system inlet. MS information was collected by the 5975C system and analyzed with the Agilent Chemstation software.

Density functional theory (DFT) calculations for each n-type molecule was carried out with Gaussian 09 using a hybrid B3LYP correlation functional and the 6-31G(d) basis set.

UV-vis absorption spectra of neat films, thin-film blends, and solutions were gathered at room temperature using a Varian Cary 50 Conc spectrophotometer. Neat thin-films were spuncoat from CHCl$_3$ onto untreated quartz slides. Thin films of the p-type/n-type material blends were spuncoat from solutions comprised of the optimal ratios for each DPP-Py:small molecule acceptor BHJ solar cell. Absorption spectra in solution were measured using a quartz cuvette with a 1-cm path length.

Cyclic voltammograms were collected using a Solartron 1285 potentiostat under the control of CorrWare II software. A standard three electrode cell based on a Pt wire working electrode, a silver wire reference electrode (calibrated vs. Fc/Fc⁺ at -5.13 eV), and a Pt wire counter electrode was purged with nitrogen and maintained under a nitrogen atmosphere during all measurements. Anhydrous acetonitrile was purchased from Aldrich, and tetrabutylammonium hexafluorophosphate (0.1 M) was used as the supporting electrolyte. Polymer films were drop cast onto a Pt wire working electrode from a 1% (w/w) chloroform solution and dried under nitrogen prior to measurement.

5.4.1.1. Synthesis of Precursors

1   **EH-2**
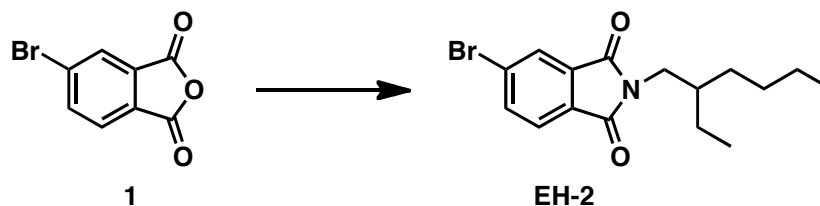
    5-Bromo-2-(2-ethylhexyl)isoindoline-1,3-dione   **(EH-2).**   5-Bromophthalic anhydride (**1**) (4.00 g, 17.6 mmol) and 2-ethylhexylamine (2.32 g, 18.0 mmol) were combined with THF (40 mL) in a 100 mL flask and heated to 60 °C for 2 h. After cooling the reaction mixture to room temperature, thionyl chloride (9 mL) was added, and the reaction contents were stirred at 60 °C for another 2 h. The reaction mixture was quenched with water, and THF was removed under reduced pressure. The resulting residue was extracted with diethyl ether, washed with brine, dried over MgSO₄ and filtered. Volatiles were removed under reduced pressure. The crude product was dissolved into CHCl₃, poured onto a silica pad and eluted with CHCl₃. The volatiles from the filtrate were removed under reduced pressure to yield 4.31 g of white solid (72 %). ¹H NMR (400 MHz, CDCl₃, δ): 7.94 (s, 1 H), 7.82 (d, $J = 7.90$ Hz, 1 H), 7.68 (d, $J = 7.90$ Hz, 1 H), 3.55 (d, $J = 7.30$ Hz, 2 H), 1.84-1.75 (m, 1 H), 1.35-1.19 (m, 8 H), 0.88 (t, $J = 7.42$ Hz, 3 H), 0.86 (t, $J = 6.39$ Hz, 3 H). ¹³C (100 MHz, CDCl₃, δ): 168.0, 167.4, 136.9, 133.8, 130.7, 128.8, 126.7, 124.6, 42.2, 38.3, 30.6, 28.6, 23.9, 23.1, 14.2, 10.5. GC-MS (m/z): [M]⁺ calculated for $C_{16}H_{20}BrNO_2$, 337.1; found, 337.1.

   **EH-2**   **EH-3**
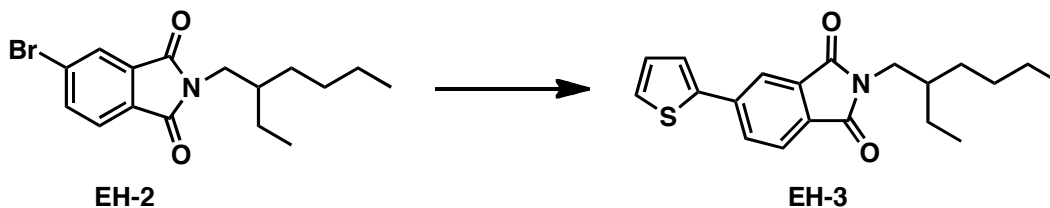
    2-(2-Ethylhexyl)-5-(thiophen-2-yl)isoindoline-1,3-dione   **(EH-3).** Compound **EH-2** (4.00 g, 11.8 mmol) and 2-(tributylstannyl)thiophene (6.18 g, 16.6 mmol) were combined with tris(dibenzylideneacetone)dipalladium(0) (Pd₂dba₃) (217 mg, 237 μmol) and tri(o-tolyl)phosphine (P(o-tol)₃) (288 mg, 946 μmol) in a 100 mL flask. The reaction

vessel was purged with three vacuum/nitrogen cycles before toluene (39.2 mL) and DMF (7.8 mL) were added to the reaction flask. After stirring at 90 °C for 16 h, the reaction mixture was quenched with water, and the reaction contents were extracted with diethyl ether, washed with brine, dried over $MgSO_4$ and filtered. Volatiles were removed under reduced pressure. The crude material was purified by flash chromatography (1:1 $CHCl_3$:hexanes) to yield 4.20 g of a yellow oil (100%). ^{1}H NMR (400 MHz, $CDCl_3$, δ): 8.01 (s, 1 H), 7.87 (d, J = 7.82 Hz, 1 H), 7.78 (d, J = 7.81 Hz, 1 H), 7.45 (d, J = 3.55 Hz, 1 H), 7.39 (d, J = 5.03 Hz, 1 H), 7.11 (at, J = 4.32 Hz, 1 H), 3.56 (d, J = 7.25 Hz, 2 H), 1.87-1.76 (m, 1 H), 1.40-1.19 (m, 8 H), 0.91 (t, J = 7.32 Hz, 3 H), 0.87 (t, J = 6.45 Hz, 3 H). ^{13}C (100 MHz, $CDCl_3$, δ): 168.5, 168.4, 142.1, 140.2, 133.2, 130.6, 130.2, 128.7, 127.3, 125.4, 123.9, 120.1, 42.0, 38.3, 30.6, 28.6, 23.9, 23.1, 14.2, 10.5. GC-MS (m/z): $[M]^+$ calculated for $C_{20}H_{23}NO_2S$, 341.1; found, 341.1.

EH-3 → **EH-4**
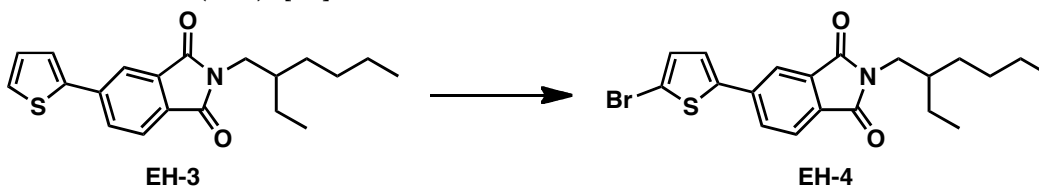
5-(5-Bromothiophen-2-yl)-2-(2-ethylhexyl)isoindoline-1,3-dione (EH-4). Compound **EH-3** (4.20 g, 11.8 mmol) was dissolved in $CHCl_3$ (40 mL) and acetic acid (20 mL) in a 250 mL flask and chilled to 0 °C. *N*-Bromosuccinimide (NBS) (2.21 g, 12.4 mmol) was added to the reaction mixture in one portion, and the reaction mixture was stirred for 16 h at room temperature. The reaction contents were quenched with water, extracted with $CHCl_3$, washed with brine, dried over $MgSO_4$ and filtered. Volatiles were removed under reduced pressure to yield 4.59 g of light yellow solid (92 %). The crude product was used without any further purification. ^{1}H NMR (400 MHz, $CDCl_3$, δ): 7.95 (s, 1 H), 7.84-7.76 (m, 2 H), 7.22 (d, J = 3.82 Hz, 1 H), 7.10 (d, J = 3.83 Hz, 1 H), 3.58 (d, J = 7.27 Hz, 2 H), 1.89-1.79 (m, 1 H), 1.40-1.21 (m, 8 H), 0.91 (t, J = 7.16 Hz, 3 H), 0.88 (t, J = 6.12 Hz, 3 H). ^{13}C (100 MHz, $CDCl_3$, δ): 168.41, 168.35, 143.5, 139.4, 133.4, 131.6, 130.6, 130.4, 125.7, 124.1, 119.8, 114.4, 42.2, 38.4, 30.6, 28.6, 23.9, 23.1, 14.2, 10.5. GC-MS (m/z): $[M]^+$ calculated for $C_{20}H_{22}BrNO_2S$, 419.1; found, 419.1.


EH-4 → **EH-5**
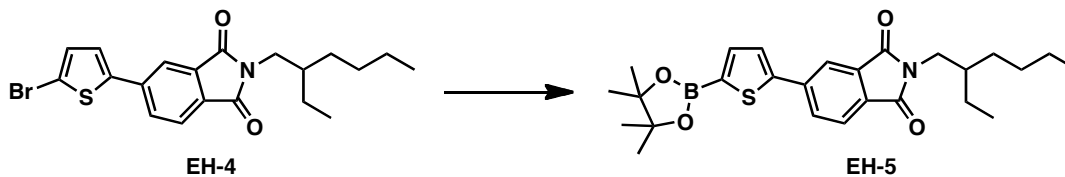
2-(2-Ethylhexyl)-5-(5-(4,4,5,5-tetramethyl-1,3,2-dioxaborolan-2-yl)thiophen-2-yl)isoindoline-1,3-dione (EH-5). Compound **EH-4** (700 mg, 1.67 mmol) and bis(pinacolato)diboron (B_2pin_2) (846 mg, 3.33 mmol) were combined with [1,1'-bis(diphenylphosphino)ferrocene] dichloropalladium(II), dichloromethane adduct (Pd(dppf)Cl_2-DCM) (40.8 mg, 50.0 μmol) and potassium acetate (KOAc) (490 mg, 5.00 mmol) in a 100 mL flame-dried flask. The reaction vessel was purged with three

vacuum/nitrogen cycles before dioxane (34 mL) was added to the reaction flask. After stirring at 80 °C for 24 h, the reaction mixture was quenched with water, and the reaction contents were extracted with CHCl$_3$, washed with brine, dried over MgSO$_4$ and filtered. Volatiles were removed under reduced pressure. The crude material was purified by flash chromatography (gradient of 1:1 DCM:hexanes to pure DCM) to yield 578 mg of green solid (74%). ^{1}H NMR (500 MHz, CDCl$_3$, δ): 8.05 (s, 1 H), 7.91 (d, J = 7.82 Hz, 1 H), 7.80 (d, J = 7.80 Hz, 1 H), 7.60 (d, J = 3.63 Hz, 1 H), 7.50 (d, J = 3.63 Hz, 1 H), 3.55 (d, J = 7.29 Hz, 2 H), 1.86-1.76 (m, 1 H), 1.34 (s, 12 H), 1.32-1.18 (m, 8 H), 0.89 (t, J = 7.52 Hz, 3 H), 0.85 (t, J = 6.97 Hz, 3 H). ^{13}C (150 MHz, CDCl$_3$, δ): 168.4, 168.3, 148.6, 140.1, 138.4, 133.3, 131.0, 130.6, 126.5, 123.9, 120.4, 84.5, 83.6, 42.1, 38.4, 30.6, 28.6, 25.1, 24.9, 23.9, 23.1, 14.1, 10.5. MALDI-TOF MS (m/z): [M]$^-$ calculated for C$_{26}$H$_{34}$BNO$_4$S, 467.2; found, 467.2.

1   *n*12-2
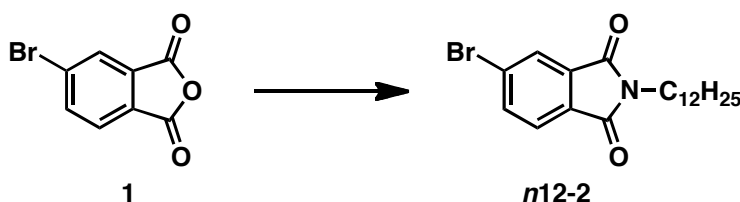
5-Bromo-2-dodecylisoindoline-1,3-dione (n12-2). 4-Bromophthalic anhydride (**1**) (4.00 g, 17.6 mmol) and dodecylamine (3.59 g, 19.4 mmol) were combined with THF (40 mL) in a 100 mL flask and heated to 50 °C for 16 h. After cooling the reaction mixture to room temperature, thionyl chloride (5 mL) was added, and the reaction contents were stirred at 60 °C for another 2 h. The reaction mixture was quenched with water, and THF was removed under reduced pressure. The resulting residue was extracted with CHCl$_3$, washed with brine, dried over MgSO$_4$ and filtered. Volatiles were removed under reduced pressure. The crude material was purified by flash chromatography (2:1 CHCl$_3$:hexanes) to yield 4.36 g of white solid (63 %). ^{1}H NMR (600 MHz, CDCl$_3$, δ): 7.96 (s, 1 H), 7.84 (d, J = 7.89 Hz, 1 H), 7.70 (d, J = 7.89 Hz, 1 H), 3.66 (t, J = 7.35 Hz, 2 H), 1.68-1.60 (m, 2 H), 1.35-1.18 (m, 18 H), 0.87 (t, J = 7.02 Hz, 3 H). ^{13}C (150 MHz, CDCl$_3$, δ): 167.8, 167.2, 137.0, 134.0, 130.9, 128.9, 126.7, 124.7, 38.5, 32.1, 29.8, 29.7, 29.6, 29.5, 29.3, 28.7, 27.0, 22.8, 14.3. GC-MS (m/z): [M]$^+$ calculated for C$_{20}$H$_{28}$BrNO$_2$, 393.1; found, 393.1.


*n*12-2   *n*12-3
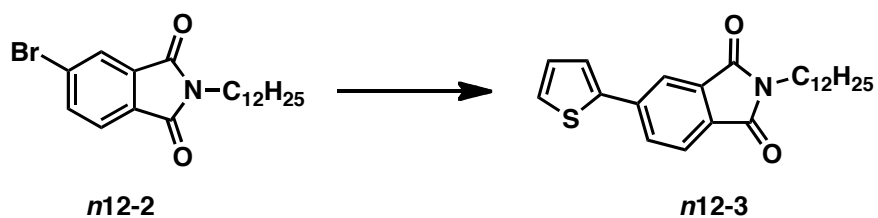
2-Dodecyl-5-(thiophen-2-yl)isoindoline-1,3-dione (n12-3). Compound *n*12-2 (4.00 g, 10.1 mmol) and 2-(tributylstannyl)thiophene (5.68 g, 15.2 mmol) were combined with Pd$_2$dba$_3$ (186 mg, 203 μmol) and P(o-tol)$_3$ (247 mg, 811 μmol) in a 100 mL flask. The reaction vessel was purged with three vacuum/nitrogen cycles before toluene (33.6 mL) and DMF (6.7 mL) were added to the reaction flask. After stirring at 90 °C for 16 h, the reaction mixture was quenched with water, and the reaction contents were extracted with

diethyl ether, washed with brine, dried over $MgSO_4$ and filtered. Volatiles were removed under reduced pressure. The crude material was purified by flash chromatography (3:1 $CHCl_3$:hexanes) to yield 4.57 g of white solid (98%). ^1H NMR (400 MHz, $CDCl_3$, δ): 8.05 (s, 1 H), 7.90 (d, J = 7.81 Hz, 1 H), 7.81 (d, J = 7.81 Hz, 1 H), 7.48 (d, J = 3.39 Hz, 1 H), 7.41 (d, J = 4.97 Hz, 1 H), 7.14 (at, J = 4.32 Hz, 1 H), 3.68 (t, J = 7.30 Hz, 2 H), 1.73-1.63 (m, 2 H), 1.38-1.18 (m, 18 H), 0.87 (t, J = 6.69 Hz, 3 H). ^{13}C (100 MHz, $CDCl_3$, δ):168.4, 168.3, 142.2, 140.3, 133.4, 130.6, 130.3, 128.7, 127.3, 125.5, 124.0, 120.2, 38.3, 32.0, 29.8, 29.7, 29.6, 29.5, 29.3, 28.8, 27.0, 22.8, 14.3. MALDI-TOF MS (m/z): [M]$^-$ calculated for $C_{24}H_{31}NO_2S$, 397.6; found, 397.2.
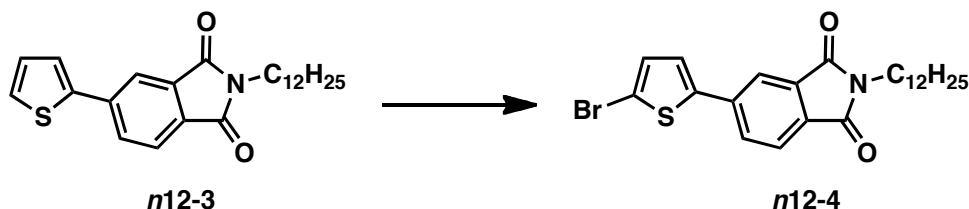
5-(5-Bromothiophen-2-yl)-2-dodecylisoindoline-1,3-dione **(n12-4).**
Compound *n12-3* (4.40 g, 11.1 mmol) was dissolved in $CHCl_3$ (40 mL) and acetic acid (20 mL) in a 100 mL flask and chilled to 0 °C. NBS (2.17 g, 12.2 mmol) was added to the reaction mixture in one portion, and the reaction mixture was stirred for 16 h at room temperature. The reaction contents were quenched with water, extracted with $CHCl_3$, washed with brine, dried over $MgSO_4$ and filtered. Volatiles were removed under reduced pressure to yield 5.21 g of light beige solid (99 %). The crude product was used without any further purification. ^1H NMR (600 MHz, $CDCl_3$, δ): 7.95 (s, 1 H), 7.83-7.77 (m, 2 H), 7.22 (d, J = 3.65 Hz, 1 H), 7.10 (d, J = 3.65 Hz, 1 H), 3.67 (t, J = 7.29 Hz, 2 H), 1.70-1.63 (m, 2 H), 1.36-1.18 (m, 18 H), 0.87 (t, J = 6.91 Hz, 3 H). ^{13}C (150 MHz, $CDCl_3$, δ): 168.13, 168.05, 143.5, 139.4, 133.5, 131.6, 130.7, 130.3, 125.7, 124.1, 119.8, 114.5, 38.4, 32.1, 29.8, 29.7, 29.6, 29.5, 29.3, 28.7, 27.0, 22.8, 14.3. MALDI-TOF MS (m/z): [M]$^-$ calculated for $C_{24}H_{30}BrNO_2S$, 475.1; found, 474.8.
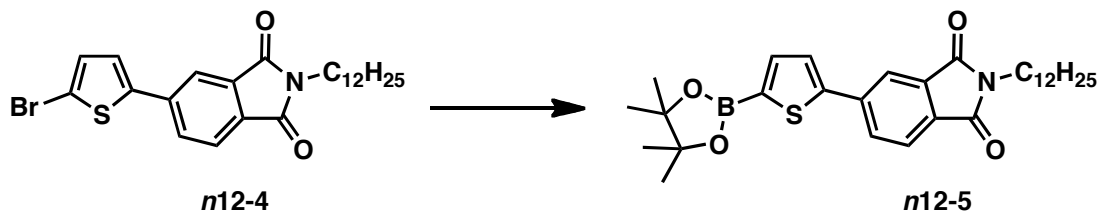

2-Dodecyl-5-(5-(4,4,5,5-tetramethyl-1,3,2-dioxaborolan-2-yl)thiophen-2-yl)isoindoline-1,3-dione (n12-5). Compound *n12-4* (600 mg, 1.26 mmol) and B_2pin_2 (640 mg, 2.52 mmol) were combined with Pd(dppf)Cl_2-DCM (30.9 mg, 37.8 μmol) and KOAc (371 mg, 3.78 mmol) in a 100 mL flame-dried flask. The reaction vessel was purged with three vacuum/nitrogen cycles before dioxane (25 mL) was added to the reaction flask. After stirring at 80 °C for 24 h, the reaction mixture was quenched with water, and the reaction contents were extracted with $CHCl_3$, washed with brine, dried over $MgSO_4$ and filtered. Volatiles were removed under reduced pressure. The crude material was

purified by flash chromatography (gradient of 1:1 DCM:hexanes to pure DCM) to yield 494 mg of green solid (75%). ^{1}H NMR (500 MHz, CDCl$_3$, δ): 8.08 (s, 1 H), 7.93 (d, J = 7.80 Hz, 1 H), 7.82 (d, J = 7.81 Hz, 1 H), 7.63 (d, J = 3.64 Hz, 1 H), 7.53 (d, J = 3.65 Hz, 1 H), 3.67 (t, J = 7.34 Hz, 2 H), 1.70-1.63 (m, 2H), 1.36 (s, 12 H), 1.34-1.19 (m, 18 H), 0.86 (t, J = 6.94 Hz, 3 H). ^{13}C (150 MHz, CDCl$_3$, δ): 167.94, 167.88, 148.4, 139.9, 138.3, 133.2, 130.8, 130.5, 126.4, 123.8, 120.3, 84.3, 83.4, 38.1, 31.9, 29.6, 29.5, 29.4, 29.3, 29.1, 28.5, 26.8, 25.0, 24.7, 22.6, 14.1. MALDI-TOF MS (m/z): [M]$^-$ calculated for C$_{30}$H$_{42}$BNO$_4$S, 523.3; found, 522.8.
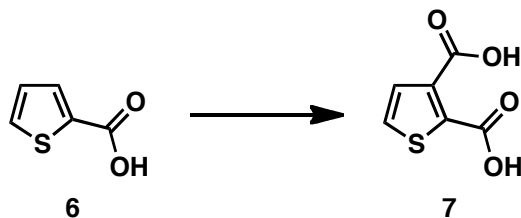

Thiophene-2,3-dicarboxylic acid (7). Thiophene-2-carboxylic acid (**6**) (6.00 g, 46.8 mmol) was added to a flame-dried 500 mL flask. The reaction vessel was purged with three vacuum/nitrogen cycles before THF (150 mL) was added, and the reaction contents were chilled to -78 °C. *N*-butyllithium (39.3 mL of a 2.5 M solution in hexanes, 6.31 mmol) was added to the reaction mixture over 30 min. After stirring for 1 h on the melting bath, 1 cup of crushed dry ice was added to the reaction mixture. The reaction contents were stirred for another 2 h at room temperature before water (50 mL) was added to the reaction mixture. After stirring at room temperature for 16 h, volatiles were removed from the reaction mixture under reduced pressure. Concentrated hydrochloric acid (18 mL) was added the reaction contents, and the resulting precipitates were filtered to yield 7.11 g of beige solid (88 %). The crude product was used without any further purification. ^{1}H NMR (400 MHz, DMSO-d_6, δ): 10.60-8.70 (bs, 2 H), 7.82 (d, J = 5.11 Hz, 1 H), 7.39 (d, J = 5.12 Hz, 1 H). ^{13}C (100 MHz, DMSO-d_6, δ): 165.5, 162.7, 137.4, 136.5, 131.2, 130.0.
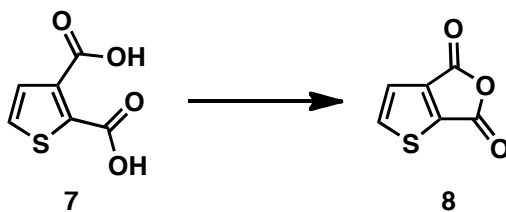

Thieno[2,3-c]furan-4,6-dione (8). Compound **7** (7.09 g, 41.2 mmol) was combined with acetic anhydride (40 mL) in a 100 mL flask and heated at 110 °C for 2 h. The reaction contents were cooled to room temperature, and volatiles were removed under reduced pressure to yield 6.46 g of beige crystals (100 %). The crude product was used without any further purification. ^{1}H NMR (600 MHz, Acetone-d_6, δ): 8.42 (d, J = 4.84 Hz, 1 H), 7.57 (d, J = 4.83 Hz, 1 H). ^{13}C (150 MHz, CDCl$_3$, δ): 158.8, 158.1, 146.7, 144.7, 142.6, 122.6. GC-MS (m/z): [M]$^+$ calculated for C$_6$H$_2$O$_3$S, 154.0; found, 154.0.
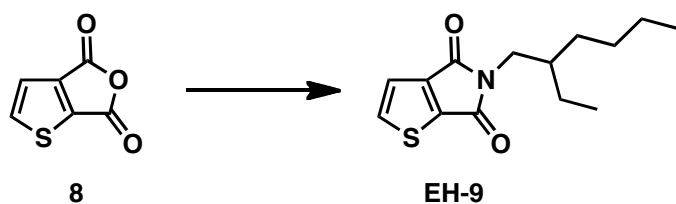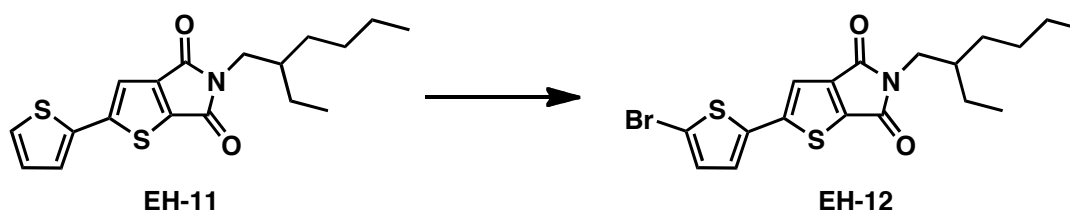
5-(2-Ethylhexyl)-4H-thieno[2,3-c]pyrrole-4,6(5H)-dione (EH-9). Compound **8** (3.44 g, 22.3 mmol) and 2-ethylhexylamine (3.17 g, 24.5 mmol) were combined with THF (45 mL) in a 100 mL flask and heated to 50 °C for 16 h. After cooling the reaction mixture to room temperature, thionyl chloride (8 mL) was added, and the reaction contents were stirred at 50 °C for another 2 h. The reaction mixture was quenched with water, and THF was removed under reduced pressure. The resulting residue was extracted with diethyl ether, washed with brine, dried over MgSO$_4$ and filtered. Volatiles were removed under reduced pressure. The crude material was purified by flash chromatography (3:1 CHCl$_3$:hexanes) to yield 5.05 g of a yellow oil (85 %). ^{1}H NMR (600 MHz, CHCl$_3$, δ): 7.74 (d, J = 4.69 Hz, 1 H), 7.29 (d, J = 4.68 Hz, 1 H), 3.48 (d, J = 7.26 Hz, 2 H), 1.81-1.74 (m, 1 H), 1.37-1.21 (m, 8 H), 0.89 (t, J = 7.39 Hz, 3 H), 0.87 (t, J = 6.65 Hz, 3 H). ^{13}C (150 MHz, CHCl$_3$, δ): 164.4, 163.1, 144.7, 140.9, 137.3, 121.2, 42.4, 38.5, 30.5, 28.6, 23.8, 23.1, 14.2, 10.5. GC-MS (*m/z*): [M]$^+$ calculated for C$_{14}$H$_{19}$NO$_2$S, 265.1 found, 265.1.
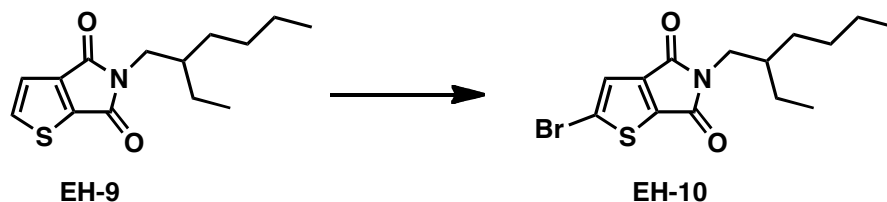

2-Bromo-5-(2-ethylhexyl)-4H-thieno[2,3-c]pyrrole-4,6(5H)-dione (EH-10). Compound **EH-9** (2.50 g, 9.42 mmol) was dissolved in trifluoroacetic acid (TFA) (38 mL) in a 100 mL flask and chilled to 0 °C. Sulfuric acid (4.5 mL) and NBS (1.76 g, 9.89 mmol) were added to the reaction mixture, and the reaction contents were stirred for 1 h at room temperature. The reaction mixture was quenched with water, extracted with DCM, washed with brine, dried over MgSO$_4$ and filtered. Volatiles were removed under reduced pressure. The crude material was purified by flash chromatography (1:1 CHCl$_3$:hexanes) to yield 2.68 g of light beige solid (83 %). ^{1}H NMR (600 MHz, CHCl$_3$, δ): 7.25 (s, 1 H), 3.42 (d, J = 7.25 Hz, 2 H), 1.74-1.66 (m, 1 H), 1.31-1.15 (m, 8 H), 0.84 (t, J = 7.44 Hz, 3 H), 0.82 (t, J = 6.96 Hz, 3 H). ^{13}C (150 MHz, CHCl$_3$ δ): 163.1, 162.1, 143.8, 140.4, 125.3, 123.8, 42.4, 38.3, 30.4, 28.4, 23.7, 23.0, 14.1, 10.4. GC-MS (*m/z*): [M]$^+$ calculated for C$_{14}$H$_{18}$BrNO$_2$S, 343.0; found, 343.0.

EH-10 → **EH-11**
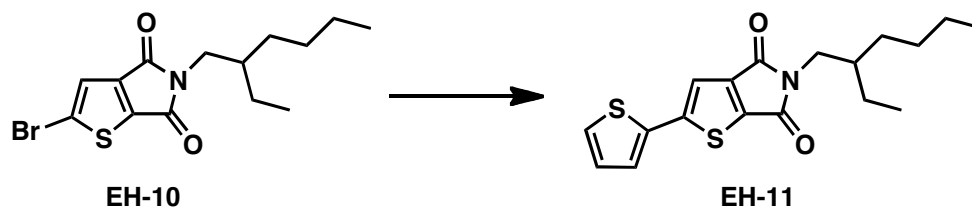
5-(2-Ethylhexyl)-2-(thiophen-2-yl)-4H-thieno[2,3-c]pyrrole-4,6(5H)-dione

(EH-11). Compound **EH-10** (1.60 g, 4.65 mmol) and 2-(tributylstannyl)thiophene (2.60 g, 6.97 mmol) were combined with Pd_2dba_3 (85.1 mg, 93.0 μmol) and P(o-tol)$_3$ (113 mg, 372 μmol) in a 50 mL flask. The reaction vessel was purged with three vacuum/nitrogen cycles before toluene (15.5 mL) and DMF (3.1 mL) were added to the reaction flask. After stirring at 90 °C for 16 h, the reaction mixture was quenched with water, and the reaction contents were extracted with DCM, washed with brine, dried over $MgSO_4$ and filtered. Volatiles were removed under reduced pressure. The crude material was purified by flash chromatography (1:1 CHCl$_3$:hexanes) to yield 1.29 g of yellow solid (80%). ^{1}H NMR (400 MHz, CDCl$_3$, δ): 7.38 (d, J = 5.00 Hz, 1 H), 7.33 (d, J = 5.16 Hz, 1 H), 7.32 (s, 1 H), 7.09 (at, J = 4.33 Hz, 1 H), 3.50 (d, J = 7.28 Hz, 2 H), 1.84-1.74 (m, 1 H), 1.40-1.20 (m, 8 H), 0.91 (t, J = 7.67 Hz, 3 H), 0.89 (t, J = 7.34 Hz, 3 H). ^{13}C (150 MHz, CDCl$_3$, δ): 164.4, 163.3, 150.3, 145.3, 137.6, 135.4, 128.5, 127.4, 126.2, 116.8, 42.6, 38.6, 30.6, 28.7, 24.0, 23.2, 14.2, 10.6. GC-MS (m/z): [M]$^+$ calculated for $C_{18}H_{21}NO_2S_2$, 347.1; found, 347.1.


EH-11 → **EH-12**

2-(5-Bromothiophen-2-yl)-5-(2-ethylhexyl)-4H-thieno[2,3-c]pyrrole-4,6(5H)-dione (EH-12).

Compound **EH-11** (800 mg, 2.30 mmol) was dissolved in CHCl$_3$ (4.5 mL) and TFA (4.5 mL) in a 25 mL flask and chilled to 0 °C. Sulfuric acid (0.9 mL) and NBS (430 mg, 2.42 mmol) were added to the reaction mixture, and the reaction contents were stirred for 16 h at room temperature. The reaction contents were quenched with water, extracted with DCM, washed with brine, dried over $MgSO_4$ and filtered. Volatiles were removed under reduced pressure. The crude material was purified by flash chromatography (1:2 CHCl$_3$:hexanes) to yield 750 mg of yellow solid (76%). ^{1}H NMR (400 MHz, CDCl$_3$, δ): 7.25 (s, 1 H), 7.07 (d, J = 3.86 Hz, 1 H), 7.04 (d, J = 3.88 Hz, 1 H), 3.49 (d, J = 7.26 Hz, 2 H), 1.84-1.74 (m, 1 H), 1.39-1.21 (m, 8 H), 0.90 (t, J = 7.56 Hz, 3 H), 0.89 (t, J = 7.23 Hz, 3 H). ^{13}C (100 MHz, CDCl$_3$, δ): 164.2, 163.1, 148.9, 145.2, 137.9, 136.7, 131.3, 126.3, 117.0, 114.5, 42.6, 38.6, 30.6, 28.6, 23.9, 23.2, 14.2, 10.6. GC-MS (m/z): [M]$^+$ calculated for $C_{18}H_{20}BrNO_2S_2$, 425.0; found, 425.0.

8   **n12-9**
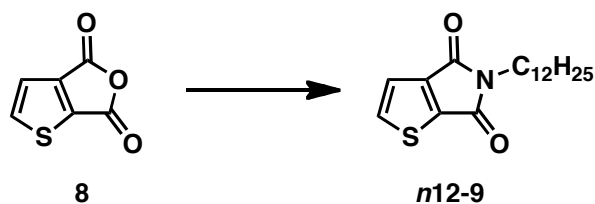
5-Dodecyl-4H-thieno[2,3-c]pyrrole-4,6(5H)-dione (n12-9). Compound **8** (1.50 g, 9.73 mmol) and dodecylamine (1.89 g, 10.2 mmol) were combined with THF (20 mL) in a 100 mL flask and heated to 60 °C for 16 h. After cooling the reaction mixture to room temperature, thionyl chloride (6 mL) was added, and the reaction contents were stirred at 50 °C for another 16 h. The reaction mixture was quenched with water, and THF was removed under reduced pressure. The resulting residue was extracted with diethyl ether, washed with brine, dried over $MgSO_4$ and filtered. Volatiles were removed under reduced pressure. The crude material was purified by flash chromatography (1:2 $CHCl_3$:hexanes) to yield 2.62 g of beige solid (84 %). ^{1}H NMR (400 MHz, $CDCl_3$, δ): 7.74 (d, J = 4.74 Hz, 1 H), 7.30 (d, J = 4.74 Hz, 1 H), 3.59 (t, J = 7.25 Hz, 2 H), 1.67-1.59 (m, 2 H), 1.36-1.20 (m, 18 H), 0.87 (t, J = 6.80 Hz, 3 H). ^{13}C (150 MHz, $CDCl_3$, δ): 164.0, 162.8, 144.8, 141.0, 137.3, 1321.1, 38.6, 32.0, 29.70, 29.68, 29.64, 29.58, 29.4, 28.9, 26.9, 22.8, 14.2. GC-MS (*m/z*): [M]$^+$ calculated for $C_{18}H_{27}NO_2S$, 321.2; found, 321.2.

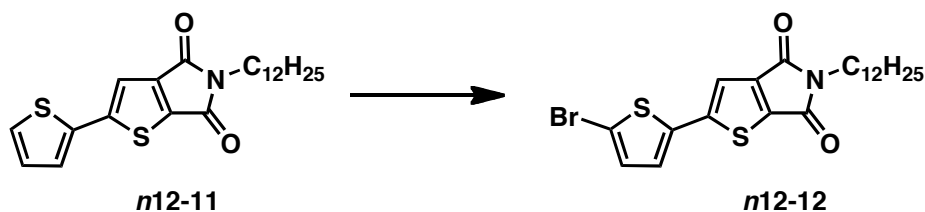**n12-9**   **n12-10**
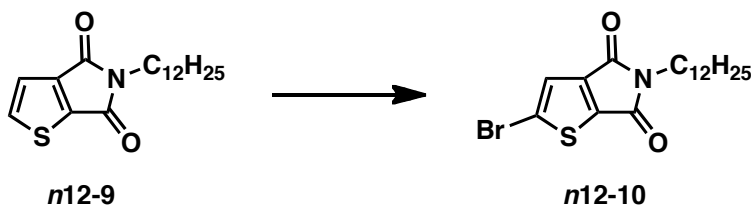
2-Bromo-5-dodecyl-4H-thieno[2,3-c]pyrrole-4,6(5H)-dione   **(n12-10).** Compound **n12-9** (2.40 g, 7.47 mmol) was dissolved in TFA (30 mL) in a 100 mL flask and chilled to 0 °C. Sulfuric acid (4 mL) and NBS (1.40 g, 7.84 mmol) were added to the reaction mixture, and the reaction contents were stirred for 1 h at room temperature. The reaction mixture was quenched with water, and the reaction contents were extracted with $CHCl_3$, washed with brine, dried over $MgSO_4$ and filtered. Volatiles were removed under reduced pressure. The crude material was purified by flash chromatography (1:2 $CHCl_3$:hexanes) to yield 2.58 g of white solid (86 %). ^{1}H NMR (400 MHz, $CDCl_3$, δ): 7.30 (s, 1 H), 3.57 (t, J = 7.30 Hz, 2 H), 1.66-1.56 (m, 2 H), 1.34-1.20 (m, 18 H), 0.87 (t, J = 6.58 Hz, 3 H). ^{13}C (100 MHz, $CDCl_3$, δ): 163.1, 162.1, 144.0, 140.6, 125.5, 123.9, 38.8, 32.1, 29.8, 29.7, 29.6, 29.5, 29.3, 28.9, 26.9, 22.8, 14.3. GC-MS (*m/z*): [M]$^+$ calculated for $C_{18}H_{26}BrNO_2S$, 399.1; found, 399.1.

n12-10 → **n12-11**
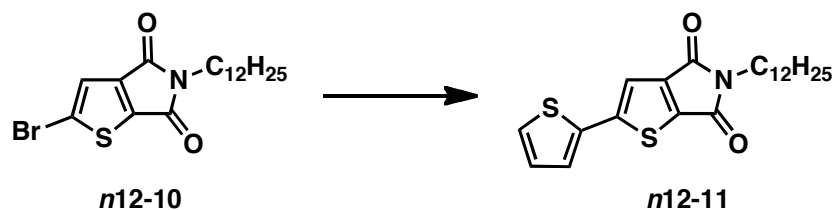
**5-Dodecyl-2-(thiophen-2-yl)-4H-thieno[2,3-c]pyrrole-4,6(5H)-dione (n12-11).** Compound ***n*12-10** (1.20 g, 3.00 mmol) and 2-(tributylstannyl)thiophene (1.34 g, 3.60 mmol) were combined with Pd_2dba_3 (55.0 mg, 60.0 μmol) and P(*o*-tol)$_3$ (73.0 mg, 240 μmol) in a 25 mL flask. The reaction vessel was purged with three vacuum/nitrogen cycles before toluene (10 mL) and DMF (2 mL) were added to the reaction flask. After stirring at 90 °C for 16 h, the reaction mixture was quenched with water, and the reaction contents were extracted with CHCl$_3$, washed with brine, dried over MgSO$_4$ and filtered. Volatiles were removed under reduced pressure. The crude material was purified by flash chromatography (1:1 CHCl$_3$:hexanes) to yield 1.16 g of yellow solid (96%). ^{1}H NMR (600 MHz, CDCl$_3$, δ): 7.38 (d, J = 5.03 Hz, 1 H), 7.32 (d, J = 3.59 Hz, 1 H), 7.31 (s, 1 H), 7.08 (at, J = 4.36 Hz, 1 H), 3.59 (d, J = 7.31 Hz, 2 H), 1.66-1.60 (m, 2 H), 1.33-1.21 (m, 18 H), 0.87 (t, J = 6.97 Hz, 3 H). ^{13}C (150 MHz, CDCl$_3$, δ): 164.1, 163.0, 150.3, 145.3, 137.6, 135.3, 128.5, 127.4, 126.2, 116.7, 38.7, 32.0, 29.8, 29.73, 29.69, 29.6, 29.5, 29.3, 26.9, 22.8, 14.2. MALDI-TOF MS (*m/z*): [M]$^-$ calculated for C$_{22}$H$_{29}$NO$_2$S$_2$, 403.2; found, 403.0.


n12-11 → **n12-12**

2-(5-Bromothiophen-2-yl)-5-dodecyl-4H-thieno[2,3-c]pyrrole-4,6(5H)-dione (n12-12). Compound ***n*12-11** (1.00 g, 2.48 mmol) was dissolved in CHCl$_3$ (5 mL) and TFA (5 mL) in a 25 mL flask and chilled to 0 °C. Sulfuric acid (1 mL) and NBS (463 mg, 2.60 mmol) were added to the reaction mixture, and the reaction contents were stirred for 16 h at room temperature. The reaction contents were quenched with water, extracted with CHCl$_3$, washed with brine, dried over MgSO$_4$ and filtered. Volatiles were removed under reduced pressure. The crude material was purified by flash chromatography (1:2 CHCl$_3$:hexanes) to yield 460 mg of yellow solid (34%). ^{1}H NMR (600 MHz, CDCl$_3$, δ): 7.24 (s, 1 H), 7.07 (d, J = 3.66 Hz, 1 H), 7.04 (d, J = 3.62 Hz, 1 H), 3.58 (d, J = 7.24 Hz, 2 H), 1.66-1.59 (m, 2 H), 1.34-1.20 (m, 18 H), 0.87 (t, J = 6.86 Hz, 3 H). ^{13}C (150 MHz, CDCl$_3$, δ): 164.0, 162.8, 148.9, 145.3, 137.9, 136.7, 131.3, 126.3, 116.9, 114.5, 38.8, 32.1, 29.8, 29.7, 29.6, 29.5, 29.3, 28.9, 26.9, 22.8, 14.3. MALDI-TOF MS (*m/z*): [M]$^-$ calculated for C$_{22}$H$_{28}$BrNO$_2$S$_2$, 481.1; found, 480.8.

### 5.4.1.1. Synthesis of Small Molecule N-Type Materials
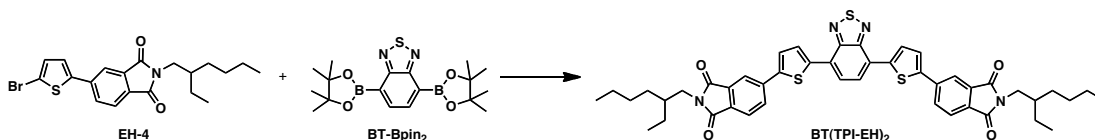
5,5'-(5,5'-(Benzo[c][1,2,5]thiadiazole-4,7-diyl)bis(thiophene-5,2-diyl))bis(2-(2-ethylhexyl)isoindoline-1,3-dione) (BT(TPI-EH)2). Compound **EH-4** (596 mg, 1.42 mmol) and 4,7-bis(4,4,5,5-tetramethyl-1,3,2-dioxaborolan-2-yl)benzo[c][1,2,5]thiadiazole (BT-Bpin$_2$) (250 mg, 644 mmol) were combined with Pd$_2$dba$_3$ (17.7 mg, 19.3 μmol), P(o-tol)$_3$ (23.5 mg, 77.3 μmol), potassium carbonate (K$_2$CO$_3$) (712 mg, 5.15 mmol) and Aliquat 336 (1 drop) in a 50 mL Schlenk tube. The reaction vessel was purged with three vacuum/nitrogen cycles before toluene (12.9 mL) and water (2.6 mL) were added to the reaction flask. After stirring at 90 °C for 16 h, the reaction contents were cooled to room temperature, diluted with CHCl$_3$ (10 mL) and then precipitated into methanol (175 mL). The crude solid was purified by flash chromatography (CHCl$_3$) followed by precipitation into hexanes (100 mL) to yield 205 mg of reddish black solid (39%). ^{1}H NMR (500 MHz, CDCl$_3$, δ): 8.17 (d, J = 4.21 Hz, 2 H), 8.16 (s, 2 H), 8.02 (d, J = 7.82 Hz, 2 H), 7.98 (s, 2 H), 7.87 (d, J = 7.77 Hz, 2 H), 7.61 (d, J = 3.95 Hz, 2 H), 3.61 (d, J = 7.28 Hz, 4 H), 1.89-1.83 (m, 2 H), 1.41-1.25 (m, 16 H), 0.93 (t, J = 7.44 Hz, 6 H), 0.90 (t, J = 6.94 Hz, 6 H). EI-MS (m/z): [M]$^+$ calculated for C$_{46}$H$_{46}$N$_4$O$_4$S$_3$, 814.2681; found, 814.2687. Anal. calculated for C$_{46}$H$_{46}$N$_4$O$_4$S$_3$: C, 67.78; H, 5.69; N, 6.87; found: C, 67.72; H, 5.89; N, 6.63.
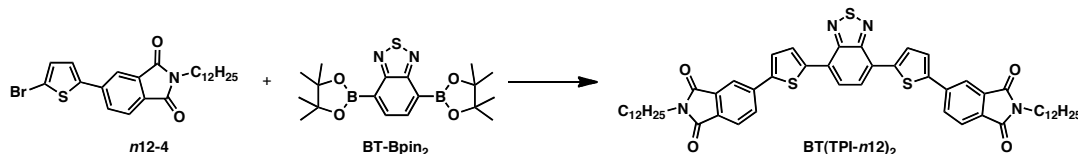
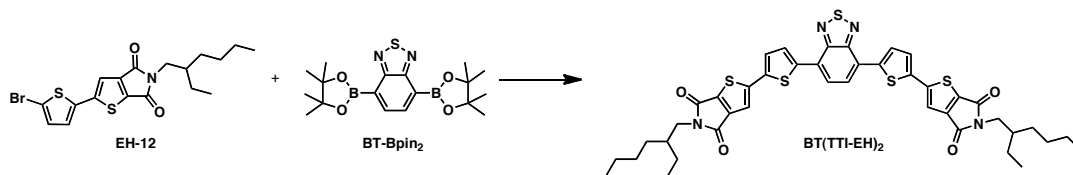**5,5'-(5,5'-(Benzo[c][1,2,5]thiadiazole-4,7-diyl)bis(thiophene-5,2-diyl))bis(2-dodecylisoindoline-1,3-dione) (BT(TPI-n12)2).** Compound **n12-4** (675 mg, 1.42 mmol) and BT-Bpin$_2$ (250 mg, 644 mmol) were combined with Pd$_2$dba$_3$ (17.7 mg, 19.3 μmol), P(o-tol)$_3$ (23.5 mg, 77.3 μmol), K$_2$CO$_3$ (712 mg, 5.15 mmol) and Aliquat 336 (1 drop) in a 50 mL Schlenk tube. The reaction vessel was purged with three vacuum/nitrogen cycles before toluene (12.9 mL) and water (2.6 mL) were added to the reaction flask. After stirring at 90 °C for 16 h, the reaction contents were cooled to room temperature, diluted with CHCl$_3$ (10 mL) and then precipitated into methanol (200 mL). The crude solid was purified by flash chromatography (CHCl$_3$) followed by precipitation into hexanes (150 mL) to yield 195 mg of black solid (33%). ^{1}H NMR (500 MHz, CDCl$_3$, δ): 8.17 (d, J = 4.00 Hz, 2 H), 8.16 (s, 2 H), 8.02 (d, J = 7.80 Hz, 2 H), 7.98 (s, 2 H), 7.87 (d, J = 7.84 Hz, 2 H), 7.61 (d, J = 3.96 Hz, 2 H), 3.70 (7, J = 7.36 Hz, 4 H), 1.73-1.65 (m, 4 H), 1.39-1.21 (m, 36 H), 0.88 (t, J = 6.95 Hz, 6 H). EI-MS (m/z): [M]$^+$ calculated for C$_{54}$H$_{62}$N$_4$O$_4$S$_3$, 926.3933; found, 926.3914. Anal. calculated for C$_{54}$H$_{62}$N$_4$O$_4$S$_3$: C, 69.94; H, 6.74; N, 6.04; found: C, 69.80; H, 6.80; N, 6.00.
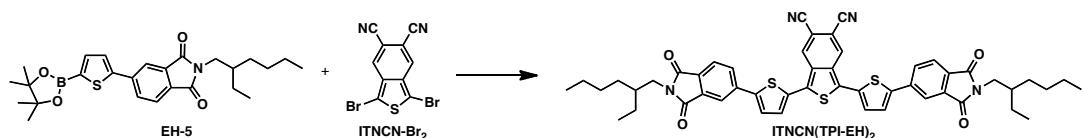
1,3-Bis(5-(2-(2-ethylhexyl)-1,3-dioxoisoindolin-5-yl)thiophen-2-yl)benzo[c]thiophene-5,6-dicarbonitrile (ITNCN(TPI-EH)2). Compound **EH-5** (222 mg, 475 μmol) and 1,3-dibromobenzo[c]thiophene-5,6-dicarbonitrile (ITNCN-Br$_2$) (73.8 mg, 216 mmol) were combined with Pd$_2$dba$_3$ (5.93 mg, 6 μmol), P(o-tol)$_3$ (7.88 mg, 26 μmol), K$_2$CO$_3$ (239 mg, 1.73 mmol) and Aliquat 336 (1 drop) in a 50 mL Schlenk tube. The reaction vessel was purged with three vacuum/nitrogen cycles before toluene (4.3 mL) and water (0.8 mL) were added to the reaction flask. After stirring at 90 °C for 16 h, the reaction contents were cooled to room temperature diluted with CHCl$_3$ (10 mL) and then precipitated into methanol (200 mL). The crude solid was purified by flash chromatography (CHCl$_3$) followed by precipitation into methanol (150 mL) to yield 90 mg of black solid (48%). ^{1}H NMR (600 MHz, CDCl$_3$, δ): 8.49 (s, 2 H), 8.11 (s, 2 H), 7.98 (d, J = 7.92 Hz, 2 H), 7.90 (d, J = 7.92 Hz, 2 H), 7.60 (d, J = 3.93 Hz, 2 H), 7.47 (d, J = 3.96 Hz, 2 H), 3.61 (d, J = 7.27 Hz, 4 H), 1.90-1.82 (m, 2 H), 1.41-1.22 (m, 16 H), 0.93 (t, J = 7.43 Hz, 6 H), 0.89 (t, J = 6.93 Hz, 6 H). EI-MS (m/z): [M]$^+$ calculated for C$_{50}$H$_{46}$N$_4$O$_4$S$_3$, 862.2681; found, 862.2664. Anal. calculated for C$_{50}$H$_{46}$N$_4$O$_4$S$_3$: C, 69.58; H, 5.37; N, 6.49; found: C, 69.27; H, 5.44; N, 6.49.
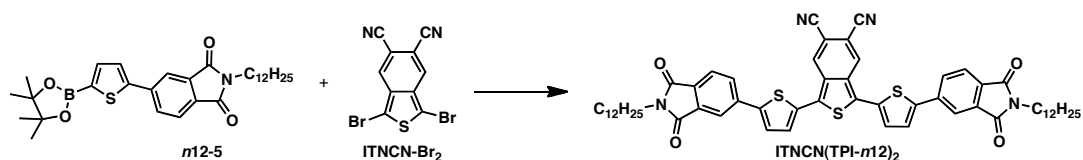
1,3-Bis(5-(2-dodecyl-1,3-dioxoisoindolin-5-yl)thiophen-2-yl)benzo[c]thiophene-5,6-dicarbonitrile (ITNCN(TPI-n12)2). Compound **n12-5** (523 mg, 999 μmol) and ITNCN-Br$_2$ (155 mg, 454 mmol) were combined with Pd$_2$dba$_3$ (12.5 mg, 13.6 μmol), P(o-tol)$_3$ (16.6 mg, 54.5 μmol), K$_2$CO$_3$ (415 mg, 3.00 mmol) and Aliquat 336 (1 drop) in a 50 mL Schlenk tube. The reaction vessel was purged with three vacuum/nitrogen cycles before toluene (14.1 mL) and water (1.5 mL) were added to the reaction flask. After stirring at 90 °C for 16 h, the reaction contents were cooled to room temperature, diluted with CHCl$_3$ (10 mL) and then precipitated into methanol (175 mL). The crude solid was purified by flash chromatography (CHCl$_3$) followed by recrystallization via solvent diffusion in CHCl$_3$ (100 mL) and hexanes (100 mL) to yield 45 mg of black solid (10%). ^{1}H NMR (500 MHz, CDCl$_3$, δ): 8.51 (s, 2 H), 8.13 (s, 2 H), 7.99 (d, J = 7.81 Hz, 2 H), 7.91 (d, J = 7.78 Hz, 2 H), 7.61 (d, J = 3.86 Hz, 2 H), 7.47 (d, J = 3.81 Hz, 2 H), 3.71 (t, J = 7.28 Hz, 4 H), 1.71-1.65 (m, 4 H), 1.67 (m, 4 H), 1.39-1.20 (m, 36 H), 0.87 (t, J = 6.89 Hz, 6 H). EI-MS (m/z): [M]$^+$ calculated for C$_{58}$H$_{62}$N$_4$O$_4$S$_3$, 974.3933; found, 974.3906. Anal. calculated for C$_{58}$H$_{62}$N$_4$O$_4$S$_3$: C, 71.42; H, 6.41; N, 5.74; found: C, 71.04; H, 6.33; N, 5.84.

2,2'-(5,5'-(Benzo[c][1,2,5]thiadiazole-4,7-diyl)bis(thiophene-5,2-diyl))bis(5-(2-ethylhexyl)-4H-thieno[2,3-c]pyrrole-4,6(5H)-dione) (BT(TTI-EH)2). Compound **EH-12** (363 mg, 850 μmol) and BT-Bpin$_2$ (150 mg, 386 mmol) were combined with tetrakis(triphenylphosphine)palladium(0) (Pd(PPh$_3$)$_4$) (22.3 mg, 19.3 μmol) and cesium fluoride (CsF) (126 mg, 850 μmol) in a 50 mL Schlenk tube. The reaction vessel was purged with three vacuum/nitrogen cycles before dioxane (7.5 mL) was added to the reaction flask. After stirring at 90 °C for 16 h, the reaction contents were cooled to room temperature, diluted with CHCl$_3$ (10 mL) and then precipitated into methanol (150 mL). The crude solid was purified by flash chromatography (gradient from 3:1 CHCl$_3$:hexanes to CHCl$_3$) followed by recrystallization via solvent diffusion in CHCl$_3$ (25 mL) and hexanes (100 mL) to yield 150 mg of black solid (47%). ^{1}H NMR (600 MHz, CDCl$_3$, δ): 8.09 (d, J = 3.93 Hz, 2 H), 7.94 (s, 2 H), 7.44 (s, 2 H), 7.44 (d, J = 4.65 Hz, 2 H), 3.52 (d, J = 7.25 Hz, 4 H), 1.84-1.77 (m, 2 H), 1.40-1.24 (m, 16 H), 0.92 (t, J = 7.59 Hz, 6 H), 0.90 (t, J = 7.04 Hz, 6 H). EI-MS (*m/z*): [M]$^+$ calculated for C$_{42}$H$_{42}$N$_4$O$_4$S$_5$, 826.1810; found, 826.1804. Anal. calculated for C$_{42}$H$_{42}$N$_4$O$_4$S$_5$: C, 60.99; H, 5.12; N, 6.77; found: C, 61.06; H, 5.26; N, 6.54.
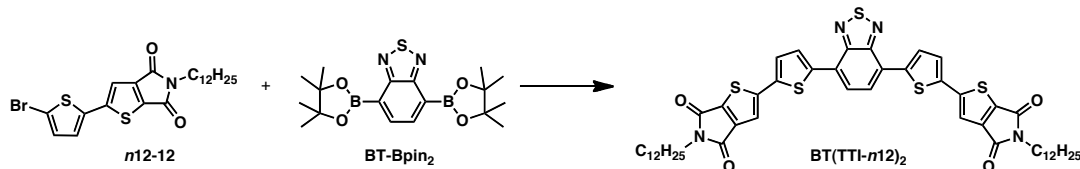
2,2'-(5,5'-(Benzo[c][1,2,5]thiadiazole-4,7-diyl)bis(thiophene-5,2-diyl))bis(5-dodecyl-4H-thieno[2,3-c]pyrrole-4,6(5H)-dione) (BT(TTI-n12)2). Compound ***n*12-12** (374 mg, 776 μmol) and BT-Bpin$_2$ (140 mg, 361 mmol) were combined with Pd(PPh$_3$)$_4$ (20.8 mg, 18.0 μmol) and CsF (121 mg, 794 μmol) in a 50 mL Schlenk tube. The reaction vessel was purged with three vacuum/nitrogen cycles before dioxane (12.2 mL) was added to the reaction flask. After stirring at 90 °C for 16 h, the reaction contents were cooled to room temperature, diluted with CHCl$_3$ (10 mL) and then precipitated into methanol (150 mL). The crude solid was purified by flash chromatography (gradient from 3:1 CHCl$_3$:hexanes to CHCl$_3$) followed by recrystallization via solvent diffusion in CHCl$_3$ (125 mL) and methanol (125 mL) to yield 191 mg of black solid (56%). ^{1}H NMR (400 MHz, CDCl$_3$, δ): 8.08 (d, J = 3.92 Hz, 2 H), 7.93 (s, 2 H), 7.43 (s, 2 H), 7.43 (d, J = 4.91 Hz, 2 H), 3.61 (t, J = 7.22 Hz, 4 H), 1.70-1.61 (m, 4 H), 1.38-1.21 (m, 36 H), 0.88 (t, J = 6.71 Hz, 6 H). EI-MS (*m/z*): [M]$^+$ calculated for C$_{50}$H$_{58}$N$_4$O$_4$S$_5$, 938.3062; found, 938.3038. Anal. calculated for C$_{50}$H$_{58}$N$_4$O$_4$S$_5$: C, 63.93; H, 6.22; N, 5.96; found: C, 63.69; H, 6.27; N, 5.94.

5.4.2. Device Fabrication and Characterization

Thin-film BHJ solar cells were fabricated using DPP-Py as the p-type material and BT(TPI)$_2$, ITNCN(TPI)$_2$, or BT(TTI)$_2$ (n12 or EH) as the n-type material. All devices were fabricated on indium tin oxide (ITO) coated glass substrates (pre-patterned, R = 20 Ω^{-1}, Thin Film Devices, Inc.). Prior to use, the ITO substrates were cleaned by sonication in a surfactant solution (Hellmanex III, 2% in deionized water), deionized water, acetone, and isopropyl alcohol for 20 minutes each. The substrates were rinsed with isopropyl alcohol, dried under a nitrogen stream, and then exposed to UV/O$_3$ for 5 minutes (UVOCS, Inc. ultraviolet-ozone cleaning system, model T10X10). A thin layer of PEDOT:PSS (Clevios PVP AI, 30–40 nm) was deposited by spincoating at 4000 RPM for 40 s, and then dried on a hotplate for 10 minutes at 140°C in air. The samples were transferred to a N$_2$ filled glovebox where the active layers were spuncoat at 2000 RPM for 40 s then 4000 RPM for 4 s. The thickness of the thin films was measured by profilometry (Veeco Dektat 150). Cathodes (20 nm Ca followed by 100 nm Al) were thermally evaporated under vacuum (~10^{-7} torr) through a shadow mask, resulting in an active area of ~0.03 cm^2. Some of the samples were then thermally annealed by placing them substrate-side down (active layer facing up) on a hot plate. Details of the optimized processing conditions for each molecule are shown in **Table 5-2**.

Table 5-2. Optimized processing conditions for each material.

Molecule	Donor Conc.	Acceptor Conc.	Bled Ratio	Spin Conditions	Average Film Thickness	Annealing Conditions
BT(TPI-n12)$_2$	15 mg/ml	15 mg/ml	1:2	2000RPM (40s); 4000RPM (4s)	132 nm	130°C 10 min
BT(TPI-EH)$_2$	15 mg/ml	15 mg/ml	1:2	2000RPM (40s); 4000RPM (4s)	124 nm	130°C 10 min
ITNCN(TPI-n12)$_2$	15 mg/ml	10 mg/ml	1:1	2000RPM (40s); 4000RPM (4s)	105 nm	130°C 5 min
ITNCN(TPI-EH)$_2$	20 mg/ml	10 mg/ml	1:1	2000RPM (40s); 4000RPM (4s)	93 nm	130°C 5 min
BT(TTI-n12)$_2$	15 mg/ml	20 mg/ml	1:2	2000RPM (40s); 4000RPM (4s)	104 nm	130°C 15 min
BT(TTI-EH)$_2$	15 mg/ml	20 mg/ml	1:2	2000RPM (40s); 4000RPM (4s)	116 nm	130°C 15 min

Solar cell devices were tested under AM 1.5 G solar illumination at 100 mW/cm^2 using a Thermal-Oriel 150W solar simulator. Current-voltage (J-V) curves were measured using a Keithley 2400 source-measure unit.

For external quantum efficiency (EQE) measurements, a 150 W xenon light source (Newport 6255), housed within an arc lamp housing unit (Newport 66902), was directed through a Princeton Instruments Spectra Pro 2300i monochromator. The light

source was chopped at 30 Hz with a Scitec optical chopper and referenced with a calibrated silicon photodiode (ThorLabs S120VC). Signal from the substrate was moderated with a Stanford Research Systems low-noise current preamplifier followed by a Scitec 420 dual-phase lock-in amplifier (referenced to the optical shopper). EQE curves were measured using a Keithly 2612A source-measure unit.
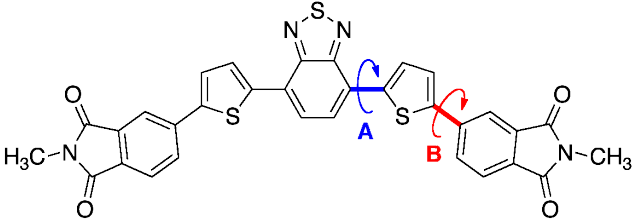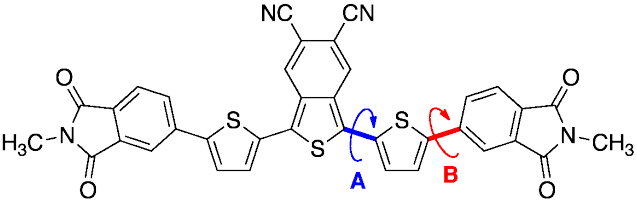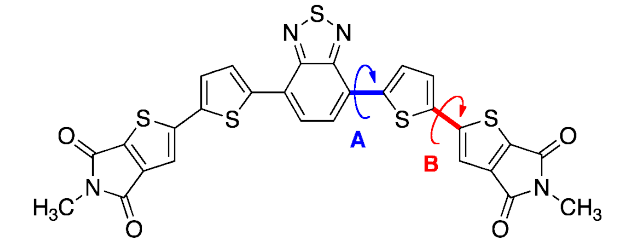
Height profiles of the active layers of devices were imaged using a Veeco Multimode V Atomic Force Microscope (AFM) operated in tapping mode, under ambient conditions using an aluminum coated silicon cantilever (Veeco; TAP150A, f_o = 122-169 kHz, k = 5N/m).

Grazing-incidence x-ray diffraction (GIXD) experiments were conducted at the Stanford Synchrotron Radiation Lightsource on beam-line 11-3. Substituting Si for ITO on glass, samples were prepared following the aforementioned procedure for solar cell devices. Both neat films and p-type:n-type material blends using the optimal solar cell conditions were tested. Samples were irradiated at a fixed incident angle of approximately 0.1°, and their GIXD patterns were recorded with a 2-D image detector (MAR345 image plate detector). GIXD patterns were recorded with an X-ray energy of 12.71 keV (λ = 0.975 Å). To maximize the intensity from the sample, the incident angle (~0.08° – 0.12°) was carefully chosen such that the X-ray beam penetrated the sample completely but did not interact significantly with the silicon substrate. Typical exposure times were 30-900 s.

5.4.3. Additional Figures
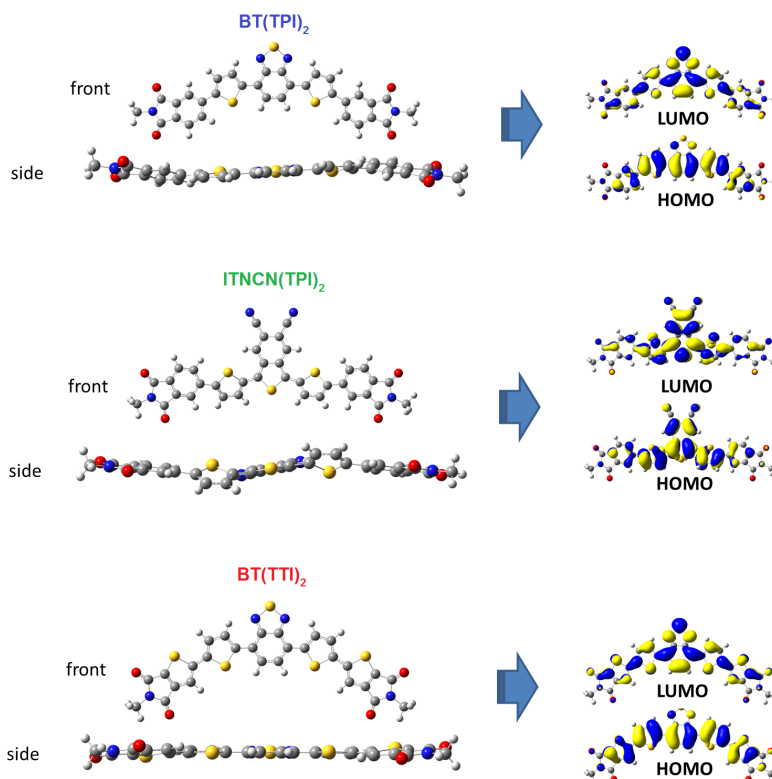
Figure 5-5. Molecular conformation and energy levels of n-type molecules BT(TPI)$_2$, ITNCN(TPI)$_2$, and BT(TTI)$_2$ calculated by DFT.

n-Type Small Molecule	Torsion A (θ)	Torsion B (θ)
	1.1°	22.2°
	30.3°	24.0°
	2.0°	12.0°

Figure 5-6. DFT calculated torsion angles of n-type molecules BT(TPI)$_2$, ITNCN(TPI)$_2$, and BT(TTI)$_2$.
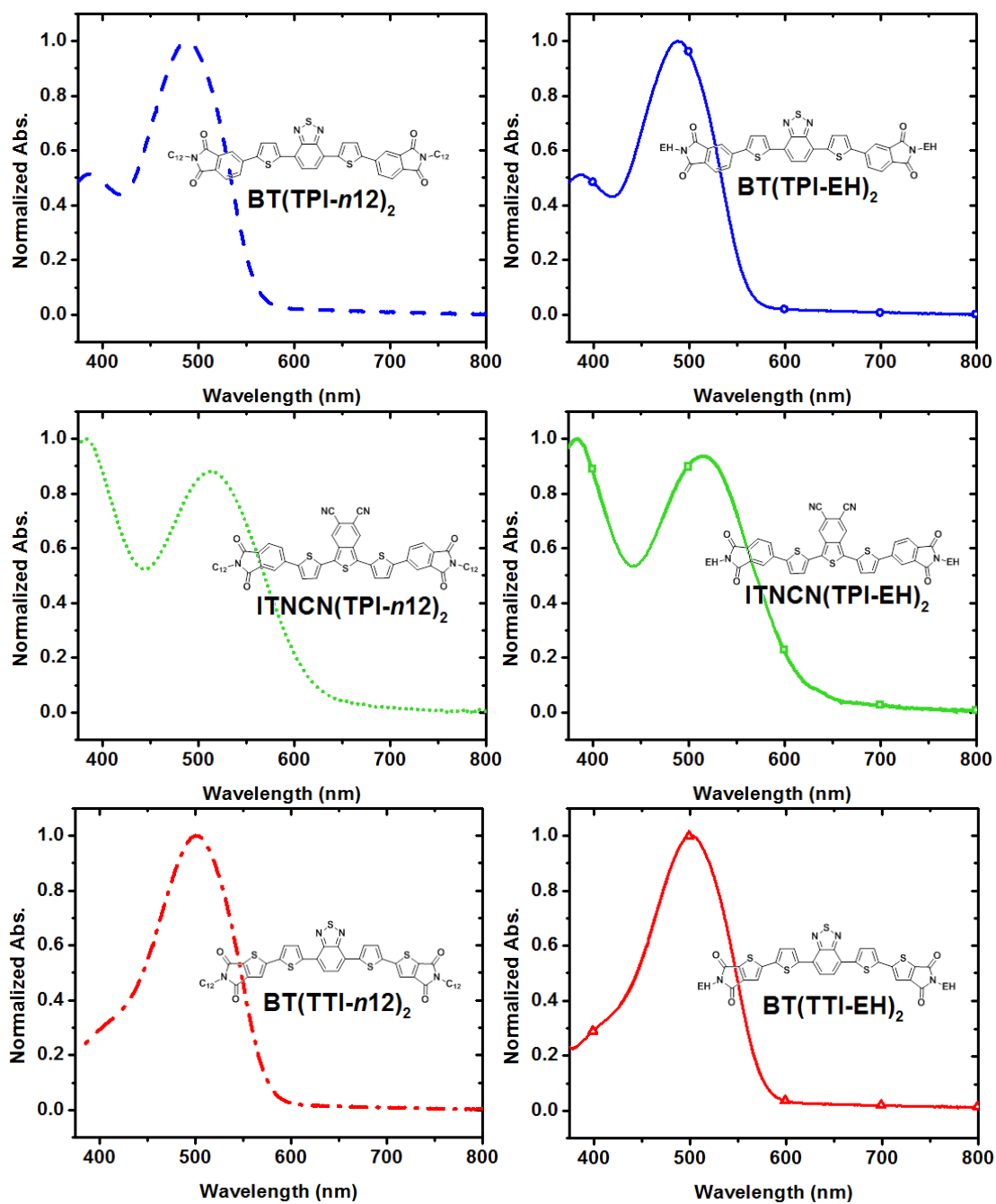
Figure 5-7. UV-vis absorption spectra of n-type molecules BT(TPI)$_2$, ITNCN(TPI)$_2$, and BT(TTI)$_2$ in chloroform solutions.
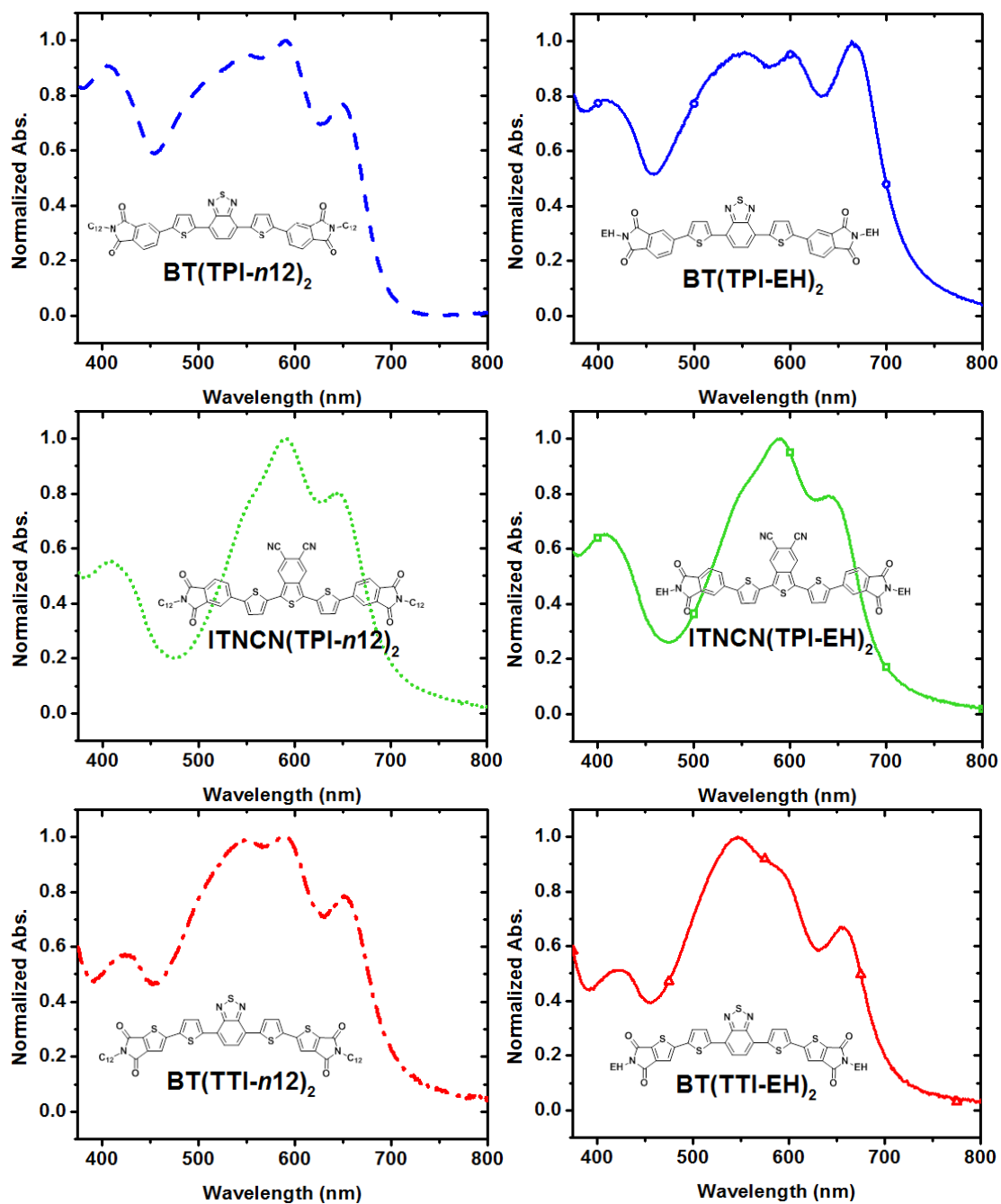
Figure 5-8. UV-vis absorption spectra of DPP-Py:n-type thin-film blends. Films were blended at the optimal ratio for solar cell performance.
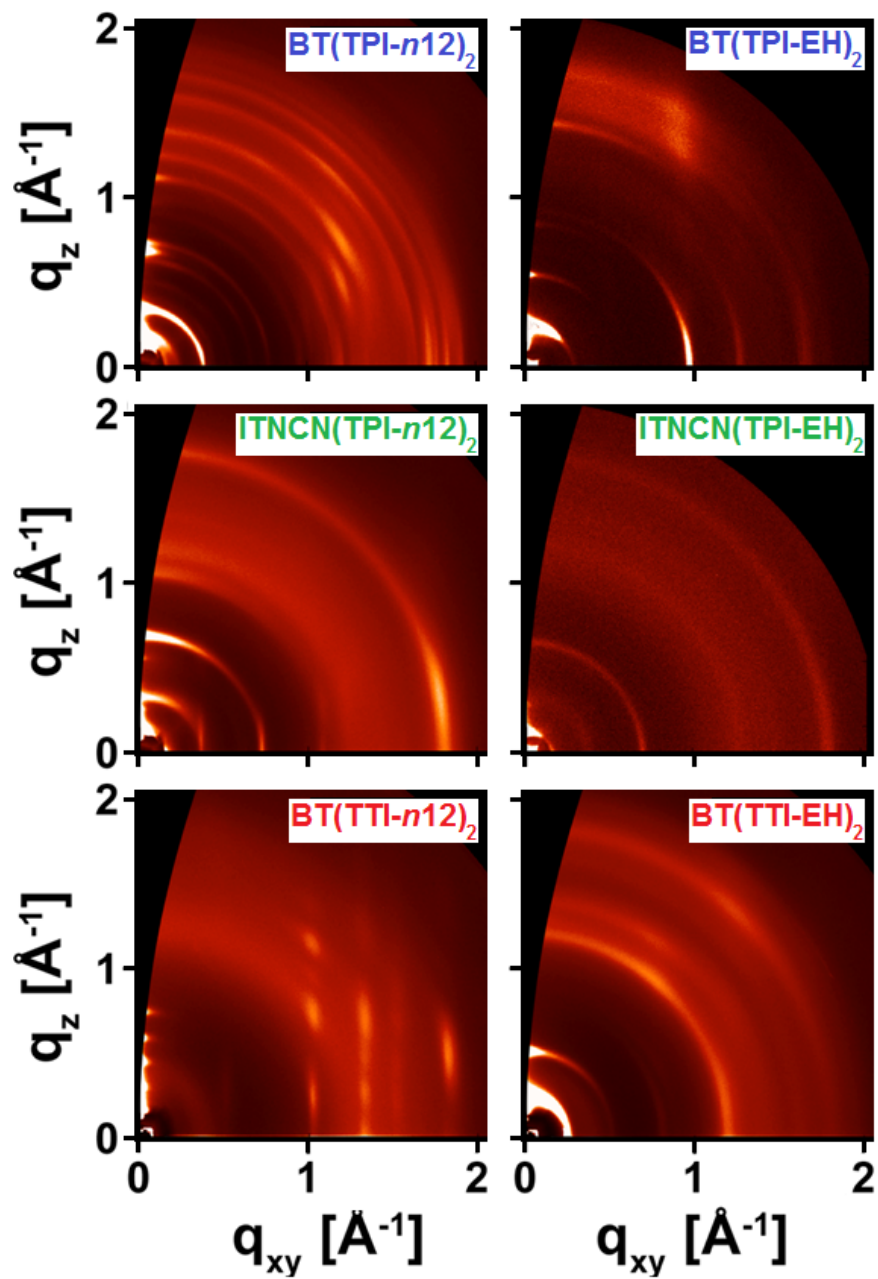
Figure 5-9. Grazing incidence X-ray diffraction (GIXD) spectra of films spuncoat from solutions of only the n-type molecules.
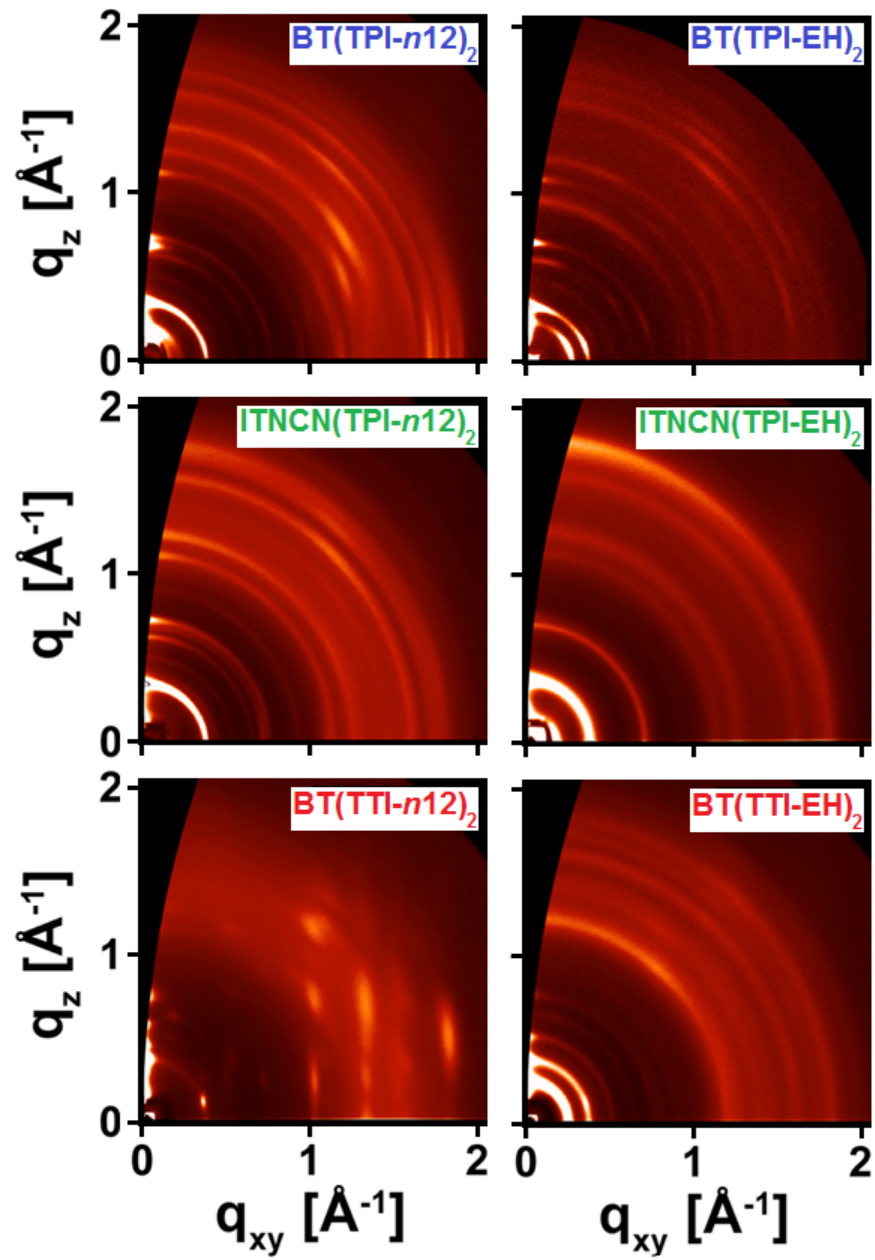
Figure 5-10. Grazing incidence X-ray diffraction (GIXD) spectra of DPP-Py:n-type molecule blends.
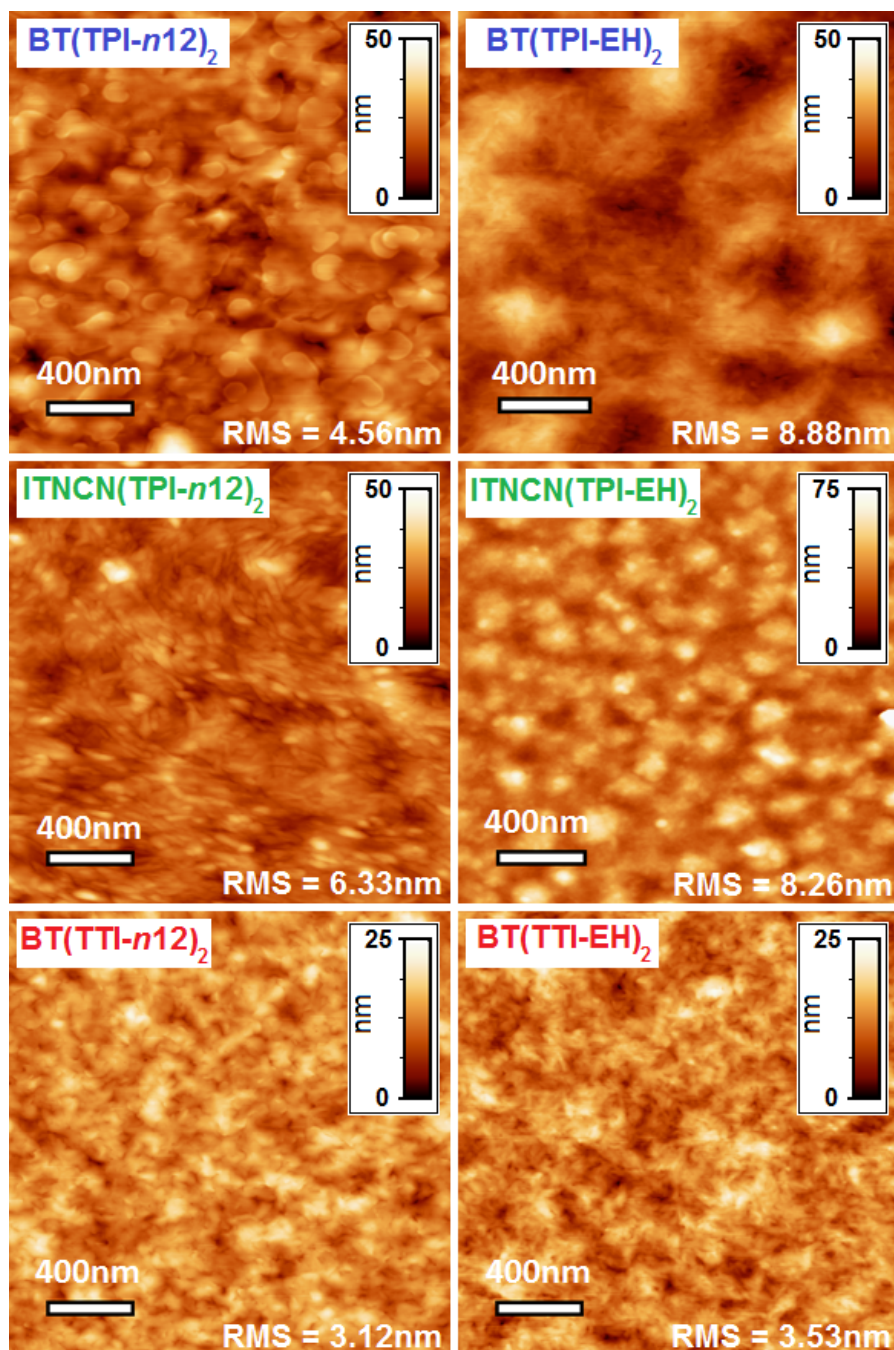
Figure 5-11. Atomic force microscopy images of DPP-Py:n-type molecule blends.
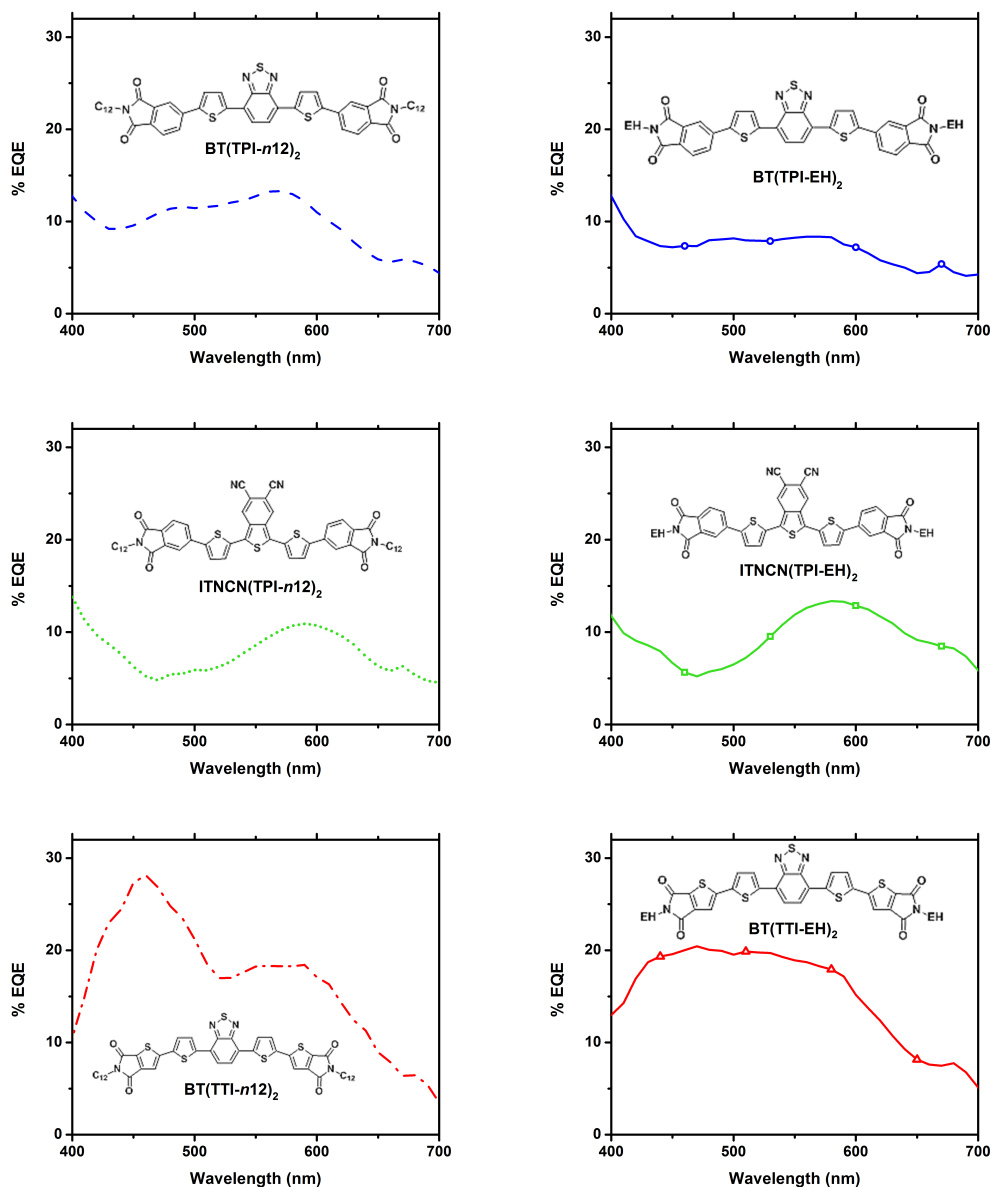
Figure 5-12. External quantum efficiency spectra of DPP-Py:n-type molecule optimized blends.

5.5. References

(1)   M. C. Scharber, D. Mühlbacher, M. Koppe, P. Denk, C. Waldauf, A. J. Heeger, C. J. Brabec, *Adv. Mater.* **2006**, *18*, 789–794.

(2)   S. Günes, H. Neugebauer, N. S. Sariciftci, *Chem. Rev.* **2007**, *107*, 1324–1338.

(3)   B. C. Thompson, J. M. J. Fréchet, *Angew. Chem. Int. Ed.* **2008**, *47*, 58–77.

(4)   Z. He, C. Zhong, X. Huang, W.-Y. Wong, H. Wu, L. Chen, S. Su, Y. Cao, *Adv. Mater.* **2011**, *23*, 4636–4643.

(5)   C. E. Small, S. Chen, J. Subbiah, C. M. Amb, S.-W. Tsang, T.-H. Lai, J. R. Reynolds, F. So, *Nat. Photon.* **2012**, *6*, 115–120.

(6)   Z. He, C. Zhong, S. Su, M. Xu, H. Wu, Y. Cao, *Nat. Photon.* **2012**, *6*, 591–595.

(7)   L. Lu, Z. Luo, T. Xu, L. Yu, *Nano Lett.* **2013**, *13*, 59–64.

(8)   M. T. Dang, L. Hirsch, G. Wantz, *Adv. Mater.* **2011**, *23*, 3597–3602.

(9)   S. Paek, N. Cho, S. Cho, J. K. Lee, J. Ko, *Org. Lett.* **2012**, *14*, 6326–6329.

(10)   H. C. Hesse, J. Weickert, C. Hundschell, X. Feng, K. Müllen, B. Nickel, A. J. Mozer, L. Schmidt-Mende, *Adv. Energy Mater.* **2011**, *1*, 861–869.

(11)   Y. He, H.-Y. Chen, J. Hou, Y. Li, *J. Am. Chem. Soc.* **2010**, *132*, 1377–1382.

(12)   C. J. Brabec, G. Zerza, G. Cerullo, S. De Silvestri, S. Luzzati, J. C. Hummelen, S. Sariciftci, *Chem. Phys. Lett.* **2001**, *340*, 232–236.

(13)   P. Schilinsky, C. Waldauf, C. J. Brabec, *Appl. Phys. Lett.* **2002**, *81*, 3885–3887.

(14)   V. D. Mihailetchi, J. K. J. van Duren, P. W. M. Blom, J. C. Hummelen, R. A. J. Janssen, J. M. Kroon, M. T. Rispens, W. J. H. Verhees, M. M. Wienk, *Adv. Funct. Mater.* **2003**, *13*, 43–46.

(15)   C. J. Brabec, A. Cravino, D. Meissner, N. S. Sariciftci, T. Fromherz, M. T. Rispens, L. Sanchez, J. C. Hummelen, *Adv. Funct. Mater.* **2001**, *11*, 374–380.

(16)   M. M. Wienk, J. M. Kroon, W. J. H. Verhees, J. Knol, J. C. Hummelen, P. A. van Hal, R. A. J. Janssen, *Angew. Chem. Int. Ed.* **2003**, *42*, 3371–3375.

(17)   T. J. Savenije, J. E. Kroeze, X. Yang, J. Loos, *Adv. Funct. Mater.* **2005**, *15*, 1260–1266.

(18)   J. A. Bartelt, Z. M. Beiley, E. T. Hoke, W. R. Mateker, J. D. Douglas, B. A. Collins, J. R. Tumbleston, K. R. Graham, A. Amassian, H. Ade, J. M. J. Fréchet, M. F. Toney, M. D. McGehee, *Adv. Energy Mater.* **2012**, n/a–n/a.

(19)   G. F. Burkhard, E. T. Hoke, S. R. Scully, M. D. McGehee, *Nano Lett.* **2009**, *9*, 4037–4041.

(20)   F. G. Brunetti, X. Gong, M. Tong, A. J. Heeger, F. Wudl, *Angew. Chem. Int. Ed.* **2010**, *49*, 532–536.

(21)   Y. Shu, Y.-F. Lim, Z. Li, B. Purushothaman, R. Hallani, J. E. Kim, S. R. Parkin, G. G. Malliaras, J. E. Anthony, *Chem. Sci.* **2011**, *2*, 363–368.

(22)   P. E. Schwenn, K. Gui, A. M. Nardes, K. B. Krueger, K. H. Lee, K. Mutkins, H. Rubinstein-Dunlop, P. E. Shaw, N. Kopidakis, P. L. Burn, P. Meredith, *Adv. Energy Mater.* **2011**, *1*, 73–81.

(23)   E. Zhou, J. Cong, Q. Wei, K. Tajima, C. Yang, K. Hashimoto, *Angew. Chem. Int. Ed.* **2011**, *50*, 2799–2803.

(24)   T. Zhou, T. Jia, B. Kang, F. Li, M. Fahlman, Y. Wang, *Adv. Energy Mater.* **2011**, *1*, 431–439.

(25)   G. Ren, E. Ahmed, S. A. Jenekhe, *Adv. Energy Mater.* **2011**, *1*, 946–953.

(26)   J. T. Bloking, X. Han, A. T. Higgs, J. P. Kastrop, L. Pandey, J. E. Norton, C. Risko, C. E. Chen, J.-L. Brédas, M. D. McGehee, A. Sellinger, *Chem. Mater.* **2011**, *23*, 5484–5490.

(27)   Y. Zhou, L. Ding, K. Shi, Y.-Z. Dai, N. Ai, J. Wang, J. Pei, *Adv. Mater.* **2012**, *24*, 957–961.

(28)   B. Walker, X. Han, C. Kim, A. Sellinger, T.-Q. Nguyen, *ACS Appl. Mater. Interfaces* **2012**, *4*, 244–250.

(29)   Y. Fang, A. K. Pandey, A. M. Nardes, N. Kopidakis, P. L. Burn, P. Meredith, *Adv. Energy Mater.* **2012**, *3*, 54–59.

114

(30)   M. T. Lloyd, J. E. Anthony, G. G. Malliaras, *Mater. Today* **2007**, *10*, 34–41.

(31)   J. Roncali, *Acc. Chem. Res.* **2009**, *42*, 1719–1730.

(32)   B. Walker, C. Kim, T.-Q. Nguyen, *Chem. Mater.* **2011**, *23*, 470–482.

(33)   Y. Liu, X. Wan, F. Wang, J. Zhou, G. Long, J. Tian, J. You, Y. Yang, Y. Chen, *Adv. Energy Mater.* **2011**, *1*, 771–775.

(34)   Y. Liu, X. Wan, F. Wang, J. Zhou, G. Long, J. Tian, Y. Chen, *Adv. Mater.* **2011**, *23*, 5387–5391.

(35)   G. Wei, S. Wang, K. Sun, M. E. Thompson, S. R. Forrest, *Adv. Energy Mater.* **2011**, *1*, 184–187.

(36)   J. Zhou, X. Wan, Y. Liu, G. Long, F. Wang, Z. Li, Y. Zuo, C. Li, Y. Chen, *Chem. Mater.* **2011**, *23*, 4666–4668.

(37)   Z. Li, G. He, X. Wan, Y. Liu, J. Zhou, G. Long, Y. Zuo, M. Zhang, Y. Chen, *Adv. Energy Mater.* **2012**, *2*, 74–77.

(38)   Y. Sun, G. C. Welch, W. L. Leong, C. J. Takacs, G. C. Bazan, A. J. Heeger, *Nat. Mater.* **2012**, *11*, 44–48.

(39)   T. S. van der Poll, J. A. Love, T.-Q. Nguyen, G. C. Bazan, *Adv. Mater.* **2012**, *24*, 3646–3649.

(40)   O. P. Lee, A. T. Yiu, P. M. Beaujuge, C. H. Woo, T. W. Holcombe, J. E. Millstone, J. D. Douglas, M. S. Chen, J. M. J. Fréchet, *Adv. Mater.* **2011**, *23*, 5359–5363.

(41)   D. Mühlbacher, M. Scharber, M. Morana, Z. Zhu, D. Waller, R. Gaudiana, C. Brabec, *Adv. Mater.* **2006**, *18*, 2884–2889.

(42)   J. Peet, J. Y. Kim, N. E. Coates, W. L. Ma, D. Moses, A. J. Heeger, G. C. Bazan, *Nat. Mater.* **2007**, *6*, 497–500.

(43)   N. Blouin, A. Michaud, M. Leclerc, *Adv. Mater.* **2007**, *19*, 2295–2300.

(44)   S. H. Park, A. Roy, S. Beaupré, S. Cho, N. Coates, J. S. Moon, D. Moses, M. Leclerc, K. Lee, A. J. Heeger, *Nat. Photon.* **2009**, *3*, 297–303.

(45)   H. Zhou, L. Yang, A. C. Stuart, S. C. Price, S. Liu, W. You, *Angew. Chem. Int. Ed.* **2011**, *50*, 2995–2998.

(46)   A. C. Stuart, J. R. Tumbleston, H. Zhou, W. Li, S. Liu, H. Ade, W. You, *J. Am. Chem. Soc.* **2013**, DOI 10.1021/ja309289u.

(47)   C. H. Woo, T. W. Holcombe, D. A. Unruh, A. Sellinger, J. M. J. Fréchet, *Chem. Mater.* **2010**, *22*, 1673–1679.

(48)   J. D. Douglas, G. Griffini, T. W. Holcombe, E. P. Young, O. P. Lee, M. S. Chen, J. M. J. Fréchet, *Macromolecules* **2012**, *45*, 4069–4074.

(49)   C. Piliego, T. W. Holcombe, J. D. Douglas, C. H. Woo, P. M. Beaujuge, J. M. J. Fréchet, *J. Am. Chem. Soc.* **2010**, *132*, 7595–7597.

(50)   T.-Y. Chu, J. Lu, S. Beaupré, Y. Zhang, J.-R. Pouliot, S. Wakim, J. Zhou, M. Leclerc, Z. Li, J. Ding, Y. Tao, *J. Am. Chem. Soc.* **2011**, *133*, 4250–4253.

(51)   C. M. Amb, S. Chen, K. R. Graham, J. Subbiah, C. E. Small, F. So, J. R. Reynolds, *J. Am. Chem. Soc.* **2011**, *133*, 10062–10065.

(52)   O. Inganäs, M. Svensson, F. Zhang, A. Gadisa, N. K. Persson, X. Wang, M. R. Andersson, *Appl. Phys. A* **2004**, *79*, 31–35.

(53)   M.-H. Chen, J. Hou, Z. Hong, G. Yang, S. Sista, L.-M. Chen, Y. Yang, *Adv. Mater.* **2009**, *21*, 4238–4242.

(54)   J. M. Szarko, J. Guo, Y. Liang, B. Lee, B. S. Rolczynski, J. Strzalka, T. Xu, S. Loser, T. J. Marks, L. Yu, L. X. Chen, *Adv. Mater.* **2010**, *22*, 5468–5472.

(55)   J. L. Brédas, *J. Chem. Phys.* **1985**, *82*, 3808–3811.

(56)   J. L. Brédas, A. J. Heeger, F. Wudl, *J. Chem. Phys.* **1986**, *85*, 4673–4678.

(57)   J. L. Brédas, *Synt. Met.* **1987**, *17*, 115–121.

(58)   L. J. A. Koster, S. E. Shaheen, J. C. Hummelen, *Adv. Energy Mater.* **2012**, *2*, 1246–1253.

(59)   S. Cook, R. Katoh, A. Furube, *J. Phys. Chem. C* **2009**, *113*, 2547–2552.

(60)   A. A. Bakulin, J. C. Hummelen, M. S. Pshenichnikov, P. H. M. van Loosdrecht, *Adv. Funct. Mater.* **2010**, *20*, 1653–1660.

(61)   A. A. Bakulin, S. D. Dimitrov, A. Rao, P. C. Y. Chow, C. B. Nielsen, B. C. Schroeder, I. McCulloch, H. J. Bakker, J. R. Durrant, R. H. Friend, *J. Phys. Chem. Lett.* **2013**, *4*, 209–215.

(62)   N. C. Nicolaidis, B. S. Routley, J. L. Holdsworth, W. J. Belcher, X. Zhou, P. C. Dastoor, *J. Phys. Chem. C* **2011**, *115*, 7801–7805.

(63)   S. D. Dimitrov, C. B. Nielsen, S. Shoaee, P. S. Tuladhar, J. Du, I. McCulloch, J. R. Durrant, *J. Phys. Chem. Lett.* **2012**, *3*, 140–144.

Chapter 6

The Effect of Substrate Interlayers on Solvent Additive Modulation of Solid-State Nanostructure

Abstract

High-boiling solvent additives, such as 1,8-diiodooctane, are often used in organic photovoltaic device processing to improve device performance. Such additives are typically thought to modify solution-phase thermodynamics and also slow the rate of drying during spin-coating. However, little work had been done to consider the effects of the substrate in studying the effects of additives. In this work, we show that the extent to which solvent additives affect the nanostructure of thin-film BHJ OPV devices depends on the underlying substrate interlayer. We demonstrate that, in OPV devices, the same additive can produce a modest or dramatic improvement in performance depending on the underlying substrate interlayer. These results confirm our hypothesis that solution-substrate interactions play an important role in the evolution of nanostructure during the film formation process and underscore the need for more comprehensive study of the effect of solvent additives. To explore the different effects of the interlayer, we examine top and bottom surfaces of blend films using atomic force microscopy (AFM) and grazing-incidence wide-angle X-ray scattering (GIWAXS). GIWAXS data shows a clear correlation between π-π stacking correlation length and device PCE across all additives and interlayers. In addition, we show that additives modulate the π-π stacking correlation length over a much broader range on PFN than they do on PEDOT:PSS.

6.1. Introduction

In the near future, everyday electronic devices such as solar cells, simple circuits, and displays could be manufactured by roll-to-roll printing at near-ambient conditions. With such a scalable process, production costs could be kept disruptively low. A considerable amount of basic research has been devoted thus far to the synthesis, processing, and characterization of solution-processed organic semiconductor materials suitable for printed electronics[1-10]. In order for this technology to come to fruition, however, more work must be done to elucidate how material properties and device performance can be deliberately and systematically controlled through molecular design and processing. Properties of particular interest to our group include solid-state nanostructure and microstructure in the active layer. Domain size, intermolecular π-π stacking distance, preferred crystallite orientation, and crystalline correlation length have been shown to have a dramatic impact on device performance in both organic photovoltaics (OPVs) and field-effect transistors (OFETs)[11-18]. Nanostructure can be controlled by factors intrinsic to the material, such as chemical structure, but it can also be influenced by factors extrinsic to the material, such as processing conditions. In this work, we explore the effect of different combinations of substrate and solvent additive on the nanostructure and performance of P3HT:PCBM solar cells.

For solution-processed bulk-heterojunction (BHJ) OPV devices, the thin-film active layer is typically deposited from solution by spin-coating. Spin-coating is a dynamic process that produces a film with kinetically-trapped film nanostructure. The evolution of film nanostructure—and thus the final state of the film—has been shown to depend strongly on different solvent additives and substrate coatings. Solvent additives have been shown to affect solid-state film nanostructure and blend morphology, and can have a large impact on device performance[19,20]. A number of solution-phase mechanisms have been proposed and studied to explain these effects: additives can selectively solubilize one material component (e.g., PCBM)[21,22] and/or slow the solvent drying rate[23,24], changing the phase separation of the two components[21,25,26]. In parallel, the use of thin-film substrate coatings—interlayers coated onto the substrate prior to spin-coating the active layer—can also dramatically affect device performance by enhancing charge selectivity or interfacial charge transfer[27-30]. Interlayers are in intimate contact with the active layer solution during the spin-coating process and, subsequently, with the active layer thin-film during device operation. Given this, they can affect the microstructure and nanostructure in the active layer[31-33]. Although both solvent additives and substrate interlayer coatings have such clear impacts on device performance, their effects have rarely been studied in unison.

In this study, we examine two different substrate interlayers: the electron-blocking ionomer blend poly(3,4-ethylenedioxythiophene):poly(styrenesulfonate) (PEDOT:PSS) and the recently-introduced hole-blocking semiconducting polymer poly [(9,9-bis(3′-(N,N-dimethylamino)propyl)-2,7-fluorene)-alt-2,7-(9,9–dioctylfluorene)] (PFN). In conventional-architecture OPV devices, PFN has been spin-coated on top of the active layer as a hole-blocking interlayer[34,35]. As in this work, PFN can also be employed as a substrate coating in inverted OPV devices, where it can replace hole-blocking substrate interlayers such as ZnO[36]. The inverted OPV device architecture has gained prominence

in recent years and has been employed in studies of a number of the highest-performing materials in the literature[36,37]. Compared their conventional analogs, inverted devices can offer improved light absorption, charge collection, and device durability[36,38,39]. As the inverted architecture continues to gain traction, it is important to understand how well the accumulated understanding built on conventional PEDOT:PSS-based OPV systems will translate to inverted systems. Beyond contributing an understanding of the impact of substrate-solution interaction on solid-state nanostructure, our hope in this study is to facilitate the transition of device processing insight from conventional to inverted device structures.

Herein, we examine how the choice of substrate interlayer affects the impact of solvent additives. Although solvent additives have so far been thought to primarily affect solution-phase thermodynamics, we hypothesize that solution-substrate interactions during the spin-coating process also play a large role in determining the solid-state microstructure and nanostructure of the spin-coated active layer film. In particular, the choice of interlayer should affect the blend morphology and nanostructure of the active layer at the buried film-substrate interface. The local interfacial composition and nanostructure can dramatically impact charge injection and transport[31,33]. This interface is also the region of primary interest for OFET devices, as it is responsible for nearly all charge conduction[40]. Thus, while this study examines OPV systems, many of the principles and results employed here may also be translated to OFET device processing. We show that the same solvent additive can have a different effect on performance for devices fabricated on PEDOT:PSS-coated substrates versus those fabricated on PFN-coated substrates.

6.2. Results and Discussion

Solar Cell Performance. As a model system for this work, we fabricated BHJ OPV devices from the electron-donating polymer poly(3-hexylthiophene) (P3HT) and the electron-accepting small molecule [6,6]-phenyl-C_{61}-butyric acid methyl ester (PCBM). Thin-film active layers were spin-coated from chlorobenzene solution at a P3HT:PCBM weight ratio of 1:0.8. Films were spun onto ITO-on-glass substrates coated with either PEDOT:PSS (conventional device architecture) or PFN (inverted device architecture) interlayers. Experimental device processing conditions are summarized in **Table 6-1**. With each interlayer, devices were fabricated with one of three commonly-used solvent additives: 1-chloronaphthalene (CN), 1,8-dioodoocatne (DIO), or 1,8-octanedithiol (ODT). Each additive was evaluated at four different concentrations: 0.25%, 0.5%, 1%, and 3% (v/v). For each interlayer, control devices were fabricated without any solvent additive, both with and without thermal annealing. Conventional devices had the structure glass/ITO/PEDOT:PSS/P3HT:PCBM/Al, while inverted devices had the structure glass/ITO/PFN/P3HT:PCBM/MoO$_x$/Al. MoO$_x$ was used as an electron-blocking interlayer in the inverted devices to enhance device performance. Although they are commonly used in conventional devices, the hole-blocking interlayers Ca and LiF, as well PFN, were not used in our conventional devices because devices fabricated with these interlayers performed poorly in thermally-annealed control devices.

Average power conversion efficiencies (PCEs) for devices processed at each condition are presented in **Table 6-1**. For each condition presented, device performance was averaged over $n = 8$ samples. For the highest-performing devices obtained at each interlayer-additive condition (PCEs bolded in **Table 6-1**), the corresponding current density (J) vs. bias (V) curves are shown in **Fig. 6-1**. The best performance was achieved using PEDOT:PSS (conventional device) with no solvent additive, and with post-fabrication thermal annealing at 200 °C for 10 minutes ($PCE_{avg} = 4.2\%$). Among PEDOT:PSS-based devices, the solvent additive that gave the best device performance was ODT ($PCE_{avg} = 2.0\%$), followed by CN ($PCE_{avg} = 1.8\%$), followed by DIO ($PCE_{avg} = 1.5\%$). In contrast, among PFN-based devices, the solvent additive that gave the best device performance was DIO (PCE = 3.5%), followed by CN and ODT, which performed comparably (PCE ~ 2.5%).

As these device results show, solvent additives can have different effects on PEDOT:PSS- and PFN-based solar cells. For instance, with PEDOT:PSS-based devices, additives only produce a relatively modest improvement in PCE relative to the as-cast additive-free control (up to 43% increase), with DIO providing the least improvement with only a 7% increase in PCE (from 1.4% to 1.5%). As the J-V curves show (**Fig. 6-1**), PCE improvement comes primarily from the increase in photocurrent and fill factor (FF): relative to the additive-free control, solvent additives increase the short-circuit current density (J_{SC}) from around 6 mA/cm² to between 8–10 mA/cm² and FF from 0.38 to over 0.5. However, at the same time, solvent additives decrease device open-circuit voltage (V_{OC}) from around 0.6 V for the additive-free control to between 0.3–0.4 V, hence the modest overall PCE improvement. In PFN-based devices, solvent additives increase J_{SC} from 3.4 mA/cm² to 8–10 mA/cm² and FF from 0.39 to above 0.5, while having minimal effect on device V_{OC}. As a result, they dramatically improve PCE, and DIO leads the way with a sevenfold improvement in PCE (0.5% to 3.5%). That PEDOT:PSS- and PFN-based devices respond differently to solvent additives suggests that the additives may do more than modulate solution-phase thermodynamics. They may also affect the solution-substrate interaction, leading to substrate-dependent changes in the blend morphology and nanostructure of the active layer.
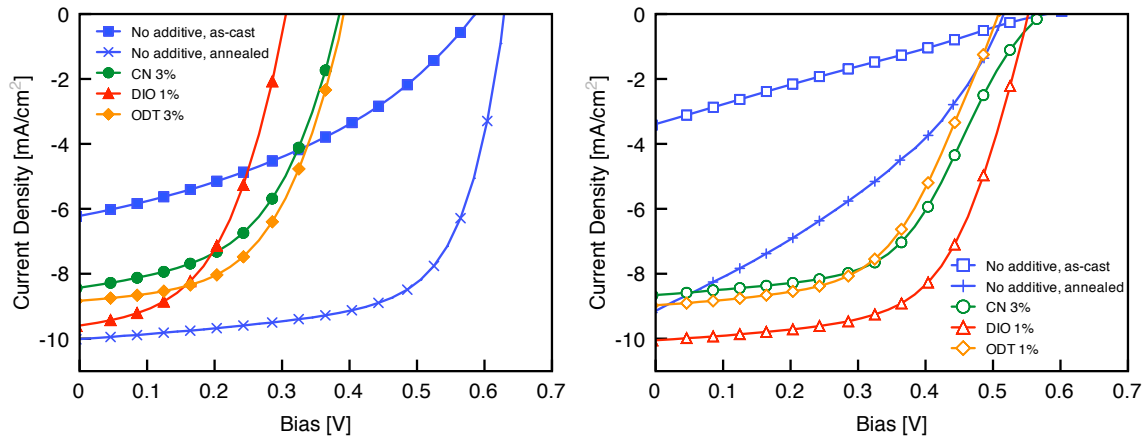
Figure 6-1. Average J-V curves for the highest-performing devices at each combination of substrate interlayer and solvent additive.

Table 6-1. Solar cell power conversion efficiencies

Additive	Additive Concentration (v/v)	On PEDOT:PSS (conventional)	On PFN (inverted)
None (as-cast)	---	1.4% ± 0.1%	0.5% ± 0.1%
None (annealed)	---	4.2% ± 0.1%	2.0% ± 0.3%
1-chloronaphthalene (CN)	0.25%	1.5% ± 0.1%	2.1% ± 0.1%
	0.5%	1.7% ± 0.1%	2.1% ± 0.1%
	1%	1.8% ± 0.1%	2.5% ± 0.2%
	3%	**1.8%** ± 0.2%	**2.6%** ± 0.1%
1,8-diiodooctane (DIO)	0.25%	1.3% ± 0.1%	2.6% ± 0.1%
	0.5%	1.5% ± 0.1%	3.4% ± 0.1%
	1%	**1.5%** ± 0.1%	**3.5%** ± 0.2%
	3%	1.4% ± 0.1%	2.5% ± 0.3%
1,8-octanedithiol (ODT)	0.25%	1.6% ± 0.1%	2.5% ± 0.2%
	0.5%	1.6% ± 0.1%	2.4% ± 0.2%
	1%	1.8% ± 0.1%	**2.5%** ± 0.2%
	3%	**2.0%** ± 0.2%	2.1% ± 0.3%

Blend Film Morphology. To evaluate the impact of additive-substrate interaction on the resulting blend morphology of the active layers, surfaces of blend films were imaged using atomic force microscopy (AFM). Typically, only the top (air-side) surfaces of films are imaged, but we also imaged the bottom (substrate-side) surfaces to see if the solvent-substrate interaction had an effect on the local interfacial blend morphology. Blend films were prepared using the same processing conditions as in device fabrication, but SiO$_2$ substrates were used in place of ITO-on-glass substrates. To transpose (flip) a film and expose its bottom surface, polydimethylsiloxane (PDMS) was gently adhered onto the top of the film to act as a solid support. The supported film was then lifted off of the SiO$_2$ substrate by immersion in 0.1% NaOH in water (w/w) for 5 minutes, followed by immersion in 1% acetic acid (AcOH) in water (v/v) for 10 minutes to dissolve residual PEDOT:PSS or PFN. Transposed films were then dried under a stream of nitrogen for 1 minute, followed by 10 minutes of further drying under low vacuum. Control studies were performed to ensure that this liftoff procedure does not affect device performance or blend morphology (see Section 6.4, Experimental).

Representative AFM images of the top and bottom surfaces of blend films are presented in **Fig. 6-2**. The root mean square roughness (R_q) corresponding to these images are presented in **Table 6-2**. The top and bottom of as-cast films on both PEDOT:PSS and PFN are relatively smooth, with vertical features barely distinguishable past 5 nm and R_q values less than 1 nm. With the addition of solvent additive, however, the films become much rougher. DIO and ODT result in the roughest films, with R_q
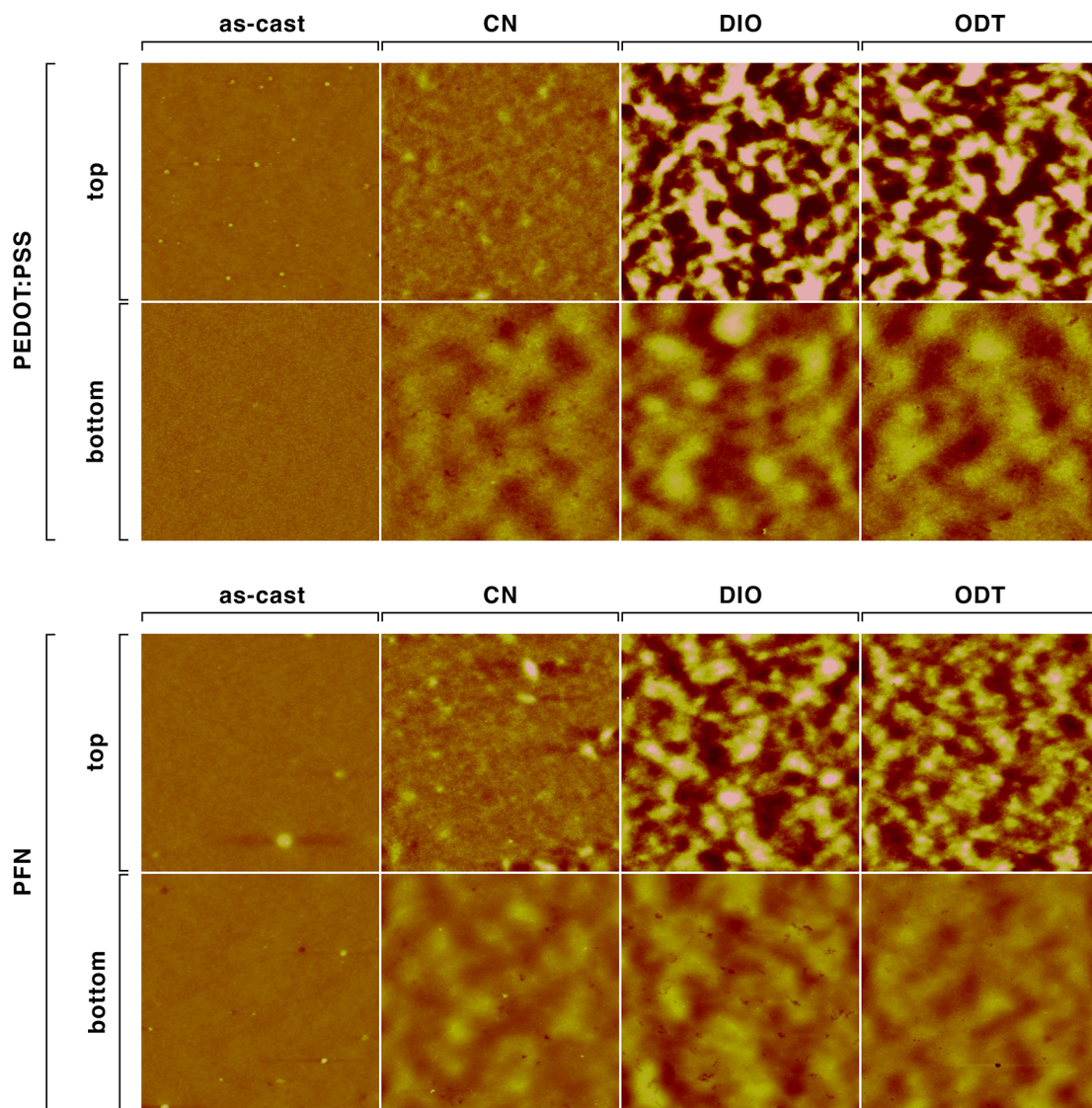
Figure 6-2. AFM images of the top (air side) and bottom (substrate side) of blend films prepared at the highest-performing additive concentrations on PEDOT:PSS and PFN interlayers. Images cover a 5 μm x 5 μm area. The dark red to light pink color height scale covers 50 nm.

Table 6-2. Root mean square roughness of blend films

Interlayer	Additive	R_q, top [nm]	R_q, bottom [nm]
PEDOT:PSS	None (as-cast)	0.67	0.89
	CN	1.81	2.81
	DIO	18.9	5.38
	ODT	18.6	4.83
PFN	None (as-cast)	0.93	0.76
	CN	3.12	2.23
	DIO	9.49	3.62
	ODT	7.86	2.58

reaching ~19 nm for the top side of films prepared on PEDOT:PSS. The bottom surfaces of films prepared on both PEDOT:PSS and PFN tend to be smoother than the top surfaces, particularly for films prepared with additives. As a general trend, films prepared on PEDOT:PSS have larger bottom-side R_q values than films prepared on PFN. A rougher bottom surface, which may be caused by dewetting between the film and substrate during spin-coating, could result in poorer interfacial contact between the active layer and the PEDOT:PSS or PFN interlayer. In addition, film roughness may also suggest larger crystalline domains and less donor-acceptor interfacial contact within the blend film. Both of these may lead to decreased performance and may contribute to the reduced V_{OC} of devices prepared with additives on PEDOT:PSS. However, there is not a clear correlation between film roughness and device performance. To further explore the differences in device performance between additives on the two different interlayers, we looked to solid-state nanostructure.

Thin-Film Nanostructure. As mentioned earlier, solid-state nanostructure in the active layer can have a large impact on device performance. In particular, intermolecular π-π interactions serve as a primary mechanism for charge transport through the film. Thus, improved π-π stacking parameters—tighter spacing, more out-of-plane orientation, and longer correlation length—have been associated with improved solar cell performance through increased photocurrent and/or fill factor[16,18,41]. To probe these π-π stacking parameters in our BHJ blend films, we employed grazing-incidence wide-angle X-ray scattering (GIWAXS). GIWAXS has become a preferred technique for this kind of study because it allows for rapid sampling of a wide and complete range of reciprocal space, while offering good signal-to-noise ratio and relatively low beam intensity[33,42].
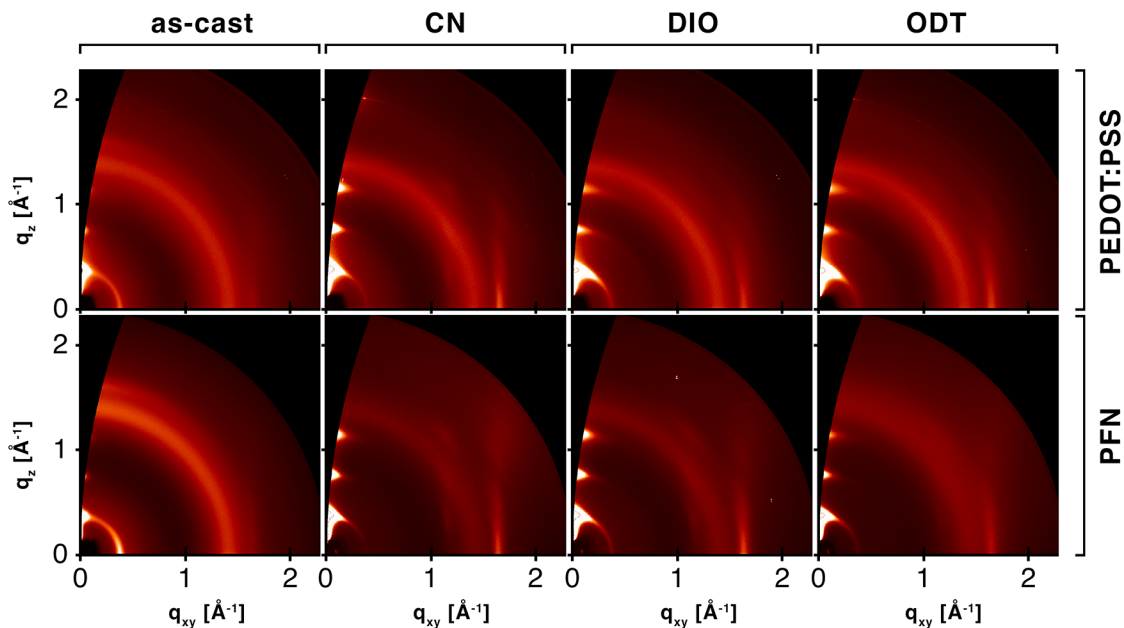
Figure 6-3. GIWAXS 2-D diffraction patterns of blend films prepared under the same conditions as the highest-performing devices.

Diffraction patterns of blend films on SiO_2 substrates, prepared following the same procedure as for the highest-performing devices, are shown in **Fig. 6-3**. The ring closest to the origin at q ~ 0.4 corresponds to the lamellar stacking of P3HT, which is the side-to-side distance between P3HT chains along the direction orthogonal to π-π stacking. The ring at q ~ 1.4 corresponds to the spacing of PCBM, and its breadth reflects the relative disorder present in PCBM domains. The ring or peak at q ~ 1.7 corresponds to the π-π stacking of P3HT. Note that for films prepared with additives, this π-π stacking peak is only visible at small values of the quasi-polar angle χ (closer to the $q_z = 0$ horizon), indicating that the preferred orientation of π-π stacking is in-plane relative to the substrate. For OPV devices, π-π stacking out-of-plane is desired for optimal charge transfer to electrodes at the top or bottom of the active layer, and is often associated with higher device performance[33,43]. This may explain in part why additives do not improve the performance of P3HT:PCBM devices as much as they may that of other systems.

To obtain more detailed information on the nature of π-π stacking described by our diffraction images, we fit peaks to the GIWAXS data averaged over χ = 15° ± 2° and χ = 70° ± 2°, as described in previous studies[16,18]. The center of the π-π peak in reciprocal space translates to the π-π stacking distance, which is 3.8 Å for the as-cast films and ~3.7 Å for the films prepared with additives. Tighter π-π spacing is correlated with improved charge carrier mobility, which may help explain the increased photocurrent, FF, and PCE observed with the use of solvent additives. In addition to π-π stacking distance, we also calculated the correlation length (L_C) associated with π-π stacking. Correlation length is a measure of nanostructural order—which increases with crystallite size and perfection— and has been implicated in improved charge carrier mobility and OPV device performance. As shown in **Fig. 6-4**, additives increase L_C for films spun on both PEDOT:PSS and on PFN. Importantly, a clear positive correlation can be drawn between π-π stacking correlation length and device PCE. Additionally, films prepared on PEDOT:PSS have values of L_C clustered between 40 and 47 Å, while films prepared on PFN have a much broader range of L_C from 34 to 61 Å. In line with our original hypothesis, these results suggest that, compared to PEDOT:PSS, the PFN substrate interlayer allows for a greater range of modulation of solid-state nanostructure.
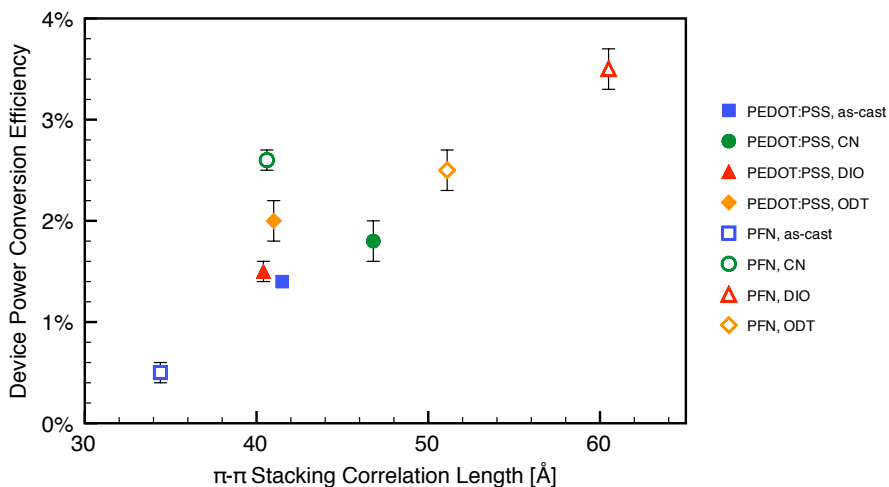
Figure 6-4. π-π stacking correlation length versus device power conversion efficiency for blend films. Error bars represent one standard deviation of device PCE.

In addition to the conventional GIWAXS studies in which the X-ray beam enters the sample from the top surface of the film, we also attempted to use GIWAXS to study the bottom surfaces of our blend films. Depending on the angle of incidence between the film surface and the X-ray beam, different parts of the film will account for the observed scattering. Below the critical angle, only the top few nanometers of the film will contribute to scattering[44]. Because of this phenomenon, it is possible to probe the nanostructure just at or near (within a few nanometers of) the film-air interface, which may be different from the nanostructure in the bulk of the film. In our case, the film-air interface of a transposed (flipped) film would actually the film-substrate interface (bottom surface) in a device. We had predicted that the nanostructure at this film-substrate would change based on additive-substrate interactions during the spin-coating process. We flipped films over using the same PDMS-adhesion technique used to flip samples for AFM imaging of the bottom surfaces. However, we were not able to use GIWAXS obtain information on the crystallographic structure of the film. As shown in **Fig. 6-5**, the background amorphous scattering halo of PDMS was too strong and dominated the scattering images. In addition, the PDMS surface was likely not smooth enough to provide a suitable substrate for X-ray scattering studies, which further weakened the signal of any peaks of interest relative to the substrate background.
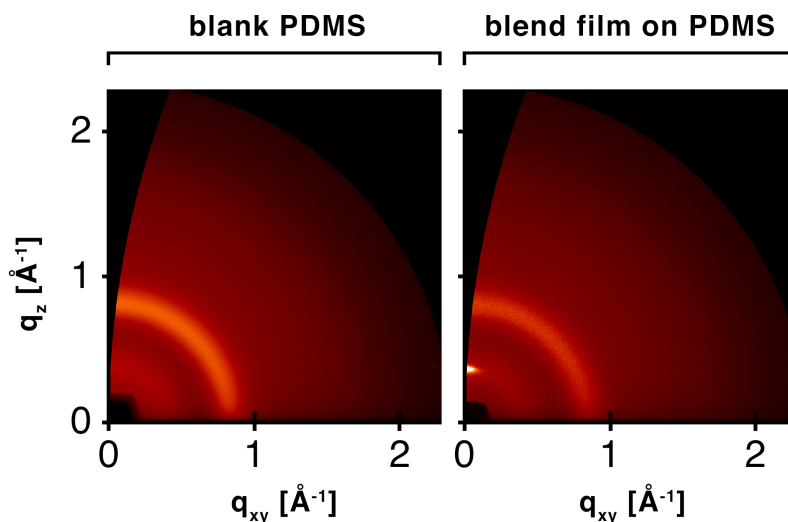
Figure 6-5. GIWAXS 2-D diffraction pattern of a blank PDMS substrate (left) and a representative blend film flipped upside down onto PDMS (right).

6.3. Conclusion

In this work, we have demonstrated that the choice of substrate interlayer has a significant effect on the extent to which solvent additives modulate the nanostructure of thin-film BHJ OPV devices. We hypothesized that, during the spin-coating process, different substrate-solution combinations would have different interactions and might result in different film properties and device performance. Through a systematic OPV device study of P3HT:PCBM blend films prepared using different additives at different concentrations, we show that the same additive can have a different impact depending on

whether the underlying substrate interlayer is PEDOT:PSS or PFN. The additive DIO, for instance, causes a modest improvement in device performance on PEDOT:PSS but produces a dramatic improvement in PCE on PFN. These results confirm our hypothesis and add an important dimension to the broader understanding of the effect of solvent additives. Previously, it was thought that solvent additives operate primarily by modifying solution-phase thermodynamics and also by slowing the rate of drying, but little work had been done to explore effects of the substrate. To explain the differences in additive effect on PEDOT:PSS versus on PFN, we investigated blend films using AFM and GIWAXS. Using GIWAXS, we find a clear correlation between π-π stacking correlation length and device PCE across all additives and interlayers. In addition, we show that additives modulate the π-π stacking correlation length over a much broader range on PFN than they do on PEDOT:PSS.

The results described in this study emphasize the importance of interfacial interactions in solution-processed OPV device fabrication. As materials and device architectures grow in number and complexity, inter-component interactions will only grow in importance. Moving forward, studying and understanding the mechanisms underlying nanostructural evolution during the film formation process will be invaluable in optimizing complete systems of interlayers, active layer materials, and solvent additives.

6.4. Experimental

Solar Cell Device Fabrication. All devices were fabricated on ITO-coated glass substrates (pre-patterend, R = 20 Ω^{-1}) from Thin Film Devices. Substrates were sonicated for 20 minutes each in 2% Helmanex soap water (followed by extensive rinsing in DI water), DI water, acetone, and isopropanol, followed by drying under a stream of N_2. They were then UV-ozone cleaned for 5 minutes. PEDOT:PSS-based (conventional) devices, a thin (~30 nm) layer of PEDOT:PSS (Clevios PVP AI) was spin-coated onto each substrate at 4000 RPM for 40 s, followed by 10 minutes of drying in air at 140 °C. For PFN-based (inverted) devices, a very thin (~10 nm) layer of PFN (synthesized as described elsewhere[45]), was spin-coated onto each substrate from a 2 mg/mL solution in methanol (with 2 μL acetic acid added per mL of solution) at 1200 RPM for 40 s inside a N_2 glovebox. In the same glovebox, active layers were spun from a blend solution containing 8.33 mg/mL P3HT from Rieke Metals (BS 16-65) and 6.67 mg/mL PCBM from Nano-C, with a blend ratio of P3HT:PCBM = 1:0.8. in chlorobenzene (kept at 110 °C) at 800 RPM for 40 s, followed by 4000 RPM for 10 s. For conventional devices, the metal cathode (100 nm Al) was then evaporated through a shadow mask defining a device active area of 0.03 cm². For inverted devices, the metal anode (10 nm MoO_x/100 nm Al) was evaporated through the same shadow mask. Some control devices were annealed by placing the substrates glass-side down on a hot plate which was set to the desired temperature (200 °C).

Solar Cell Device Testing. Current-voltage (J-V) curves were measured using a Keithley 2400 source-measure unit. Solar cell were tested under AM 1.5 G solar illumination at 100 mW cm⁻² using a Thermal-Oriel 150 solar simulator.

AFM and GIWAXS Sample Preparation. Blend films were prepared following the same procedure as for device fabrication, except with SiO_2 substrates instead of ITO-coated glass substrates.

To flip films to expose the underside, PDMS stamps were first adhered to the top surface of the film. PDMS (Dow Corning Sylgard® 184) was prepared by mixing per manufacturer's specifications, degassing under low vacuum for 30 minutes, and then allowing to cure overnight to form sheets ~4 mm in thickness. These sheets were cut into rectangular stamps ~5 mm x ~10 mm for AFM and ~5 mm x ~20 mm for GIWAXS samples. The substrate/interlayer/blend-film/PDMS assemblies were then immersed in 0.1% NaOH (aq) for 5 minutes to remove the film/PDMS assembly from the substrate/interlayer. The flipped film on PDMS was then immersed in 1% acetic acid (aq) for 10 minutes. It was then dried under a stream of N_2 and dried further under low vacuum for 10 minutes.

As a control to ensure that the liftoff procedure does not affect device performance or blend morphology, ITO/P3HT:PCBM/Al devices were either exposed to air for 15 minutes or subjected to the same NaOH/AcOH treatment described above (5 min immersion in 0.1% NaOH (aq.), followed by 10 min immersion in 1% AcOH (aq)). As shown by the device J-V curves, UV-Vis absorption spectra (obtained using a Cary 50 spectrophotometer), and AFM images in **Fig. 6-6**, the NaOH and AcOH immersions do not affect device performance or blend morphology. By AFM, the devices exposed to air had an average R_q of 0.52 nm, compared to 0.42 nm for the immersed devices.
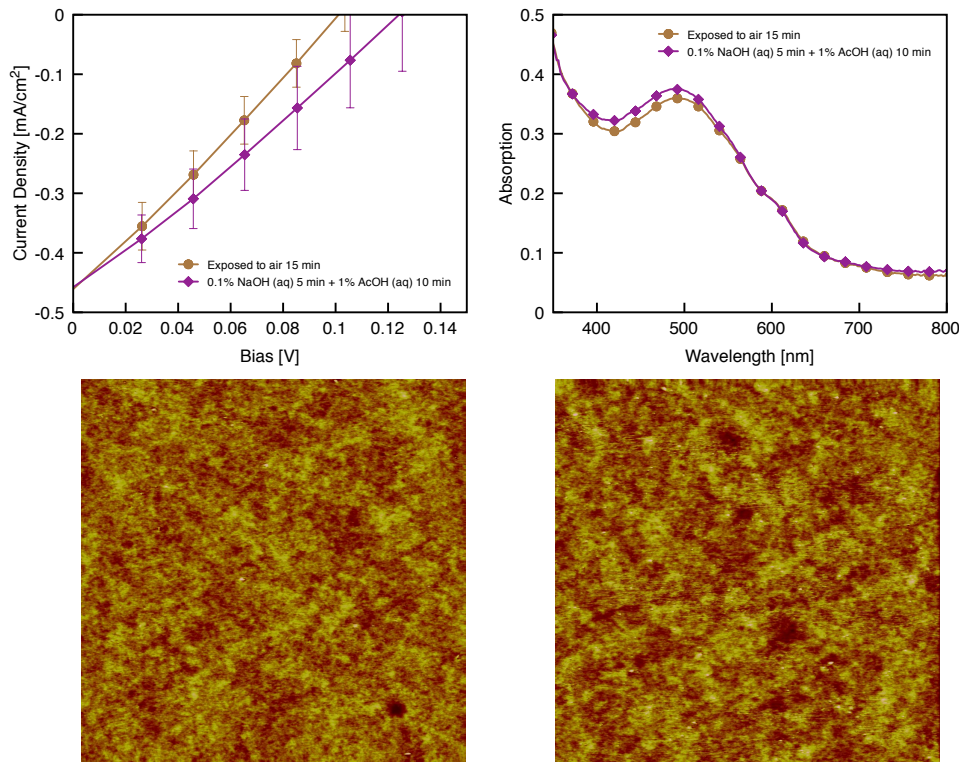
Figure 6-6. Device J-V curves (top left) and UV-vis absorption spectra (top right) for ITO/P3HT:PCBM/Al devices exposed to air for 15 minutes or immersed in 0.1% NaOH (5 min) and 1% AcOH (10 min). AFM images of the air (bottom left) and immersed (bottom right) devices (5 μm x 5 μm, height scale = 5 nm).

Atomic Force Microscopy. Blend films surface topography was imaged using a Veeco Multimode V AFM operated in tapping mode using Veeco TAP150A tips.

X-ray Scattering. Grazing-incidence wide-angle X-ray scattering (GIWAXS) experiments were conducted at the Stanford Synchrotron Radiation Lightsource on beamline 11-3. Samples were irradiated at an incidence angle of 0.12° (0.08° or smaller for attempted below-critical-angle studies of flipped films on PDMS) and their diffraction patterns were recorded with a 2-D image detector (MAR345 image plate detector) placed 400 mm from the sample. Diffraction patterns were recorded with an X-ray energy of 12.71 keV ($\lambda = 0.975$ Å). Typical exposure times were 150-600 s.

6.5. References

(1)   Beaujuge, P. M.; Fréchet, J. M. J. *Journal of the American Chemical Society* **2011**, *133*, 20009.

(2)   Scharber, M. C.; Mühlbacher, D.; Koppe, M.; Denk, P.; Waldauf, C.; Heeger, A. J.; Brabec, C. J. *Adv. Mater.* **2006**, *18*, 789.

(3)   Gunes, S.; Neugebauer, H.; Sariciftci, N. S. *Chem. Rev.* **2007**, *107*, 1324.

(4)   Chen, J.; Cao, Y. *Acc. Chem. Res.* **2009**, *42*, 1709.

(5)   Bundgaard, E.; Krebs, F. C. *Sol. Energ. Mat. Sol. Cells* **2007**, *91*, 954.

(6)   Boudreault, P.-L. T.; Najari, A.; Leclerc, M. *Chem. Mater.* **2011**, *23*, 456.

(7)   Dennler, G.; Scharber, M. C.; Brabec, C. J. *Adv. Mater.* **2009**, *21*, 1323.

(8)   Li, C.; Liu, M.; Pschirer, N. G.; Baumgarten, M.; Müllen, K. *Chem. Rev.* **2010**, *ASAP*.

(9)   Thompson, B. C.; Fréchet, J. M. J. *Angew. Chem. Int. Ed.* **2008**, *47*, 58.

(10)   Spanggaard, H.; Krebs, F. C. *Solar Energy Materials and Solar Cells* **2004**, *83*, 125.

(11)   Szarko, J. M.; Guo, J.; Liang, Y.; Lee, B.; Rolczynski, B. S.; Strzalka, J.; Xu, T.; Loser, S.; Marks, T. J.; Yu, L.; Chen, L. X. *Advanced Materials* **2010**, *22*, 5468.

(12)   Brabec, C. J.; Heeney, M.; McCulloch, I.; Nelson, J. *Chemical Society Reviews* **2011**, *40*, 1185.

(13)   Li, G.; Shrotriya, V.; Huang, J.; Yao, Y.; Moriarty, T.; Emery, K.; Yang, Y. *Nat Mater* **2005**, *4*, 864.

(14)   Jung, B. J.; Tremblay, N. J.; Yeh, M.-L.; Katz, H. E. *Chemistry of Materials* **2010**, *23*, 568.

(15)   Campoy-Quiles, M.; Ferenczi, T.; Agostinelli, T.; Etchegoin, P. G.; Kim, Y.; Anthopoulos, T. D.; Stavrinou, P. N.; Bradley, D. D. C.; Nelson, J. *Nat Mater* **2008**, *7*, 158.

(16)   Rogers, J. T.; Schmidt, K.; Toney, M. F.; Kramer, E. J.; Bazan, G. C. *Advanced Materials* **2011**, *23*, 2284.

(17)   Chen, D.; Nakahara, A.; Wei, D.; Nordlund, D.; Russell, T. P. *Nano Letters* **2010**, *11*, 561.

(18)   Yiu, A. T.; Beaujuge, P. M.; Lee, O. P.; Woo, C. H.; Toney, M. F.; Fréchet, J. M. J. *Journal of the American Chemical Society* **2011**, *134*, 2180.

(19)   Peet, J.; Kim, J. Y.; Coates, N. E.; Ma, W. L.; Moses, D.; Heeger, A. J.; Bazan, G. C. *Nat Mater* **2007**, *6*, 497.

(20)   Sun, Y.; Welch, G. C.; Leong, W. L.; Takacs, C. J.; Bazan, G. C.; Heeger, A. J. *Nat Mater* **2012**, *11*, 44.

(21)   Peet, J.; Senatore, M. L.; Heeger, A. J.; Bazan, G. C. *Advanced Materials* **2009**, *21*, 1521.

(22)   Lee, J. K.; Ma, W. L.; Brabec, C. J.; Yuen, J.; Moon, J. S.; Kim, J. Y.; Lee, K.; Bazan, G. C.; Heeger, A. J. *Journal of the American Chemical Society* **2008**, *130*, 3619.

(23)   Yao, Y.; Hou, J.; Xu, Z.; Li, G.; Yang, Y. *Advanced Functional Materials* **2008**, *18*, 1783.

(24)   Moulé, A. J.; Meerholz, K. *Advanced Materials* **2008**, *20*, 240.

(25)   Hoven, C. V.; Dang, X.-D.; Coffin, R. C.; Peet, J.; Nguyen, T.-Q.; Bazan, G. C. *Advanced Materials* **2010**, *22*, E63.

(26)   Woo, C. H.; Beaujuge, P. M.; Holcombe, T. W.; Lee, O. P.; Fréchet, J. M. J. *J. Am. Chem. Soc.* **2010**, *132*, 15547.

(27)   Hung, L. S.; Tang, C. W.; Mason, M. G. *Applied Physics Letters* **1997**, *70*, 152.

(28)   White, M. S.; Olson, D. C.; Shaheen, S. E.; Kopidakis, N.; Ginley, D. S. *Applied Physics Letters* **2006**, *89*, 143517.

(29)   Hau, S. K.; Yip, H.-L.; Ma, H.; Jen, A. K. Y. *Applied Physics Letters* **2008**, *93*, 233304.

(30)   Peumans, P.; Forrest, S. R. *Applied Physics Letters* **2001**, *79*, 126.

(31)   Germack, D. S.; Chan, C. K.; Hamadani, B. H.; Richter, L. J.; Fischer, D. A.; Gundlach, D. J.; DeLongchamp, D. M. *Applied Physics Letters* **2009**, *94*, 233303.

(32)   Schmidt-Hansberg, B.; Sanyal, M.; Klein, M. F. G.; Pfaff, M.; Schnabel, N.; Jaiser, S.; Vorobiev, A.; M$\sqrt{\ }^{o}$ller, E.; Colsmann, A.; Scharfer, P.; Gerthsen, D.; Lemmer, U.; Barrena, E.; Schabel, W. *ACS Nano* **2011**, *5*, 8579.

(33)   DeLongchamp, D. M.; Kline, R. J.; Herzing, A. *Energy & Environmental Science* **2012**, *5*, 5980.

(34)   Zhang, L.; He, C.; Chen, J.; Yuan, P.; Huang, L.; Zhang, C.; Cai, W.; Liu, Z.; Cao, Y. *Macromolecules* **2010**, *43*, 9771.

(35)   He, Z.; Zhong, C.; Huang, X.; Wong, W.-Y.; Wu, H.; Chen, L.; Su, S.; Cao, Y. *Advanced Materials* **2011**, *23*, 4636.

(36)   He, Z.; Zhong, C.; Su, S.; Xu, M.; Wu, H.; Cao, Y. *Nat Photon* **2012**, *6*, 591.

(37)   Small, C. E.; Chen, S.; Subbiah, J.; Amb, C. M.; Tsang, S.-W.; Lai, T.-H.; Reynolds, J. R.; So, F. *Nat Photon* **2012**, *6*, 115.

(38)   Chen, L.-M.; Hong, Z.; Li, G.; Yang, Y. *Advanced Materials* **2009**, *21*, 1434.

(39)   Xu, Z.; Chen, L.-M.; Yang, G.; Huang, C.-H.; Hou, J.; Wu, Y.; Li, G.; Hsu, C.-S.; Yang, Y. *Advanced Functional Materials* **2009**, *19*, 1227.

(40)   Horowitz, G. *Journal of Materials Research* **2004**, *19*, 1946.

(41)   Piliego, C.; Holcombe, T. W.; Douglas, J. D.; Woo, C. H.; Beaujuge, P. M.; Fréchet, J. M. J. *Journal of the American Chemical Society* **2010**, *132*, 7595.

(42)   Baker, J. L.; Jimison, L. H.; Mannsfeld, S.; Volkman, S.; Yin, S.; Subramanian, V.; Salleo, A.; Alivisatos, A. P.; Toney, M. F. *Langmuir* **2010**, *26*, 9146.

(43)   Guo, J.; Liang, Y.; Szarko, J.; Lee, B.; Son, H. J.; Rolczynski, B. S.; Yu, L.; Chen, L. X. *The Journal of Physical Chemistry B* **2009**, *114*, 742.

(44)   Toney, M. F.; Russell, T. P.; Logan, J. A.; Kukuchi, H.; Sands, J. M.; Kumar, S. K. *Nature* **1995**, *374*, 709.

(45)   Huang, F.; Wu, H.; Wang, D.; Yang, W.; Cao, Y. *Chemistry of Materials* **2004**, *16*, 708.